

Gas-side fouling in heat-recovery boilers

Citation for published version (APA):

Beek, van, M. C. (2001). *Gas-side fouling in heat-recovery boilers*. [Phd Thesis 1 (Research TU/e / Graduation TU/e), Mechanical Engineering]. Technische Universiteit Eindhoven. <https://doi.org/10.6100/IR539107>

DOI:

[10.6100/IR539107](https://doi.org/10.6100/IR539107)

Document status and date:

Published: 01/01/2001

Document Version:

Publisher's PDF, also known as Version of Record (includes final page, issue and volume numbers)

Please check the document version of this publication:

- A submitted manuscript is the version of the article upon submission and before peer-review. There can be important differences between the submitted version and the official published version of record. People interested in the research are advised to contact the author for the final version of the publication, or visit the DOI to the publisher's website.
- The final author version and the galley proof are versions of the publication after peer review.
- The final published version features the final layout of the paper including the volume, issue and page numbers.

[Link to publication](#)

General rights

Copyright and moral rights for the publications made accessible in the public portal are retained by the authors and/or other copyright owners and it is a condition of accessing publications that users recognise and abide by the legal requirements associated with these rights.

- Users may download and print one copy of any publication from the public portal for the purpose of private study or research.
- You may not further distribute the material or use it for any profit-making activity or commercial gain
- You may freely distribute the URL identifying the publication in the public portal.

If the publication is distributed under the terms of Article 25fa of the Dutch Copyright Act, indicated by the "Taverne" license above, please follow below link for the End User Agreement:

www.tue.nl/taverne

Take down policy

If you believe that this document breaches copyright please contact us at:

openaccess@tue.nl

providing details and we will investigate your claim.

Gas-Side Fouling in Heat-Recovery Boilers

PROEFSCHRIFT

ter verkrijging van de graad van doctor aan de
Technische Universiteit Eindhoven, op gezag van de
Rector Magnificus, prof.dr. M. Rem, voor een
commissie aangewezen door het College voor
Promoties in het openbaar te verdedigen
op donderdag 4 januari 2001 om 16.00 uur

door

Marinus Cornelis van Beek

geboren te Waalwijk

Dit proefschrift is goedgekeurd door de promotoren:

prof.dr.ir. A.A. van Steenhoven

en

prof.dr.ir. J.T.F. Keurentjes

en de copromotor:

dr.ir. C.C.M. Rindt

This work was financially supported by the centre 'Technologie voor Duurzame Ontwikkeling (TDO)' at the Technische Universiteit Eindhoven.

Copyright © 2001 by M.C. van Beek

All rights reserved.

No part of the material protected by this copyright notice may be reproduced in any form whatsoever or by any means, electronic or mechanical, included photocopying, recording or by any information storage and retrieval system, without permission from the author.

Printed by the Eindhoven University Press.

CIP-DATA LIBRARY TECHNISCHE UNIVERSITEIT EINDHOVEN

Beek, Marinus C. van

Gas-side fouling in heat-recovery boilers / by Marinus C. van Beek.

Eindhoven: Technische Universiteit Eindhoven, 2001.

Proefschrift. – ISBN 90-386-2632-0

NUGI 837

Trefwoorden: ketels / warmteterugwinning / warmte-overdracht / vervuiling / deeltjestransport / deeltjestechologie

Subject headings: boilers / heat recovery / heat transfer / fouling / particle transport / particle technology

Contents

1. Introduction	1
1.1 Fouling in heat recovery boilers.....	1
1.2 Refuse-waste incineration in the Netherlands	2
1.3 Problem definition and approach.....	3
1.4 Outline of this thesis	4
2. Fouling behaviour in refuse-waste incinerators	7
2.1 System description.....	7
2.1.1 Heat recovery boiler.....	8
2.2 Description of boiler fouling.....	10
2.3 Influence of fouling on the boiler performance	11
2.3.1 Boiler temperatures.....	12
2.3.2 Fouling resistance.....	13
2.3.3 System efficiency	15
2.4 Conclusions	17
3. Fouling mechanism	19
3.1 Layer analysis.....	20
3.2 Deposition rate	23
3.3 Transport mechanism	25
3.4 Sticking efficiency	28
3.5 Conclusions	30
4. Numerical deposition model	31
4.1 Problem characterization.....	33
4.2 Flow-model	35
4.3 Flow-model; numerical test cases	40
4.4 Particle transport-model	42
4.5 Deposition on a cylinder in cross-flow.....	46
4.5.1 Global deposition rates.....	47
4.5.2 Local deposition rates and characteristics	48
4.6 Conclusion and discussion	51
5. Theoretical sticking model	53
5.1 Introduction	53
5.2 Two-body collision model.....	54
5.3 Coefficient of restitution	59

5.3.1 Elastic impact.....	59
5.3.2 Limiting elastic case	62
5.3.3 Elastic-plastic impact	65
5.3.4 Overall model for the coefficient of restitution	67
5.4 Friction coefficient and proportionality factor	71
5.5 Numerical sticking model: packing and bed position	71
5.6 Sticking efficiency	73
5.7 Conclusion.....	79
6. Experimental method	81
6.1 Design considerations experimental set-up.....	81
6.2 Description of the set-up.....	82
6.3 Data analysis.....	85
6.4 Error analysis	87
6.5 Experimental conditions and procedure	90
7. Experimental results	95
7.1 Experiments with a solid layer	95
7.2 Experiments with a powdery layer	99
7.2.1 Standard layer	100
7.2.2 Glued layer	104
7.2.3 Powdery layer composed of finer particles	105
7.3 Discussion and conclusion	107
8. Fouling and design	113
8.1 Method and conditions.....	113
8.2 Deposition on a cylinder in cross-flow.....	115
8.3 Deposition in a tube bundle geometry	116
8.4 Design optimization	121
8.5 Design recommendations.....	127
9. Conclusions and recommendations	131
Bibliography	137
Appendices	
A. Deposition rates by diffusion and thermophoresis	143
B. Equation of motion	145
B.1 Equation of motion for a particle	145
B.2 Simplified equation of motion	147
B.3 Particle relaxation time and Stokes number	147
C. Calibration of length scale parameter C_l	149
D. Impact of two bodies	151
D.1 Impact of two-bodies in plane motion.....	151
D.2 Impact of two-bodies in a three-dimensional motion.....	154

E. Model of Rogers and Reed	157
E.1 Elastic impact	157
E.2 Elastic – plastic impact.....	159
E.3 Adhesion energy	160
F. Experimental set-up	163
G. Particle size distributions	165
Nomenclature	167
Summary	173
Samenvatting	175
Nawoord	177

Chapter 1

Introduction

Heat exchangers are applied in waste heat recovery systems to recover energy from different kinds of process streams. Depending on the conditions in the heat exchanger, an insulating layer can form on the heat transfer surface. This process is known as fouling and in some cases it can be so severe that it leads to failure of the system with possible serious economic consequences. Although in most cases fouling does not lead to failure, it does decrease the rate with which energy is recovered because it reduces the overall heat transfer coefficient. This reduction results in a lower efficiency of the heat exchanger.

1.1 Fouling in heat recovery boilers

Many industrial processes drain off heat to the surroundings. This heat is denoted as waste heat. The total amount of waste heat losses is estimated to amount 39% of the total energy consumption [1]. With the ongoing emphasis on the efficient use of energy, much effort is put on the development and application of various heat recovery technologies.

Hot gas streams as flue and process gases present the largest and most readily exploited source of recovered heat [11]. Especially gas streams with a temperature above 500°C are already exploited while streams with a temperature between 200 and 500°C are believed to have the greatest potential [1]. To recover heat from these gas streams, heat recovery boilers are widely applied. The boilers consist of tubes placed in different arrangements like a bundle or a coil with the gas either inside or outside the tubes. The recovered energy is used to heat a second medium like a thermal oil or to generate steam that can be used to heat a process or to generate electricity.

With respect to the recovery of heat from flue and process gases, fouling problems have been reported for the heat recovery from the flue gases of glass furnaces, cement kilns, foundry cupola furnaces and steel converters and for the heat recovery from process gas in a gasification plant [36]. Problems are also found to occur in heat recovery boilers applied for electricity generation, e.g. coal-fired power plants, refuse-waste incinerators and biomass gasification plants. In these applications the fouling takes place in the production process itself and not in the

recovery of energy from a waste stream and the definition of waste heat recovery does not apply anymore. Nevertheless, these applications are included in this study because fouling negatively influences the efficiency of these applications leading to an increased use of fossil fuels.

The mechanisms behind the formation of fouling layers in heat recovery boilers can be expected to exhibit a strong analogy in the different applications. In principle three mechanisms contribute to the growth of a fouling layer being particulation, condensation and chemical reaction. Particulation is defined as the deposition of fly-ash particles (or droplets) from the gas on the heat transfer surface (figure 1.1).

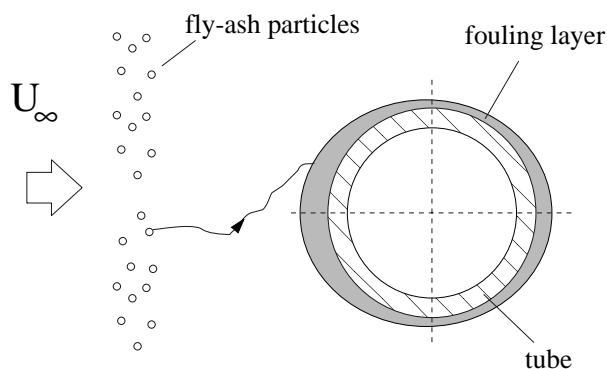


Figure 1.1 Particulation process for tube bundles placed in cross-flow with the flue gas stream

Particles are present in the gas stream as a result of incombustible material in the used fuels or as a result of condensation of gaseous compounds. The effectiveness of particulation is strongly influenced by the degree of sticking of the particles to the surface. This degree of sticking increases when, dependent on the local temperature, a liquid phase appears at the surface of either the particle or the fouling layer. Condensation can also contribute directly to the growth of the layer when condensation takes place on the heat transfer surface itself. Besides particulation and condensation, chemical reactions can also lead to an increase in the deposited mass. Reactions can occur between gaseous compounds and the tube wall (corrosion) or between gaseous compounds and the material already deposited.

This study describes the fouling as occurring in the boiler of a refuse-waste incinerator. Because of the analogy in contributing fouling mechanisms, it is believed that the findings for the fouling in a refuse-waste incinerator are also applicable to gas-side fouling in heat recovery boilers in general.

1.2 Refuse-waste incineration in the Netherlands

In 1986 the Dutch government stated that the amount of refuse-waste generated by households and companies should be minimized. From the resulting amount of waste as much material as possible should be recycled. After recycling, the combustible part of the remaining waste is to be incinerated and only the incombustible part is allowed to be dumped. As a result of this change in policy, the

capacity for waste incineration had to be increased from 2,500 kton per year in 1993 to 5,000 kton per year by the year 2000. To realize this capacity, existing installations were extended and new installations, like in Alkmaar and Moerdijk, were built.

The first objective for incineration was volume reduction of the refuse-waste stream such that massive garbage dumpsites could be avoided. Initially, the generated heat was cooled away by spraying water in the flue gases. Later, heat recovery boilers were placed in the flue gas stream and the recovered heat was used to generate steam. The steam is used to generate electricity or is used for heating purposes. In table 1.1 the evolution of the amount of waste incinerated and the amount of electricity and heat generated by the incinerators is given. It should be noted that the amount of energy generated includes the amount of energy internally used by the incinerator.

Year	Waste Burned kton	Generated Electricity GWh	Heat generated TJ	Number of households
1994	2655	1189	2419	511,000
1995	2888	1323	2421	550,000
1996	3457	1858	3168	752,000
1997	4477	2657	3064	964,000
1998	4902	2859	2646	987,000

Table 1.1 Time evolution of the amount of waste burned in the Netherlands and the amount of energy generated from it [68].

The electricity generated by the incinerators in 1995, 1323 GWh, represented 1.5% of the total use of electricity in 1995 which amounted 89,590 GWh [60] for both households and industry. The total amount of energy generated, electricity and heat, can be converted to the equivalent electricity use of a certain number of households. Assuming that 15% of the energy generated is internally used by the incinerators and that a household uses 3094 kWh of electricity per year, the energy generated in 1995 by refuse-waste incineration in the Netherlands is equivalent to the electricity use of 550,000 households. By 1999 this number has increased to 987,000 which is about 20% of the total number of households.

1.3 Problem definition and approach

In the boiler of refuse-waste incinerators fouling layers develop that negatively influence the overall heat transfer coefficient in the boiler and consequently influence its efficiency. Therefore, it is important to know how the formation of a fouling layer on the heat transfer surface can be minimized. For this purpose several approaches can be followed. One possible approach is to focus on the way the composition of the flue gases with respect to fly-ash content and gaseous species can be altered to yield less fouling. A second approach could be to focus on how the design of the boiler and its tube bundles can be improved to reduce fouling. Another interesting approach could be to focus on an on-line cleaning system and to

find a concept that removes the developing layer. Besides these approaches that start from the given concept of the incinerator, a fourth approach could be to focus on a different concept for refuse-waste incineration combined with heat recovery.

The problem approach chosen in this thesis is to focus on the design of the tube bundle in order to minimize the formation of a fouling layer. The design of the bundle with respect to the tube arrangement, the distance between successive tube rows (pitch) and the shape of the tubes can have a significant influence on the growth rate of the layer. Also modifications like the use of a spoiler in front of the boiler or a differently shaped tube can lead to a strong reduction in the formation of a layer. To obtain insight in the relation between the geometry of the bundle and its fouling tendency, a model will be developed that predicts the growth rate of a fouling layer by the deposition of particulate matter. Using the model, suggestions are made on how to improve the geometry such that fouling is minimized.

In developing a model for the deposition of particulate matter, two critical parts can be distinguished. The first one is the development of a reliable transport model. The particles are brought to the surface by a combination of convection and (turbulent) diffusion. The numerical models available for this type of transport are not yet developed to such a state that they can be applied to the present problem. The second critical part is the proper description of the sticking behaviour of a particle to the surface. An adequate model describing this interaction is essential to obtain a model with which the growth of fouling layers can be predicted.

At this moment already a significant research effort concerns the accurate prediction of the transport of particles. With respect to the sticking of particles only few models are available with hardly any data to verify the models and their important parameters. Therefore, the choice is made to model the fluid flow and particle transport with a commercial package (CFX) and to mainly focus on the development of a sticking model including well-defined experiments. The model for the transport of the particles is adapted in such a way that the results correspond with a reference situation. Although some of the changes might be disputable, it is believed that the developed growth model including sticking gives a reliable indication of the effects expected when varying the geometry of the tube bundle.

1.4 Outline of this thesis

To set the scope of this study and to quantify the effect of fouling on the performance of the boiler, the fouling behaviour as found in the boiler of Dutch refuse-waste incinerators is described in chapter 2. In chapter 3 the controlling mechanisms behind the formation of a fouling layer in a refuse-waste incinerator are retrieved by analysing samples taken from layers as found in the boiler, estimating growth rates for the layers in the boiler and comparing these rates with values reported in different studies for different conditions. Given these controlling mechanisms, in chapter 4 a numerical deposition model based on the package CFX is treated with which growth rates can be calculated as a function of the geometry. This model requires knowledge about the sticking efficiency of fly-ash particles to the surface for which the theory is discussed in chapter 5. To show the validity of

the particle-surface interaction model and to determine some important parameters, an experimental set-up is developed to study the impact of particles on different surfaces. The set-up is described in chapter 6 and the results of the impact experiments are discussed in chapter 7. With the developed sticking model as part of the numerical deposition model, simulations are carried out for various tube bundle geometries. From the results of these simulations, in chapter 8 suggestions are made to improve the design of the tube bundles such that deposition or fouling is significantly reduced. This thesis is ended in chapter 9 with conclusions and recommendations for further research.

Chapter 2

Fouling behaviour in refuse-waste incinerators

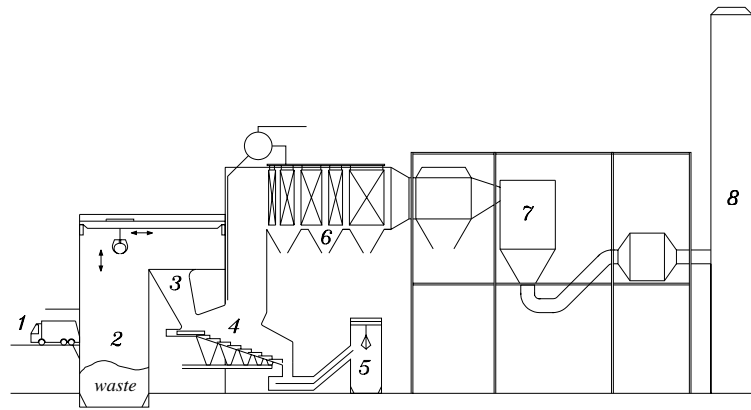
In the heat recovery boiler of a refuse-waste incinerator fouling layers are able to develop on the tubes of the tube bundles that are installed in the boiler. Before the mechanisms responsible for the formation of these layers are discussed, the fouling behaviour is described for two Dutch refuse-waste incinerators in Moerdijk and Alkmaar. For the installation in Alkmaar also the influence of fouling on the performance of the boiler is quantified using plant process data. From these process data the local influence of fouling, being the decrease in the overall heat transfer coefficient of a tube bundle, is derived. Also, the global influence of fouling represented by a change in the efficiency of the boiler is calculated and discussed. The influence of fouling on the overall heat transfer coefficient will be later used in chapter 3 to estimate the deposition rate of fly-ash material onto the boiler tubes.

In section 2.1 a system description is given for the incinerator and its boiler. The fouling occurring in the boiler, as observed during several plant shutdowns, is described in section 2.2. In section 2.3 the influence of this fouling on the performance of the boiler is quantified by an analysis of process data for the incinerators in Alkmaar.

2.1 System description

For two Dutch refuse-waste incinerators, located in Moerdijk and Alkmaar, the fouling behaviour is analysed. These installations have a comparable plant layout as given in figure 2.1.

The refuse-waste is supplied to the plant by trucks that dump the waste in a large bunker. From this bunker the waste is delivered to the burning grid using a crane that puts the waste in one of the feed funnels. From the feed funnels, it is pushed on the burning grid with a feed ram. On the grid it burns with combustion air. A small fraction of the total volume of waste leaves the grid as incombustible ashes and these are stored in a separate bunker. The combustion of waste generates hot flue gases ($T > 1000$ °C) which are cooled with a heat recovery boiler to generate steam. In the heat recovery boiler fouling problems occur.



- | | | | | | |
|---|-------------------|---|----------------------|---|-------------------------|
| 1 | Delivery platform | 4 | Burning grid | 7 | Flue gas cleaning plant |
| 2 | Waste bunker | 5 | Ashes bunker | 8 | Stack |
| 3 | Waste feed funnel | 6 | Heat recovery boiler | | |

Figure 2.1 Plant layout of a refuse-waste incinerator

After the boiler the flue gases are cleaned in the gas cleaning plant before being released to the environment through the stack.

2.1.1 Heat recovery boiler

In figure 2.2 the system layout of the heat recovery boiler for the incinerator in Alkmaar is given. For the same boiler more detailed specifications are given in table 2.1.

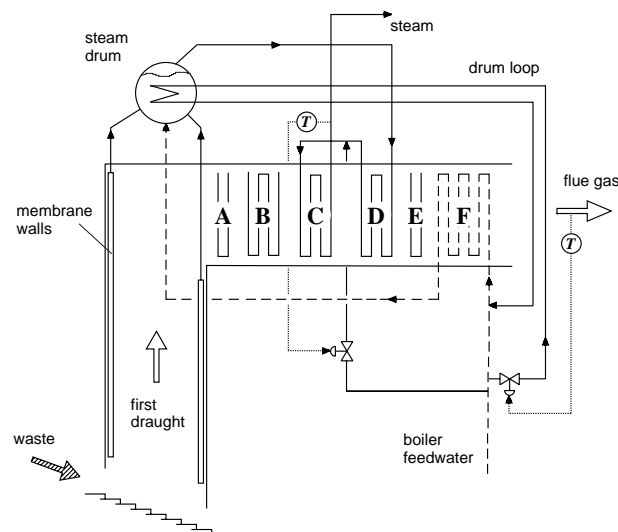


Figure 2.2 System layout of a heat recovery boiler; (A) tube screen evaporator, (B) first evaporator, (C) final superheater, (D) low temperature superheater, (E) the second evaporator and (F) economiser.

The boiler contains a vertical section, called the first draught, and a horizontal section. In the first draught, where heat is mainly transferred by radiation, membrane walls are installed and in the horizontal section, where the heat transfer (except for the entrance) is dominated by convection, tube bundles are installed.

Type Boiler	Double draught	Water/steam temperatures	
Steam production	17 kg/s	boiler feed water	140 °C
pressure	40 bar	outlet economiser	212 °C
temperature	400 °C	entrance final superheater	335 °C
Flue gas temperatures		Flue gas velocity	5 m/s
end of first draught	830 °C	Tube diameter	50 mm
before final superheater	580 °C	Reynolds number	5000
before economiser	340 °C	Tube materials	
boiler outlet	200 °C	superheater	15Mo3
		economiser	St35-8
		Fly ash concentration	4 g/kg

Table 2.1 Boiler specifications for the refuse-waste incinerator in Alkmaar

Before steam is generated, boiler feedwater is preheated in the economisers. This preheated boiler feedwater is fed to the steam drum (with saturated steam on top of water), forming steam in the evaporator stages of the boiler by means of a natural convection system. The major part of the evaporation takes place in the membrane walls of the first draught but water is also evaporated in the membrane walls and the two tube bundles in the horizontal section. Before the steam can be sent to the steam turbine, it needs to be superheated. The superheating is done in two steps: first in the low temperature superheater and later in the final superheater.

Because of a fluctuating heating value of the waste and changing operating conditions due to fouling of the boiler's heat transfer surfaces, control loops are added to maintain a stable steam production. The first and most important loop regulates the amount of steam generated to an operator set value. This is achieved by changing the amount of waste supplied to the burning grid. The second control loop maintains the outlet temperature of boiler flue gases at 200°C which is required for the operation of the flue gas cleaning plant. This is done by varying the amount of water sent through the drum loop which serves as additional heat transfer surface installed in the steam drum. Varying the amount of water sent through the drum loop changes the water-side inlet temperature of the economiser and the amount of energy that is transferred in the economiser. The third control loop regulates the final steam temperature to 400°C by injecting cold boiler feedwater between the low temperature superheater and the final superheater.

Because of expected corrosion problems with soot blowers, a mechanical cleaning system is installed in the boiler to minimize fouling during operation. This system consists of shafts which are mounted in the horizontal section of the boiler. These shafts periodically bring a weight in motion that knocks on the vertical hanging tube bundles. Once a year, the boiler is taken off-line for maintenance. When taking the boiler off-line, the temperature of the boiler is gradually lowered and the cleaning system is continuously operated. In a maintenance period, the boiler is cleaned by means of grid blasting.

2.2 Description of boiler fouling

The deposits found in the horizontal section of the boiler are globally described, to get information on the types of fouling that occur. The descriptions of the deposits are based on the observations made at the start of a boiler maintenance period of the waste incinerator installation in Moerdijk and the installation in Alkmaar. Also, use is made of information given by the boiler manufacturer 'de Schelde' [59]. The fouling will be described in the order in which the bundles appear in the horizontal section, see A up to F in figure 2.2.

The character of the deposits varied over the different tube bundles: tube screen (A), first evaporator (B), final superheater (C), low-temperature superheater (D), and finally the second evaporator (E) and economisers (F). In figure 2.3, the difference in fouling over the bundles is illustrated with a picture of the fouling found on the economisers (F, left picture) and on the superheaters (C, right picture). In the horizontal section of the boiler flue gases are first cooled with an entrance tube screen (A) to reduce the flue gas temperature from about 800 – 850 °C to temperatures slightly below 700 °C. Because of the still sticky nature of the particles in this temperature range, the distance between two rows of tubes is as large as 6 times the tube diameter to prevent serious fouling. On the tubes of the tube-screen a very brittle and soft layer was found of a few millimetres thick. The layer was so brittle that it was not possible to take a sample to be used for microscopy. The outside surface of the layer was very irregular. The layer was coloured successively white/beige, yellowish and dark red with a tiny corrosion layer lining the deposit, going from the outside of the layer towards the tube wall.



Figure 2.3 Deposits observed on the tubes in the final superheater C (left picture) and in the economiser F (right picture) of the boiler in Moerdijk.

After the tube screen the flue gases are cooled to about 580 °C with an evaporator bundle (B). This bundle reduces the flue gas temperature in front of the superheater to eliminate high flue gas temperatures in combination with high tube temperatures, as would be the case when the superheaters were placed directly after the tube-screen, thus preventing serious fouling problems. The fouling observed in

the first evaporator is a hard but still brittle layer of 3 to 5 mm thick. The layer breaks up in pieces of a few centimetres when taking a sample. The outside layer is again coloured white/beige with the inside more yellowish and with a dark red corrosion layer at the interface between the deposit and the tube wall. The outside of the deposit is a smooth but humpbacked surface.

Large deposits were found on the tubes in the final superheater (C). Here the steam reaches its final temperature of 400 °C, which means that the tube surface temperatures are reasonably higher than in the first evaporator of the boilers. The deposition layer can be divided into two parts, an inside layer over the whole perimeter of the tube and an outside deposit only at the upstream side of the tube. The inside layer, about 5 mm thick, had the same characteristics as the layer found on the first evaporator. The outside deposit consisted of separate light grey coloured ridges, 2 to 3 cm high in the middle and gradually decreasing to the edge of the tube. These ridges were oriented upwards as if they were forced to grow in an upward direction. The ridges were not removed by the cleaning system though they were easily separable from the inside layer, were easily broken, and their outside easily crumbled off.

At the entrance of the low temperature superheater (D) the deposition layer showed, although less significant, the same behaviour as in the final superheater. At the entrance, the tube side temperature is higher than at the entrance of the low temperature superheater where the steam enters with the saturation temperature. In the middle of the bundle over the whole circumference of the tubes a hard scale layer of a few millimetres thick was found with the same visible characteristics as the layer in the evaporators. The deposit was lined with a thin corrosion layer. At the outlet the layer was only 1 to 2 millimetres thick, white coloured, had no corrosion layer lining the deposit and had a very regular surface. The characteristics of the layer resemble that of the layer found in the economiser.

In the second evaporator (E) as well as in the economiser (F) a dusty, powdery deposit was found. This layer was in the order of 1 millimetre thick and was very soft and brittle. It easily crumbled off the tubes upon contact and it is rather surprising that this layer was not removed by the cleaning system. This might be explained by the weakness and elasticity of the layer preventing the layer to brake off when the tube bundle starts to vibrate. The deposit did not include a corrosion layer.

2.3 Influence of fouling on the boiler performance

The performance of the heat recovery boiler in a refuse-waste incinerator was also monitored to examine the influence of fouling on its operation in a more quantitative way. For this purpose process data were collected and analysed for one of the Dutch waste incinerator plants, namely the HVC Alkmaar household waste incineration plant. The following data were recorded: temperatures on the gas as well as on the steam side, steam pressures, flow rates of the boiler feedwater and steam output, the flow rate of the combustion air and its temperature, the amount of waste burned (on a daily basis), and the oxygen concentration of the wet flue gases.

The total period for which the data were collected was 25 April until 15 November 1996 and was chosen such that the first major shut-down of the boiler was included to quantify the difference between the system's operation in fouled and clean conditions. This period was also selected because in this period plant operation was more stable with respect to steam output, amount of combustion air, and oxygen concentration in the flue gases than in the first months of operation. This makes changes in operation due to fouling more apparent.

2.3.1 Boiler temperatures

The influence of fouling is best observed from the temperature profile of the flue gas over the horizontal section of the boiler. Because fouling results in a lowered heat transfer coefficient, less heat can be transferred with the same surface. This means that the temperature drop of the flue gases over a tube bundle will decrease and that the flue gas temperatures over the whole section will increase with time.

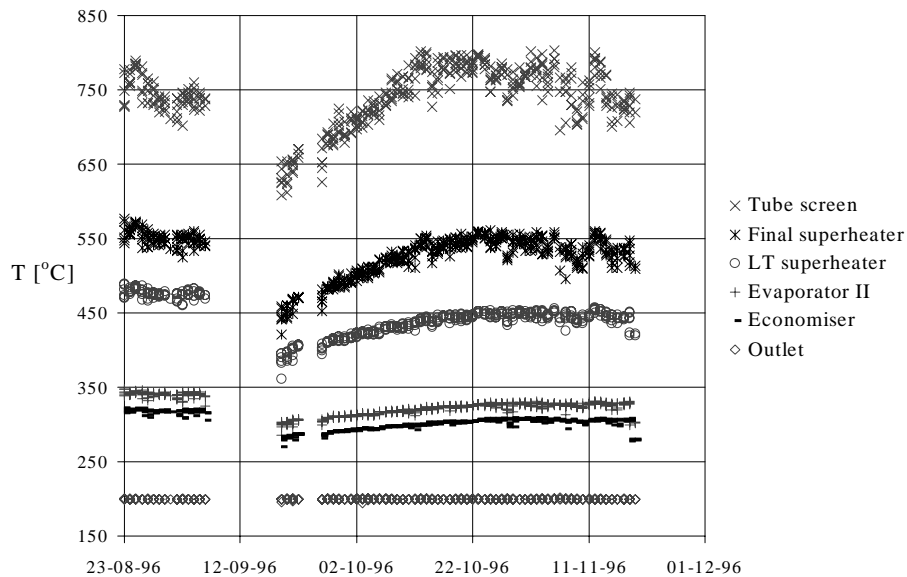


Figure 2.4 Flue gas temperatures at various positions in the boiler

From figure 2.4 where the flue gas temperatures are given as function of time, it follows that immediately after the major shut down around 12-09-1996 the flue gas temperatures start to rise. After about one month the temperatures in the boiler stabilize to a final temperature.

With time or with ongoing fouling the outlet temperature of the boiler flue gas would also start to rise. This temperature increase is not allowed in the installation and to maintain a constant boiler outlet temperature the heat transferred by the economisers is increased by lowering the water-side inlet temperature of the economiser. The inlet temperature is lowered by sending less water through the drum loop and is shown over time in figure 2.5.

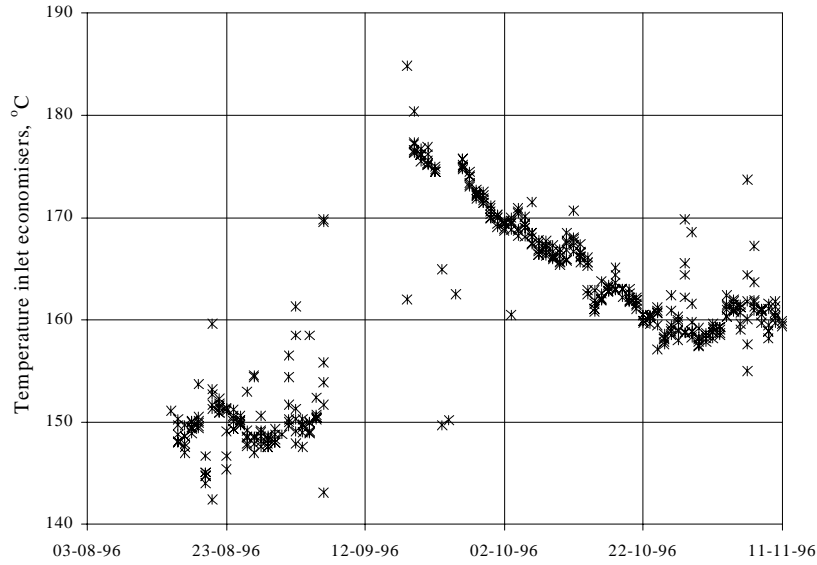


Figure 2.5 Inlet temperature economisers as a function of time

From figure 2.5 can be seen that under clean conditions the water-side inlet temperature was indeed the highest and as fouling occurs the inlet temperature decreases such that a constant outlet temperature is maintained of the boiler flue gas.

2.3.2 Fouling resistance

The influence of fouling on the performance is shown by monitoring the overall heat transfer coefficient of two bundles in the boiler. The decrease in heat transfer coefficient is expressed by the fouling resistance. This quantity will also be used in chapter 3 to estimate the deposition rate. The heat transferred by a tube bundle is given by:

$$\dot{Q} = U_o A_o F LMTD \quad (2.1)$$

with \dot{Q} the heat transfer rate of the bundle, U_o the overall heat transfer coefficient, A_o the surface of the tube bundle and $LMTD$ the log mean temperature difference for the tube bundle multiplied by a correction factor F to account for the tube bundle not being an ideal parallel or counter flow heat exchanger. Because of the large number of passages over the bundle this factor can be assumed equal to unity [67]. From the retrieved process data, the overall heat transfer coefficient is calculated, using equation 2.1, for a 50 day period after the boiler had been cleaned by grid blasting. In this equation the heat transferred by the tube bundle, \dot{Q} , is calculated using the measured steam flow rate. The $LMTD$ is calculated using the in- and outlet temperatures on the water/steam side and the flue gas temperatures measured in front and behind the relevant tube bundle. The design-values of these quantities are given in table 2.1.

The fouling resistance, R_f , is used to express the decrease in the overall heat transfer coefficient, as given by:

$$R_f = \frac{1}{U_o} - \frac{1}{U_{o,c}} \quad (2.2)$$

with $U_{o,c}$ the overall heat transfer coefficient under clean conditions. In equation 2.2, it is assumed that the heat transfer coefficient h_o from the outer surface (either the tube wall or the surface of the fouling layer) to the flue gas flow is not affected by the formation of a deposition layer.

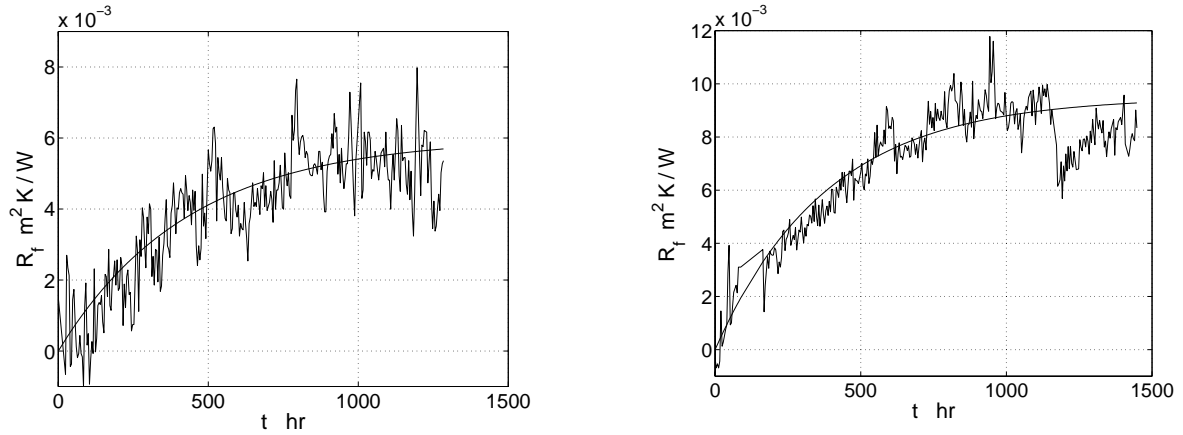


Figure 2.6 Fouling resistance as a function of time for the superheater (left figure) and economiser (right figure).

In figure 2.6, the fouling resistance is shown as a function of time for respectively the economiser and the final superheater tube bundle. It appears that both curves level off to an asymptotic value implying that the overall heat transfer coefficient reaches a time-averaged constant value denoted with $U_{o,f}$. The asymptotic behaviour is probably caused by the removal of deposited material due to erosion and fluid stresses. The fouling curve can be approximated by:

$$R_f = R_{f,\infty} \left(1 - e^{-t/\tau} \right) \quad (2.3)$$

with $R_{f,\infty}$ the asymptotic value and τ the time constant which is defined as:

$$\tau = \frac{R_{f,\infty}}{\left. \frac{dR_f}{dt} \right|_{t=0}} \quad (2.4)$$

Both the asymptotic value and the time constant are given in table 2.2 together with the initial and the final overall heat transfer coefficient for the economiser and superheater tube bundle.

	$U_{o,c}$	$U_{o,f}$	$R_{f,\infty}$	τ
Tube bank	W/m ² K	W/m ² K	m ² K/W	hr
Economiser	41 ± 5	30 ± 5	0.009 ± 0.001	380 ± 10
Final superheater	65 ± 5	45 ± 5	0.006 ± 0.001	430 ± 10

Table 2.2 Overall heat transfer coefficient and fouling resistance for economiser and superheater tube bundle.

From table 2.2, it appears that fouling for both the economiser and the final superheater results in a decrease in the overall heat transfer coefficient of about 27%. This implies that the thin and powdery layer found on the economiser has the same relative influence on the overall heat transfer coefficient as the thick and sintered deposit formed on the tubes of the superheater bundle. The large influence of the thin powdery layer implies that the thermal conductivity of this layer is much smaller than that for the superheater deposit.

2.3.3 System efficiency

From the acquired data the system efficiency of the boiler is calculated. For a waste incinerator and in particular the heat recovery boiler, the efficiency can be determined by two different methods. The first method calculates the efficiency directly from the ratio of the useful amount of energy produced, in this installation the energy content of the steam generated, and the amount of energy supplied to the system. The energy supplied to the system consists of the sensible heat in the air supplied to the furnace and the energy flux supplied with the refuse-waste given by the mass flow rate of the waste and its heating value. For refuse-waste this heating value is not known ‘a priori’ nor measured. Therefore in case of a refuse-waste incineration plant, it is more suitable to calculate the efficiency using the indirect method as defined in DIN1942.

In the indirect method the total amount of energy supplied to the system is set equal to the sum of the amount of steam generated and the energy losses of the system. The system efficiency can then be written as:

$$\eta = \frac{\dot{Q}_{st}}{\dot{Q}_{st} + \sum \dot{Q}_{loss}} \quad (2.5)$$

with \dot{Q}_{loss} representing the different energy losses in the system. These losses consist of the heat content of the flue gases leaving the boiler, the heat content and the heating value of a small fraction of combustible material that remains in the slacks and fly-ashes, the heat loss from the boiler itself to the environment and the not used heating value of the CO in the flue gases. For the installation in Alkmaar, in table 2.3 the energy flows are given as derived during measurements done by KEMA [26].

	Energy flows	
	kW	in % of total
Steam generated	44426	85.1%
Boiler flue gases	6438	12.3%
Slacks	838	1.6%
Heat losses	436	0.8%
Fly-ash	69	0.1%
Unburned CO in flue gases	2	0.0%
Subtotal losses	7783	14.9%
Energy supplied to system	52209	100%

Table 2.3 Energy flows as found during KEMA measurements (mass flow rate waste 4.97 kg/s) for the refuse-waste incinerator in Alkmaar

The efficiency of the boiler is given in table 2.3 by the energy flow for the steam generated relative to the total energy supplied to the system. The heat content of the flue gases leaving the boiler is the most important energy loss for the boiler that can be calculated from:

$$\dot{Q}_{loss,g} = \dot{m}_g c_p (T_g - T_{ref}) \quad (2.6)$$

with \dot{m}_g the mass flow rate of the flue gases leaving the boiler.

A change in efficiency because of fouling would manifest itself in the temperature of the flue gases at the end of the boiler. However, for the incinerator in Alkmaar this temperature is, due to limitations set by the flue gas cleaning, regulated by the drum loop and kept constant over time at 200 °C. So, for this installation no change in efficiency is noticeable. Because of the application of the drum loop the efficiency is initially not equal to the maximum efficiency.

If initially no feedwater would be sent through the drum loop, the water-side inlet temperature before the economisers would be around 142 °C instead of the 175 °C in the actual case, see figure 2.5. This lower inlet temperature would give a higher driving force for the economisers and it can be calculated that in that case the flue gas temperatures are cooled from 290 °C down to almost 170 °C which is a difference of 30 °C with the actual outlet temperature of 200 °C. This extra recovered heat would increase the efficiency of the boiler by almost 2%.

Thus, with the system configuration for the boiler in the refuse-waste incinerator in Alkmaar a stable system efficiency is achieved. However, initially this efficiency is about 2% lower than the maximum obtainable efficiency of the installation. For older installations no precautions, like a drum loop, were taken to maintain a constant outlet temperature of the boiler flue gases and for these installations it is known that the efficiency of the installation indeed drops with about 2 to 4% over time [68].

2.4 Conclusions

The character of the fouling layers developing on the tubes in the boiler of a refuse-waste incinerator is found to vary strongly over the different bundles. In the final superheater a thick and sintered layer was found where in the economiser only a thin powdery layer had formed. From the analysis of process data, it was established that both type of layers resulted in a 27% drop in the overall heat transfer coefficient.

With respect to the efficiency of the boiler no noticeable change is found because of fouling. This stable efficiency is the result of the drum loop applied in the installation in Alkmaar. Without this drum loop the initial efficiency of the boiler would be about 2% higher than the value measured by KEMA (table 2.3) of 85%. With time the efficiency would then drop with the same 2% which is comparable to the decrease known for older installations. Considering an average decrease in efficiency of 2% for the boiler in a refuse-waste incinerator, fouling results in a not recovered amount of energy for all incinerators that is equivalent to the energy use of 20,000 households.

Chapter 3

Fouling mechanism

The mechanism of fouling of heat transfer surfaces in a combustion environment is complex because it consists of condensation and chemical reaction in addition to particulation. Particulation, the deposition of particulate matter on the tubes in the boiler, is responsible for most of the deposited mass [13]. The deposition rate of particles is determined by the transport of particles to the surface and the sticking efficiency of these particles at the surface.

Fly-ash particles are transported to the heat transfer surface as a result of different phenomena. In the flue gases of a refuse waste incinerator, particles with sizes ranging from sub-micron to a few hundred microns are present. The particles are transported towards the tubes that are placed in cross-flow with the flue gases. For sub-micron particles transport is diffusion controlled. Due to the temperature gradient in the heat exchanger, these particles experience a force in the direction of the cooler surface. This so-called thermophoretic effect augments the transport of particles to the surface for particles with sizes up to a few micron. The velocity with which these particles arrive at the surface is low, and, therefore, most of them are captured by the surface and stick. For particles larger than a few microns, inertia becomes important and the transport changes to inertia-controlled. With this mechanism transport rates are at least one order of magnitude larger than for diffusion and thermophoresis. The higher transport rates not automatically result in higher deposition rates because the particles reach the surface with higher velocities. Therefore, not all particles stick but some experience a rebound. The sticking efficiency in this case is a function of the kind of layer already deposited and increases strongly when a liquid phase appears at the surface of the deposit or on the particle itself.

This chapter focuses on the mechanisms that control the deposition of particulate matter on the tubes in the boiler. In section 3.1 samples taken from the layer found on the final superheater and on the economiser in the boiler are analysed with respect to composition and structure. In section 3.2 the deposition rate is estimated from the fouling resistance as calculated in the previous chapter for the economiser and the superheater tube bundle. Comparing these deposition rates with

* This chapter has been accepted for publication in Journal of Heat Transfer Engineering [6]

the expected rates for a situation with only transport of particles by diffusion and thermophoresis, in section 3.3 the controlling transport mechanism is derived. In section 3.4 the deposition rates are compared with rates reported in literature for different conditions. Based on this comparison the different sticking mechanisms are discussed and the controlling mechanisms for the fouling as occurring in the boiler of a refuse waste incinerator are derived.

3.1 Layer analysis

The fouling was visually examined during a boiler shutdown of the refuse waste incinerators in Alkmaar and Moerdijk. To analyse the structure and composition of the fouling layers, samples were taken of the layers that were still present on the tubes after the boiler had been taken off-line. One sample was taken from the deposit on the final superheater and one from a powdery deposit formed on the evaporator bundle prior to the economiser. The samples were analysed using XRD (X-ray Diffraction), EPXMA (Electron Probe X-ray Micro Analysis) and SEM (Scanning Electron Microscopy).

From the visual examination, it appeared that the character of the fouling layer strongly varied as a function of local gas and tube temperatures. Thick deposits were found on the final superheater where the steam reaches its final temperature of 400 °C. Contrary, the deposit on the economiser was thin and powdery (see figure 3.1).

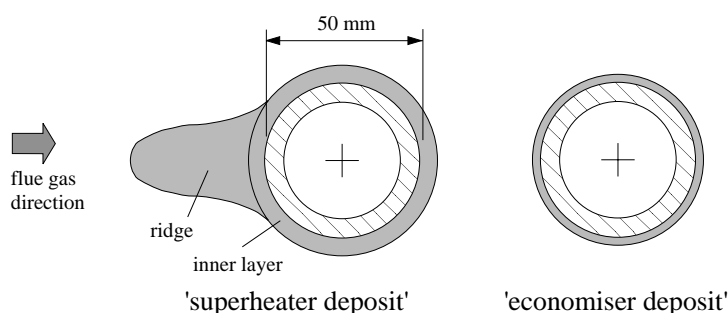


Figure 3.1 Schematic deposit shapes found on the superheater and the economiser bundle.

Final Superheater

The deposit on the final superheater consisted of a hard and brittle inner layer over the whole perimeter of the tube with a thickness of about 4 mm. This inner layer was lined at the tube side with a very thin corrosion layer. At the upstream side of the tube, on top of the inner layer, 2 to 3 cm high grey coloured ridges had formed. The ridges were easily separable from the inner layer and crumbled off easily.

A sample taken from the deposit at the upstream side of a tube in the first row of the superheater tube bundle was analysed to determine the structure and composition of the layer. In figure 3.2 an overview, made using Scanning Electron Microscopy, is given of a cross-section of the 4 mm thick inner layer of this deposit.

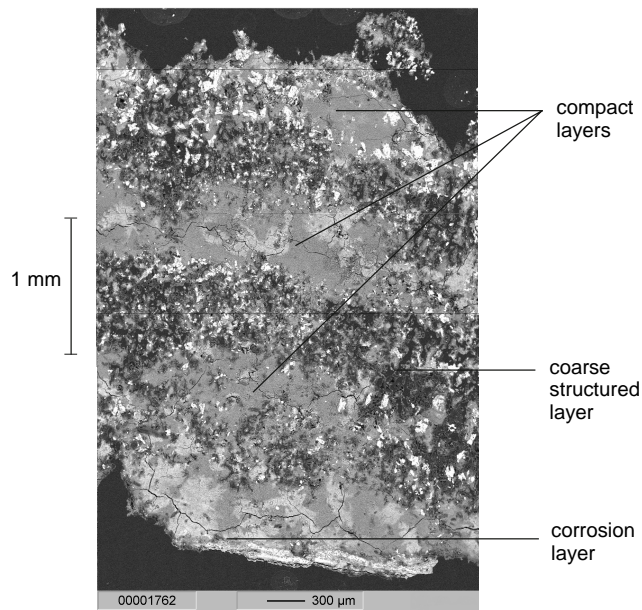


Figure 3.2 Cross-section of the inner layer found on the final superheater tubes of the boiler in Moerdijk

The cross-section shows a regular pattern of alternating compact and coarser structured sub-layers that are each about 0.5 mm thick. The coarse structured layer that looks more porous than the compact layer consists of particles with sizes ranging from 5 to 30 μm that are embedded in a matrix material. The matrix, built of particles with sizes in the order of 1 μm , consists from sulphates of sodium, potassium and zinc, probably in a mixed compound with silica because this element was also detected homogeneously over the deposit. The elements detected by EPXMA correspond with the elements found in an XRD-analysis of a grinded sample of the deposit; Na, Al, Si, S, Cl, K, Ca, Fe, Zn, and Pb.

The compact layer is composed of the same fine-structured matrix with particle inclusions up to 30 μm . Within this matrix, local structures are found with sizes much larger than that of the particles present. In these structures, there appeared to be a clear separation between the detected elements as indicated in figure 3.3.

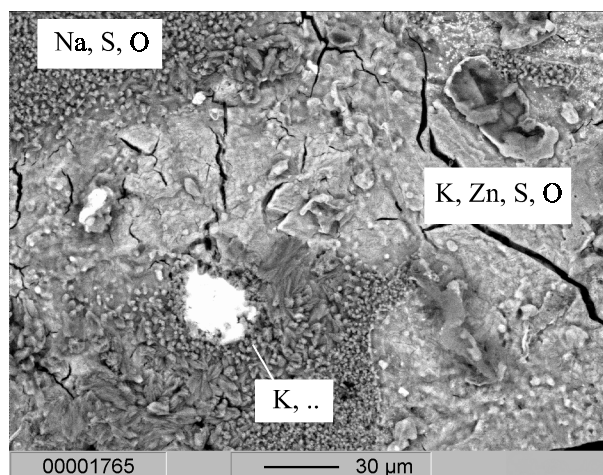


Figure 3.3 Element distribution in one of the local structures as detected in the compact layer in the superheater deposit.

The detected distribution in elements over the local structure in the sample of the superheater deposit indicates the formation of a melt in the deposit. In case of the formation of a melt in a multi-component system, it is possible that different phases separate. It can be seen that over a distance much larger than the particle sizes found in the deposit, one region in the compact layer shows sodium but no potassium and zinc, where in another region there is no sodium but potassium and zinc. The formation of a melt in deposits taken from refuse waste incinerators was also found by Kerekes [34]. Kerekes reported peaks in the thermographs made of these deposits, indicating melting, in the temperature range between 400 and 450 °C, which is just above the tube temperatures occurring in the final superheater. These temperatures were found to coincide with melting points of the binary system $\text{Na}_2\text{SO}_4 \cdot \text{ZnSO}_4$ and the tertiary system $\text{Na}_2\text{SO}_4 \cdot \text{ZnSO}_4 \cdot \text{K}_2\text{SO}_4$. The elements in these systems correspond with the detected elements over the structure as given in figure 3.3.

The formation of a melt in the superheater deposit can be part of an explanation for the layered structure of the superheater deposit given schematically in figure 3.2. The reasoning is that due to the formation of a deposit the surface temperature at the interface between deposit and the flue gas increases and at a certain moment it reaches the melting point of the deposited substances. Although the temperature below the interface is lower, a melt once initiated at the surface of the deposit can proceed for a certain distance into the deposit. Melting starts at a local point in the deposit where the melting temperature is determined by the local composition. Once a melt is formed more particles are brought into contact with the melt and the global composition can change due to the heterogeneity of the materials deposited resulting in possible lower melting temperatures. Another possibility is that the composition of the melt can have an eutecticum with a temperature below the local temperature such that the melt can persist for lower temperatures. The formation of a melt results in a higher thermal conductivity of the layer, which, on its turn, leads to a lower surface temperature. The surface temperature then becomes lower than the critical temperature for melting to occur and the layer solidifies. Further deposition, however, makes the surface temperature to increase again and the process repeats itself.

Economisers

On the tubes of the economiser, a thin, white and powdery layer had formed. The layer, only a few millimetres thick, is soft and weak such that upon the slightest contact the layer is removed. It should be noted that despite the weakness of the layer, the layer was not removed by the mechanical cleaning system installed in the boiler. The deposit found on the evaporator bundle, prior to the economiser, has the same character as on the economiser except that the layer is somewhat stronger, which made it possible to take a sample that could be used for electron microscopy. The sample was taken from the upstream side of a cylinder positioned in the last row of tubes in the evaporator bundle.

Pictures taken of a cross-section of the economiser sample showed a porous, fine structured layer consisting of particles of 1 to 10 μm . The absence of larger particles in the deposit indicates that the powdery layer has a lower sticking efficiency compared to that of the superheater deposit. This is in agreement with the appearance of a liquid phase in the layer of the superheater.

Fly-ash

For both analysed deposits the particle sizes observed (1 to 10 μm for the economisers and 1 to 30 μm for the superheater) represent only a small fraction of the particle sizes in the fly ash. The size distribution of the fly ash was measured using a sample taken from the boiler in Moerdijk. The cumulative mass distribution of the fly ash is given in figure 3.4.

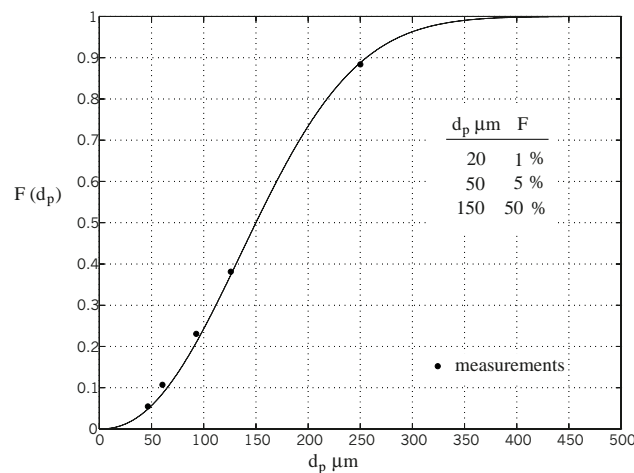


Figure 3.4 Fly-ash size distribution as measured for the boiler in Moerdijk

The fly ash sample was collected at the bottom of the boiler at the position of the tube screen and was analyzed using standard sieves. The sampling position is likely to have affected the measured distribution. However, because the measured distribution matches a distribution measured earlier for a Dutch refuse waste incinerator, it is regarded as representative for the size distribution in the boiler.

3.2 Deposition rate

The fouling resistances given in section 2.3.2 are used to estimate the deposition rate for both the economiser and the superheater. Information about this deposition rate is important to know because it gives insight in the mechanisms controlling the deposition of particulate matter. When assuming the influence of the curvature to be negligible, the fouling resistance is determined by:

$$R_f = \frac{\delta_f}{k_f} \quad (3.1)$$

with k_f the thermal conductivity of the layer. The change in thickness of the layer δ_f can be written as the net result of deposition and removal divided by the effective density of the deposited material:

$$\frac{d \delta_f}{d t} = \frac{\phi_d - \phi_r}{\rho_f} \quad (3.2)$$

with ϕ_d and ϕ_r respectively the deposition and removal rates in mass per unit time and per unit area, and ρ_f the effective density of the deposited material being a function of the porosity of the deposit. Following Kern and Seaton [35], an asymptotic behaviour as defined in equation 2.3 is found for the fouling resistance when it is assumed that the deposition rate is constant and the removal rate is proportional to the thickness of the already deposited layer. In that case, initially the removal rate is negligible and the change of the fouling resistance can be written as:

$$\left. \frac{d R_f}{d t} \right|_{t=0} = \frac{\phi_d}{\rho_f k_f} \quad (3.3)$$

from which, using the definition for the time constant given in equation 2.4, the deposition rate can be derived:

$$\phi_d = \frac{\rho_f k_f R_{f,\infty}}{\tau} \quad (3.4)$$

In the derivation of equation 3.4, it is assumed that the growth rate of the layer is constant over both the perimeter and along the length of the tube surface. The error introduced is expected to be small, because the thickness of the inner layer found on the superheater as well as the powdery deposit showed only a small non-uniformity.

To evaluate the deposition rate in addition to the already known parameters from the fouling curve, the thermal conductivity and effective density of the deposit need to be known. Using equation 3.1, the characteristic thermal conductivity of both layers can be estimated from the calculated asymptotic heat transfer resistance and the observed layer thickness. The effective density is estimated by weighing the different samples and measuring their volume. The thermal conductivity and the effective density are given in table 3.1 for the layer found on the final superheater and on the economiser.

	$\delta_{f,\infty}$	$k_{f,\infty}$	ρ_f	ϕ_d
Tube bank	mm	W/mK	kg/m ³	kg/m ² s
Economiser	1 ± 0.5	0.12 ± 0.07	1.3 ± 0.1 · 10 ²	10 ± 5 · 10 ⁻⁷
Final superheater	4 ± 0.5	0.8 ± 0.3	1.9 ± 0.1 · 10 ²	6 ± 4 · 10 ⁻⁶

Table 3.1 Layer properties and deposition rates for the economiser and superheater

The thermal conductivity of the powdery layer, given in table 3.1, proves to be much smaller than that of the superheater deposit. Both conductivities correspond with the indicative values given in Raask [52], 0.1 W/mK for a powdery deposit and 1 W/mK for a sintered deposit, and also agree with values found in thermal conductivity measurements for different slags by Wain et al. [70]. The difference in density between the economiser and the superheater deposits is the result of a difference in porosity that is likely the result of melting in the superheater deposit. The deposition rate is calculated using equation 3.4 and given in table 3.1. The deposition rate found for the economiser is a factor of 5 smaller than that found for the superheater.

3.3 Transport mechanism

The deposition rate of particles on a tube in cross-flow is a function of the particle sizes present in the flue gases that determine the controlling mode of transport. The different modes of particle transport are given in figure 3.5.

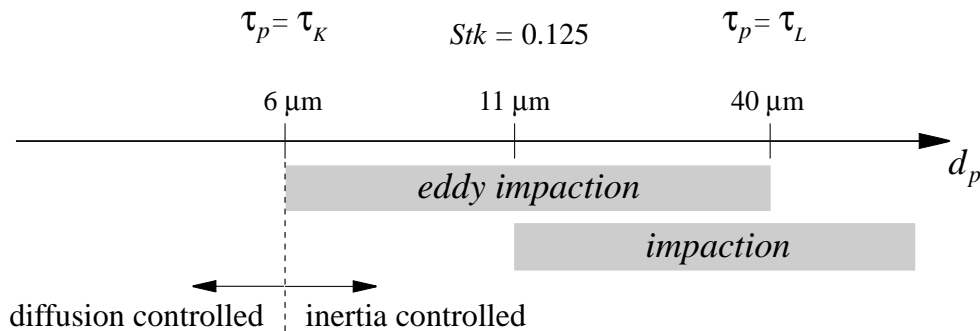


Figure 3.5 Transport regimes as a function of particle size

For small particles, approximately sub to a few microns in diameter, transport is controlled by diffusion and thermophoresis while for larger particles transport rates increase because inertia becomes important. A measure for the importance of the inertia of the particle is given by the particle relaxation time τ_p , the time scale in which a particle can adapt to a change in the fluid velocity. The particle relaxation time is defined by (see Appendix B):

$$\tau_p = \frac{\rho_p d_p^2}{18 \mu_g} \quad (3.5)$$

with ρ_p the particle density, d_p the particle diameter, and μ_g the dynamic viscosity of the gas. The particle relaxation time is made dimensionless using the mainstream velocity U_∞ and the radius of the tube $\frac{1}{2} D_{tube}$ yielding the Stokes number Stk :

$$Stk = \frac{U_\infty \tau_p}{\frac{1}{2} D_{tube}} \quad (3.6)$$

For the flow around a cylinder a distinction needs to be made between particle transport driven by the action of turbulent eddies in the flow and transport because particle paths deviate from the mean flow. These regimes are denoted with eddy-impaction and impaction, respectively.

Transport by eddy-impaction becomes important when the particle is not capable anymore to follow the smallest fluid fluctuations that are characterized by the Kolmogorov time scale τ_K , so when $\tau_p > \tau_K$. Eddy-impaction vanishes when the particle cannot even follow the largest turbulent fluid motions characterized by the macro time scale τ_L , so when $\tau_p > \tau_L$. Using these criteria the particle range defining the eddy-impaction regime can be found by substituting τ_K and τ_L for the particle relaxation time τ_p in equation 3.5. For a turbulent flow, the time scale for the largest motions respectively the smallest or Kolmogorov motions are defined by [41]:

$$\tau_K = \sqrt{\frac{\nu_g L}{U^3}}, \quad \tau_L = \frac{L}{U} \quad (3.7)$$

with L and U the length and velocity scale of the most energetic eddies and ν_g the kinematic viscosity of the gas. Based on LDA measurements in tube bundles, L is taken equal to the radius of the tube and U to half the mainstream velocity [3]. For a mainstream velocity of 5 m/s and a tube diameter of 5 cm, the Kolmogorov time scale is $2 \cdot 10^{-4}$ s and the macro time scale $1 \cdot 10^{-2}$ s. So, by substituting these values for τ_p in equation 3.5, it is found that inertia starts to be important in particle transport for particles of 6 μm and that eddy-impaction ends for particles of 40 μm . The particle density is taken as 2600 kg/m^3 and a dynamic viscosity of $3 \cdot 10^{-5} \text{ kg/ms}$.

Transport by impaction starts for particles with Stokes numbers above a critical value of about 0.125 [27]. This critical value is based on numerical integration of the equation of motion for a particle using a velocity field based on potential flow (see Appendix B). Using the same values for the relevant parameters, the impaction regime starts for particles with a diameter above 11 μm .

For the particle sizes found in both deposits, up to 30 μm , inertia-controlled transport influences the growth of both layers. For the economiser, where particles up to 10 μm were found, inertia-controlled transport will be mainly in the eddy-impaction regime because the sizes are mostly below the critical diameter for impaction. For the superheater with particles up to 30 μm , inertia-controlled transport will also include impaction.

To determine the relative importance of inertia-controlled transport for the deposition at the economiser, in table 3.2 the deposition rates found in this study for the economiser are compared with the deposition rates measured by Mutsaers in a configuration where transport is only due to diffusion and thermophoresis.

Study	Re	d_p μm	$C_{p,d}$ g/m^3	T_g $^\circ\text{C}$	T_w $^\circ\text{C}$	ϕ_d $\text{kg}/\text{m}^2\text{s}$
This study; economiser	5600	0.1-400	0.10*	280	170	$1 \cdot 10^{-6}$
Mutsaers [47]: original data	87	0.12	0.14	477	241	$3 \cdot 10^{-7}$
Mutsaers [47]: scaled data	5600	0.12	0.02*	280	170	$4 \cdot 10^{-9}$

Table 3.2 Measured deposition rates as function of particle size and process conditions. * The concentration is based on the cumulative mass distribution curve for the fly-ash in the waste incinerator as given in figure 3.4 with a cut-off diameter of 50 μm for the economisers and the superheater and 5 μm for the scaled data of Mutsaers.

Mutsaers [47] measured the deposition of Na_2SO_4 dust particles on air-cooled cylindrical tubes in cross-flow with the flue gases. In the laboratory set-up, the sub-micron sized particles were generated by adding an aspirated sodium sulphate solution to the propane-air mixture fed to the burner. At the upstream stagnation point of the cylinder, a deposition rate of 20 $\text{mg}/\text{min m}^2$ was found. Mutsaers used a Stanton relation, explained in appendix A, to predict the deposition rates. Comparison with the measured deposition rates showed good agreement.

As can be seen from table 3.2, the conditions for the economisers are different from the conditions encountered in the experiments of Mutsaers. Therefore, to compare the two, the results of Mutsaers are scaled to the conditions as apply for the economisers. The scaling is done using the Stanton relation that was also used by Mutsaers and of which the functionality is given by:

$$St = \frac{\phi_d}{C_{p,d} U_\infty} = St_o \cdot f \left(d_p, \alpha_{T,w}, \frac{T_g - T_w}{T_w}, \dots \right) \quad (3.8)$$

In this relation the standard Stanton number St_o which accounts for the transport to a cylinder in cross-flow by convection and diffusion is multiplied by a correction factor f taking into account the influence of thermophoresis on the mass transfer to the cooler surface (see appendix A). The correction factor, derived by Rosner [57], is a strong function of the thermal diffusion factor $\alpha_{T,w}$ evaluated at the wall temperature. As is shown in appendix A, for Na_2SO_4 particles this factor drops significantly below temperatures of about 250 $^\circ\text{C}$. Because the average wall temperature is only 170 $^\circ\text{C}$ the correction factor becomes 5 yielding a Stanton number for the scaled case of $4 \cdot 10^{-5}$. The deposition rate expected for the economiser due to the transport by diffusion and thermophoresis then becomes $4 \cdot 10^{-9}$ $\text{kg}/\text{m}^2\text{s}$. This value is found by multiplying the Stanton number with a particle concentration of 0.02 g/m^3 and a main stream velocity of 5 m/s . The used particle concentration is based on the cumulative size distribution given in figure 3.4, a cut-off diameter of 5 μm and a fly ash concentration of 4 g/kg . In these calculations the

particle diameter is maintained at $0.12\ \mu\text{m}$ as was used in the experiment of Mutsaers. Because condensation in flue gases is known to give particles between 0.1 and $0.3\ \mu\text{m}$, the calculation is repeated using a particle size of $0.24\ \mu\text{m}$ resulting in a deposition rate of $9 \cdot 10^{-9}\ \text{kg}/\text{m}^2\text{s}$. The average deposition rates calculated using the Stanton relation are two orders of magnitude smaller than the deposition rates estimated for the economiser, which indicates that most of the deposited mass is due to inertia-controlled transport.

3.4 Sticking efficiency

Particulate deposition is the combined effect of transport and sticking. The latter is a strong function of the local gas and tube temperatures. The effect of these conditions is shown in table 3.3 where the measured deposition rates are compared with results reported in literature. Because the deposition rates can be expected to be proportional to the mass concentration of the particles, they are converted to characteristic deposition velocities (V_d) by dividing the deposition rate by the concentration ($C_{p,d}$). Because deposition rates are relatively small, it is assumed that the fly ash concentration and size distribution are equal for both the superheater and the economiser.

Howarth et al. [20,25] measured deposition rates using a fouling probe installed in a refuse waste incinerator plant at Toulon, France. The cylindrical fouling probe consisted of two halves with one sample at the upstream side and one downstream. Deposition rates were calculated from a change in weight of the sample over a period of a few hours. For a few characteristic runs, the results for the deposition at the upstream side are given in table 3.3. In the experiments of Howarth the mass loading of fly ashes amounted $2\ \text{g}/\text{m}^3$. Based on the particle sizes found in the deposits, for a refuse waste incinerator only a minor part of the particle size distribution results in deposition. Therefore, to calculate the deposition velocity for the experiments of Howarth, the particle concentration is taken only 5% of the total mass loading.

Deposition rates are also reported in Wessel and Wagoner [69,72] for a subscale test furnace firing finely ground coal. Deposition was measured for an array of closely spaced air-cooled tubes. Particle sizes ranged from sub-micron up to $20\ \mu\text{m}$. In the experiments the partially sintered deposition layer grew about $2\ \text{mm}$ per hour. For the above studies, the conditions such as the particle sizes, local gas and tube temperatures (T_g and T_w), and the measured deposition rates are given in table 3.3.

The deposition rates found for the economiser and those measured in run T-4-01 of Howarth, given in table 3.3, are an order of magnitude smaller than the deposition rate for the superheater and run T-2-06. In view of the range of particle sizes present in the flue gases, the transport mechanism is expected to be the same in both cases. Therefore, the observed difference is the result of a difference in the sticking efficiency that is known to be a strong function of gas and wall temperatures. The enhanced sticking efficiency is usually associated with the

existence of a liquid phase in the deposit that is confirmed by the analysis of the superheater deposit.

Study	Re	d_p μm	T_g °C	T_w °C	ϕ_d kg/m ² s	V_d m/s
This study; economiser	6100	0.1-400	280	170	$1 \cdot 10^{-6}$	0.01
This study; final superheater	3400	0.1-400	500	400	$6 \cdot 10^{-6}$	0.06
Wessel and Wagoner [72]	6800	0.1-20	1149	510	$7 \cdot 10^{-4}$	1.3
Howarth: T-4-01 [20,25]	4200	0.1-100	393	182	$1 \cdot 10^{-6}$	0.01
Howarth: T-2-06 [20,25]	3200	0.1-100	719	320	$2 \cdot 10^{-5}$	0.2

Table 3.3 Comparison of the measured deposition rates and deposition rates reported in literature for comparable situations

The deposition rate reported by Wessel and Wagoner is another order of magnitude larger than the deposition rate found for the superheater. The difference is thought to be the result of the particles becoming sticky, which is likely, considering the flue gas temperature in their installation of around 1100 °C. To prevent a fast growing layer on the superheater because of these ‘sticky’ particles, in the refuse waste incinerator an additional evaporator bundle was placed prior to the superheater bundles to reduce the flue gas temperature at the entrance of the superheaters.

As is shown, the sticking efficiency determines to a large extent the deposition rate of particles on the tube wall. If a liquid phase appears at the surface of the already formed layer or at the surface of the particles the sticking efficiency increases and deposition rates increase with an order of magnitude. The presence of a liquid phase increases the sticking efficiency, because a liquid bridge is formed in the impact of a particle with the layer. The energy required to rupture this bridge is higher than to overcome the adhesion force in a dry contact. Without the presence of a liquid phase, a layer is still able to develop as is seen on the economisers. This powdery layer contains particles up to the size of approximately 10 μm. In this case the sticking efficiency is determined by the different characteristics of a powdery layer compared to that of a bare surface. Initially, with a bare-tube surface, only the sub-micron particles can deposit to form an initial layer. It are only the sub-micron particles that can deposit because these particles, transported by diffusion and thermophoresis, deposit with modest velocities. Larger particles, transported to the surface because of their inertia, have too large impact velocities to deposit directly and experience a rebound [56]. Because of the absence of a liquid phase, the particles have a weak adherence to each other as well as to the tube wall and are easy to remove. The formation of an initial layer is confirmed by Steadman [65]. For coal-fired boilers, he reported an initial layer with a thickness of tens to hundreds of microns depending on the position on the tube. After the formation of an initial layer, incoming particles impact with a dusty layer that shows a totally different

material behaviour than the clean tube wall. Because of this changed behaviour, not only the smallest particles are able to stick, but also above micron-sized particles as is shown by the particle sizes found in the analysis of the economiser deposit. Smouse [63] found the same range of particle sizes in layers formed on an experimentally simulated superheater tube using gas firing with Al_2O_3 particles. In his experiments the deposit contained particles up to 20 μm .

3.5 Conclusions

Deposition of particulate matter is the result of the transport of particles and the sticking of these particles to the wall. It is found that the sticking efficiency determines to a great extent the deposition rate and needs to be modelled carefully. The sticking efficiency is a function of the kind of layer on the tube and increases strongly when a liquid phase appears at the surface of the layer or on the particle itself. The occurrence of a liquid phase is confirmed for the layer formed on the superheater. Electron microscopy revealed structures in the deposit with sizes much larger than that of single deposited particles. In these structures a separation of elements was found that is attributed to the formation of a melt in a multi-component system consisting of sodium, potassium and zinc sulphates. In absence of a liquid phase a powdery layer develops as is found on the economisers. This powdery layer has a low density compared to the layer on the superheater indicating a higher porosity. This higher porosity corresponds with the lower thermal conductivity of the layer formed on the economiser. With respect to the transport of particles, inertia-controlled transport proves to be responsible for most of the deposited mass. Based on the particle sizes found in the deposit, it is concluded that inertia-controlled transport is mainly in the eddy-impaction regime and in the early stages of impaction.

Starting with a clean tube, first an initial layer of sub-micron particles will form. Assuming the particles in the flue gasses to be non-sticky, a powdery layer consisting of also larger particles can develop on top of this initial layer. Because of rising surface temperatures due to the heat resistance of the layer a melt can occur initiating a different fouling regime. In this study the problem is confined to the formation of a powdery deposit and a suitable model will be developed to predict the sticking efficiency of such a powdery layer. In the developed model it should be possible, for use in future studies, to incorporate a sticky phase.

Chapter 4

Numerical deposition model

With the numerical deposition model it should be possible to calculate local deposition rates of particulate matter (fly-ash) on the tubes of tube bundles like installed in heat recovery boilers, see figure 4.1.

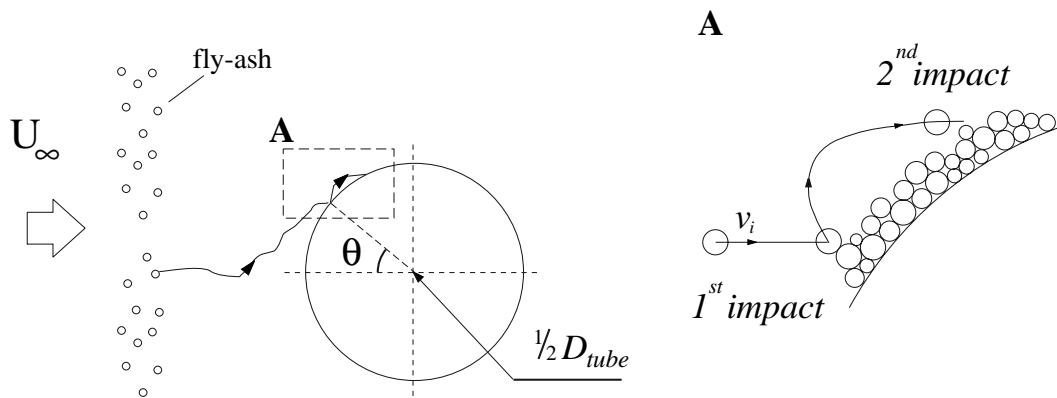


Figure 4.1 Problem definition: deposition of particulate matter on a tube in cross flow.

Deposition of the fly-ash particles is the result of the transport of particles to the heat exchange surface and the possible sticking of these particles to this surface. If the kinetic energy of the incident particle is too large to be dissipated by the layer, deposition is prevented and the particle rebounds. The rebounding particle may be transported to the surface again and may lead to deposition in its 2nd, 3rd or ...th impact (detail A in figure 4.1).

In the numerical deposition model it is chosen to uncouple the transport and sticking of particles. This assumes that the flow field only determines the transport of particles through the heat exchanger and has no influence on the sticking of the particle to the surface. The sticking part is covered by a sticking model which is treated in Chapter 5 and will be experimentally verified in Chapter 7. As a function of the impact velocity and the angle of impact, this model predicts whether the particle sticks or rebounds and gives the rebound velocity and angle in case of a rebound. Compared to other studies that calculate deposition rates, in this study the emphasis is put on the sticking model and it is therefore chosen to use the commercially available CFX-package to cover the transport of particles.

In figure 4.2 the flowchart is given of the numerical deposition model that consists of a transport model and a sticking model.

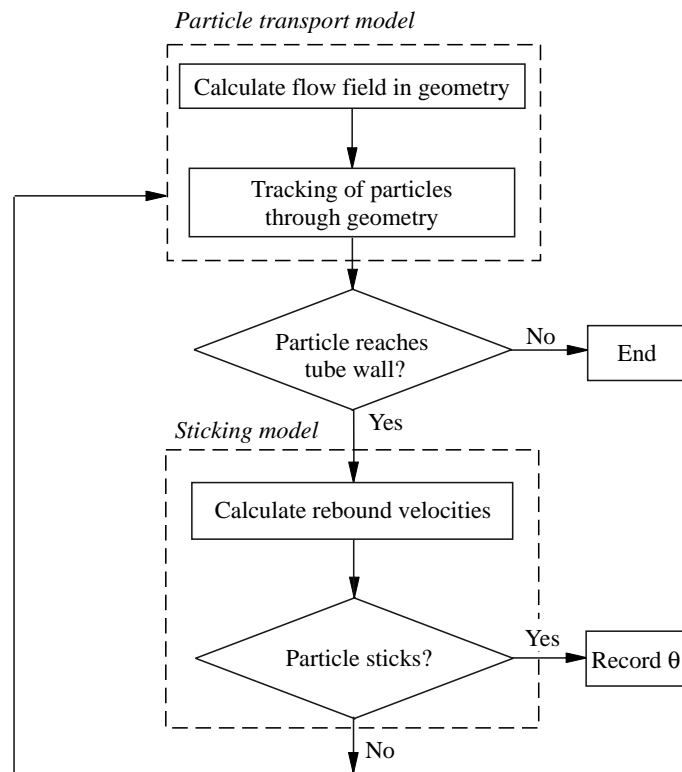


Figure 4.2 Flowchart numerical model

In the transport model, first the transport of particles to the heat exchange surface is calculated by tracking individual particles through the flow domain for which the flow field is already known. This Lagrangian approach is chosen because it yields the impact position, incident velocity and angle of impact for each particle reaching the heat exchange surface. Because these parameters are expected to determine the sticking efficiency, this allows for a direct coupling with the sticking model. With the named quantities as input, this model determines for all particles reaching the tube wall whether the particle sticks or rebounds. In case of a rebound, the tracking of the rebounding particle is continued until it reaches the heat exchange surface again or it leaves the flow domain. For the particles that stick, the position on the tube, defined by the angle θ (figure 4.1), is recorded. The recorded positions are used later to calculate local deposition rates.

The remaining of this chapter focuses on the particle transport model. In section 4.1, the transport problem is further characterized using the Reynolds and the Stokes numbers. As the calculation of individual particle tracks requires knowledge of the flow field, in section 4.2 a description is given of the CFD-model used to calculate this flow field. The flow model will be tested in section 4.3 for two cases; the laminar flow around a cylinder at $Re = 20$ and the turbulent flow around a cylinder in which special attention is given to the characteristics of the boundary layer. Given the flow model, the particle tracking model is discussed in section 4.4. This particle transport model is used in section 4.5 to calculate the deposition onto a

cylinder in cross-flow and the results are compared with results reported in literature. The chapter ends with a discussion in section 4.6.

4.1 Problem characterization

Before the particle transport model is described, the problem will be characterized by the Reynolds number (defining the flow regime) and the Stokes number (defining the transport regime).

Reynolds numbers

The Reynolds number is defined by:

$$Re = \frac{U_{\infty} D_{tube}}{\nu_g} \quad (4.1)$$

with D_{tube} the diameter of the tube and U_{∞} the main stream velocity. Both the main stream velocity and the kinematic viscosity vary along the boiler because of the decreasing flue gas temperature over the successive tube bundles. In table 4.1 the kinematic viscosity (of air) is given as a function of temperature. Using these viscosities the Reynolds number is calculated for two main stream velocities, 5 and 10 m/s, resembling the range of velocities expected in heat recovery boilers. The diameter of the tube is taken to be 50 mm.

T_g, K	$\rho_g, kg/m^3$	$\nu_g, m^2/s$	$Re;$	$Re;$
			$U_{\infty} = 5 \text{ m/s}$	$U_{\infty} = 10 \text{ m/s}$
1100	0.3	$1.4 \cdot 10^{-4}$	1800	3600
900	0.4	$1.0 \cdot 10^{-4}$	2500	5000
700	0.5	$6.5 \cdot 10^{-5}$	3800	7700
500	0.7	$3.6 \cdot 10^{-5}$	7000	14,000
300	1.2	$2.4 \cdot 10^{-5}$	10,400	20,800

Table 4.1 Reynolds numbers within heat recovery boilers

The range of Reynolds number expected in heat recovery boilers is between 2000 and 20,000 where especially the intermediate numbers are of interest because these comply with the situation as valid for the economisers.

Stokes number

To characterize the transport regime, the simplest form of the equation of motion for a particle in fluid flow, treated in Appendix B, is made dimensionless using the main stream velocity U_{∞} and the radius of the tube $\frac{1}{2} D_{tube}$. The dimensionless equation of motion then reads:

$$\frac{d\vec{u}_p}{dt} = \frac{1}{Stk} (\vec{u}_f - \vec{u}_p) \quad (B.14)$$

with the Stokes number Stk , already defined in equation 3.6, equal to the ratio between the particle relaxation time τ_p (equation 3.5) and the time scale imposed on the flow by the tube τ_{flow} . The time scale τ_{flow} is equal to $1/2 D_{tube}/U_\infty$. Hence, the Stokes number reads:

$$Stk = \frac{\tau_p}{\tau_{flow}} = \frac{\rho_p d_p^2 U_\infty}{9 \mu_g D_{tube}} \quad (4.2)$$

Because of velocity and length scales measured in the turbulent flow of a tube bundle [3], the time scale imposed on the flow τ_{flow} is half of the time scale of the most energetic eddies τ_L as defined in equation 3.7.

As explained in section 3.3 and figure 3.5, for inertia-controlled transport two different regimes can be distinguished: eddy impaction and impaction. Transport of particles is influenced by the action of turbulent eddies for particles with a relaxation time between the Kolmogorov time scale τ_K and the time scale for the most energetic eddies τ_L . These flow time scales defined in equation 3.7 are evaluated using half the main stream velocity U_∞ and the tube radius $1/2 D_{tube}$ for the velocity and length scale of the most energetic eddies, respectively. These values are based on LDA measurements made in a tube bundle [3]. The range of particle sizes defining the eddy-impaction regime is calculated by substituting the flow time scales for the particle relaxation time in equation 3.5. Further, in the equations a main stream velocity of 5 m/s and a particle density of 2500 kg/m³ are used. The particle sizes are given in table 4.2. In this table also the particle size indicating the start of the second transport regime, impaction, is given. The particle size is calculated using the critical Stokes number of 0.125. For all particle sizes the accompanying Stokes numbers are also calculated.

T_g , K	$d_p (\tau_p = \tau_K)$ μm	$d_p (Stk = 0.125)$ μm	$d_p (\tau_p = \tau_L)$ μm
1100	12 (0.09)	14 (0.125)	56 (2)
900	10 (0.08)	13 (0.125)	53 (2)
700	9 (0.07)	12 (0.125)	49 (2)
500	7 (0.05)	11 (0.125)	44 (2)
300	5 (0.03)	9 (0.125)	36 (2)

Table 4.2 Particle sizes defining transport regimes as a function of fluid properties. Behind the particle sizes, between brackets, the accompanying Stokes numbers are given.

As can be seen from table 4.2, the transport is in the eddy-impaction regime ($\tau_K < \tau_p < \tau_L$) for particles between approximately 5 and 50 μm , or for Stokes numbers between 0.03 and 2. As this corresponds to the range observed in the deposits, further calculations will be based on this range of Stokes numbers.

Tubebank geometry

The tubes in the tube bundle of a heat recovery boiler are normally either arranged in an ‘in-line’ or in a ‘staggered’ pattern. Both patterns are schematically given in figure 4.3 and are characterized by the transverse, S_T , and the longitudinal distance between the tubes, S_L , that are denoted as pitch.

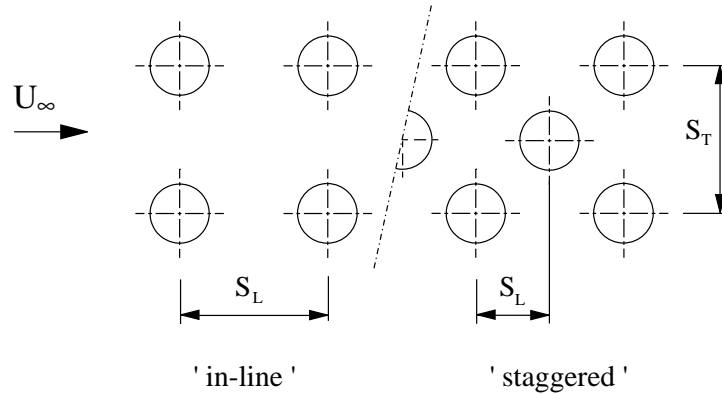


Figure 4.3 Definitions staggered and in-line tube arrangement

To minimize problems with fouling, in both the boilers in Alkmaar and Moerdijk the tubes were placed in an ‘in-line’ arrangement. For the boiler in Alkmaar, the applied pitches are given in table 4.3.

	D_{tube} mm	S_T/D_{tube}	S_L/D_{tube}
Final Superheater	51	2.5	2
LT Superheater	51	2.2	2
Second evaporator / Economisers	48.3	2	2

Table 4.3 Dimensions for the tube bundles in the boiler of the refuse waste incinerator in Alkmaar.

In the calculations both the in-line and the staggered configurations will be used.

4.2 Flow-model

For the relevant range of Reynolds numbers (see table 4.1) the flow around a cylinder in cross-flow is sub-critical, meaning that the boundary layer developing from the upstream stagnation point remains laminar. The flow behind the cylinder is instationary, due to the alternating vortex shedding process from both sides of the cylinder, and it has a turbulent character.

For the flow in a tube bundle, the flow exhibits the same features as for a single cylinder in cross-flow. In spite of the high turbulence levels generated by preceding tubes in the bundle, the boundary layers remain laminar. As found in measurements done by Balabani [3] for the flow in a staggered tube bank, the flow away from the wall exhibits a 2-D character.

Governing equations

The model is based on the Reynolds Averaged Navier Stokes (RANS) equations to calculate the flow around a single cylinder and in a tube bank geometry. In these equations an instantaneous quantity ϕ is considered to be a fluctuation ϕ' superimposed on an average $\bar{\phi}$, the so-called Reynolds decomposition:

$$\phi = \bar{\phi} + \phi' \quad (4.3)$$

The RANS equations are found by substituting this decomposition in the regular mass and momentum conservation equations for stationary and incompressible flow and averaging each term. When using the Einstein convention, the mean mass and momentum equations read;

$$\begin{aligned} \frac{\partial \bar{u}_j}{\partial x_j} &= 0 \\ \bar{u}_j \frac{\partial \bar{u}_i}{\partial x_j} &= -\frac{1}{\rho} \frac{\partial \bar{p}}{\partial x_i} + \frac{\partial}{\partial x_j} \left[\frac{\mu}{\rho} \frac{\partial \bar{u}_i}{\partial x_j} - \overline{u'_i u'_j} \right]; \quad i = 1, 2 \end{aligned} \quad (4.4)$$

For the Reynolds stresses $-\overline{\rho u'_i u'_j}$, it is assumed that they are proportional to the mean velocity gradients as given by:

$$-\overline{\rho u'_i u'_j} = \mu_T \left(\frac{\partial \bar{u}_i}{\partial x_j} + \frac{\partial \bar{u}_j}{\partial x_i} \right) \quad (4.5)$$

where μ_T is the so called turbulent viscosity given by [38]:

$$\mu_T = \frac{C_\mu \rho k^2}{\varepsilon} \quad (4.6)$$

with C_μ an empirical model constant. The turbulent kinetic energy k ($\equiv \frac{1}{2} u_i'^2$) and the dissipation rate ε are found respectively from the k and ε equations as formulated by Launder and Spalding [38]. The standard $k - \varepsilon$ model is suitable for high Reynolds number flows. In the model wall functions are used that represent the influence of the boundary layer on the main stream. Wall functions are based on the assumption that the boundary layer is turbulent and that the velocity profile in the layer is known. This is not applicable for a sub-critical flow around a cylinder where the boundary layer up to the separation point is laminar.

To make the $k - \varepsilon$ model suitable to predict the flow in low turbulent regions like a boundary layer, Jones, Launder and Sharma [32,39] have suggested a number of modifications to the standard k and ε equations resulting in the low-Reynolds variant of the $k - \varepsilon$ model. The k and ε equations in this model are given by:

$$\frac{\partial}{\partial x_j} \left[\rho \bar{u}_j k - \left(\mu + \frac{\mu_T}{\sigma_k} \right) \frac{\partial k}{\partial x_j} \right] = -\rho \varepsilon + \underbrace{(\mu + \mu_T) \left[\frac{\partial \bar{u}_i}{\partial x_j} + \frac{\partial \bar{u}_j}{\partial x_i} \right] \frac{\partial \bar{u}_i}{\partial x_j} - \frac{2}{3} \left[(\mu + \mu_T) \frac{\partial \bar{u}_i}{\partial x_i} + \rho k \right] \frac{\partial \bar{u}_i}{\partial x_i}}_P - \underbrace{2\mu \left(\frac{\partial \sqrt{k}}{\partial x_j} \right)^2}_D \quad (4.7)$$

$$\frac{\partial}{\partial x_j} \left[\rho \bar{u}_j \varepsilon - \left(\mu + \frac{\mu_T}{\sigma_\varepsilon} \right) \frac{\partial \varepsilon}{\partial x_j} \right] = C_{\varepsilon 1} f_1 \frac{\varepsilon}{k} P - C_{\varepsilon 2} f_2 \rho \frac{\varepsilon^2}{k} + \underbrace{2\mu \mu_T \left(\frac{\partial^2 \bar{u}_i}{\partial x_j^2} \right)}_E \quad (4.8)$$

with P the shear production defined in the k equation.

Compared to the original model in both the k and the ε equation an extra term is added. In the k equation the term D is added such that the isotropic part of the dissipation represented by ε goes to zero near the wall and in the ε equation a term E is added such that the k profile near the wall exhibits the same features as measured. Additionally, the eddy viscosity is multiplied by a damping function f_μ as given by:

$$\mu_T = f_\mu \frac{C_\mu \rho k^2}{\varepsilon} \quad (4.9)$$

which is assumed to be dependent on the local turbulent Reynolds number R_T :

$$R_T = \frac{\rho k^2}{\mu_g \varepsilon} \quad (4.10)$$

The exact form of the damping function is found from the prediction of constant stress Couette flows where the original ε equation is adjusted to predict a reasonable turbulent energy distribution in the viscous sub-layer region and is given by:

$$f_\mu = \exp \frac{-3.4}{\left(1 + \frac{R_T}{50} \right)^2} \quad (4.11)$$

Besides the introduction of the damping function f_μ , in the ε equation the terms with constants $C_{\varepsilon 1}$ and $C_{\varepsilon 2}$ (given in table 4.4) were also multiplied with a damping function f_1 and f_2 , respectively. Based on the prediction of the turbulent kinetic energy in the boundary layer and the decay of isotropic turbulence, the following form is chosen for the damping functions [32]:

$$\begin{aligned} f_1 &= 1.0 \\ f_2 &= 1.0 - 0.3 \exp(-R_T^2) \end{aligned} \quad (4.12)$$

C_μ	σ_k	σ_ε	$C_{\varepsilon 1}$	$C_{\varepsilon 2}$
0.09	1.0	1.3	1.44	1.92

Table 4.4 Constants applied in the k and ε - model

In the low Reynolds variant the k and ε equations are solved up to the wall where both k and ε are prescribed to be 0. With the low-Reynolds model the entire boundary layer can be resolved demanding a highly refined grid near the wall. Because of this dense grid, the velocity field in the boundary layer is precisely known which is required to accurately calculate the particle paths up to the wall.

Geometry and boundary conditions

The flow is solved on a structured grid as is given in figure 4.4 for a cylinder in cross-flow.

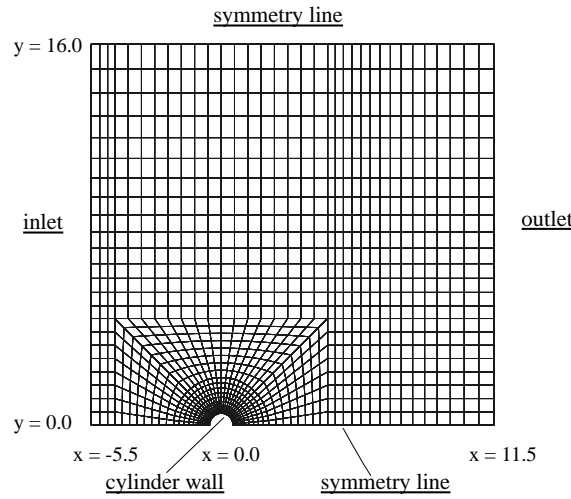


Figure 4.4 Geometry and grid used in the calculations for a cylinder in cross-flow.

The flow solver used allows for non-rectangular geometries by the application of body-fitted coordinates. To resolve the flow in the boundary layer, it is ensured that the radial position of the centre of the first row of cells denoted with the dimensionless wall coordinate y^+ is smaller than 0.05. This criterion is found to give grid-independent results for the boundary layer characteristics as discussed later in section 4.3. The dimensionless wall coordinate is defined by:

$$y^+ = \frac{\rho_g u^* y}{\mu_g} \quad (4.13)$$

with u^* the friction velocity that is defined by the local shear-stress at the wall τ_w as given by:

$$u^* = \sqrt{\frac{\tau_w}{\rho_g}} \quad (4.14)$$

On the edges of the flow domain boundary conditions are imposed. At the inlet Dirichlet boundary conditions are applied. The u and v velocities are set to the main stream velocity U_∞ and zero, respectively. The turbulent kinetic energy k is taken equal to:

$$k = \frac{3}{2} I^2 U_\infty^2 \quad (4.15)$$

with I the turbulence intensity. It is assumed that the flow approaching a single cylinder or the first row of tubes of a tube bundle at the inlet is low turbulent. Therefore, in all calculations the turbulence intensity at the inlet is set to 5%. The dissipation rate is derived from the turbulent kinetic energy as given by [24]:

$$\varepsilon = \frac{C_\mu^{3/4} k^{3/2}}{l_E} \quad (4.16)$$

with l_E the dissipation length scale. For the low turbulent flow at the inlet, the dissipation length scale is taken an order smaller than the local domain size given by the diameter of the tube [58]. At the cylinder wall all the transport quantities (u , v , k , and ε) are equal to zero. At the symmetry axis, a homogeneous Neumann boundary condition is imposed for all transport quantities except for the v -velocity that is set to zero. At the outlet of the domain, the gradients of the transport quantities are set to zero in the normal direction.

Flow solver

The governing equations are solved using the finite volume method applied by the commercial CFD-package CFX version 4.2. To find the values for the transport quantities at the cell faces, the values are interpolated from the values at neighbouring cells. For all but the advection terms, use is made of a second-order central differencing scheme. In the equations for the velocity components, use is made of the third order QUICK interpolation scheme for the advection terms. For the k and ε equations the first order HYDRID-scheme is applied which is more stable than the QUICK scheme and ensures the k and ε values to remain positive in the converged solution. In the computations use is made of the SIMPLEC pressure-correction scheme in which the pressure field is indirectly specified via the continuity equation. The set of linearized difference equations is solved by iteration. For the u and the v velocity use is made of the Stone's method, for the turbulence quantities a line-relaxation method is used and an algebraic multi-grid method is applied for the pressure equation.

4.3 Flow-model; numerical test cases

Test-case; $Re=20$

The flow model is evaluated for the flow around a cylinder at $Re = 20$ by comparing the results obtained using the flow model with the experimental results obtained by Coutanceau [15]. The flow model is applied with and without the low-Reynolds $k - \varepsilon$ model, which, because the flow is laminar, should yield equal results. In figure 4.5 the results are presented in terms of the relative axial velocity u/U_∞ over the centre-line behind the cylinder ($y=0$) and over the positive y -axis at $x=0$.

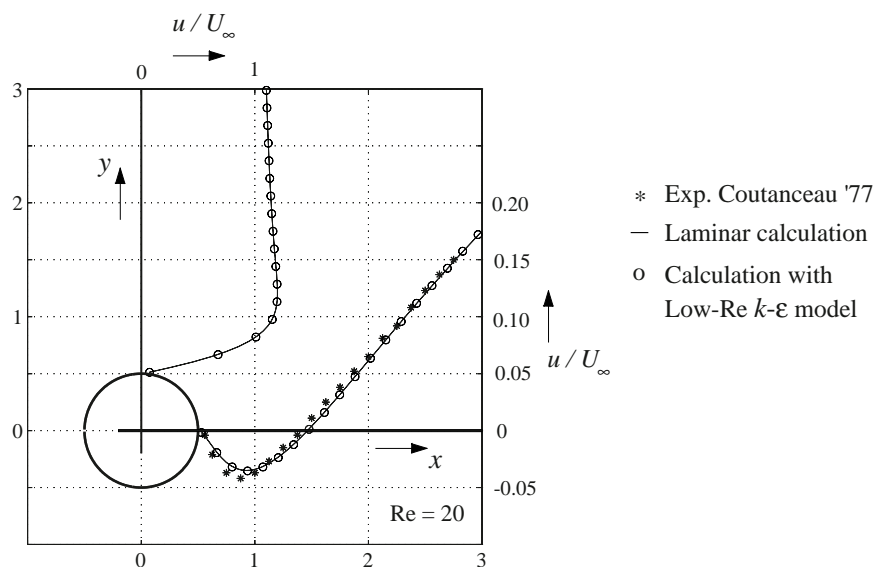


Figure 4.5 Comparison between numerical results for $Re = 20$ in case of a laminar calculation and one using the low-Reynolds $k - \varepsilon$ model with experimental results of Coutanceau [15].

The predicted velocities are equal for the calculation with and without the application of the low Reynolds turbulence model. This confirms that the turbulence model indeed ‘switches off’ for non-turbulent conditions. Comparison of the predictions with the measurements yields good agreement. The slight difference found in the length of the recirculation zone is also found by Bouris and Bergeles [10] and Rindt [53] and is not considered to be disturbing.

Test-case; $Re = 2000- 50,000$ (boundary layer characteristics)

The performance of the flow model is also evaluated by comparing the calculated boundary layer characteristics with experimental results. The calculated skin-friction and the angle at which separation occurs for a cylinder in cross-flow are compared with experimental results of Achenbach [2], Ballangee [4] and Son [64]. In the calculations the Reynolds number is varied between 2000 and 20,000. The results, given in figure 4.6, are expressed using the boundary layer separation angle θ_s and the skin friction coefficient C_f which is defined as:

$$C_f = \frac{\tau_w Re^{1/2}}{\rho_g U_\infty^2} \quad (4.17)$$

It is found that the results for the boundary layer separation angle and the skin friction are insensitive to the imposed inlet conditions of k and ε .

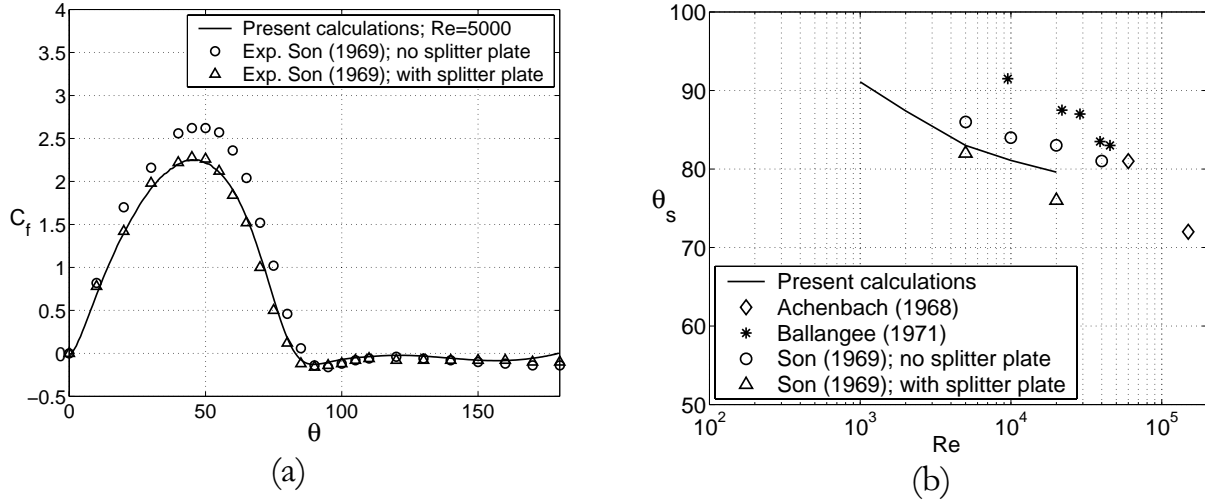


Figure 4.6 Comparison between numerical and experimental results for the skin friction coefficient C_f at $Re = 5000$ and the boundary layer separation angle θ_s at various Reynolds numbers.

Comparison of the predicted skin-friction with the measurements of Son et al [64] in figure 4.6 (a) shows that the predicted values for the skin-friction prior to separation of the boundary layer are lower than measured and that separation is predicted to occur for smaller angles. The latter effect persists for Reynolds numbers higher than 5000 as is shown in figure 4.6 (b). The two observed differences can be attributed to the symmetry constraint that is imposed in the flow model on the x-axis through the centre of the cylinder. This constraint prevents an oscillating motion behind the cylinder as occurs in reality and yields a stationary solution for the flow field in the wake. A similar kind of constraint is imposed in the experiments of Son et al [64] by placing a splitter plate over a length of $5.3 D_{cyl}$ along the cylinder axis at a small distance ($0.5 D_{cyl}$) behind the cylinder. Comparing the results of these experiments with the predictions yields good agreement (see figure 4.6 (a)). Thus, the low-Reynolds $k - \varepsilon$ model is capable to predict the boundary layer characteristics correctly. However, the solved average flow field is somewhat different from the time-averaged experimental flow around the cylinder at the current Reynolds numbers.

4.4 Particle transport-model

To calculate the transport of particles from the gas to the tubes in the heat exchanger, the extended equation of motion given by (appendix B):

$$\frac{d\vec{u}_p}{dt} = \frac{1}{Stk} \left(1 + 0.15 \left(Re_p \left| \vec{u}_g - \vec{u}_p \right| \right)^{0.687} \right) (\vec{u}_g - \vec{u}_p) \quad (4.18)$$

with \vec{u}_g the local gas velocity. The equation of motion is solved in time for each individual particle starting from an initial position and velocity. In this equation Re_p is the particle Reynolds number which is based on the main stream velocity and the particle diameter:

$$Re_p = \frac{d_p U_\infty}{\nu_g} \quad (4.19)$$

As discussed in Appendix B, it is assumed that all forces except the drag force are negligible for the transport of particles through the gas. It is also assumed that the particles are spherical and non-rotating and that their concentration is such that the effect of the particles on the flow can be neglected.

To incorporate the influence of turbulence on the particle paths the eddy-interaction model available in CFX is applied. This model considers the turbulent flow field as a collection of randomly directed eddies. Assuming isotropy, periodically and independently a u' and a v' fluctuation are sampled from a Gaussian probability distribution with zero mean and a variance σ dependent on the turbulent kinetic energy k as given by:

$$\sigma(u') = \sigma(v') = \sqrt{\frac{2}{3}k} \quad (4.20)$$

The sampled fluctuation is added to the mean flow field to give the gas velocity that is used to evaluate equation 4.18. After a certain eddy-interaction time, a new fluctuation is sampled.

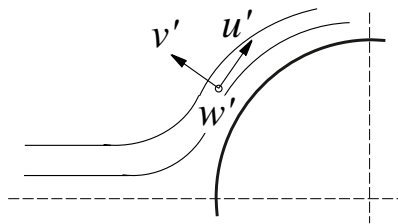


Figure 4.7 Definitions fluctuation directions

In the boundary layer the flow is not isotropic. Here both the fluctuation normal to the wall as the span-wise fluctuation are smaller than the fluctuation tangential to the wall [29]. The tangential, normal and spanwise direction are indicated with u' , v' and w' , respectively (figure 4.7). The contribution of the tangential fluctuation u' to the turbulent kinetic energy is therefore larger than that

of the normal fluctuation v' . In that case, when sampling both fluctuations from a distribution related to the turbulent kinetic energy as described above, a too large fluctuation is sampled in the direction normal to the wall and a too small fluctuation tangential to the wall. This leads to an over-prediction of transport rates and impact velocities. Therefore, the original model of Shuen [61] as adapted in CFX is modified to correct for the anisotropy in the boundary layer. In the modified dispersion model the sampled fluctuations will be based on the fluctuation expected in normal direction to the wall. Because this fluctuation is not calculated in the $k - \varepsilon$ model, it will be based on measurements made of the fluctuations in a laminar boundary layer surrounded by a turbulent main flow.

In the modified dispersion model, it is assumed that the fluctuations in tangential direction are not important for deposition because they can be assumed negligible compared to the mean tangential velocity. Fluctuations in the direction normal to the wall, however, are expected to have a strong influence on the deposition rate. Therefore, in the modified eddy-interaction model the turbulent kinetic energy is recalculated in such a way that the sampled fluctuations normal to the wall are correct. This approach is similar to the approach followed by Kallio and Reeks [33]. In the modified model the fluctuations are again sampled from a Gaussian probability distribution with zero mean and a variance of $(2/3 k_{corr})^{0.5}$. The corrected turbulent kinetic energy k_{corr} is based on the fluctuations normal to the wall and is given by:

$$k_{corr} = \frac{3}{2} \overline{v'^2} \quad (4.21)$$

The corrected turbulent kinetic energy k_{corr} becomes equal to the turbulent kinetic energy k for isotropic conditions. For regions where the flow is anisotropic the turbulent kinetic energy k_{corr} can be calculated when the ratio between the fluctuations in all three directions is known:

$$k_{corr} = \frac{3k \left(\frac{v'}{u'}\right)^2}{1 + \left(\frac{v'}{u'}\right)^2 + \left(\frac{w'}{u'}\right)^2} \quad (4.22)$$

with u' defined as $\sqrt{\overline{u'^2}}$, the root mean square value.

For the flow cases considered, a laminar boundary layer develops around the cylinder. To the author's knowledge, for this situation the fluctuations in the boundary layer have not been measured. It is, therefore, chosen to use the ratios as measured by Roach et al [55] in the laminar part of a developing boundary layer on a flat plate. The ratio between fluctuations is fitted from the measured fluctuations that are given in figure 4.8 for two different positions along the plate. Run T3A1108 with a local Reynolds number of $1.4 \cdot 10^5$ was located closer to the transition point than run T3A1105 with a local Reynolds number of $3.2 \cdot 10^4$. In the experiments a zero pressure gradient was maintained over the plate and the free stream turbulence intensity varied from 2 to 3%. In the fit a third order polynomial is used which does not account for the drop that is observed for the ratio between u' and w' close to

the wall. The fitted functions give a value of 1 for distances normal to the wall larger than 2 times the boundary layer thickness δ so that outside the boundary layer region the isotropic conditions are met. The fitted functions are used in the modified model to calculate k_{corr} according to equation 4.22.

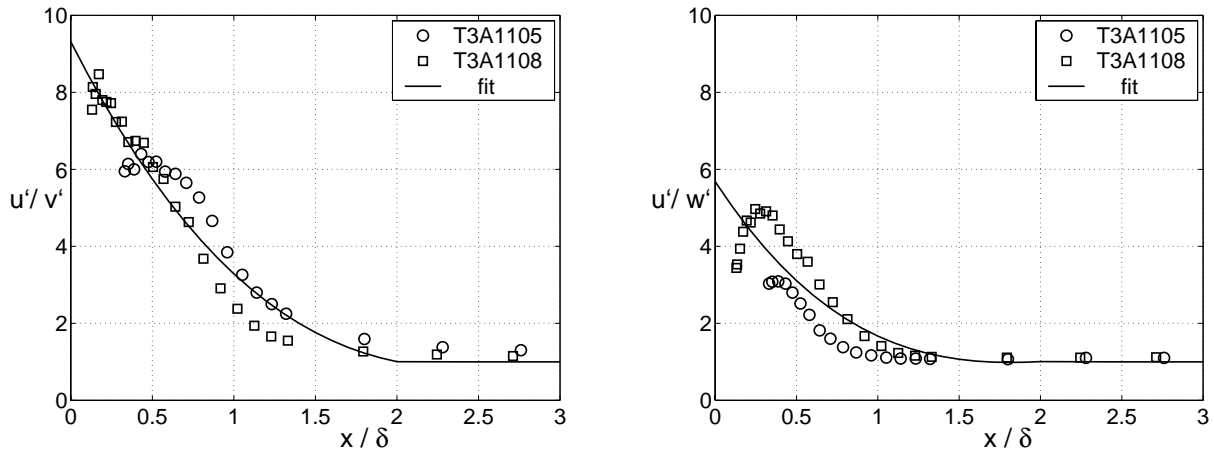


Figure 4.8 Ratio between the velocity fluctuations (u' = tangential, v' = normal and w' = transverse) as a function of the relative distance from the wall in a laminar boundary layer as measured by Roach [55] for the flow over a flat plate.

In more advanced eddy-interaction models the interaction time is taken equal to the minimum of the eddy lifetime and the eddy crossing time [23]. In the Shuen model as implemented in CFX, however, only the eddy-life time is considered. The eddy-life time is found from the eddy length l_E divided by the variance of the distribution function for the velocity fluctuation. Here, the eddy length is taken equal to the dissipation length scale, Shuen [61]:

$$l_E = C_\mu^{3/4} \frac{k^{3/2}}{\varepsilon} \quad (4.23)$$

The eddy lifetime τ_E then becomes:

$$\tau_E = 1.5^{1/2} C_\mu^{3/4} \frac{k}{\varepsilon} \quad (4.24)$$

Using the given eddy lifetime, Shuen showed that the predicted dispersion of small particles in the turbulent flow behind a grid showed fair agreement with the values measured by Snyder and Lumley [61]. For the deposition on a single cylinder or on the first tubes of a tube bundle as considered here, agreement between measured and predicted deposition rates is much less. Because the flow approaching a single cylinder or the first tube row in the bundle is assumed low-turbulent, the sudden change imposed on the flow by the cylinder will result in unreliable transport rates. This can be understood by looking, more closely, to the eddy lifetime upstream of the first tube. Based on an eddy length scale of $0.1 D_{tube}$ and a velocity fluctuation of $0.05 U_\infty$, the eddy lifetime upstream of these tubes is equal to $2 D_{tube}/U_\infty$.

Multiplying this eddy lifetime by the particle velocity, in the order of the main stream velocity U_∞ , a particle is transported over a distance $2 D_{tube}$ before a new fluctuation is sampled. This implies that when sampling a fluctuation upstream of the first tube where the flow is not yet influenced by the tube, a particle can reach the cylinder before a new fluctuation is sampled in the eddy-interaction model. This problem is not so pronounced or even disappears for more downstream tubes where the flow is more turbulent and has smaller time scales.

To correct for this problem, the eddy-interaction model is modified by imposing an additional constraint on the eddy length scale in front of the cylinder directly influencing the eddy lifetime. In the modified model, it is assumed that the maximum eddy length upstream of the cylinder is proportional to the distance from the wall. So, in the turbulent dispersion model the applied eddy length, that is used to determine the eddy lifetime in front of the cylinder ($x_{rel} < 0$), becomes:

$$l_E = \begin{cases} C_\mu^{3/4} \frac{k^{3/2}}{\varepsilon}; & l_E < l_{E,max} ; \quad x_{rel} \leq 0 \\ l_{E,max}; & l_E \geq l_{E,max} \end{cases} \quad (4.25)$$

with $l_{E,max} = C_l \cdot r$ and r the distance to the cylinder wall. The model is calibrated using numerical and experimental results obtained by Bailer [5] for the deposition of particles on to a single cylinder in cross flow at a Reynolds number of 1900. In the calibration, treated in detail in appendix C, the optimum value for C_l is chosen such that an increase in particle diameter resulted in a higher collection efficiency and that the deposition rate is higher for the upstream than for the downstream side of the cylinder. Using these criteria, a value of 0.14 is selected. Using this value for C_l , the eddy lifetime used in the present model and that when applying the model of Shuen [61] are given in figure 4.9.

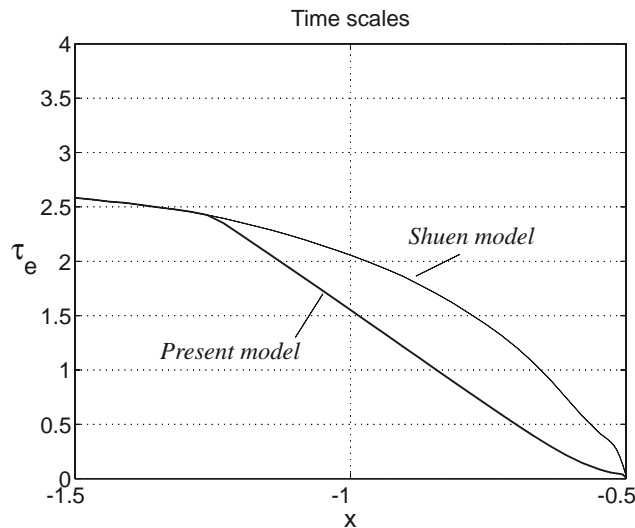


Figure 4.9 Applied time scales upstream on the cylinder axis as a function of the dimensionless coordinate x ($Re=1900$). Cylinder is located at $x=0$ and has a radius of 0.5.

Figure 4.9 illustrates that the time scales applied in the present model are, up to a relative distance of $0.75 D_{tube}$, different from the times scales when applying the original model of Shuen [61]. Using the modified model referred to as the present model, calculated deposition rates are found to be in the expected range as discussed later in the next section.

4.5 Deposition on a cylinder in cross-flow

As a benchmark problem, the deposition model is used to calculate the deposition rates for a cylinder in cross-flow. In the calculations perfect sticking is used meaning that all particles that reach the surface stick and contribute to deposition. In the calculations concerning the deposition on a cylinder in cross-flow, n particles are injected at x_{inj} over a height H_{inj} (see figure 4.10).

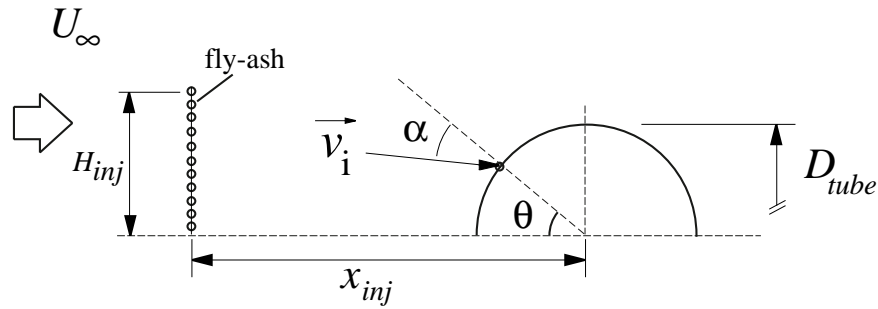


Figure 4.10 Definitions injection region, incident velocity \vec{v}_i and impact angle α .

The calculated deposition rates are expressed using the Stanton number defined in equation 3.8 and given by:

$$St(\theta) = \frac{\phi_d(\theta)}{C_{p,d} U_{\infty}} \quad (3.8)$$

with ϕ_d the mass flux of the depositing particles, $C_{p,d}$ the particle concentration in the flue gas stream and U_{∞} the main stream velocity. The collection efficiency, a second quantity to express the deposition rate, is defined in terms of the averaged deposition rate on the projected area of the cylinder. Averaging the Stanton number over the cylinder angle θ and multiplying it by π to convert to the projected area of the cylinder yields the collection efficiency η_{coll} . The overall collection efficiency then reads:

$$\eta_{coll} = \pi \overline{St}_{0-2\pi} \quad (4.26)$$

with $\overline{St}_{0-2\pi}$ the average Stanton number over the heat exchange surface.

The geometry in which the particles are tracked contains a symmetry line at the top and at the bottom side (figure 4.4). If during the particle tracking calculations a particle passes one of those symmetry lines, the particle normal velocity is changed in direction while the tangential velocity is left unchanged (mirror condition). In this

way the total number of particles leaving the flow domain and deposited on the bundle is equal to the total number of particles released at the outlet.

4.5.1 Global deposition rates

Deposition rates are calculated for the deposition of particles on a cylinder in cross-flow at a Reynolds number 1900 and are compared with values measured and calculated by Bailer [5]. In the study of Bailer deposition rates were measured for fluoresceine particles depositing on a cylinder in cross-flow at $Re=1900$. The following conditions applied for his experiments: a main stream velocity of 2 m/s, a cylinder diameter of 15 mm, a dynamic viscosity of $1.86 \cdot 10^{-5}$ Ns/m², a gas density of 1.2 kg/m³ and a particle density of 1500 kg/m³. In the experiments the sticking efficiency is assumed to be perfect. In the same study also the deposition rates were numerically determined using a DNS flow solver which yielded a velocity field resolved in both space and time. This flow field is used to calculate distinct particle tracks. In table 4.5 the experimentally and numerically found values by Bailer are compared with the values calculated using both the modified transport model (present model) and the original model of Shuen [61]. To derive results independent of the number of particles that are tracked in the computations and of the height over which the particles are released, 30,000 particles were tracked that were released at $x_{inj} = -3 D_{tube}$ over a height $H_{inj} = 0.6 D_{tube}$.

$d_p, \mu\text{m}$	Stk	Bailer [5]		Shuen [61]	Present model
		$\eta_{coll, exp}$	$\eta_{coll, num}$	$\eta_{coll, num}$	$\eta_{coll, num}$
3.76	$1.66 \cdot 10^{-2}$	$3.57 \cdot 10^{-3}$	$4.00 \cdot 10^{-3}$	$2.41 \cdot 10^{-2}$	$5.68 \cdot 10^{-3}$
5.96	$4.21 \cdot 10^{-2}$	$5.34 \cdot 10^{-3}$	$4.83 \cdot 10^{-3}$	$2.04 \cdot 10^{-2}$	$6.36 \cdot 10^{-3}$

Table 4.5 Deposition rates for a cylinder in cross-flow at $Re = 1900$.

The collection efficiency is also calculated for larger Stokes numbers and the results are given in figure 4.11. Again the deposition rates are calculated using the model of Shuen and the model proposed in this study.

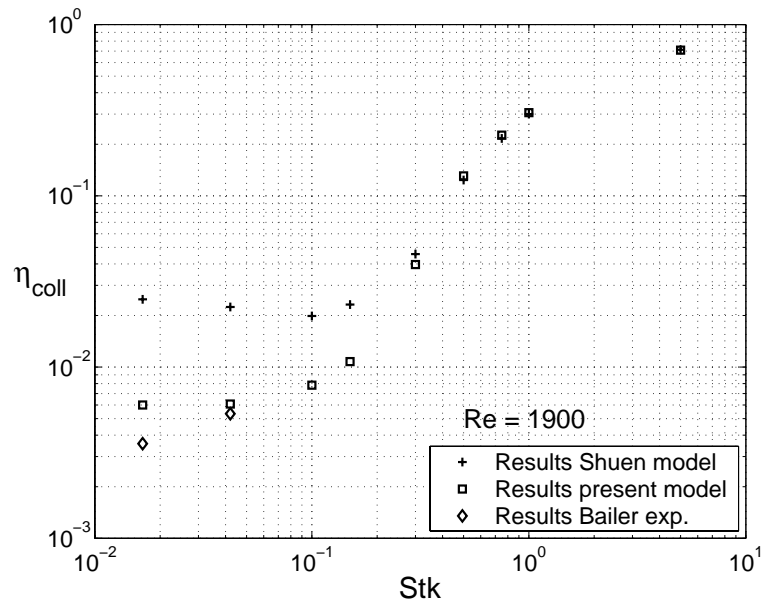


Figure 4.11 Collection efficiency for a cylinder in cross-flow at $Re = 1900$.

It is found that the results obtained with the present model become equal to the original Shuen model for particles with a Stokes number larger than 0.3. For smaller particles the Shuen model does not predict the strong decrease in collection efficiency for smaller particles as measured by Bailer. Using the eddy-interaction model proposed in this study, the expected decrease is correctly predicted and the deposition rates are in reasonable agreement with the measured and calculated values of Bailer.

4.5.2 Local deposition rates and characteristics

For a cylinder in cross-flow at $Re = 5000$ the local deposition characteristics have been calculated using the present transport model under the assumption of perfect sticking. For the calculations again 30,000 particles are tracked. Besides deposition rates also the velocity with which the particles reached the cylinder and the angle of impact (defined relative to the surface normal) are recorded. The calculations are done for the set of parameters given in table 4.6.

U_∞	4.56	m/s		
D_{tube}	50	mm		$Re = 5000$
v_g	$4.5 \cdot 10^{-5}$	m^2/s		
ρ_p	2670	kg/m^3		
d_p	7.3	12.6	23.1	μm
Stk	0.05	0.15	0.5	-

Table 4.6 Parameters in the deposition calculations for a cylinder in cross-flow at $Re = 5000$.

Local deposition rates

In figure 4.12 the calculated Stanton number is given as a function of the angle on the cylinder.

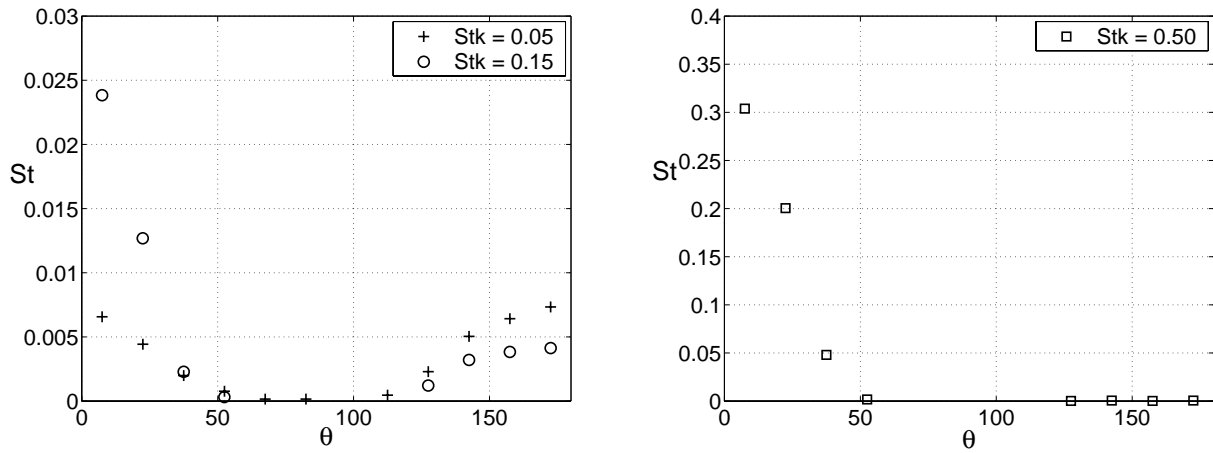


Figure 4.12 Local deposition rates for the flow around a cylinder at $Re=5000$ and for Stokes numbers of 0.05, 0.15 and 0.5.

Under the assumption of perfect sticking, the Stokes number is found to have a strong influence on the variation of the Stanton number with the angle on the cylinder. With an increasing Stokes number, the Stanton number decreases at the rear and for Stokes numbers larger than 0.5 deposition at the rear even vanishes. At the front of the cylinder an increasing Stokes number results in a strong increase of the Stanton number.

Incident velocity and impact angle

In figure 4.13 the dimensionless magnitude of the incident velocity denoted with v_i/U_∞ and the impact angle α are given as functions of the cylinder angle and the Stokes number. Both quantities are defined in figure 4.10. As can be seen in the left figures of figure 4.13, the maximum incident velocity increases, as expected, for particles with a higher Stokes number. For particles with a Stokes number of 0.05, most of the particles impact the cylinder with a velocity between 0.05 and 0.3. This velocity for the upstream side is slightly related to the angle on the tube but is randomly for the downstream side. For particles with a Stokes number above the critical number for impaction of 0.125 a much stronger dependency is found between the incident velocity and the angle on the cylinder.

The impact angle shows a similar behaviour for all Stokes numbers. At the upstream side the impact angle increases with the angle on the cylinder to reach impact angles of about 80° . For the downstream side the impact angle varies between -80° and 80° .

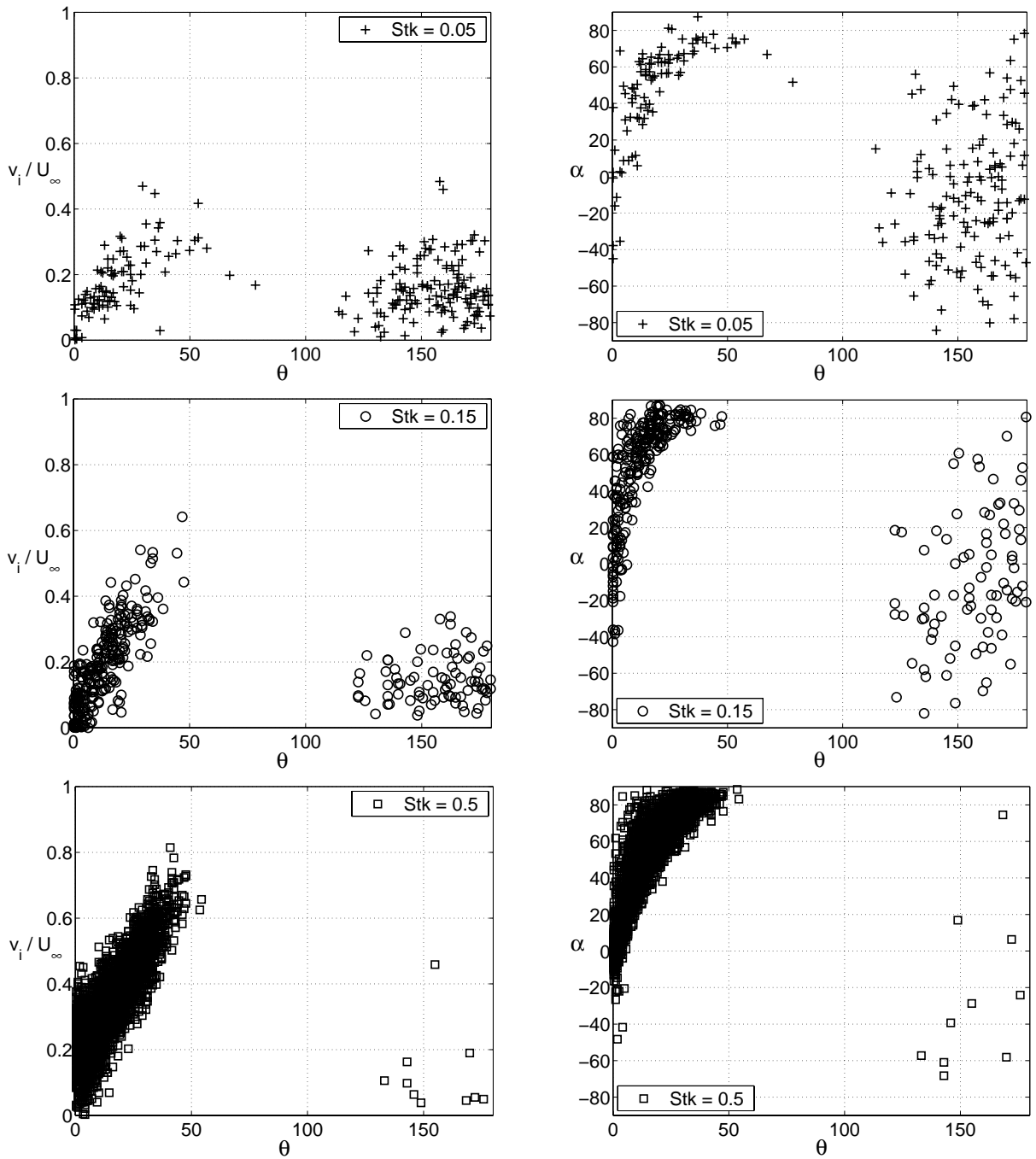


Figure 4.13 Impact characteristics; magnitude of the incident velocity and the impact angle relative to surface normal, $Re=5000$.

4.6 Conclusion and discussion

A model is presented to calculate the deposition of particles from the gas stream onto a configuration with tubes placed in a cross flow. This model uses the low Reynolds $k - \varepsilon$ model to calculate the flow field around the tubes and is adapted to solve the entire boundary layer. Based on a comparison with experimental results, the flow model is capable to predict the average boundary layer characteristics as skin friction and boundary layer separation angle.

The transport of particles is calculated by tracking distinct particles through the geometry making use of the calculated flow field. An eddy-interaction model accounts for the influence of the turbulent motions in the flow on the transport of particles. The model of Shuen [61] is modified with respect to the sampled fluctuations and the time period over which these fluctuations are maintained. Using the modified model and under the assumption of perfect sticking, the expected decrease in deposition rates for particles with a Stokes number below the critical value of 0.125 is well predicted by the model.

The applied eddy-interaction model contains a model constant C_l that relates the maximum eddy length to the distance from the wall. The value of this constant is calibrated based on a comparison with results obtained by Bailer [5] for a cylinder in cross-flow at a Reynolds number of 1900. It is disputable whether the calibrated value of 0.14 also holds for higher Reynolds number flows and the transport model will require improvement in successive studies. For now, it is assumed that when using the above value the results give a good indication of the expected transport rates towards the tubes. This applies specifically for the more downstream tubes in a tube bundle where the length scale correction is found to have almost no influence anymore on the transport rates.

It is realized that the flow model ($k - \varepsilon$) and the eddy-interaction as described here are quite crude. Although most of the relations and the model constants have a physical background, still some fitting in the particle transport model was needed to gain comparable results as found in experiments. As elucidated in chapter 1, it is chosen to focus on the sticking model instead of improving the flow model or the transport model. The reasoning is that a lot of research is carried out on the modelling of anisotropic flows with particles but that a reliable sticking model is lacking. Therefore, in the next chapters a sticking model verified by well-defined experiments is treated. This sticking model can be combined with any flow and transport model. The flow and transport model presented here will be used to illustrate the capabilities of the sticking model and to explore the influence of the geometry on the deposition rates.

Chapter 5

Theoretical sticking model

5.1 Introduction

To predict local deposition rates not only the transport of particles to the heat transfer surface, but also the efficiency with which these transported particles are retained at the surface needs to be known. To predict this so-called sticking efficiency for a powdery deposit, a theoretical sticking model is presented. This model assumes a thin layer of particles initially present and predicts the sticking efficiency as a function of the local impact conditions such as the diameter of the incident particle, the impact velocity, the angle of impact and the character of the layer. This sticking efficiency is expected to be a function of these conditions. In figure 5.1 a schematic representation of the deposition process is given.

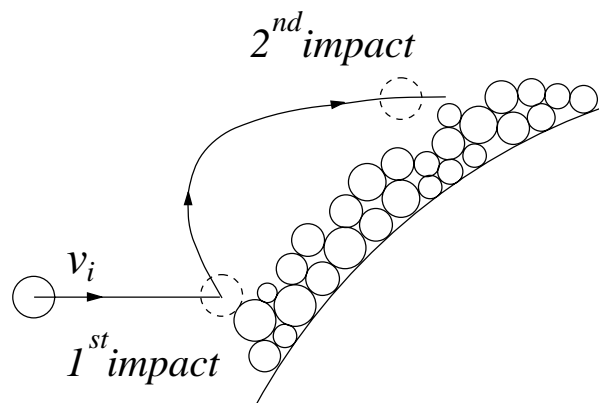


Figure 5.1 Schematic representation of the deposition process.

Deposition of particles can occur in the first impact of the particle but can also involve successive impacts. Hence, it is important to know under which conditions a particle sticks and to know the rebound velocity and the rebound angle in case of a rebound. In this study the outcome of the impact will be described using the sticking efficiency, the relative rebound velocity (defined as the ratio between the rebound velocity and the impact velocity) and the rebound angle. The sticking efficiency s is defined as the number of sticking particles divided by the total number of incident particles.

In the prediction of the deposition rate for a powdery deposit the two-body collision approach as proposed by Werner [71] is used. This model is capable to predict the rebound velocities as a function of the local impact conditions. The rebound velocity predicted by the model becomes zero in case the particle sticks. In the model, it is assumed that both the incident particles and the particles in the deposit are spherical.

In section 5.2 the physical background of the two-body approach is given together with the describing relations. One of the important parameters in the two-body collision model, the coefficient of restitution, is discussed in section 5.3 and a model is treated that predicts this coefficient. Section 5.4 deals with two other model parameters e.g. the friction coefficient and the proportionality factor. In section 5.5 the two-body approach is applied in a numerical model that predicts the sticking and rebound behaviour for particles impacting a bed of particles. Using the numerical model, in section 5.6, the sensitivity of the sticking efficiency to the model parameters is analyzed.

5.2 Two-body collision model

Model considerations

To model the sticking efficiency for the impact of a particle on a powdery deposit, the two-body approach is used as suggested by Werner [71] and later applied by Konstandopoulos [37]. Werner and co-workers performed computer simulations to predict the outcome of the impact of a particle on a bed of particles as it is relevant for the process of saltation. In the saltation process, sand grains entrained in the air interact with a sandy surface (e.g. a dune). In this interaction, sand grains either bury themselves, stick, or rebound from the surface. This process is comparable to the impact of fly-ash particles with an already formed powdery deposition layer as given in figure 5.1.

In the computer simulations of Werner, the impact of a particle is simulated by solving the equation of motion for the incident particle and all the bed particles. To solve the equation of motion for the particles, contact forces were introduced at the contact point between the touching particles. The repulsive normal component of this contact force is assumed to be proportional to indentation i.e. the approach distance of the centres after first contact. In these 2-D simulations both the incident and the bed particles were equally sized.

From the results of the computer simulations, it appeared that the outcome of an impact could also be calculated by assuming the impact to be a two-body collision. This collision involves an incident particle and a target particle possessing an effective mass larger than its true mass. The reason for this is given by the dynamic nature of the impact. Because of the repulsive force between the target particle and the incident particle, the target particle starts to move, thereby inducing new repulsive reaction forces with particles in its vicinity, which then start to move as well. The movement of the other bed particles lags behind the movement of the

target particle. When at the end of the impact the incident particle separates from the target particle, a number of particles are still moving with some fraction of the velocity of the incident particle. This is schematically illustrated in figure 5.2.

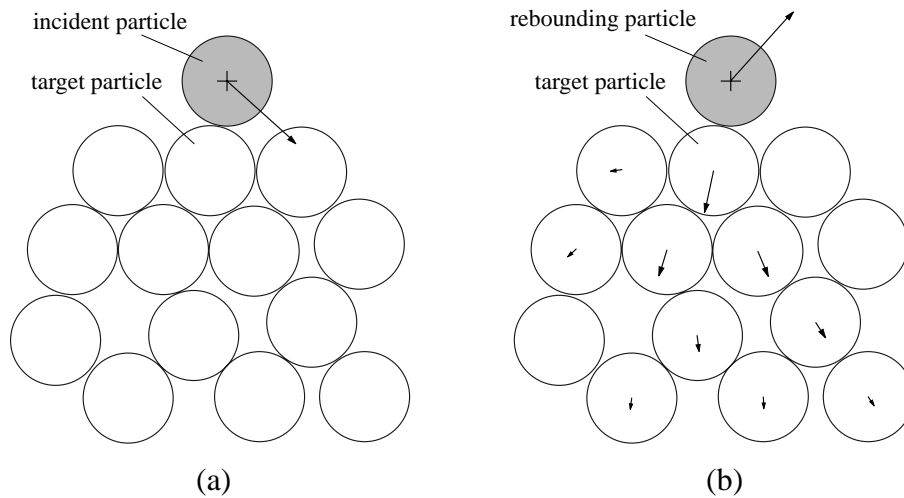


Figure 5.2 Velocity distribution in a bed of particles before, figure (a), and after, figure (b), the impact of a particle with a bed of particles.

After the incident particle has left the surface, it is possible that also bed particles are ejected from the surface. The ejection of bed particles is the result of the storage of momentum in the deposit. After the impact of the incident particle with the target particle, the target particle and, to a lesser extent, the surrounding particles are still moving. The momentum of these particles is directed towards the deposit and this momentum is transferred to particles in the layers below the surface layer. Because of this momentum transfer, these particles begin to move as well. However, they experience resistance from even lower particle-layers and their motion reflects and becomes directed outwards to the surface. By interaction of these outward moving particles with particles at the surface, surface particles can be ejected from the surface. The direction of these ejected particles is mostly close to the surface normal.

Governing equations for a two-body collision

The chosen two-body approach is based on the assumption that the impact of a particle with a layer composed of particles can be described with a two-body collision. In this collision the second body m_2 represents the layer and is given a mass proportional to the mass of the incident particle m_1 . The proportionality factor between these two masses is defined as C_m :

$$m_2 = C_m m_1 \quad (5.1)$$

Besides the proportionality factor, the outcome of the impact is determined by the coefficient of restitution e and the friction coefficient f . The coefficient of restitution gives a measure for the energy losses over the impact, e.g. due to plasticity in the

contact. The friction coefficient gives the ratio between the contact force in normal direction to that in tangential direction.

Based on Goldsmith [22], the equations describing the impact of two spherical bodies are treated in Appendix D. Here, only the important assumptions and the governing equations will be treated. In figure 5.3 a schematic representation is given for a two-body collision including the definition of some of its important quantities.

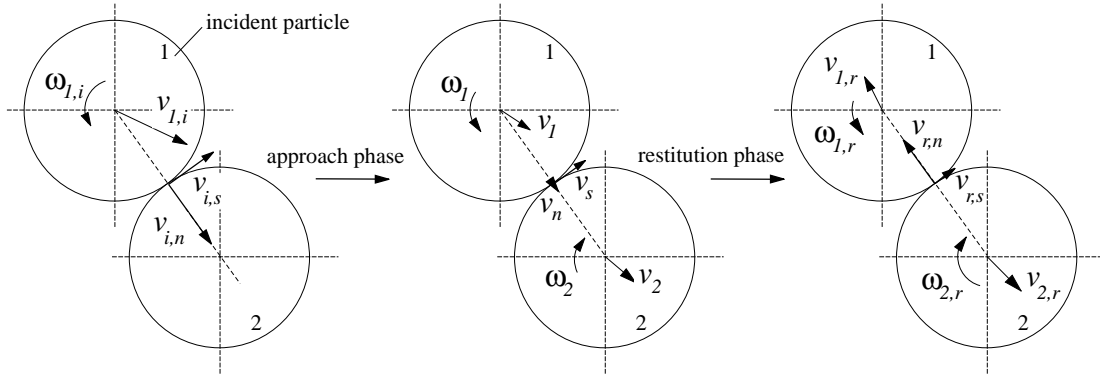


Figure 5.3 Schematic representation of a two-body collision

For a two-body collision, the impact can be divided in two phases. The first phase, the approach phase, starts when the incident particle touches the second particle that is assumed to have no initial velocity or rotation. At this moment no repulsive force is present in the contact. The relative velocity in the direction normal to the impact surface at the contact point is equal to the normal component of the velocity of the incident particle. The second relative velocity, the slip-velocity, is directed tangentially to the impact surface and is composed from the tangential component of the incident velocity and the slip-velocity induced by the angular velocity of the incident particle.

Because of the relative velocity in normal direction, the contact area deforms and repulsive forces appear. These repulsive forces decelerate the incident particle and accelerate the second body until the relative velocity in normal direction becomes zero. This is denoted as the end of the approach phase where the repulsive force is at its maximum value. In the approach phase the contact is deformed elastically and, when the pressure exceeds a critical value, plastically. During the approach, the slip-velocity is reduced by the friction force that arises as a result of the contact force in normal direction. The determining material property is the friction coefficient f that relates the forces in normal and tangential direction:

$$|\vec{F}_t| = f |\vec{F}_n| \quad (5.2)$$

In the subsequent restitution phase the particles are still in contact, but their centres start to separate again. The repulsive forces, decreasing from a maximum value to zero, reduce the slip-velocity even further. If during the approach or restitution phase the slip-velocity is reduced to zero the particles no longer slide on one

another, but start to roll. The restitution phase and also the impact ends when the particles are no longer in contact.

Following Goldsmith, the outcome of the collision between two bodies can be found by applying the impulse momentum laws using the direction normal and tangential to the local impact surface. These directions are defined in figure 5.4.

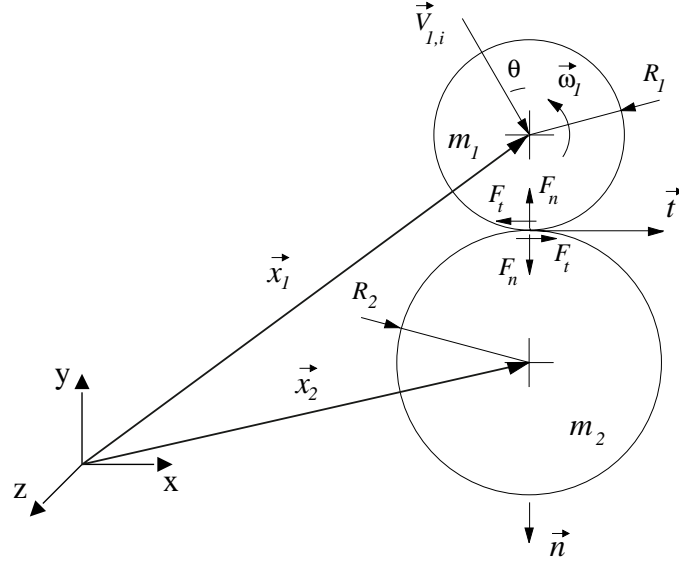


Figure 5.4 Definitions two-body collision

The unit-vector in normal direction, as defined in figure 5.4, is given by:

$$\vec{n} = \frac{\vec{x}_2 - \vec{x}_1}{|\vec{x}_2 - \vec{x}_1|} \quad (5.3)$$

with \vec{x}_1 the position of the incident particle and \vec{x}_2 the position of the second body, both at the start of the impact. Given the normal direction, the impact velocity can be split up in a normal and tangential component:

$$\begin{aligned} \vec{v}_{1i,n} &= (\vec{v}_{1i} \cdot \vec{n}) \vec{n} \\ \vec{v}_{1i,t} &= \vec{v}_{1i} - \vec{v}_{1i,n} \end{aligned} \quad (5.4)$$

From the momentum equations and the definition of the coefficient of restitution, the rebound velocities of the incident particle in normal direction becomes (Appendix A):

$$\vec{v}_{1r,n} = \vec{v}_{1i,n} - (1+e) \frac{m_2}{m_1+m_2} \vec{v}_{1i,n} \quad (5.5)$$

with e the coefficient of restitution which is introduced to describe the degree of energy losses ΔQ over the impact:

$$e^2 = 1 - \frac{\Delta Q}{\frac{1}{2} \frac{m_1 m_2}{m_1 + m_2} |\vec{v}_{1i,n}|^2} \quad (5.6)$$

Sticking occurs when the coefficient of restitution e becomes 0 or when the post-impact velocities of the incident particle and the target particle are equal.

The tangential rebound velocity depends on the initial slip-velocity and the magnitude of the friction force that is defined in equation 5.2. The friction force reduces the slip-velocity during the impact. If the slip-velocity becomes zero during the impact the motion in the contact changes from sliding to rolling. The minimum friction coefficient required to bring the slip-velocity to zero just at the end of the impact is derived in Appendix D and is given by:

$$f_{v_s=0} = \frac{\frac{2}{7} |\vec{v}_{i,s}|}{(1+e) |\vec{v}_{1i,n}|} \quad (5.7)$$

where $\vec{v}_{i,s}$ represents the initial slip-velocity between the surfaces in the contact point that is given by:

$$\vec{v}_{i,s} = \vec{v}_{1i,t} + R_1 (\vec{\omega}_{1i} \times \vec{n}) \quad (5.8)$$

If the friction coefficient for a certain combination of materials is smaller than this minimum friction coefficient the impact will end in a sliding motion. Otherwise the impact will end in a rolling motion. For an impact ending in a sliding motion, the tangential and angular rebound velocities become:

$$\vec{v}_{1r,t'} = \vec{v}_{1i,t} - f(1+e) \frac{m_2}{m_1 + m_2} \frac{|\vec{v}_{1i,n}|}{|\vec{v}_{i,s}|} \vec{v}_{i,s} \quad (5.9)$$

and

$$\vec{\omega}_{1r} = \vec{\omega}_{1i} + \frac{5}{2} f(1+e) \frac{m_2}{m_1 + m_2} \frac{|\vec{v}_{1i,n}|}{|\vec{v}_{i,s}|} \frac{(\vec{v}_{i,s} \times \vec{n})}{R_1} \quad (5.10)$$

respectively. The subscript t' refers to the tangential direction of the rebound velocity which, due to an initial rotation of the incident particle, can be different from the tangential direction of the incident velocity (Appendix D).

However, when during the impact the sliding motion changes to a rolling motion the rebound velocity in tangential direction and the angular velocity are given by:

$$\vec{v}_{1r,t'} = \vec{v}_{1i,t} - \frac{2}{7} \frac{m_2}{m_1 + m_2} \vec{v}_{i,s} \quad (5.11)$$

$$\vec{\omega}_{1r} = \vec{\omega}_{1i} + \frac{5}{7} \frac{m_2}{m_1 + m_2} \frac{(\vec{v}_{i,s} \times \vec{n})}{R_1} \quad (5.12)$$

Resuming, to apply the two-body approach information on the magnitude of three different parameters is required. These parameters are the proportionality factor C_m , the coefficient of restitution e and the friction coefficient f . The last two

parameters e and f depend on the materials involved in the impact and are discussed in the following sections. In the computer simulations by Werner [71] the proportionality factor is found to be about two. The proportionality factor is dependent on the bed properties and the particle-interaction parameters like the coefficient of restitution and the friction coefficient. In the simulations these interaction parameters were set to 0.85 and 0.5, respectively. It also appeared that the proportionality factor is approximately independent of the incident velocity, the angle of impact and the position at which the particle impacts the bed.

5.3 Coefficient of restitution

The coefficient of restitution defined in equation 5.6 is an important parameter in the two-body collision model. For a pure elastic impact without any other sources of energy loss, the coefficient is equal to 1. However, in a real impact some part of the initial kinetic energy is lost during the impact due to elastic wave propagation, plastic deformation, electrostatic charges and adhesion. The model developed by Rogers and Reed [56, 54] that on its turn is based on the work done by Bitter [9] is adapted to predict the coefficient of restitution as a function of the impact velocity and the material properties of the bodies involved in the impact.

The relations describing the impact of a particle with mass m_1 and radius R_1 on a particle with mass m_2 and radius R_2 are equivalent to those describing the impact of particle with mass m^* and radius R^* on a particle with infinite mass and radius. The mass m^* is defined by:

$$m^* = \frac{m_1 m_2}{m_1 + m_2} \quad (5.13)$$

which, making use of the assumed proportionality between the masses m_1 and m_2 , also can be written as:

$$m^* = \frac{C_m}{1 + C_m} m_1 \quad (5.14)$$

Besides, the effective radius R^* reads:

$$R^* = \frac{R_1 R_2}{R_1 + R_2} \quad (5.15)$$

5.3.1 Elastic impact

In the approach phase of an impact, the particle is decelerated until zero velocity by a repulsive force that arises because the contact area is deformed. During this phase the kinetic energy of the incident particle Q_k is stored in the contact area as elastic energy Q_e . Because in this phase a mutual surface is developed between the two bodies that has a lower energy level than two separate surfaces, a surface energy

term $Q_{A,a}$ is added to the system. The end of the approach phase is described using the following energy balance:

$$Q_k + Q_{A,a} = Q_e \quad (5.16)$$

where $Q_k = \frac{1}{2} m^* v_{i,n}^2$ is the kinetic energy of the incident particle with effective mass m^* . In the description of the approach phase the energy lost due to elastic wave propagation is not included. It has been shown by Reed [54] that this effect only results in an energy loss of a few percent over the impact. Also, the effect of electrostatic charges on the particle is not taken into account.

Upon impact the contact area between the particle and the surface is elastically deformed. In that case, the distribution of stresses in the contact area follows a Hertzian distribution as given in figure 5.5 (a).

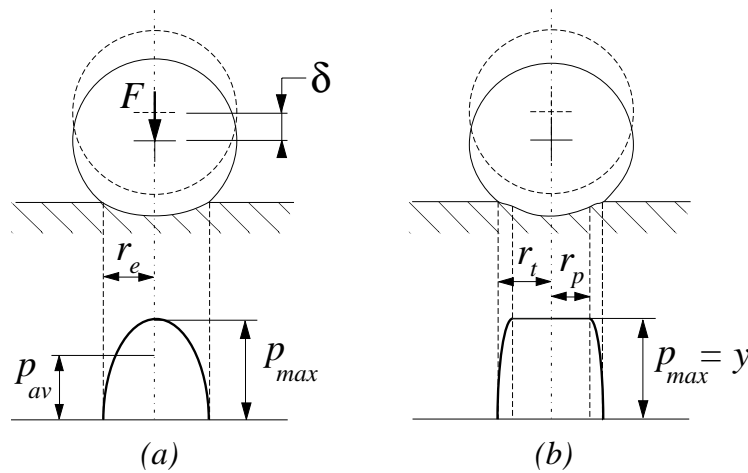


Figure 5.5 Pressure distribution for a pure elastic contact (Hertz distribution), figure (a), and an elastic-plastic contact, figure (b), Bitter [9].

The Hertzian distribution exhibits a maximum pressure at the centre, p_{max} , going to zero at the outside of the contact area with radius r_e . Hertz showed that the average pressure in the contact area is two-thirds of the maximum pressure, which results in the following contact load:

$$F = \frac{2}{3} \pi r_e^2 p_{max} \quad (5.17)$$

The amount of elastic energy stored in the contact area is found by integrating the contact load over the distance the particles have approached. Using the Hertz equations as written down in Appendix E, the elastic energy can be written as:

$$Q_e = \frac{2}{5} \left(\frac{2}{3} \right)^5 \frac{\pi^5 R^3 p_{max}^5}{(4/3 E^*)^4} \quad (5.18)$$

where E^* is given by:

$$\frac{1}{E^*} = \frac{1 - \nu_1^2}{E_1} + \frac{1 - \nu_2^2}{E_2} , \quad (5.19)$$

in which E_i and ν_i are the Youngs modulus and the Poisson constant for body i , respectively. The surface energy $Q_{A,a}$ is given by:

$$Q_{A,a} = \Gamma \pi r_e^2 \quad (5.20)$$

with Γ the work of adhesion as will be defined in equation 5.25. The maximum contact pressure at the end of the approach phase can be found by substituting equation 5.18 for the elastic energy Q_e and equation 5.20 for the adhesion energy $Q_{A,a}$ in equation 5.16.

In the restitution phase, the stored elastic energy is returned to the particle and the particle starts to move away from the surface. If the amount of elastic energy stored in the contact is larger than the adhesion energy $Q_{A,r}$ (required to break the contact), the particle rebounds otherwise it sticks. A rebound occurs when:

$$Q_e > Q_{A,r} \quad (5.21)$$

The adhesion energy in the restitution phase is larger than the surface energy acquired in the approach phase (Appendix E). The difference between the two adhesion energies is the only energy loss source taken into account for an elastic impact. In case of a rebound, the rebound velocity v_r and the coefficient of restitution become:

$$v_r = \sqrt{\frac{Q_k - (Q_{A,r} - Q_{A,a})}{\frac{1}{2} m^*}} \quad \text{and} \quad (5.22)$$

$$e^2 = 1 - \frac{(Q_{A,r} - Q_{A,a})}{\frac{1}{2} m^* v_{li,n}^2} \quad (5.23)$$

respectively. These functions can be evaluated using the following relation for the net adhesion energy:

$$Q_{A,r} - Q_{A,a} = 7.09 \left(\frac{R_c^4 \Gamma^5}{E^{*2}} \right)^{\frac{1}{3}} \quad (5.24)$$

as derived in Johnson [31] and discussed in Appendix E. In the above relation R_c represents the contact radius which for an elastic impact is equal to the radius R^* and Γ represents the work of adhesion that is a function of the surface free energy γ of the two surfaces 1 and 2 as given by [18]:

$$\Gamma = 2 \sqrt{\gamma_1 \gamma_2} \quad (5.25)$$

The surface free energy is determined by the intermolecular forces acting between the molecules near the surface. For most materials, interaction is by dispersion forces only. For metals and ionic solids, it can also include electrostatic interactions that are induced at the contact surface. In table 5.1 the surface free energy is given for some materials. It should be noted that for ionic solids the free surface energy is a function of the orientation of the surface in the crystal lattice.

	γ J/m ²
NaCl	0.32 ^a {100}
CaCO ₃	0.23 ^a {1010}
Glass	0.07 ^b
Copper	0.06 ^b
Steel	0.09 ^b

Table 5.1 Surface free energy (if relevant the lattice orientation is given between brackets); ^a Gilman [19], ^b Rogers and Reed [56].

The free surface energies reported by Rogers and Reed for the metals copper and steel were determined from the measurement of the contact angle between a drop of model fluid and the surface. It appeared that the values of the free surface energy for these metal surfaces were such that the expected metal-metal interaction did not affect the work of adhesion and the interaction was by dispersion forces only. Probably, the presence of thin oxide films on the steel and copper surface prevented the electrostatic interaction that only exists at very short distances, to occur. The same situation can occur in the impact of two crystalline solids where it is also unlikely that the two crystal faces touch in perfect alignment and without any contamination in between the surfaces. Therefore, it is more likely that for crystalline solids the surface energy is anywhere between the surface free energies of the materials with and without electrostatic interaction.

To incorporate the effect of a liquid phase at the surface of either the particle or the surface on the impact, an additional energy term can be added to equation 5.24. This term should account for the energy required to rupture a liquid bridge between two surfaces as for example treated by Simons [62].

5.3.2 Limiting elastic case

For an impact where during the approach phase the maximum pressure in the contact p_{max} (figure 5.5) exceeds a critical value, plastic deformation is initiated in the softer of the two bodies. The critical pressure for plastic deformation to occur in the contact area is defined as the elastic load limit y , being a material property. With plastic deformation occurring during the impact, part of the kinetic energy of the incident particle is dissipated and this can significantly influence the coefficient of restitution.

To verify whether, for the materials encountered in a refuse-waste incinerator, plastic deformation is likely to occur, the maximum incident velocity below which

the impact remains elastic is discussed. This maximum velocity is defined as the limiting elastic velocity.

Assuming the adhesion energy acquired in the approach phase to be negligible compared to the kinetic energy of the incident particle, the limiting elastic velocity can be found from the balance between the kinetic energy of the incident particle and the limiting amount of elastic energy Q_{el} . The limiting amount of elastic energy is found by substituting the elastic load limit y for the maximum pressure in equation 5.18. Hence, the limiting elastic velocity $v_{i,l}$ becomes:

$$v_{i,l} = \frac{\pi^2}{2\sqrt{10}\rho_1} \frac{y^{5/2}}{E^{*2}} \left(\frac{R_2}{R_1 + R_2} \right)^{3/2} \sqrt{\frac{1+C_m}{C_m}} \quad (5.26)$$

For the impact of a spherical particle with a flat second body of infinite mass ($C_m \rightarrow \infty$), the limiting elastic velocity is independent of the radius of the particle and is only a function of the material properties. In the case of a two-body impact, the ratio in diameters and masses does influence the impact velocity for which the impact changes from elastic to plastic.

To calculate the limiting elastic velocity, the elastic load limit y needs to be known for the materials involved in the impact. The elastic load limit is a function of the uni-axial yield stress Y of a material. The yield stress of an ideal plastic material can be calculated from the Vickers hardness H_v as given by Tabor [66];

$$Y \cong \frac{H_v}{3} \quad (5.27)$$

Although the hardness is measured under static conditions, it is assumed that it is useful to predict the onset for plastic deformation to occur in a dynamic impact. The Vickers hardness is measured by pressing a diamond pyramid indenter with a known load into a surface. The size of the crater determines the hardness that is defined as the ratio of the load to the pyramidal area of indentation and is expressed in kgf/mm^2 ($= 9.81 \cdot 10^6 \text{ N}/\text{m}^2$). For minerals the hardness is mostly expressed in terms of the Mohs' scale of hardness, table 5.2.

Mineral	Chemical Formula	Mohs' hardness
Talc	$\text{Mg}_3[\text{Si}_4\text{O}_{10}] [\text{OH}]_2$	1
Gypsum	$\text{CaSO}_4 \cdot 2 \text{H}_2\text{O}$	2
Calcite	CaCO_3	3
Fluo-rite	CaF_2	4
Apatite	$\text{Ca}_5(\text{PO}_4)_3(\text{F},\text{Cl})$	5
Feldspar	KAlSi_3O_8	6
Quartz	SiO_2	7
Topaz	$\text{Al}_2\text{SiO}_4(\text{F},\text{OH})_3$	8
Corundum	Al_2O_3	9
Diamond	C	10

Table 5.2 Minerals defining Mohs' scale of hardness

The Mohs' hardness scale is based on a scratch test. Ten minerals were selected such that the one with the higher hardness number scratches the one with a lower hardness number. Although the Mohs' scale has an arbitrary basis, comparison of this scale with the hardness determined from indentation tests shows that the indentation hardness H_v for all minerals but diamond is related to the Mohs' hardness, M , as given by Tabor [66]:

$$\log H_v = 1.7 + 0.2 (M - 1) \quad (5.28)$$

Using this relation the Mohs' hardness can be converted to a Vickers hardness from which the yield stress can be estimated using equation 5.27. For different materials the material properties like density, Young's modulus, Poisson constant, Mohs' hardness and the yield stress are given in table 5.3.

Material	ρ kg /m ³	$E \times 10^9$ N/m ²	ν	H_v Kgf/mm ²	Mohs hardness	$Y \times 10^8$ N/m ²
Glass	2470	50	0.27		6.5	20
Copper	8960	124	0.33	92		3.0
Steel	7800	215	0.28	610		20
Sodium-chloride (NaCl)	2163	24.8	0.25		2	2.6
Potassium-sulphate (K ₂ SO ₄)	2665	30	0.30		3	4.1
Aluminium-oxide (Al ₂ O ₃)	3970	260	0.24		9	65

Table 5.3 Material properties for the different impact surfaces used in figure 5.6 [42, 50 and 56].

Plastic deformation starts to occur when the maximum shear stress τ_{max} in a material exceeds a critical value τ_{crit} . According to the shear-stress criterion, this critical shear stress is only half of the uni-axial yield stress Y and the criterion for plastic deformation becomes:

$$\tau_{max} > \frac{1}{2}Y (= \tau_{crit}) \quad (5.29)$$

According to Davies [16], the maximum shear stress is located below the centre of the contact at a depth of about half the radius of the projected contact area and is equal to 0.47 of the average pressure in the contact. This yields:

$$\tau_{max} = 0.47 p_{av} \rightarrow p_{av,crit} = 1.06 Y \quad (5.30)$$

Because the average pressure in the contact is two-thirds of the maximum pressure, the elastic load limit is given by:

$$y \equiv p_{max,crit} = 1.59 Y \quad (5.31)$$

Using this relation, the limiting elastic velocity can be calculated from equation 5.26. For the materials given in table 5.3, the limiting elastic velocity is

calculated for the impact of a particle with a second body assuming that both bodies consist of the same material. It is further assumed that the radii of the bodies are equal and that the proportionality factor is equal to 2 as found by Werner [71]. The limiting elastic velocity is given in figure 5.6 in which, for three different elastic load limits, the limiting elastic velocity is also given as a continuous function of E^* . In these latter calculations the density of the particle is taken to be 2500 kg/m^3 .

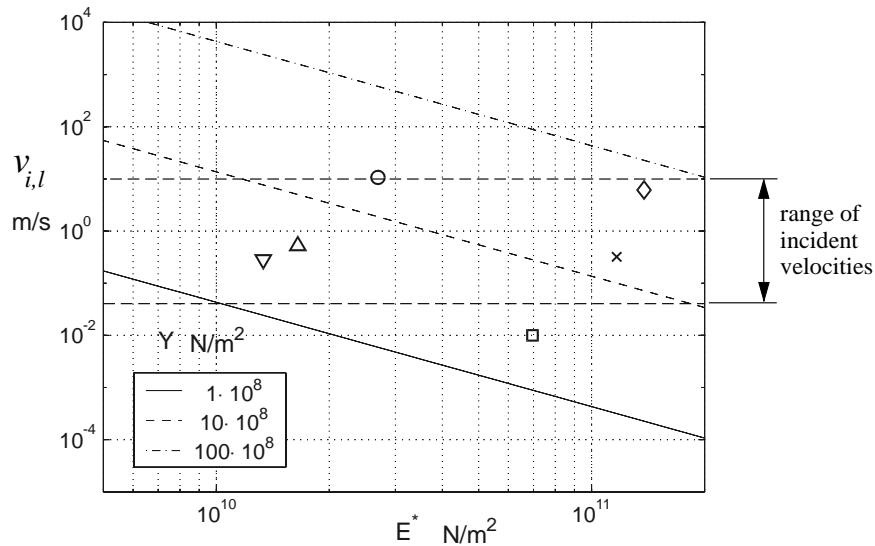


Figure 5.6 Limiting elastic velocity as a function of E^* . The solid lines represent the limiting elastic velocity for particles with a density of 2500 kg/m^3 and three different elastic load limits. The symbols give the limiting elastic velocity for the materials of table 5.3; glass (o), copper (\square), steel (x), NaCl (∇), K_2SO_4 (Δ), and Al_2O_3 (\diamond).

Of the materials given in table 5.3 the bottom three represent the materials encountered in a refuse waste incinerator. In section 4.5 it is found that the incident velocity varies from 1% to 100% of the main stream velocity. Using a minimum and a maximum main stream velocity of 5 and 10 m/s, respectively, the incident velocity is expected in the range between 0.05 to 10 m/s. Comparing this range of incident velocities with the limiting elastic velocities for the different materials shows that for the sulphates, the chlorides but also for the oxides plastic deformation can occur during the impact. So, for all these materials the coefficient of restitution (figure 5.6) can be reduced due to plastic deformation.

5.3.3 Elastic-plastic impact

If the maximum pressure in the contact exceeds the elastic load limit, plastic flow is initiated in the contact. At the moment the contact changes from elastic to elastic-plastic (referred to as the limiting case), the contact radius is equal to r_{el} and the distance of approach to h_{el} . In appendix E, for both quantities relations have been derived. As discussed by Bitter [9], with ongoing plastic deformations a plastically deformed region develops from the centre of the contact surrounded by an annulus

where deformations remain elastic, figure 5.5 (b). In Appendix E is shown that when the total contact area is small compared to the cross-section of the particle, the area of the annulus is constant and equal to the contact area in the limiting case. When assuming that also the pressure distribution remains the same, the elastic energy stored in the only elastically deformed annulus is constant and equal to Q_{el} . For the contact area with radius r_t holds:

$$r_t^2 = r_{el}^2 + r_p^2 \quad (5.32)$$

with r_p the radius of the plastically deformed area.

For an elastic-plastic impact, besides the only elastically deformed annulus also elastic energy is stored in the plastically deformed region. The latter contribution is denoted with Q_{pe} . As derived in Appendix E, Q_{pe} can be written in terms of the contact load F , the contact load F_{el} and the distance of approach h_{el} in the limiting elastic case:

$$Q_{pe} = \frac{1}{2} h_{el} (F - F_{el}) \quad (E.18)$$

The amount of energy dissipated in plastic flow is approximated by:

$$Q_p \approx \frac{(F - F_{el})^2}{4\pi R^* y} \quad (E.17)$$

and the surface energy released to the system in the approach phase by:

$$Q_{A,a} = \Gamma \pi \left(r_{el}^2 + \frac{F - F_{el}}{\pi y} \right) \quad (E.19)$$

Using the given relations for the contact energies, the energy balance 5.16 for the approach phase reads:

$$Q_k + Q_{A,a}(F) = Q_{el} + Q_{pe}(F) + Q_p(F) \quad (5.33)$$

with the contact load F as the only unknown. After solving this relation to yield F , all the contact energies at the end of the approach phase are known. Given these energies the criterion for sticking can be evaluated:

$$Q_{el} + Q_{pe} \leq Q_{A,r} \quad (5.34)$$

where the left hand side comprises the stored elastic energy in the contact that is released in the restitution phase and $Q_{A,r}$ represents the adhesion energy in the restitution phase. In case of a rebound the rebound velocity can be calculated from:

$$v_r = \sqrt{\frac{Q_k - Q_p - (Q_{A,r} - Q_{A,a})}{\frac{1}{2}m^*}} \quad (5.35)$$

and the coefficient of restitution becomes:

$$e^2 = 1 - \frac{Q_p + (Q_{A,r} - Q_{A,a})}{\frac{1}{2} m^* v_{li,n}^2}, \quad (5.36)$$

To evaluate the above relation for the coefficient of restitution, the net adhesion energy as given by equation 5.24 is used again. Because the plastic deformation has resulted in a remnant deformation of the contact, the contact radius R_c in this equation is no longer equal to R^* . Assuming that during the restitution phase only elastic deformations occur, R_c can be found by applying the Hertz equations for the conditions as apply at the end of the approach phase or at the beginning of the restitution phase. The new contact radius is then found from:

$$R_c = \frac{3/4 E^* r_t^3}{F}. \quad (5.37)$$

with the radius r_t given by equation E.20.

So far, the elastic load limit is assumed to be given by equation 5.31. However, when the plastically deformed area develops, only a part of the applied contact pressure leads to shear and the major part appears as hydrostatic pressure. For a fully developed plastic contact the average pressure becomes equal to the maximum pressure and is, according to Tabor [66], equal to 3.2 times the yield stress. The elastic load limit in that case reads:

$$y = 3.2Y \quad (5.38)$$

From the above discussion it follows that depending on the state of the contact the elastic load limit is somewhere between 1.59 and 3.2 times the yield stress. It is noted that the elastic load limit for a dynamic impact is calculated from a yield stress measured under static conditions. This elastic load limit can differ from the dynamic elastic load limit as is shown by Mulhearn [46]. In dynamic indentation experiments, it was found that the dynamic elastic load limit for a soft metal like lead is approximately 2 times higher than the elastic load limit for a full static plastic contact. The influence of the elastic load limit is discussed in section 5.6.

5.3.4 Overall model for the coefficient of restitution

With the relations given so far, it is possible to calculate the coefficient of restitution for either an elastic or an elastic-plastic impact. In figure 5.7 a schematic representation is given of the resulting model. The model requires values for the parameters defining the materials involved in the impact, parameters defining the geometry and the impact velocity in normal direction.

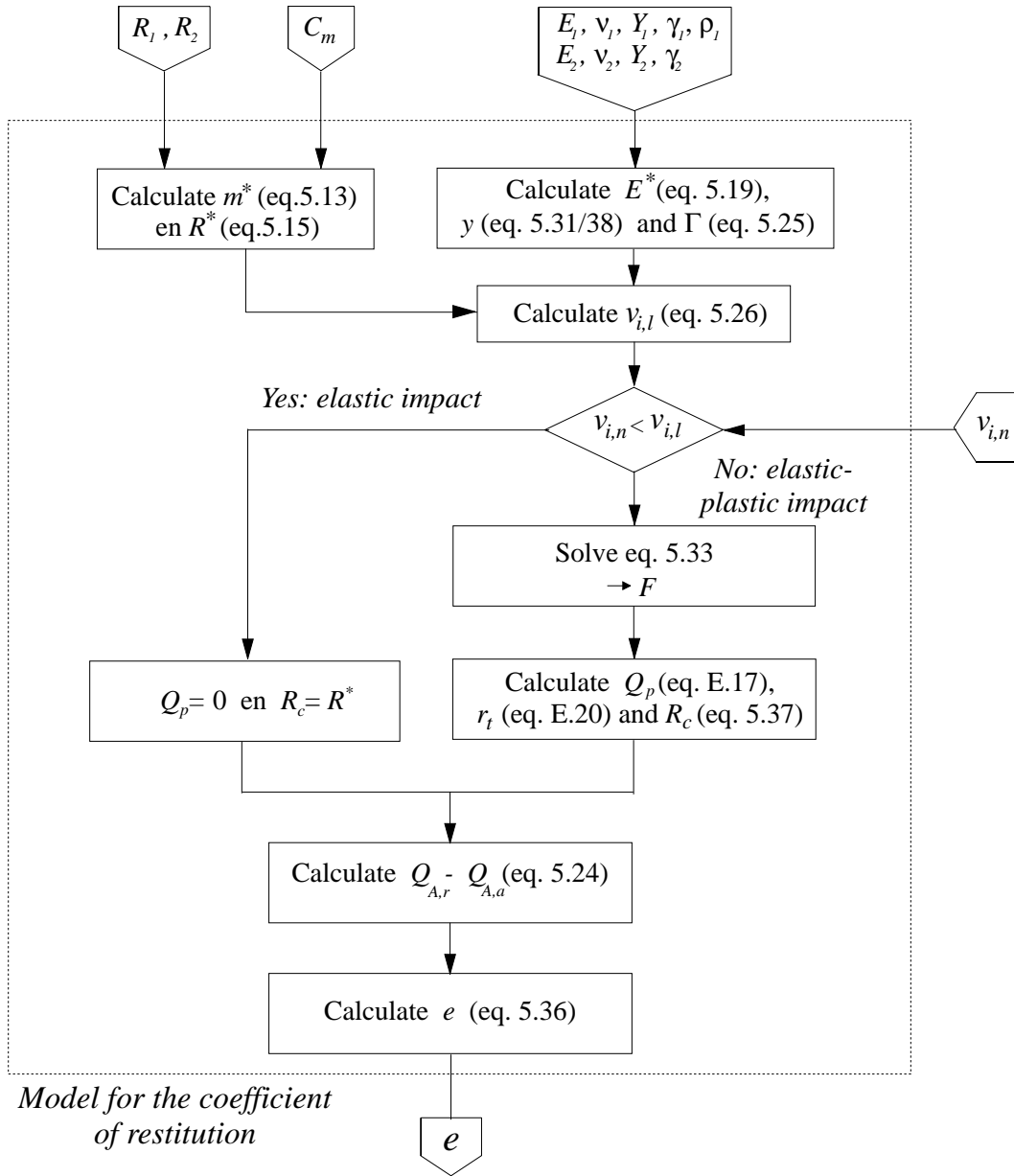


Figure 5.7 Schematic lay-out of the model for the coefficient of restitution.

The coefficient of restitution is calculated with the model for the impact of a 10 and 50 μm particle on an equally sized particle. For the impacts the proportionality factor is set to 2 and ∞ , respectively. For the material properties the values as given in table 5.3 for K_2SO_4 are used. The work of adhesion Γ is set to 0.30 J/m^2 . In figure 5.8 the coefficient of restitution is given as a function of the incident velocity.

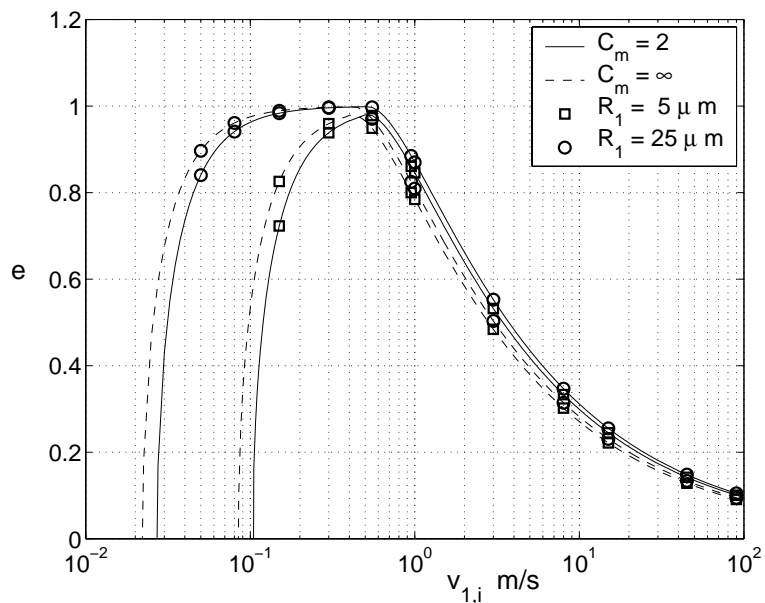


Figure 5.8 Coefficient of restitution for 10 and 50 μm K_2SO_4 particles impacting an equal sized particle of the same material. ($C_m = 2 / \infty$, $\Gamma = 0.30 \text{ J/m}^2$ and $y = 1.6 Y$). Note: markers are only used for clarification

For the impact of a K_2SO_4 particle on an equal sized particle of the same material, the coefficient of restitution shows two regimes. For velocities lower than about 0.5 m/s the impact remains elastic and the coefficient of restitution is only influenced by the work of adhesion. The velocity for which the coefficient of restitution becomes zero is defined as the critical sticking velocity. The critical sticking velocity is found to be a weak function of the proportionality factor and a strong function of the particle radius. For incident velocities above 0.5 m/s, plastic deformation starts to occur during the impact and the coefficient of restitution rapidly drops.

In figure 5.8 the elastic load limit is taken 1.59 times the yield stress (equation 5.31). As mentioned, the elastic load limit changes to 3.2 times the yield stress for a fully developed plastic contact. Using this value for the elastic load limit, the coefficient of restitution is calculated and given in figure 5.9 as a function of the incident velocity.

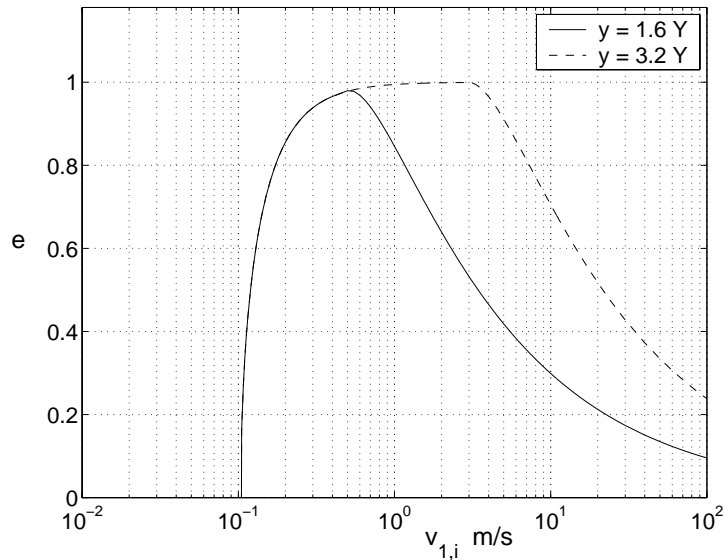


Figure 5.9 Coefficient of restitution for 10 μm K_2SO_4 particles impacting an equally sized particle of the same material. ($y = 1.6 / 3.2 Y$, $C_m = 2$ and $\Gamma = 0.30 \text{ J/m}^2$).

Using an elastic load limit as expected for a fully developed plastic contact results in a shift of the elastic-plastic part of the curve to higher velocities. As can be seen the relation between the elastic load limit and the yield stress for this material does not influence the velocity below which sticking occurs. This critical sticking velocity is denoted with v_{crit} and is given in figure 5.10 for the elastic impact of a K_2SO_4 particle on an equally sized second particle and a proportionality factor of 2. The critical sticking velocity is plotted as a function of the particle radius R_1 and the work of adhesion Γ .

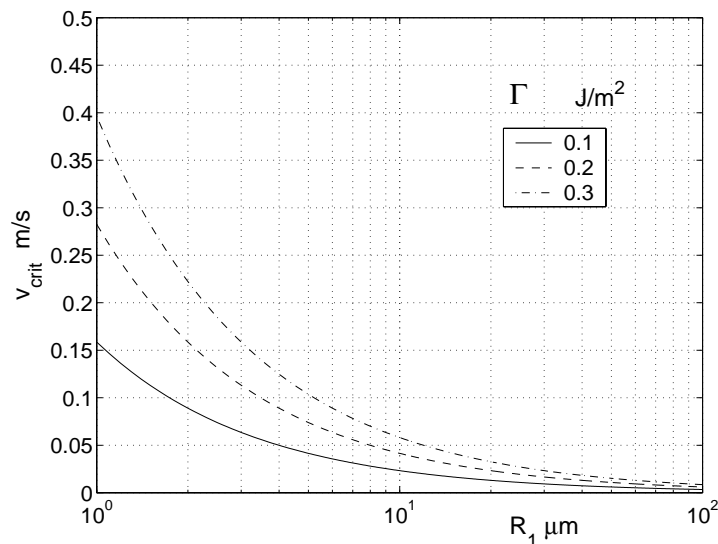


Figure 5.10 Critical sticking velocity for glass particles impacting a second surface as a function of the particle radius and the work of adhesion ($y = 1.6 Y$, $C_m = 2$).

In section 4.5 it is derived that the expected incident velocities are between 0.05 and 10 m/s. Comparing this incident velocity to the critical sticking velocity of about 0.08 m/s for a 7 μm particle, it is evident that the sticking efficiency for most impacts indeed cannot be assumed unity. To calculate the critical sticking velocity a work of adhesion Γ of 0.30 J/m² is applied.

5.4 Friction coefficient and proportionality factor

Besides the coefficient of restitution, the two-body model requires two additional parameters. The first additional parameter is the friction coefficient f . The friction coefficient is a function of the materials involved in the impact and is a function of the system parameters like pressure, humidity, cleanness of the surface and surface roughness. Because of these influences, values reported in literature exhibit a quite large spread. Even in one experiment the friction coefficient can vary by more than 100% as is illustrated by the experiments reported in Buckley [14]. In these experiments the friction coefficient of MgO in vacuum varied between 0.3 and 0.7. The variation was attributed to the removal of contaminants from the surface by the sliding movement. Another indication for the friction coefficient is given by the values reported for the friction coefficient of soft glass on itself. For a lubricated and a dry contact in vacuum a value is found of 0.04 and 0.5, respectively. Although the choice for a friction coefficient remains arbitrary, on the basis of the previous values the friction coefficient expected for the materials depositing in the boiler is between 0.1 and 0.7. The value of 0.2 used by Konstandopoulos and the value of 0.5 used by Werner are both inside the expected range of values.

The second additional parameter, required by the two-body model, is the proportionality factor C_m . This factor gives a measure for the effective number of bed particles that is accelerated during the impact by the incident particle. Therefore, it has a strong effect on the relative rebound velocity in y-direction. For a fouling layer two different regimes in the proportionality factor are expected. Based on the value found by Werner [71], a proportionality factor of about 2 is expected for a powdery layer. This factor is found for frictional beds of particles with no special binding between the particles. For layers where the particles are firmly bonded to one another the incident particle has to accelerate all the particles in touch with the target particle. In this case, the proportionality factor goes to infinity. Binding can occur in a fouling layer because of sintering or the appearance of a liquid phase in the deposit.

5.5 Numerical sticking model: packing and bed position

To predict the sticking efficiency for the impact of a single particle or an ensemble of particles on a powdery surface, the impact of the(se) particle(s) is simulated using a numerical model. A schematic representation of this model is given in figure 5.11.

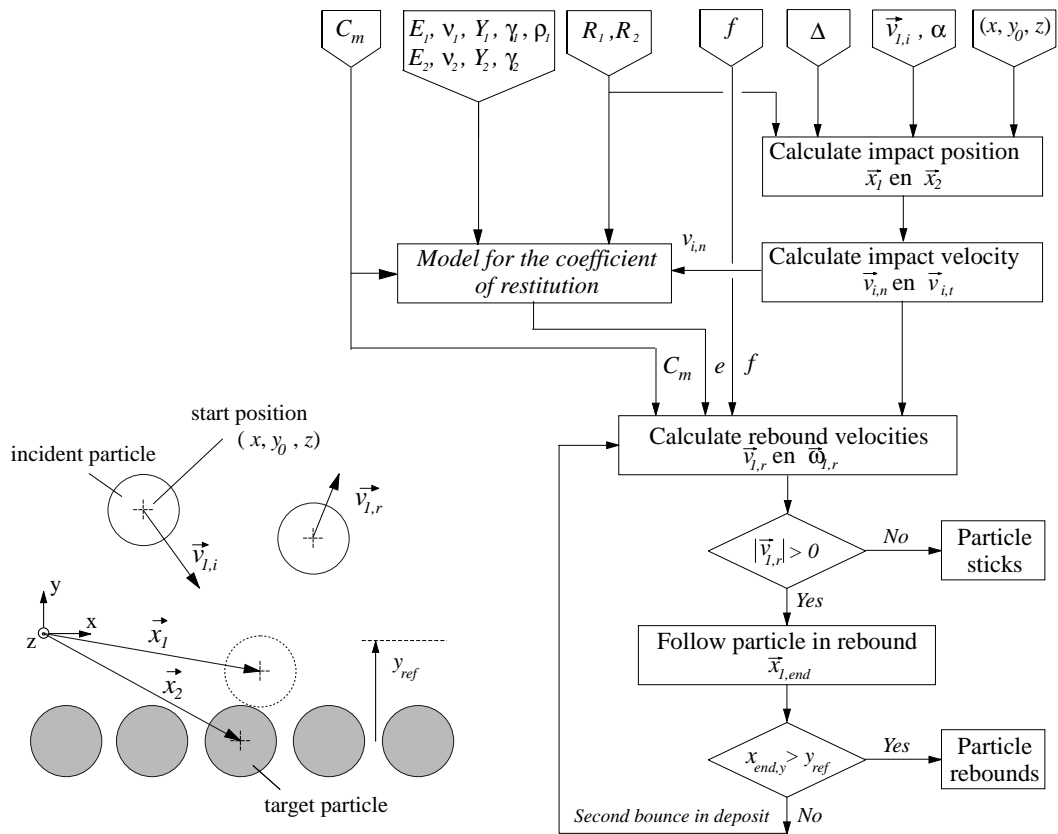


Figure 5.11 Problem definition and outline of the numerical model

In the model, a particle is tracked from a start position (x, z) at a fixed height y_0 above the bed until the particle hits one of the bed particles. The start position in x and z direction is sampled from a uniform distribution over a unit-area A^* , because in the experiments as well as in the numerical simulations the relative position of the incident particle to the bed of particles is not known. The unit-area A^* constitutes a characteristic segment of the deposition surface as pointed out in figure 5.12.

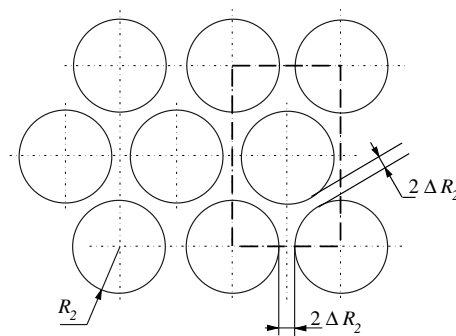


Figure 5.12 Distribution of particles used in the numerical model.

The particles in the bed are assumed to be arranged in a homogeneous packing. In this packing the particles have their centres in the same plane and are separated by a distance 2Δ . The distance Δ , further denoted as the roughness parameter, can account for inhomogenities in real deposits.

After the particle is tracked, the position of the incident particle and the position of the bed particle hit, \vec{x}_1 and \vec{x}_2 respectively, are known. From these

positions the local coordinate-system \vec{n} , \vec{t} is determined and the normal and tangential impact velocities are calculated using equation 5.4. Knowing the normal component of the incident velocity, the coefficient of restitution can be calculated using the model described in section 5.3. In case the sticking coefficient is zero the particle sticks and no rebound velocity is found. Otherwise, the rebound velocity in normal direction is calculated using equation 5.5.

To calculate the rebound velocity in tangential direction, the model first establishes whether the impact ends in a sliding or in a rolling condition by comparing the actual friction coefficient with the minimum required friction coefficient to bring the initial slip-velocity to zero (equation 5.7). If the friction coefficient is larger than the minimum friction coefficient, the impact ends in a rolling condition and the tangential rebound velocity is calculated using equation 5.11 and the angular rebound velocity from equation 5.12. However, if the friction coefficient is smaller than the required minimum coefficient the rebound velocities are calculated using equations 5.9 and 5.10.

The tracking is continued for all the rebounding particles until the particle is at some distance y_{ref} above the surface and the rebound velocities are recorded. In some cases, the particle hits another bed particle before it can leave the bed of particles. For such a second bounce in the deposit again the two-body relations are solved to obtain the rebound velocities. In general, a particle experiences no more than three local impacts before it either sticks or leaves the surface.

5.6 Sticking efficiency

The sensitivity of the model results to the important parameters like coefficient of restitution, friction coefficient and proportionality factor is determined using the two-body approach applied in the numerical sticking model. In the calculations the impact is simulated of 10,000 K_2SO_4 particles with a diameter of 10 μm on a bed of K_2SO_4 particles with the same diameter as that of the incident particles. The parameters used in the calculations are given in table 5.4 and the parameters varied in the simulations are indicated in the corresponding paragraphs.

Parameters	
Material	K_2SO_4 (table 5.3)
y	3.2 Y
C_m	2
f	0.2
Δ	0.1

Table 5.4 Set of parameters applied in calculations

The outcome of the impact is characterized using the sticking efficiency s , relative rebound velocity in y-direction ϵ_y and the rebound angle β . For the impact of a single particle the sticking efficiency is either 1 (sticking) or zero (rebound). However, for an ensemble of impacts the sticking efficiency is a statistical value

anywhere between 0 and 1. Second, for all the rebounding particles the impact is also characterized by the relative rebound velocity in y-direction and the rebound angle as defined in figure 5.13. The relative rebound velocity is defined as the ratio of the rebound to the incident velocity in y-direction as given by:

$$\varepsilon_y = \frac{v_{1r,y}}{v_{1i,y}} \quad (5.39)$$

The number of impacts simulated is chosen such that the random errors in the mean values of s , ε_y and β are less than 1%.

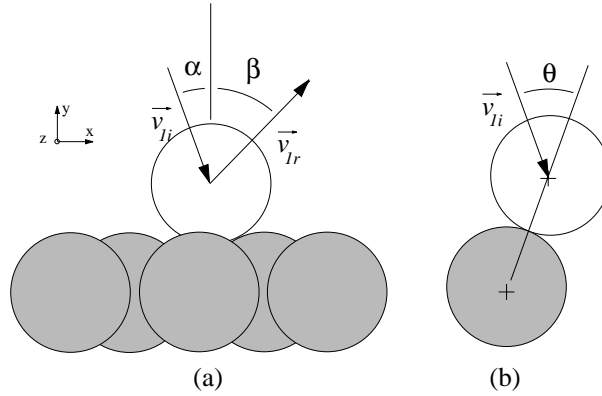


Figure 5.13 Definitions for the impact angle α , rebound angle β and local contact angle θ .

Sticking efficiency as a function of incident velocity and impact angle

The sticking efficiency is calculated as a function of the incident velocity and the impact angle. The results are given in figure 5.14 where the velocity is made dimensionless using the critical sticking velocity, which equals 0.1 m/s for the present set of parameters.

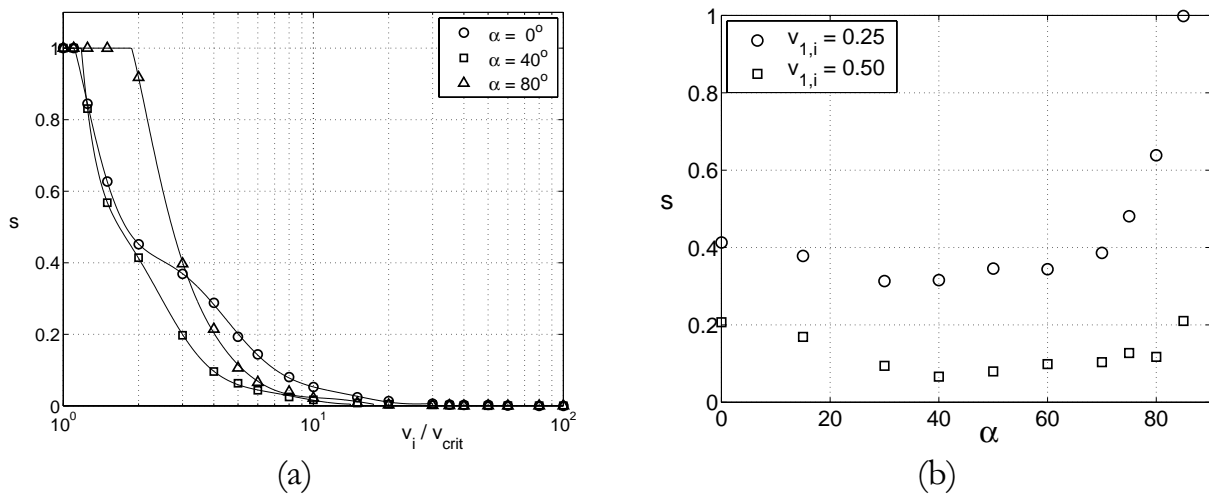


Figure 5.14 Sticking efficiency for 10 μm K_2SO_4 particles on a powdery layer ($v_{crit} = 0.1$ m/s).

For the three impact angles, the sticking efficiency is found to be unity below a certain velocity and to drop exponentially for higher velocities. For the two lowest impact angles the velocity above which the sticking efficiency starts to fall is found to coincide with the critical sticking velocity. For the largest impact angle, the sticking efficiency starts to fall at a velocity larger than the critical sticking velocity.

When increasing the incident velocity, particles will start to rebound from impact positions where the normal component of the impact velocity is maximal. For these positions the local impact angle θ , as defined in figure 5.13, is minimal. In case of a perpendicular impact, this corresponds with impact positions near the top of a bed particle where the local impact angle is zero. With increasing impact angles the position for which the local impact angle is minimal moves to the side of the bed particles. For large impact angles this position can become situated in the shade of an adjacent particle implying that an impact with zero local impact angle is not possible anymore and that the normal component of the incident velocity is always lower than the incident velocity. Hence, the incident velocity needs to be larger than the critical sticking velocity before the sticking efficiency starts to decrease.

For the two lower impact angles, the rate with which the sticking efficiency decreases reduces for the intermediate incident velocities where for the largest impact angle this effect is not seen. With an increasing incident velocity, particles start to rebound from impact positions with a small local impact angle. For even higher velocities, particles also rebound from positions with a larger local impact angle. For these impacts, the rebound velocity in normal direction is relatively small and the tangential component of the rebound velocity is directed towards the deposit (negative y-direction). This makes that the overall rebound velocity is likely to be directed towards the deposit yielding a second bounce in the deposit. For this second impact the incident velocity is smaller than for the first impact and sticking is likely in this second bounce resulting in a reduction of the rate with which the sticking efficiency decreases for the intermediate incident velocities. The occurrence of second bounces in the deposit becomes less likely for impacts with a larger impact angle, because the tangential component of the incident as well as the rebound velocity have a positive component in the y-direction. This makes that the delay in sticking efficiency is not seen at the largest simulated impact angle of 80° .

The same effect accounts for the fact that the sticking efficiency is the lowest for the intermediate impact angles (figure 5.14 (b)). For the smallest impact angles, the sticking efficiency is higher due to the occurrence of second bounces. The increase in sticking efficiency for larger impact angles is explained because for these angles most impacts are located close to the top of a bed particle where the local impact angle is small. This makes that the normal component of the incident velocity strongly reduces and sticking becomes more likely.

Sticking efficiency as a function of the coefficient of restitution

The coefficient of restitution is a strong function of the elastic load limit as already presented in figure 5.9. The influence of the elastic load limit on the sticking efficiency is given in figure 5.15.

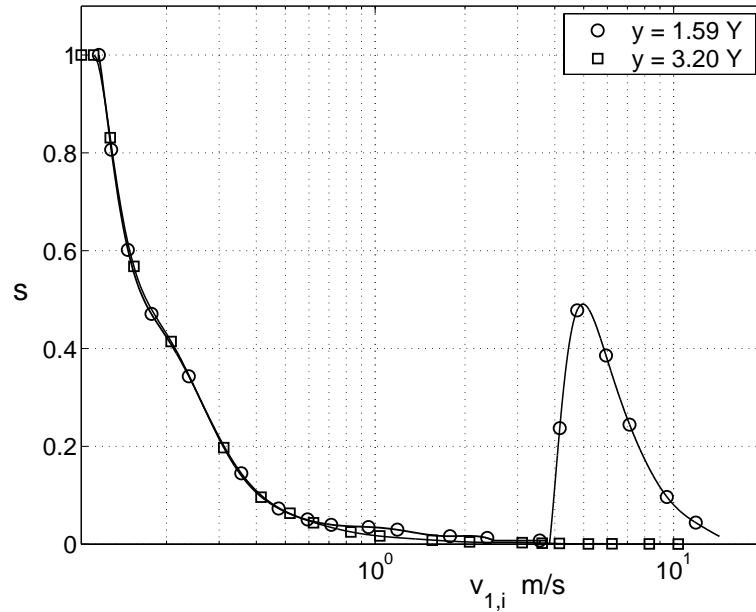


Figure 5.15 Sticking efficiency as a function of incident velocity for $10 \mu\text{m}$ K_2SO_4 particles impacting on a powdery layer. ($v_{crit} = 0.1 \text{ m/s}$, $y = 1.59 / 3.2 Y_{\text{K}_2\text{SO}_4}$ and $\alpha = 40^\circ$)

For velocities up to approximately 3 m/s the sticking efficiency is the same for both values of the elastic load limit. Above this velocity, the sticking efficiency for the lowest elastic load limit shows a peak that is not seen for the highest elastic load limit. The reason for this peak in the sticking efficiency can be seen from the relation for the rebound velocity in normal direction as given in equation 5.5. This velocity becomes negative or directed towards the deposit for a value of the coefficient less than the inverse of the proportionality factor, or:

$$e < \frac{1}{C_m}$$

With respect to an elastic load limit of 3.2 times the yield stress, this situation only occurs for velocities near the critical sticking velocity. For an elastic load limit of 1.59 times the yield stress, this situation also occurs for velocities above 3 m/s as can be seen in figure 5.9. In that case a second bounce occurs with a much lower velocity and consequently a much higher sticking efficiency. With even larger incident velocities the absolute value of the negative rebound velocity increases and particles also rebound in their second bounce.

Sticking efficiency as a function of the friction coefficient

The sticking efficiency is calculated for three different values of the friction coefficient i.e. 0.1, 0.2 and 0.4. For all three values the sticking efficiency is calculated as a function of the impact angle when keeping the incident velocity constant at 0.5 m/s. The sticking efficiency is given in figure 5.16.

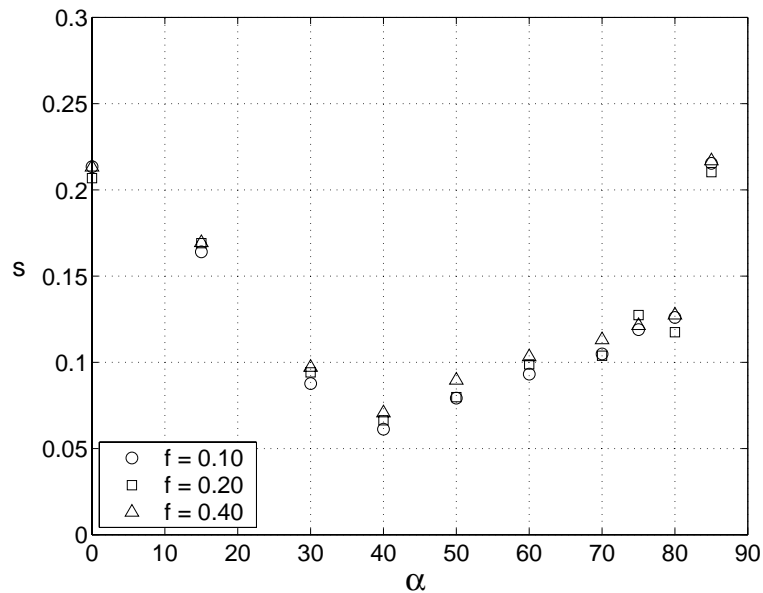


Figure 5.16 Sticking efficiency as a function of impact angle for $10 \mu\text{m}$ K_2SO_4 particles impacting on a powdery layer. ($v_{crit} = 0.1 \text{ m/s}$ and $f = 0.1, 0.2$ and 0.4).

The friction coefficient is found to have almost no influence on the sticking efficiency. This also holds for the mean relative rebound velocity in y-direction and the rebound angle, see figure 5.17.

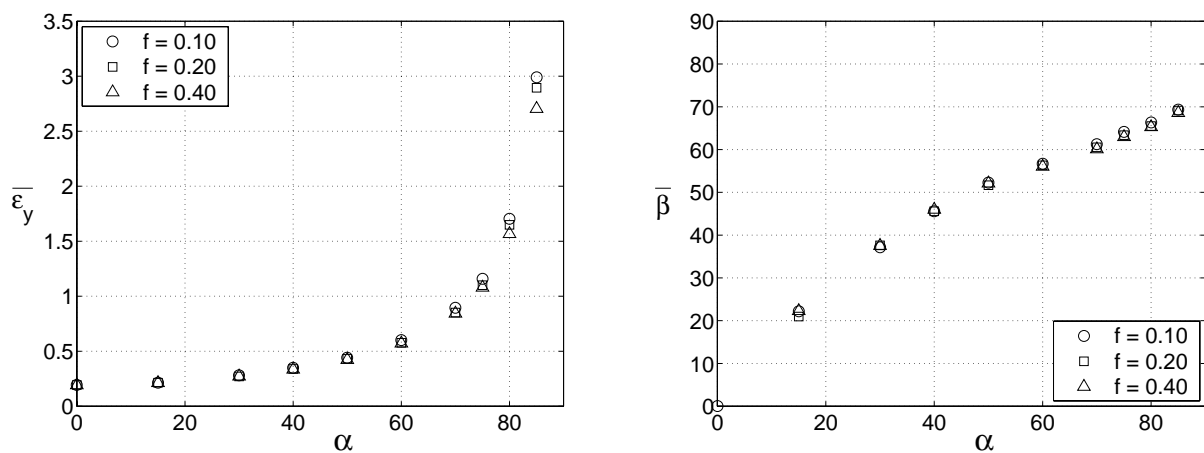


Figure 5.17 Mean relative rebound velocity and rebound angle as a function of impact angle for $10 \mu\text{m}$ K_2SO_4 particles impacting on a powdery layer. ($v_{l,i} = 0.5 \text{ m/s}$ and $f = 0.1, 0.2$ and 0.4).

Sticking efficiency as a function of the proportionality factor

So far, a value of 2 is used for the proportionality factor C_m . The influence of this parameter, that characterizes the powdery layer, is shown in figure 5.18 where the sticking efficiency is plotted as a function of the absolute incident velocity.

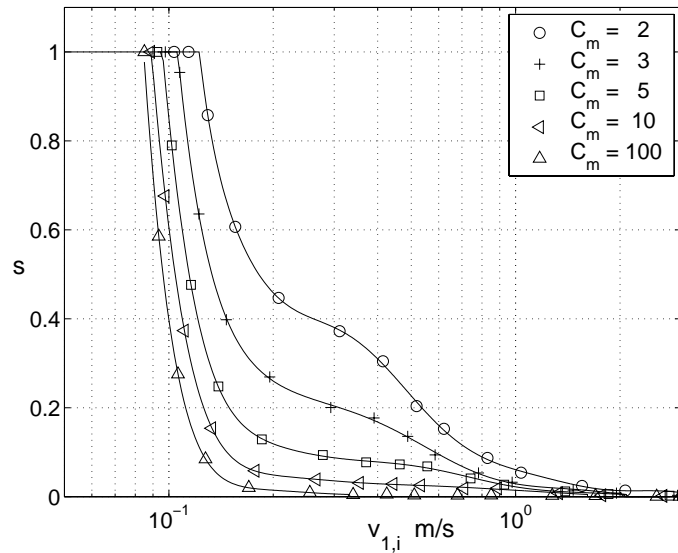


Figure 5.18 Sticking efficiency as a function of incident velocity and the proportionality factor for 10 μm K_2SO_4 particles impacting on a powdery layer ($\alpha = 0^\circ$).

The proportionality factor is found to have a strong effect on the sticking efficiency of particles impacting a powdery layer. Increasing the proportionality factor lowers the critical sticking velocity and increases the rate with which the sticking efficiency drops for velocities above the critical sticking velocity. For a proportionality factor of 100 the sticking efficiency is almost a step function of the incident velocity as expected for the impact of a particle on a flat solid surface with infinite mass.

Besides the effect of the proportionality factor on the sticking efficiency, it also has a strong influence on the rebound velocities as is shown in figure 5.19. In this figure the mean relative rebound velocity in y-direction is given as a function of the proportionality factor.

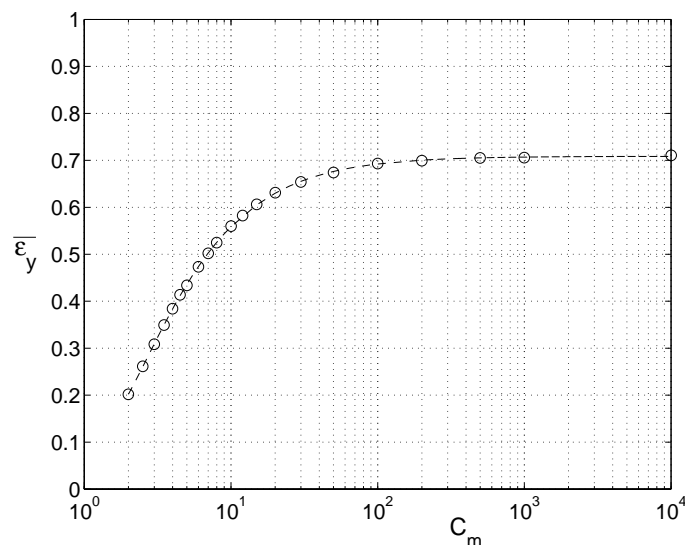


Figure 5.19 Mean relative rebound velocity in y-direction as a function of the proportionality factor. ($v_{1,i} = 1 \text{ m/s}$)

When C_m is varied the corresponding relative rebound velocity increases fast. For larger values, the increase slows down and from a C_m value of around 100 a constant value is reached. It is expected that for a powdery layer with no other binding between the particles than molecular forces, the proportionality factor is within the range between 2 and 10. A value of around 100 is expected to be representative for the proportionality factor of a sintered layer.

5.7 Conclusion

Based on the two-body approach as suggested by Werner [71], a theoretical sticking model has been developed. The model predicts the sticking efficiency as a function of the local impact conditions like the particle diameter, the impact velocity, the angle of impact and the character of the layer. The model requires the coefficient of restitution. It is a function of the materials involved in the impact and a model is presented to describe it. Besides, the model requires values for the friction coefficient and the proportionality factor. The friction coefficient is found to have a minor influence on the sticking efficiency, rebound velocity and rebound angle. The proportionality factor has a strong influence on the impact. The value to be used for powdery layers can, so far, only be based on the numerically found value by Werner [71]. From his simulations a proportionality factor of 2 was found for a layer with no binding between the particles. It is expected that the proportionality factor goes to infinity for layers where the particles are firmly bonded to one another as in a sintered layer. The validity of the two-body approach and the values to be used for the proportionality factor of a powdery layer need to be tested in well-defined impact experiments.

Chapter 6

Experimental method

The validity of the two-body approach as applied in the theoretical sticking model is examined by performing impact experiments on a powdery surface. The experiments should enable the measurement of both the incident and the rebound velocity as a function of particle size, impact velocity, angle of impact and type of surface.

In this chapter the developed experimental set-up is described and the experimental procedure is discussed. In section 6.1 some design considerations are given. The experimental set-up is described in section 6.2. Section 6.3 focuses on the data analysis and section 6.4 on the experimental errors made. The experimental conditions and the experimental procedure for a single experiment are treated in section 6.5.

6.1 Design considerations experimental set-up

The theoretical sticking model predicts the rebound characteristics: relative rebound velocity and rebound angle for the impact of a single particle on different surfaces. To obtain a direct comparison of the experimental and theoretical results, it should be possible in the experimental set-up to record a single impact of a particle on a surface. From these recordings the incident and rebound velocities should be determined. Besides, in the model the influence of the fluid flow on the impact is assumed to be negligible. Therefore, it is preferable that this influence also has a negligible influence in the experiments. The same holds for the humidity in the set-up. In the model the adhesion energy is based on a dry contact and, therefore, also in the set-up the humidity should be minimized. In the experiments it is chosen to use spherical particles with a size comparable to the size in the industrial case. Although in practice fly-ash particles have all kinds of possible shapes, the use of spherical particles allows a direct comparison with the two-body model.

As calculated in section 4.5, particles impact a cylinder in cross-flow with a range of velocities and impact angles. For the particle sizes studied the impact velocity varies from a very small fraction of the main stream velocity up to almost the main stream velocity itself. Assuming a maximum main stream velocity of around 10 m/s, the maximum impact velocity in the set-up should be of the same

order. The absolute value of the impact angle varies from 0 to a few degrees below 90° and it should be possible to obtain the same range of impact angles in the experimental set-up.

To achieve the required particle velocities, the particles need to be accelerated in some way. One method which is often used is to accelerate a gas stream with particles through a nozzle and pointing this jet at the impact surface. By varying the pressure at the entrance of the nozzle the velocity of the particles can be varied. Another approach was chosen in the study of Werner [71], where a ‘sand gun’ was used to accelerate a single sand grain (typically in the order of 1 mm). Particles can also be accelerated by dropping them under vacuum or partly vacuum conditions. In that case the velocity of the particles is directly related to the height from which the particles are released.

Here, it is chosen to drop the particles in an evacuated environment. The advantage of this method is that there is no hydrodynamic influence of a carrying gas phase on the impact as is the case for the particles accelerated using a nozzle. After a free fall in a stagnant medium, all the particles impact the surface with the same angle. The velocity of the particles is a function of the fall height, the pressure in the column and the diameter of the particle. In case of a perfect vacuum, the impact velocity is solely determined by the fall height and becomes independent of the diameter of the particles. Another advantage of the low vapor pressure in the column is the minimization of the influence of moisture on the agglomeration of the falling particles and on the impact itself.

6.2 Description of the set-up

The experimental set-up is given in figure 6.1 and is discussed, in detail, in appendix F. The experimental set-up consists of a vacuum column mounted on a vacuum chamber. In the vacuum column the particles are released from a particle feeder that can be varied in height to set the fall height. The particle feeder is installed in the top-segment of the column. A spindle mechanism in the particle feeder allows the fall height to be varied over 25 cm. To further increase the fall height additional column segments can be installed yielding a maximum impact velocity of 4 m/s for a column height of 1 m. The particle feeder, given in the detail-drawing in figure 6.1, comprises of a metal plate with the particles attached to the bottom-side. Outside the set-up particles are put on this plate. Subsequently, the plate is turned upside down without the particles being detached from it and the plate is installed in the particle feeder. Above the plate an electromagnet is placed with a steel ball stuck to it. Disconnecting the electrical circuit makes the steel ball to fall on the metal plate thereby detaching the particles from the plate. The particle feeder allows the release of particles with sizes between 20 and approximately 100 μm. The weight of larger particles predominates the adherence to the metal plate whereas for smaller particles adhesion potentially becomes a problem.

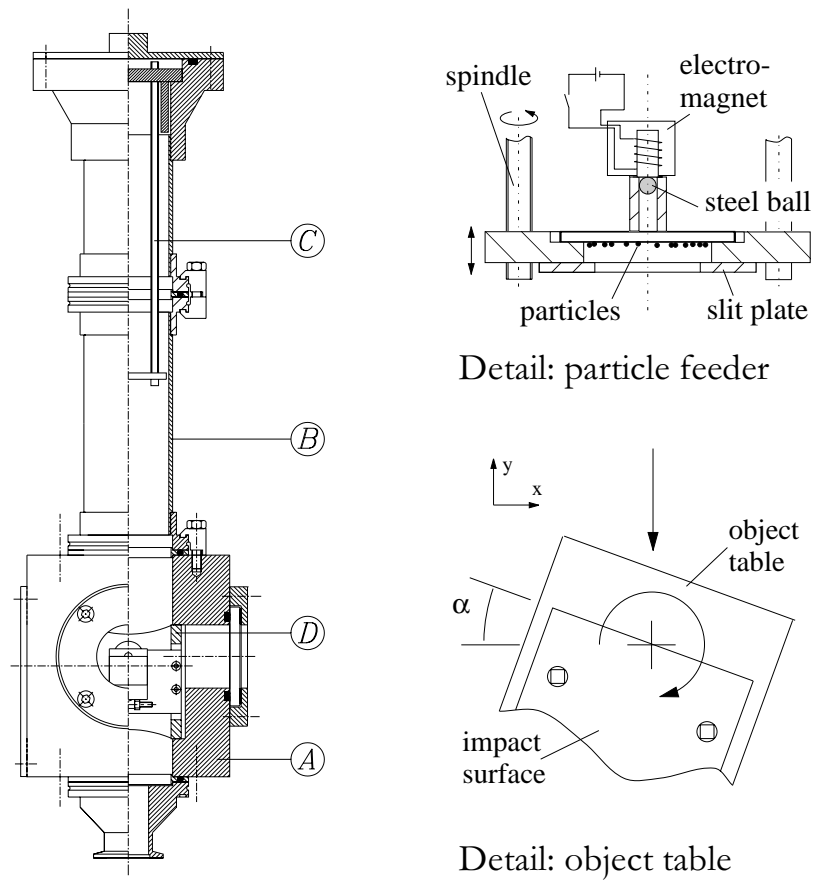


Figure 6.1 Experimental set-up; (A) vacuum chamber, (B) vacuum column, (C) particle feeder and (D) object table.

Below the particle feeder a slit plate can be installed to ensure that the particles fall in a specified plane. The slit in this plate has a width of 1.5 mm. After being released from the particle feeder, the particles fall through the column and impact a surface that is installed in the vacuum chamber. Different surfaces can be mounted on an object table constructed such that it can be rotated in clockwise direction yielding an impact angle between 0 and 70° . The vacuum chamber is optically accessible by two windows. The impacts are digitally recorded using a camera system, see figure 6.2.

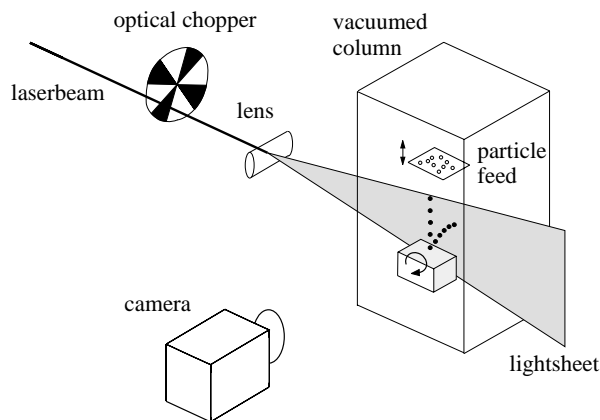


Figure 6.2 Schematic representation of the camera system in the experimental set-up.

The camera system is equipped with a zoom lens with which it is possible to focus on a domain of 2 x 2 mm. To track an incoming particle with a velocity of 4 m/s while passing through this domain, the particle has to be visible for a number of time intervals. This results in a required recording rate of up to 5000 Hz. This recording rate is realized by using an optical chopper to pulsate a continuous 5 W argon-ion laser beam. The beam is expanded in one-direction by a cylindrical lens to create a light sheet. This pulsated light sheet illuminates a particle several times in one camera image. The camera used (JAI CV-M10) gives non-interlaced images with a resolution of 512 x 512 and a frame rate of 30 Hz. The images are digitally stored in the computer. Two examples of recorded images are given in figure 6.3.

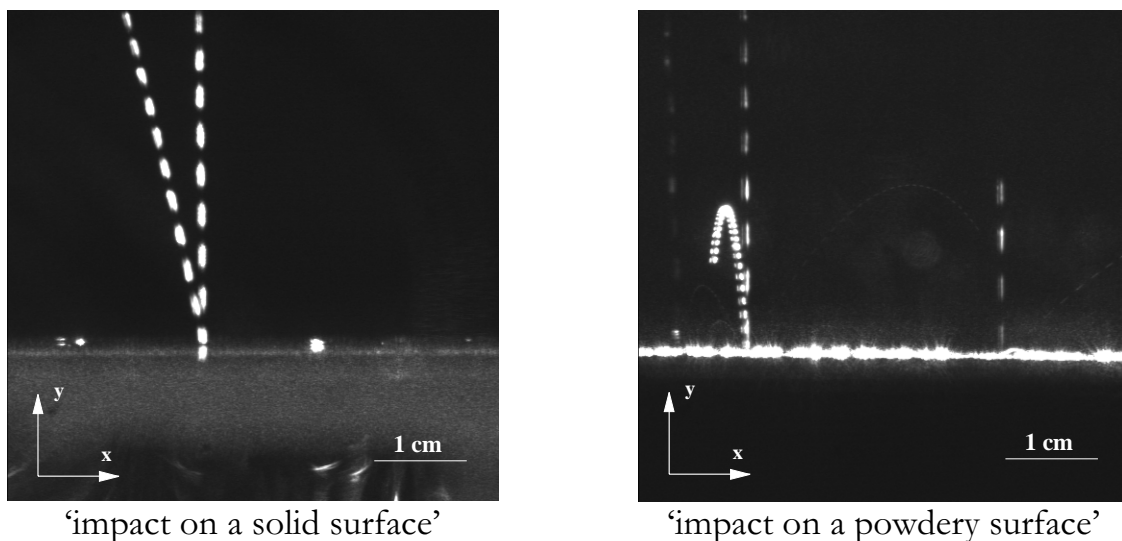


Figure 6.3 Typical recorded images by the camera system.

The left image was taken for particles impacting a smooth solid surface whereas the right image is an example for the impact of particles on a powdery layer. The powdery layer induces a lighted stroke above the surface that can obscure rebounds with small rebound velocities. The rebound characteristics are determined from the recorded images by determining the impact and, if present, the rebound velocity for each impacting particle. The impact is located in the plane defined with the x and y-direction as given in figure 6.3. The y-direction coincides by the negative direction of gravitation. The z-direction is directed outward from the images.

In case of the impact of a particle on a powdery layer, the measured rebound velocity can not be compared directly with the theoretical model because the impact position on the target particle is not known 'a priori'. Therefore, for the experiments on a powdery layer the distribution in rebound velocities is compared with the distribution simulated by the theoretical sticking model. To obtain an unbiased distribution, it is important that all the rebounds of the recorded impacts are also visible in the images and are included in the measured distribution. To ensure this, the particles are dropped through a slit plate. The particles only impact the surface inside the projected area beneath the slit (figure 6.4). In the set-up the centre-line of the projected area is aligned with the mid-plane of the laser sheet. As the slit in the plate has a smaller width (1.5 mm) than the thickness of the laser sheet (4 mm), the

impacts are located close to the centre of the laser sheet and the start of each rebound (illustrated in figure 6.4 with the black dots) is visible in the images.

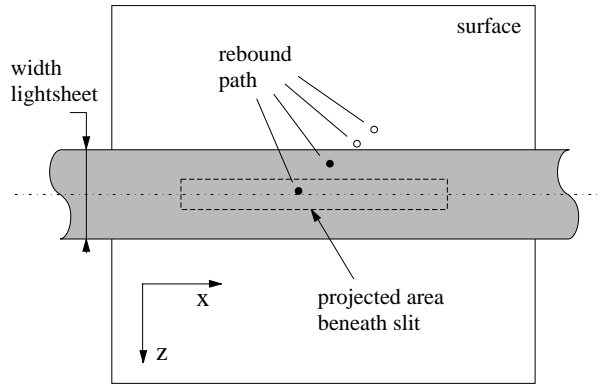


Figure 6.4 Schematic top-view of the impact surface.

6.3 Data analysis

In the experimental set-up it is possible to set the pressure at different values. In this study only experiments were done in which the pressure, between 2 and 10 Pa, was such that the drag force was negligible [51]. For this regime the method with which the recorded images are analysed will be discussed for both the impact and the rebound velocities.

Impact velocity

For each particle the impact velocity is determined from the average distance between two successive illuminations (blobs), as is shown schematically in figure 6.5.

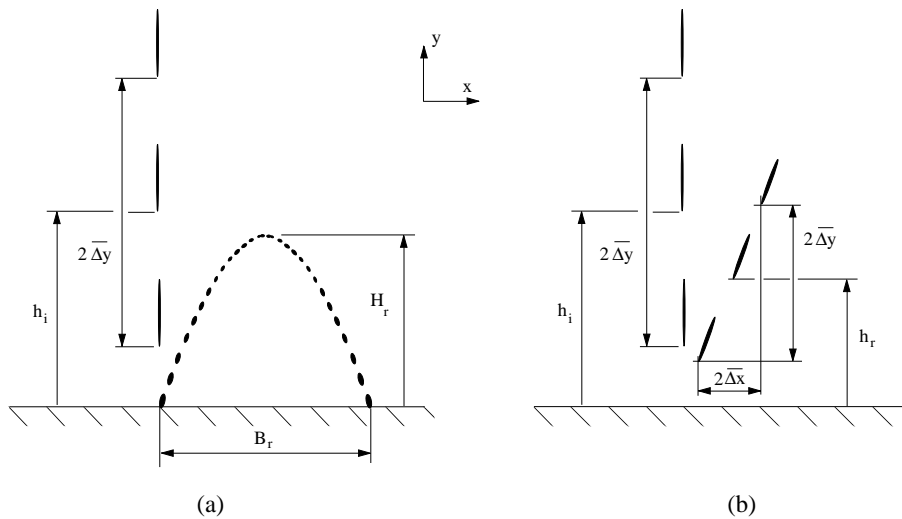


Figure 6.5 Definitions measurement method

The average distance is calculated from the distances between two neighbouring blobs. The velocity is then found from:

$$\begin{aligned}
v_{i,x} &= f_{ch} \frac{\overline{\Delta x}_{pix}}{512} b_{im} \\
v_{i,y} &= f_{ch} \frac{\overline{\Delta y}_{pix}}{512} h_{im}
\end{aligned}
\tag{6.1}$$

with $\overline{\Delta x}_{pix}$ and $\overline{\Delta y}_{pix}$ the average distances (expressed in pixels) between two blobs in x and y-direction, respectively and f_{ch} the frequency of the pulsated laser sheet. b_{im} and h_{im} represent the physical width and height of the recorded image. These two quantities are determined by recording a reference object with known size and measuring its size in pixels from a recorded image.

Rebound velocity

For most impacts the rebound velocity is found from the height and width of the rebound curve (figure 6.5 (a)). Assuming a perfect vacuum the rebound velocity is then given by:

$$\begin{aligned}
v_{r,x} &= \frac{B_{r,pix} g b_{im}}{1024 v_{r,y}} \\
v_{r,y} &= \sqrt{2 g \frac{H_{r,pix}}{512} h_{im}}
\end{aligned}
\tag{6.2}$$

with $H_{r,pix}$ and $B_{r,pix}$ the rebound height and width both measured in pixels. Unfortunately this procedure could not always be followed because the rebound curve from start to top is not always visible in the images. For those cases, the rebound velocity is determined using the distances between the blobs in the rebound case as it is also used for the impact velocity (figure 6.5 (b)).

Oblique impact

In case of an oblique impact, the measured impact and rebound velocities in the camera coordinate system x_c - y_c are transformed to the local surface coordinate system x_s - y_s that is defined in figure 6.6.

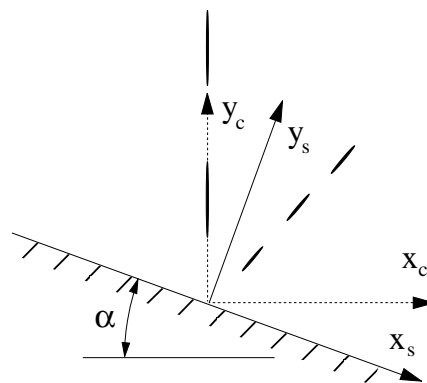


Figure 6.6 Definitions for an oblique impact with impact angle α .

The velocities are determined in the coordinate system of the camera and are transformed to the surface coordinate system using the following transformation:

$$\begin{bmatrix} v_{x_s} \\ v_{y_s} \end{bmatrix} = \begin{bmatrix} \cos(\alpha) & -\sin(\alpha) \\ \sin(\alpha) & \cos(\alpha) \end{bmatrix} \begin{bmatrix} v_{x_c} \\ v_{y_c} \end{bmatrix} \quad (6.3)$$

In all cases the coordinates of the blobs or the coordinates of the start and top of a rebound curve are determined manually from the recorded digital images using an imaging program. With the coordinates, the velocities are calculated using routines programmed in MatLab.

6.4 Error analysis

In the experiments the velocities are calculated from independent quantities as the chopper frequency, the distances between the blobs and the dimension of the camera image. These quantities contain an experimental, random error and therefore lead to an error in the calculated velocity. For v , being a function of n variables x_k with a random absolute error u_k , the uncertainty in v can be written as [17]:

$$u_v = \sqrt{\sum_{k=1}^n \left(\frac{\partial v}{\partial x_k} u_k \right)^2} \quad (6.4)$$

Before the error in the measured velocities is analyzed, the random errors in the various quantities are discussed. In this analysis also the possible systematic errors are included.

Random errors in measured quantities

In table 6.1 the random errors made are summarized for the relevant quantities. In the experiments distances in the camera image are determined with an inaccuracy of ± 1 pixel. However, because for the impact and rebound velocities the average distance between two blobs is used, the random error in this average distance is reduced to $\pm 1/2$ pixel. The height and width of the rebound curve are determined

Quantity	Symbol	Error
Dimensions camera image	h_{im}, b_{im}	$\frac{(h_{im}, b_{im})^2}{512 \cdot 3 \cdot 10^{-3}} \text{ m}^a$
Chopper frequency	f_{ch}	0.5 %
Average distance between two blobs	$\overline{\Delta x_{pix}}, \overline{\Delta y_{pix}}$	0.5 pixel
Rebound height	$H_{r,pix}$	1 pixel
Rebound width	$B_{r,pix}$	1.5 pixel

Table 6.1 Random errors made in the measured quantities. ^a The size of the reference area used is 3 x 3 mm.

from the difference in coordinates between the start and the top of the rebound curve. This approach is chosen, because the second part of the rebound curve in which the particle approaches the surface again is not always visible in the images. The random error in the rebound height is equal to the standard error of ± 1 pixel. For the rebound width the error is larger and equal to $\pm 1\frac{1}{2}$ pixel, because the top of the rebound curve in x-direction is not so well defined as the y-coordinate.

Impact velocity

The impact velocity is measured from the distances between the three exposures of the incoming particles, which are nearest to the surface. Because these exposures are located at some distance above the impact surface the measured velocity is not equal to the velocity at the point of impact and a systematic error is introduced. Assuming a perfect vacuum, this relative systematic error can be estimated to be:

$$e_{syst,i} = \frac{v_{i,y}^m - v_{i,y}^r}{v_{i,y}^r} = \sqrt{\frac{H - h_i}{H}} - 1 \quad (6.5)$$

with the superscripts m and r referring to the measured and real values, respectively. H is the fall height and h_i is the height above the surface where the velocity position is determined. On average this height is given by:

$$h_i = \frac{3 v_{i,y}^r}{2 f_{ch}} \quad (6.6)$$

which for an impact velocity of 0.6 m/s and a chopper frequency of 1000 Hz leads to a systematic error of -3% . In the data analysis, this systematic error is corrected for. Knowing the calculated velocity at a certain distance above the surface, the corrected impact velocity is determined by applying the standard equation of motion for a particle in vacuum. The distance above the surface used in the correction is taken equal to the average height of the exposures above the surface which introduces a small second systematic error which is negligible compared to the initial systematic error.

The uncertainty in the corrected measured impact velocity due to random errors can be derived using equation 6.4 and becomes for a typical situation:

$$v_{i,y} = 0.5 \pm 0.005 \text{ m/s, (relative error 1.1 \%)} \text{ with}$$

$$\begin{aligned} f_{ch} &= 1000 \pm 5 \text{ Hz} \\ \overline{\Delta y}_{pix} &= 51 \pm 0.5 \text{ pixel} \\ h_{im} &= 5 \pm 0.02 \text{ mm} \end{aligned}$$

Rebound velocity; using distances between exposures

When the rebound velocity is determined from the average distance between two exposures, the errors made are analogous to the impact velocity. The systematic error introduced as a result of the velocity being determined at a certain height

above the surface is eliminated by correcting the measured rebound velocity. The random error in the rebound velocity in y-direction becomes:

$$v_{r,y} = 0.25 \pm 0.005 \text{ m/s, (relative error 2.0 \%)} \text{ with}$$

$$f_{ch} = 1000 \pm 5 \text{ Hz}$$

$$\overline{\Delta y}_{pix} = 26 \pm 0.5 \text{ pixel}$$

$$h_{im} = 5 \pm 0.02 \text{ mm}$$

when assuming that the rebound velocity is 0.5 times the impact velocity in y-direction. For the x-direction, the absolute value of the random error is comparable. For smaller rebound velocities ($< 0.1 \text{ m/s}$), the relative error becomes larger than 5%. Therefore, for these low rebound velocities the method using the height and width of the rebound is applied to determine the rebound velocity.

Rebound velocity: using width and height of the rebound

Usually, for lower rebound velocities, the rebound curve is visible in the images up to the top of the curve. In that case the rebound velocities can be determined from the width and height of the parabolic rebound curve and no systematic error is introduced. The uncertainty in the measured rebound velocity is different from the random errors in the velocities determined from the distances between exposures.

For a rebound velocity in y-direction of 0.1 m/s and the same conditions as used above the error in the measured rebound velocity becomes:

$$v_{r,y} = 0.10 \pm 0.001 \text{ m/s, (relative error 1.0 \%)} \text{ with}$$

$$f_{ch} = 1000 \pm 5 \text{ Hz}$$

$$H_{r,pix} = 52 \pm 1 \text{ pixel}$$

$$h_{im} = 5 \pm 0.02 \text{ mm}$$

For a x-velocity of 0.1 m/s , the absolute value of the random error in the x-velocity is 0.002 m/s or 1.6% .

Another source of errors is introduced because particles with a rebound velocity below a certain threshold are not detectable anymore in the images. This can occur when the time span between the start of the rebound and the next impact is smaller than the time between two pulses. To prevent the occurrence of this situation, the chopper frequency in an experiment is chosen such that

$$f_{ch} \gg \frac{g}{2 v_{r,y}} \quad (6.7)$$

which for a minimum rebound velocity in y-direction of 0.05 m/s would mean a chopper frequency larger than 200 Hz . Another situation where the rebound is not seen occurs when the rebound is obscured by the lighted area above the surface (figure 6.3). Assuming this area to be approximately 5 pixels high over an image width of 5 mm , a rebound with a height smaller than 0.05 mm is not detectable. So, for a camera image of 5 mm the minimum rebound velocity that can be detected becomes 0.03 m/s .

6.5 Experimental conditions and procedure

The described experimental set-up will be used to perform impact experiments on powdery layers. The results will be compared with the results obtained using the theoretical sticking model.

Particles used in the experiments

In the experiments two samples of solid spherical glass spheres, obtained from Potters-Ballotini, are used. The first sample is the 2530 A-glass batch with a mean particle diameter of 71 μm and the second sample is the 5000 A-glass batch with a mean diameter $d_{p,50}$ of 7.6 μm . The 2530 batch was split into different size fractions using standard sieves with cut-off sizes of 40, 45, 50 and 56 μm respectively. The 5000 batch was not sieved. The size distributions of the obtained particle fractions measured using a Coulter particle sizer are given in Appendix G. The roundness of the particles is satisfactory as can be seen in figure 6.9.

Before carrying out an experiment, the particles were stored in a stove at 80°C to minimize problems with cohesion or agglomeration. Measurement of impact velocities in a test experiment under atmospheric conditions showed that agglomeration was not a significant problem. Because under atmospheric conditions the impact velocity is directly related to the particle diameter, in this test for each particle its diameter was calculated from the measured velocity as given by:

$$d_p = \sqrt{\frac{18 \mu_g v_{i,y}}{g \rho_p}} \quad (6.8)$$

Comparison of these particle sizes with the distribution found using the Coulter particle sizer showed no significant differences.

Preparation of a powdery layer

The powdery surfaces used in the experiments were prepared in a tablet press of which a sketch is given in figure 6.7.

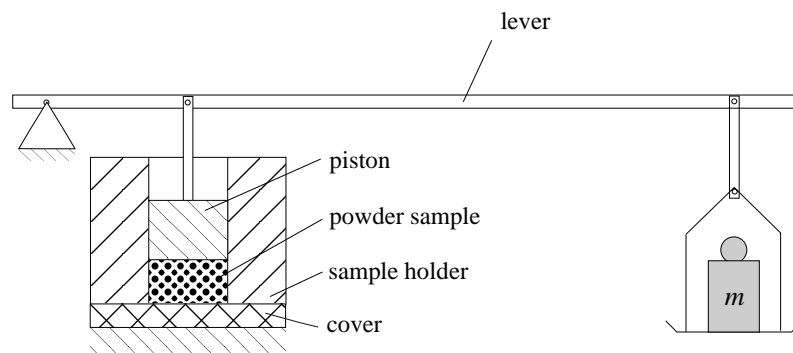


Figure 6.7 Tablet press used to prepare different powdery surfaces

A weighted powder sample is poured in the cylindrical hole of the sample holder. The cover is mounted on the sample holder and the two are installed upside

down in the tablet press. In the press a force is applied on the piston and the sample is compacted. The force is created by a weight and amplified by a lever. The weight installed is 36 kg and with an arm ratio of the lever of 45 the force applied on the sample equals 16 kN. Because the piston has a diameter of 10.05 mm the average pressure on the piston becomes 200 N/mm^2 , which proved to be sufficient to compact the powder sample.

While applying the load on the powder sample, the porosity of the powder sample reduces exponentially in time, figure 6.8. The porosity is determined by measuring the thickness of the compacted sample.

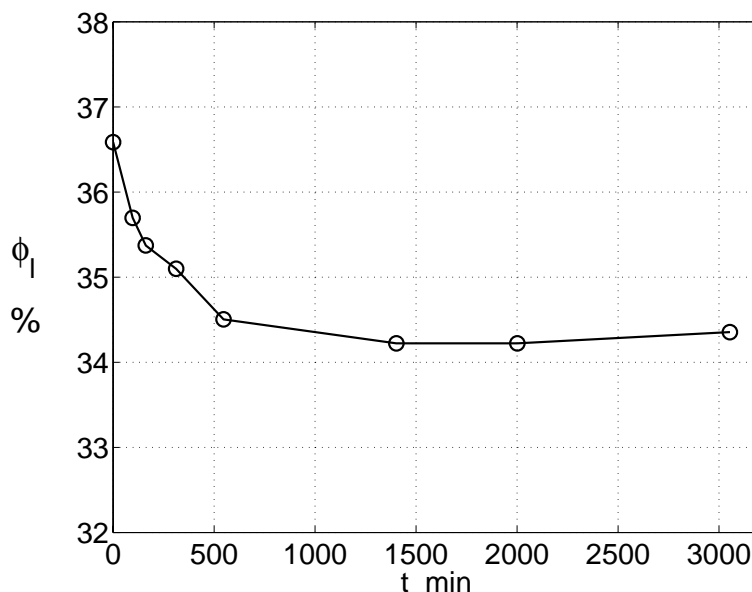


Figure 6.8 Porosity of the powder sample installed in the tablet press as a function of time.

The porosity of the sample consisting of particles between 50 and 56 μm reached its final value after approximately 18 hours. In the experiments a time period of 18 hours is applied to prepare a powdery layer. After this period the sample is removed and the position of the piston is fixed. The sample holder is then installed upside down in the experimental set-up after which the cover on the sample holder is removed. In figure 6.9 a picture is given of the prepared surface and as can be seen the described method of layer preparation results in a well-ordered layer of glass spheres. Based on the pictures made of the layer, the roughness parameter Δ in the theoretical sticking model is estimated to be 0.1.

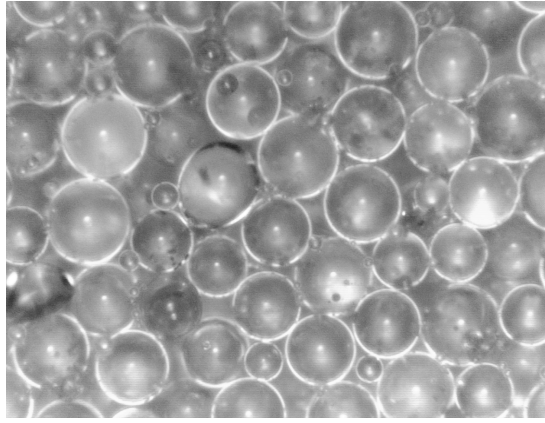


Figure 6.9 Surface structure of a powdery surface made using the tablet press from the particle fraction 50/56 μm . The pictures are made using a light microscope.

The method of surface preparation was modified to prepare a powdery layer in which the particles are bonded to one another. For this layer, the inserted powder sample was again compacted in the press. After the sample was removed from the press and the cover was removed, a second plate covered with glue was put over the prepared surface. The cover was mounted again and the pressure was resumed with a small weight. In this way the first few layers of the particles were fixed on the second plate. In figure 6.10 the structure of this glued layer is shown.

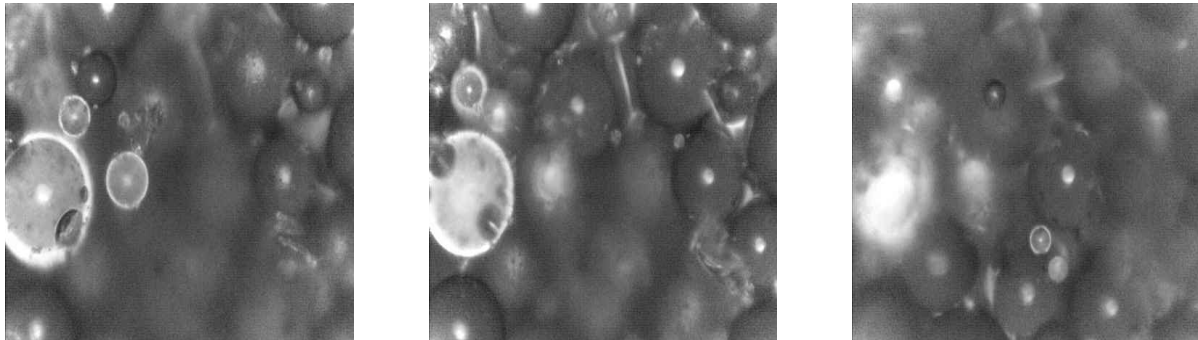


Figure 6.10 Pictures of the surface structure of the glued layer.

In the light microscopy pictures the focal plane is shifted downwards going from left to right. As shown, not all surface particle are located in the same plane indicating that the surface of this glued layer is more irregular than the surface of a powdery layer as shown in figure 6.9. To account for this irregularity, the roughness parameter Δ for this layer will be set to 0.3 in the theoretical sticking model.

Experimental procedure

To prepare the camera system at the start of an experiment, the laser sheet is aligned with the plane in which the particles fall. This plane is defined by the slit in the slit-plate that is mounted below the particle feeder. A reference object is placed in the middle of the laser sheet and the camera is focussed on this object using an x-z translation table. Then a camera image is saved to give the height and width of the

camera image. After this procedure to set up the camera system, the impact surface is mounted on the object table and the angle of impact is set. The fall-height is set using the spindle mechanism or by adjusting the column height. Just before the experiment, the particles are put on the metal plate that is installed upside down in the particle feeder. The particle feeder is put in the column and the column is closed using a cover. The set-up is then ready to be vacuumed until the pressure is between 2 and 10 Pa. In this pressure range the variation in impact velocities is about 5% [51]. After the pressure is reached, the recording system is started and the particles are released (using the electromagnet) by lifting the steel ball from and dropping it again on the plate with the particles.

Experimental data and statistics

From the recorded images for each impact the incident and rebound velocities are determined. From these velocities the rebound angle β (figure 6.11) and the relative rebound velocity in y-direction ε_y as defined earlier in section 5.6:

$$\varepsilon_y = \frac{v_{1r,y}}{v_{1i,y}} \quad (5.39)$$

are calculated. For a typical experiment on a powdery layer the measured rebound angle and relative rebound velocity are given in figure 6.11.

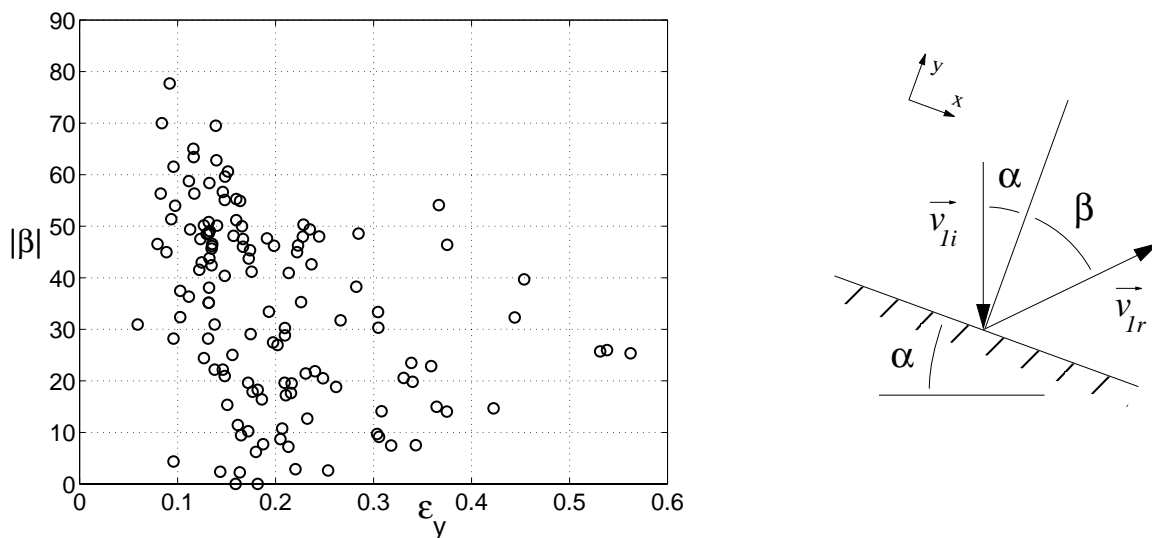


Figure 6.11 Typical result for an experiment on a powdery layer ($\alpha=0^\circ$).

The measurements show a wide scatter in rebound for small relative rebound velocities where for larger rebound velocities the distribution becomes smaller. In the first situation the incident particles impacts one of the bed particles at the top while in the second situation the impact is located near the top of one of the bed particles.

To express the variation in the measured relative rebound velocity or rebound angle use is made of the standard deviation σ . The standard deviation is also used to

indicate the confidence interval of the average value of the measured values by dividing σ by the square root of the number of measured impacts n . The confidence interval then becomes:

$$\bar{\varepsilon}_{y,\text{exp}} = \bar{\varepsilon}_{y,\text{exp}} \pm 2 \frac{\sigma}{\sqrt{n}} \quad (6.9)$$

The proportionality factor for the tested layer is found by comparing the average relative rebound velocity with the mean found by the theoretical sticking model using the relative error N . This error is defined by:

$$N = \left| \frac{\bar{\varepsilon}_{y,\text{num}}(C_m) - \bar{\varepsilon}_{y,\text{exp}}}{\bar{\varepsilon}_{y,\text{exp}}} \right| \quad (6.10)$$

Minimizing the relative error gives the proportionality factor for the powdery layer.

Chapter 7

Experimental results

Impact experiments on a powdery layer are carried out to examine the validity of the two-body approach that forms the basis of the theoretical sticking model. For the model three independent input parameters are required i.e. the coefficient of restitution, the friction coefficient and the proportionality factor. The coefficient of restitution and the friction coefficient are determined independently of the proportionality factor in an experiment where spherical particles impact a flat solid surface (section 7.1). Next, in section 7.2 impact experiments are performed for a powdery layer. In a ‘reference’ experiment the proportionality factor is determined for a layer with the particles of the same size as the incident particles. The impact experiments are then repeated for the same kind of layer varying the incident velocity and impact angle. To examine the validity of the two-body approach, the results of these experiments are compared with the results obtained using the theoretical model. The experiments are continued for a powdery layer in which the particles are glued to one another to resemble a sintered layer and for a layer that consists of particles smaller than the incident ones. For both types of layers again the proportionality factor is determined and the results are compared with the model. The chapter is ended with a discussion and conclusion in section 7.3.

7.1 Experiments with a solid layer

The coefficient of restitution e and the friction coefficient f are measured in an experiment where particles impact on a solid glass layer. Knowing these two parameters, in the experiments on a powdery layer the proportionality factor remains the only unknown. In the experiments on a solid layer, the impact angle is varied such that both e and f can be determined from the ratio between the rebound and incident velocities. For an oblique impact of a non-rotating particle on a solid layer, the rebound velocities can be derived from equations 5.5 and 5.9. Substituting an infinite mass for m_2 in these equations gives:

$$\begin{aligned}v_{1r,n} &= -e v_{1i,n} \\v_{1r,t} &= v_{1i,t} - f(1+e)v_{1i,n}\end{aligned}\tag{7.1}$$

with the tangential direction t parallel and the normal direction n normal to the impact surface. The friction coefficient can be found from the rebound velocity parallel to the surface once the coefficient of restitution is determined from the measured rebound velocity in normal direction. As discussed in section 5.2, the relation for the rebound velocity parallel to the surface only applies when the slip-velocity in the contact remains non-zero over the impact. The slip-velocity is reduced to zero during the impact when the friction coefficient is larger than the critical friction coefficient. For the impact on a flat solid layer, the critical friction coefficient can be written as (equation 5.7):

$$f_{v_s=0} = \frac{2/7 \tan(\alpha)}{(1+e)} \quad (7.2)$$

with α the impact angle. When the slip-velocity during the impact is reduced to zero, the rebound velocity in tangential direction becomes equal to $2/7$ of the incident velocity in the same direction. In that case, when determining the friction coefficient from equation 7.1, not the real friction coefficient but the critical friction coefficient as defined in equation 7.2 is found.

In the experiments on a solid surface glass particles from the 50-56 μm fraction of the C2530 batch are used to impact on a 5 mm thick glass plate for five different impact angles. In all but the last experiment, the impact velocity is kept constant at 0.51 m/s. The small fall height required for this impact velocity prevented the particle feeder to be installed at an angle of 57° underneath the feeder. Therefore, in the experiment with an impact angle of 57° the particle feeder is pulled up somewhat, yielding a larger fall height and incident velocity. For the experiment at an impact angle of 0° , the distribution in the measured coefficient of restitution is given in figure 7.1.

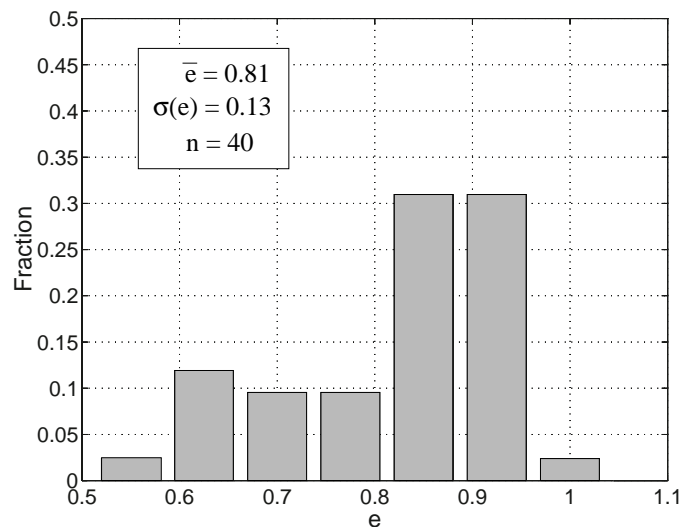


Figure 7.1 Distribution in measured coefficient of restitution for the perpendicular impact of glass particles ($d_{p,50} = 50 \mu\text{m}$) on a flat solid glass surface.

The measured coefficient of restitution of 0.81 is well below the expected elastic limit of 1. The impact is likely to remain elastic because the incident velocities in this experiment are far below the limiting elastic velocity which is 25 m/s for a 50 μm glass particle impacting a flat solid glass surface. In the experiments a fairly wide variation in the measured values is observed. For some impacts the coefficient of restitution indeed approached the elastic limit where for other impacts a considerable part of the kinetic energy is lost. This additional loss could be caused by electrostatic charges on the particle or the surface. The presence of electrostatic charges could also explain the small variation in measured rebound angles. The standard variation in rebound angle amounted 5° for the experiment at zero impact angle.

Including the results of the experiments with a non-zero impact angle, the mean value for the coefficient of restitution and the friction coefficient are given as a function of the impact angle in figure 7.2. In the figure for the friction coefficient also the critical friction coefficient ($f_{v_s=0}$) is given as a function of the impact angle.

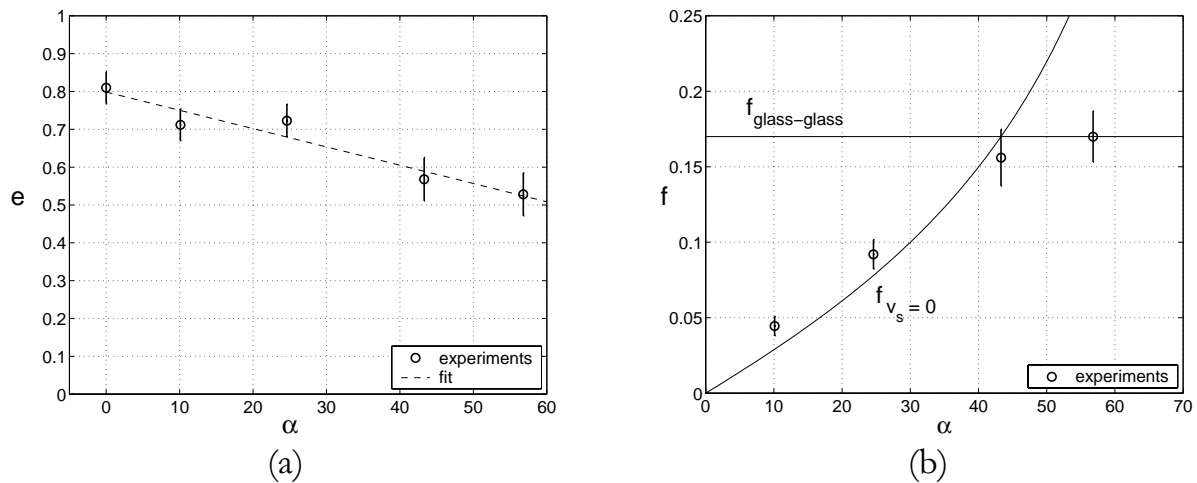


Figure 7.2 Measured coefficient of restitution (a) and friction coefficient (b) for the impact of glass particles ($d_{p,50} = 50 \mu\text{m}$) on a flat solid glass surface. The results are given as a function of the impact angle and the vertical lines indicate the error bars.

As can be seen in figure 7.2, the coefficient of restitution decreases for larger impact angles. The decrease is almost linear with the impact angle as is shown with the dashed line in the figure that gives a linear fit to the data points. With respect to the friction coefficient, the measured friction coefficient coincides with the value of the critical friction coefficient for the three lowest impact angles. This implies that during the impact the particles have stopped sliding and have started rolling on the glass surface. For the largest impact angle of 57°, the measured value is below the critical value meaning that for this impact angle the particle remains sliding and that the friction coefficient determined from equation 7.1 is the actual friction coefficient in the contact between the two glass surfaces. The value of 0.17 for the friction coefficient of the glass-glass contact is within the range of values as discussed in section 5.4. The value of 0.17 will be used in the remaining of this chapter.

Comparison with model for the coefficient of restitution

In the model for the coefficient of restitution, it is assumed that the coefficient of restitution is only a function of the impact velocity normal to the surface and is independent of the impact angle. For the elastic impact of glass particles on the solid glass surface, the coefficient of restitution as treated in section 5.3 is described by:

$$e^2 = 1 - \frac{(Q_{A,r} - Q_{A,a})}{\frac{1}{2} m^* v_{1i,n}^2} \quad (5.23)$$

with in this case m^* equal to m_I . This equation fails to predict the coefficient of restitution as measured for glass particles impacting a glass surface, figure 7.3 (a). It is expected that electrostatic charges were present on the particle or the surface and affected the coefficient of restitution.

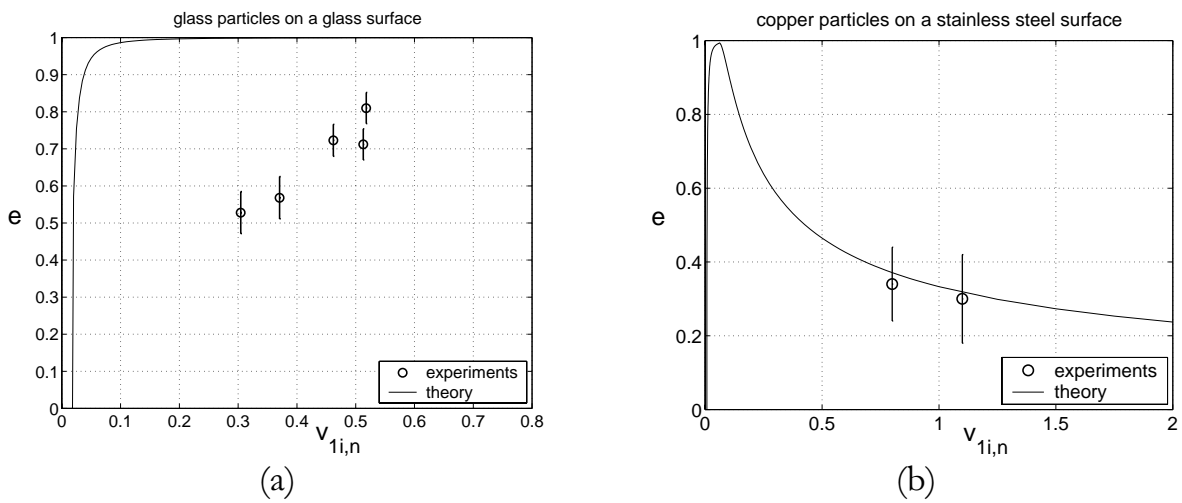


Figure 7.3 Comparison of the measured and theoretically predicted coefficient of restitution as a function of the incident velocity in normal direction

The consideration of electrostatic charges having influenced the coefficient of restitution for the impact of glass particles on a glass surface is supported by the results of preliminary experiments for the impact of two more conductive materials. In these experiments copper particles with a mean diameter of $42 \mu\text{m}$ impacted a stainless steel surface with velocities such that plastic deformation occurred during the impact. The measured coefficient of restitution in the experiment agreed rather well with the values predicted by the model. In the model the elastic load limit and the work of adhesion were taken equal to $9.6 \cdot 10^8 \text{ N/m}^2$ and 0.15 , respectively.

Another contribution to the discrepancy between the model and the glass-glass experiment is the possibility that the coefficient of restitution is not only a function of the incident velocity in normal direction but also of the impact angle. Broom [12] also reported a decrease of about 5% in the coefficient of restitution when the impact angle was changed from 0 to 45° for the impact of glass spheres on a stainless steel surface. The reason for a decrease in the coefficient of restitution with contact angle could be a larger adhesion energy due to a continuously formed and

disrupted contact surface of a moving contact or by a changed distribution of contact stresses in the contact area. Besides the normal stresses, in the contact area also stresses appear due to the friction force in this area [43].

Because the present model for the coefficient is incapable to describe the coefficient of restitution for glass particles under the experimental conditions, in the remaining of this chapter use is made of the following relation:

$$e = 0.8 - 0.005 \cdot \alpha^* - \sqrt{\frac{Q_{A,r} - Q_{A,a}}{\frac{1}{2} m^* v_{li,n}^2}}, \quad (7.3)$$

with α^* the local impact angle as defined in figure 7.4.

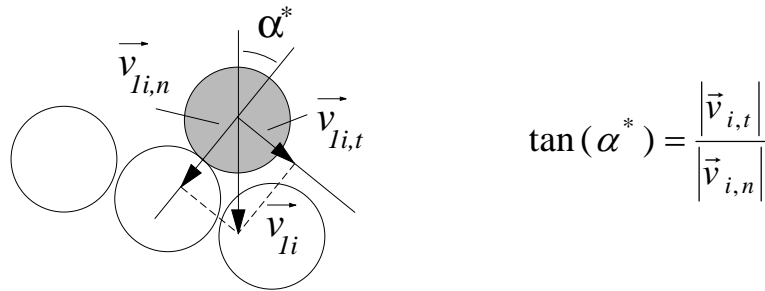


Figure 7.4 Local contact angle.

Relation 7.3 makes use of the linear fit between the coefficient of restitution and the impact angle as given in figure 7.2. The last term in equation 7.3 is added to accommodate for adhesion in the coefficient of restitution. The term is evaluated using equation 5.24 with a value for the work of adhesion Γ of 0.14 J/m^2 . The influence of the adhesion term on the numerical values is limited because incident velocities are such that sticking rarely occurs.

7.2 Experiments with a powdery layer

With a powdery layer 9 impact experiments have been carried out. For the first 6 experiments the layer was made of particles from the 50/56 size fraction which is the same as that of the incident particles. The layer is denoted as “standard”. For the remaining three experiments the layer was built from finer particles of the C5000 fraction with a mean diameter of $7.6 \mu\text{m}$. In table 7.1 the type, thickness δ , the porosity ϕ and the roughness parameter Δ are given for the layers used in the experiments. Besides, in this table the mean incident velocity and the angle of impact are given.

From the impact experiments on the standard layer, experiment A is used as a reference experiment. In this reference experiment the incident velocity is 0.5 m/s . In experiments B and C the incident velocity was increased to 0.6 and 1 m/s , respectively. The impact angle was changed to 15° and 30° in experiment D and E. In experiment F, the particles were bonded by glue to resemble a sintered layer. For this layer the porosity could not be determined. In the experiments G, H and I finer

particles were used for the layer and the impact angle was changed from 0° for exp. G to 15° and 30° for exp. H and I, respectively.

Exp.	\bar{v}_i m/s	α	Powdery layer type	Powdery layer		
				δ mm	ϕ_l %	Δ
Exp. A	0.53 ± 0.004	0	Standard	2.72 ± 0.005	35 ± 5	0.1
Exp. B	0.59 ± 0.003	0	Standard	2.37 ± 0.005	36 ± 5	0.1
Exp. C	1.03 ± 0.009	0	Standard	2.58 ± 0.005	36 ± 2	0.1
Exp. D	0.51 ± 0.005	15	Standard	2.92 ± 0.005	39 ± 4	0.1
Exp. E	0.52 ± 0.008	30	Standard	2.91 ± 0.005	37 ± 2	0.1
Exp. F	0.82 ± 0.002	0	Glued layer	-	-	0.3
Exp. G	0.52 ± 0.004	0	Finer	3.42 ± 0.005	28 ± 1	0.1
Exp. H	0.51 ± 0.007	15	Finer	2.68 ± 0.005	31 ± 2	0.1
Exp. I	0.51 ± 0.008	30	Finer	2.68 ± 0.005	31 ± 2	0.1

Table 7.1 Experimental conditions for experiments on a powdery layer

7.2.1 Standard layer

The first type of powdery layer examined is composed of particles with the same size as the incident particles. The results are used to obtain a reliable value for the proportionality factor C_m and to validate the two-body approach.

The proportionality factor C_m is an important parameter in the theoretical sticking model which gives the ratio between the effective mass of the layer m_2 and the mass of the incident particle m_1 as given by:

$$m_2 = C_m m_1 \quad (5.1)$$

The value of the proportionality factor is determined from the results of the reference experiment (exp. A). For the reference experiment the mean values and the variation for the rebound angle and the relative rebound velocity are given in table 7.2.

	\bar{v}_i	$\bar{\varepsilon}_y$	$\sigma(\varepsilon_y)$	$\bar{\beta}$	$\sigma(\beta)$
Reference Exp.	0.53	0.20 ± 0.02	0.10	1.6 ± 6.8	39

Table 7.2 Experimental results for the reference experiment.

To determine the proportionality factor, the mean relative rebound velocity is compared with the numerical value using the relative error N (section 6.5). This relative error N is given in figure 7.5 as a function of the proportionality factor.

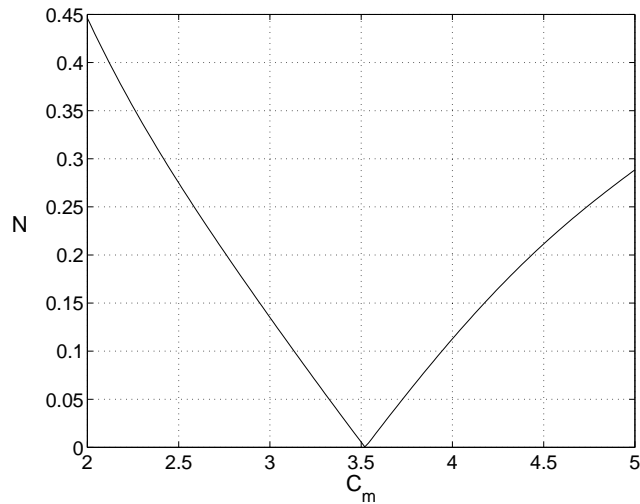


Figure 7.5 Relative error N for the reference experiment.

Minimizing the relative error N , a value of 3.5 is found for the proportionality factor. Considering a confidence interval of $\pm 10\%$ around the experimentally found mean, the proportionality factor is likely to be in the range between 3 and 4. The value of 3.5 is further used as a reference. Using the value of 3.5 for the proportionality factor, the experiment is simulated with the numerical model. For each impact in the model and in the experiment the absolute value of the rebound angle is plotted as a function of the relative rebound velocity in figure 7.6.

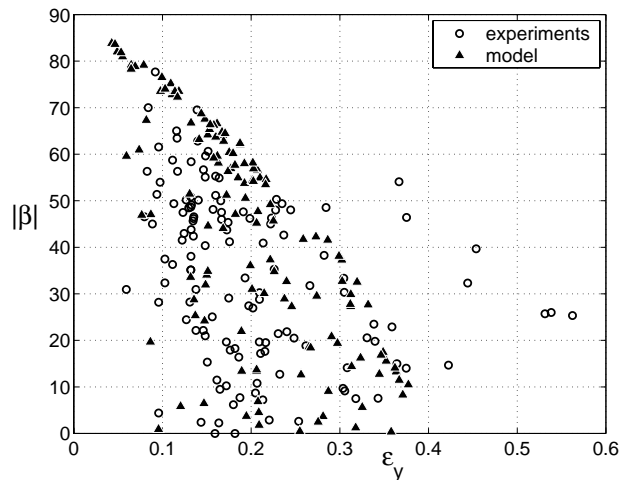


Figure 7.6 Rebound characteristics as measured in the reference experiment and simulated using the theoretical sticking model for 128 impacts ($C_m = 3.5$).

The rebound characteristics that are defined by the rebound angle β and the relative rebound velocity ε_y exhibit the same features for the measured as the simulated impacts. For a low relative rebound velocity the variation in rebound velocities is large where for larger relative rebound velocities the variation becomes smaller. For a more quantitative comparison, in figure 7.7 the frequency distribution is given of the measured and the predicted relative rebound velocities and the rebound angles.

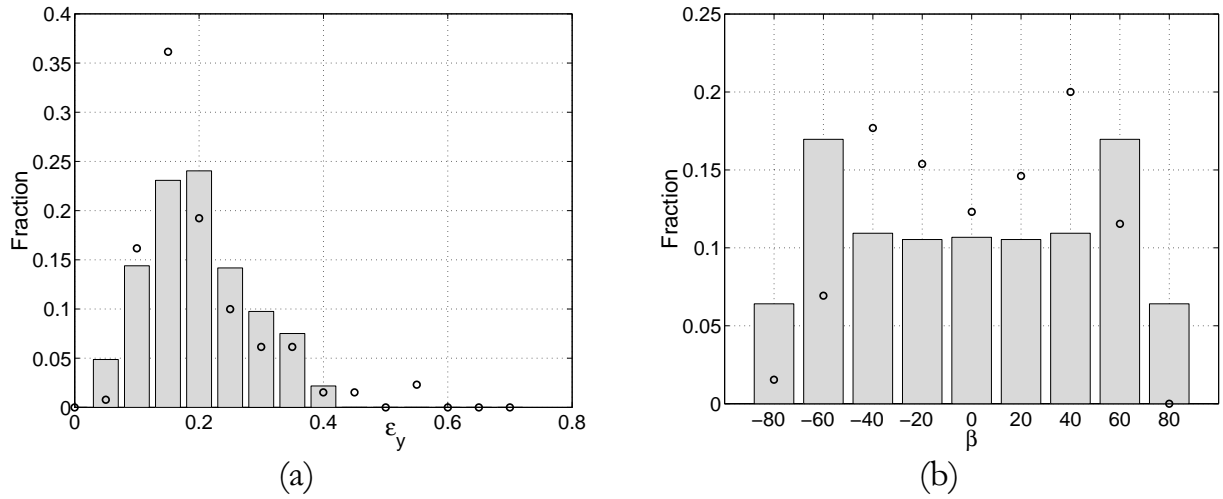


Figure 7.7 Measured (circles) and modelled (bars) distribution of the relative rebound velocity and the rebound angle for particles impacting on a powdery layer ($C_m = 3.5$).

The predicted distributions agree fairly well with the experimentally found distributions. For the relative rebound velocity the measured distribution is a little more skewed to the left and is less broad. The distribution in rebound angle from the model is broader than the experimental one that exhibits a distinct dip around a zero rebound angle. This dip is not predicted by the model. The predicted distributions agree fairly well with the measured ones giving confidence in the two-body approach applied in the theoretical sticking model.

Influence of incident velocity

Another criterion to evaluate the two-body approach is the capability of the model to predict the rebound angle and relative rebound velocity as a function of the incident velocity and the impact angle using the determined proportionality factor of 3.5. In the experiments B and C the incident velocity was increased to 0.6 and 1 m/s, respectively and the measured rebound characteristics for these experiments are given in table 7.3. In this table also the results of the reference experiment and the results calculated with the theoretical sticking model are included.

	\bar{v}_i	$\bar{\epsilon}_y$	$\sigma(\epsilon_y)$	$\bar{\beta}$	$\sigma(\beta)$	r
Ref. Exp. A	0.53	0.20 ± 0.02	0.10	1.6 ± 6.8	39	1.1
Exp. B	0.59	0.23 ± 0.02	0.10	0.0 ± 6.8	39	1.2
Exp. C	1.03	0.17 ± 0.02	0.08	3.6 ± 11.4	36	2.9
Sticking model	0.5-1	0.20	0.08	0	48	-

Table 7.3 Experimental and numerical results for the perpendicular impact ($\alpha=0^\circ$) of glass particles on a powdery surface as a function of the incident velocity.

The velocities in the experiments are such that adhesion is of minor importance. Therefore, in the sticking model the results for all three incident velocities are the same. From table 7.3 it appears that in the experiments the mean relative rebound velocity is slightly different for all three experiments but with no clear correlation. The difference may be caused by a slight deviation in the quality of the powdery layer resulting in a changed proportionality factor.

It should be noted that for some impacts in experiment C, not only the rebounding particle is detected but also some additional particle tracks. These additional tracks, illustrated by the images given in figure 7.8, indicate the ejection of bed particles from the layer as a result of the impact. The impacts leading to a splash have been included in the results as given in table 7.3. For the impacts with splash the rebounding particle is distinguished from the ejected bed particles by a significant larger absolute velocity [71].

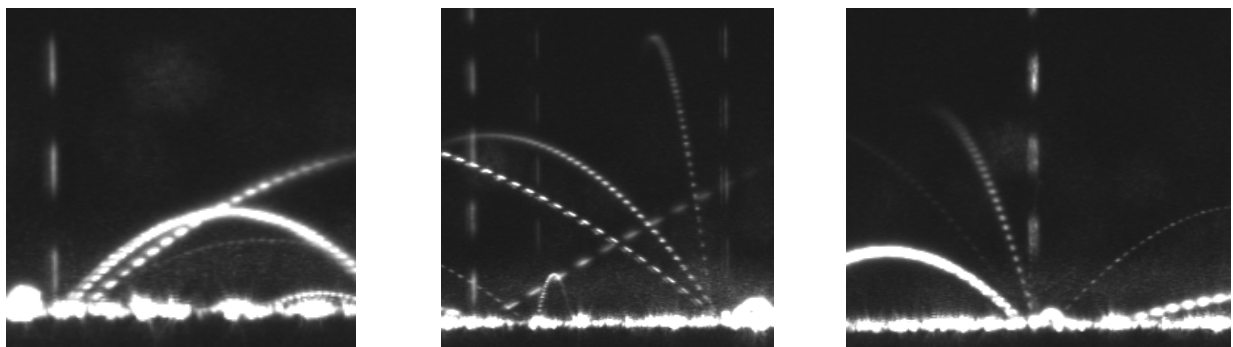


Figure 7.8 Images showing the ejection of bed particles from the powdery surface.

As discussed in section 5.2, the ejection of bed particles is caused by a reflection of momentum in the bed of particles after the impact. The ejection is characterized by the splash factor r that is defined by Werner [71] as the number of particle tracks leaving the surface per impact. The average splash factor is included in table 7.3 for the three experiments A, B and C. In the first two experiments the splash factor was almost 1. Only for a few impacts an additional ejected particle was detected. However, in the last experiment only 23% of the incident particles ended without the ejection of a bed particle. For the other particles, the impact led to the ejection of 1 up to 7 bed particles.

Influence of the impact angle

In experiments D and E the impact angle was increased to 15° and 30° , respectively. The results of these experiments, the reference experiment and the results obtained from the sticking model are given in figure 7.9.

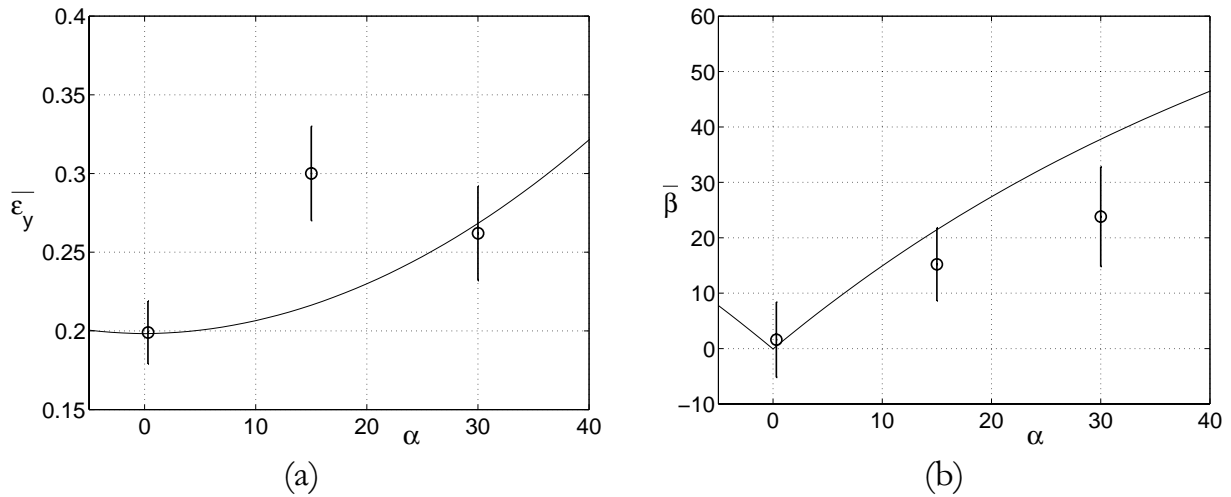


Figure 7.9 Experimental (dots) and numerical results (lines) for the oblique impact on a reference powdery layer. Figure (a) mean relative rebound velocity and figure (b) the mean rebound angle ($C_m = 3.5$).

The mean relative rebound velocity as predicted by the sticking model agrees well for experiment E ($\alpha=30^\circ$) but is totally different for experiment D. The difference is not understood and is attributed to a not noted deficiency in the preparation of the layer. Based on the agreement of the model with experiment E, the assumption that the proportionality factor is independent of the impact angle seems valid. However, a decisive conclusion would require additional experiments. Comparing the mean measured rebound angle with the numerical results, it is found that the model predicts the correct trend but in general over predicts the values.

7.2.2 Glued layer

To represent a sintered layer, in experiment F the impact surface consisted of glass particles that were glued onto a substrate. The measured rebound characteristics of this experiment and the reference experiment are given in table 7.4.

	\bar{v}_i	$\bar{\varepsilon}_y$	$\sigma(\varepsilon_y)$	$\bar{\beta}$	$\sigma(\beta)$
Ref. Exp. A:	0.59	0.23 ± 0.02	0.10	0.0 ± 7	39
Exp. F:	0.82	0.39 ± 0.03	0.20	4 ± 11	36

Table 7.4 Measured rebound characteristics for the reference experiment A and experiment F.

The mean measured relative rebound velocity in experiment F is higher compared to that of the reference experiment. Minimizing the relative error N as given in figure 7.10, a value of 40 is found for the proportionality factor for the glued layer. As expected the proportionality factor for a glued layer is an order of magnitude larger than for a powdery layer with no additional binding between the particles.

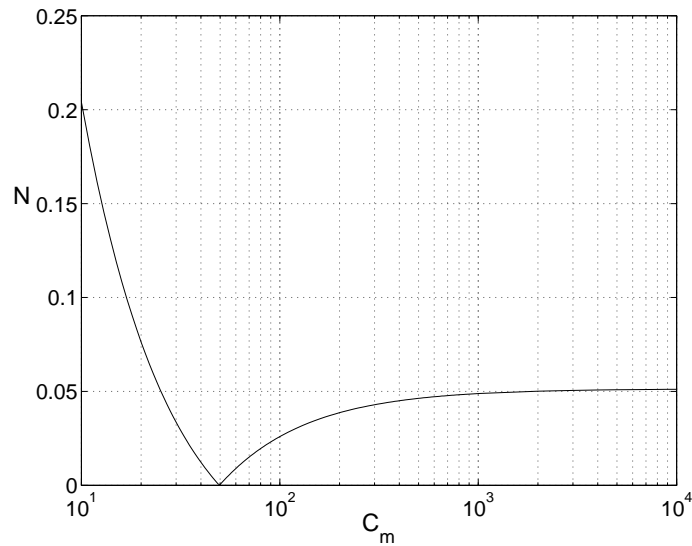


Figure 7.10 Relative error for experiment F.

7.2.3 Powdery layer composed of finer particles

So far, in the experiments the powdery layer consisted of particles with the same size as that of the incident particles. In the next set of experiments the layer was composed of particles with a mean diameter of $7.6 \mu\text{m}$ where the average diameter of the incident particles remained $50 \mu\text{m}$. So, the diameter ratio between the incident and the bed particles is 6.6 compared to 1 for the experiments with a “standard” layer. For the three impact angles in the experiments, the mean values of the measured relative rebound velocity and rebound angle are given in table 7.5.

	\bar{v}_i	$\bar{\alpha}$	$\bar{\varepsilon}_y$	$\sigma(\varepsilon_y)$	$\bar{\beta}$	$\sigma(\beta)$
Exp. G	0.52	1	0.25 ± 0.02	0.12	3 ± 5	27
Exp. H	0.51	14	0.20 ± 0.03	0.10	40 ± 7	27
Exp. I	0.51	31	0.22 ± 0.03	0.10	58 ± 5	19

Table 7.5 Experimental results for the impact on layers consisting of finer particles with a mean diameter of $7.6 \mu\text{m}$.

For the layers in the experiments G, H and I, the proportionality factor is determined by minimizing the relative error N . For these experiments the proportionality factors become 2.5, 2.3 and 2.9, respectively with an average of 2.6. Clearly, these proportionality factors are different from the value found for a powdery layer with particles equally sized to the incident particles. Using a proportionality factor of 2.2, 2.6 and 3.0, the mean value of the measured relative rebound velocities and the rebound angles are compared with the model predictions in figure 7.11.

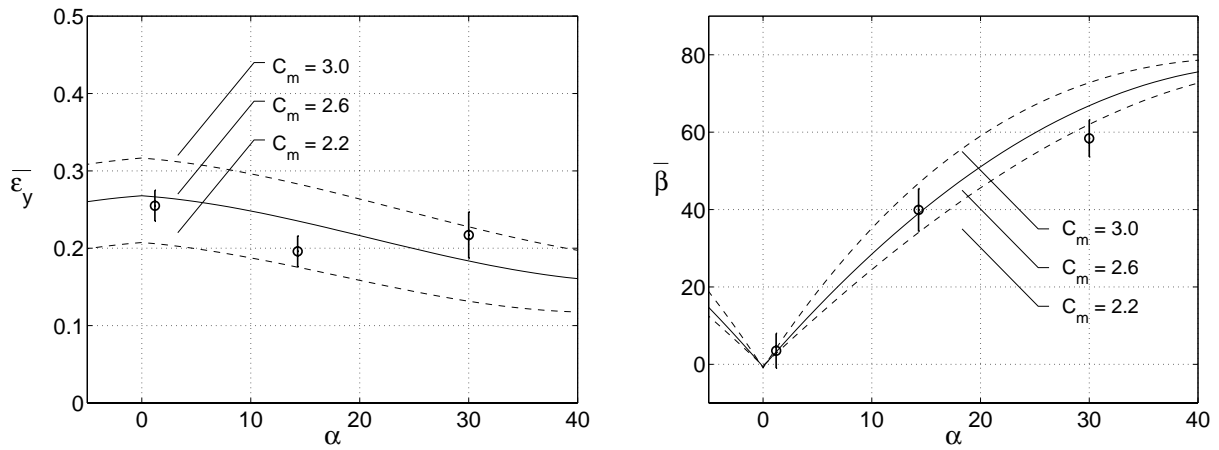


Figure 7.11 Experimental and numerical results for the impact of particles on powdery layer composed of finer particles ($d_p/d_b = 6.6$, $C_m = 2.6 \pm 0.4$).

Comparison of the measured mean relative rebound velocity with the model predictions shows that, when using a proportionality factor of 2.6, the values predicted by the model differ somewhat from the measured ones. The difference is within 20% of the measured value and corresponds to a variation in the proportionality factor of about 15%. This variation could be the result of differences in the condition of the powdery layer.

In the experiments it is found that the mean of the relative rebound velocity decreases with impact angle. This decrease is predicted correctly by the model. The negative trend of the relative rebound velocity with impact angle is opposite to the positive trend as measured and calculated for the standard layer. Comparison of the measured and predicted average rebound angle shows that the model performs fairly well when a value of 2.6 is applied for the proportionality factor.

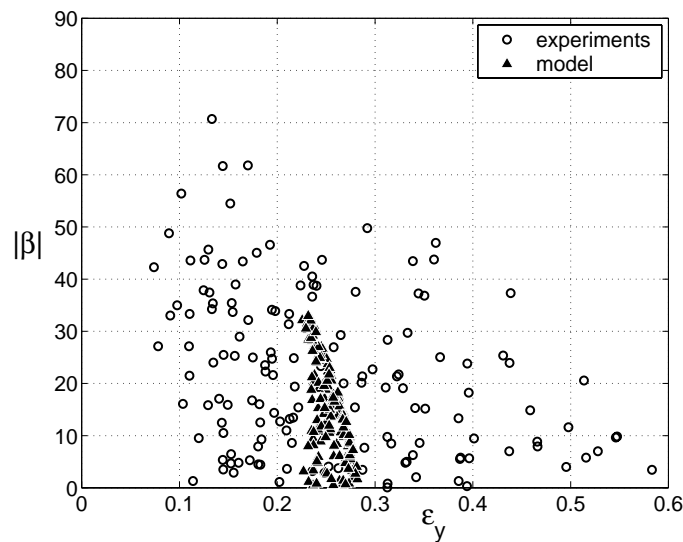


Figure 7.12 Experimental and numerical results for the impact of particles on a powdery layer composed of finer particles ($\alpha=0^\circ$, $d_p/d_b = 6.6$, $C_m = 2.6$).

The value of 2.6 will be used further as being representative for a powdery layer composed of particles with a mean diameter ratio of 6.6 between the incident and the bed particles. Using a proportionality factor of 2.6, the measured relative rebound velocity and rebound angle for experiment G are compared with the same number of impacts simulated with the numerical model in figure 7.12. It appears that the numerical results are concentrated in a small region around a relative rebound velocity of 0.25, while the experimental results show a much larger variation with respect to the relative rebound velocity. This larger variation could be caused by the variation in the coefficient of restitution as measured for the impact on a solid layer (figure 7.1). However, this is not taken into account by equation 7.3 as is applied in the theoretical sticking model to model the coefficient of restitution.

7.3 Discussion and conclusion

Coefficient of restitution and friction coefficient

From the measured values for the coefficient of restitution of glass particles on a solid glass surface, it appears that the prediction of this coefficient is not so trivial. It is found that the measured value is almost 20% below the expected value of about 1. Also, in the measurements a quite large variation is found. The measured distribution for the coefficient of restitution is skewed to the right with 60% of the values between 0.8 and 1 and a tail to the left with values as low as 0.5 (figure 7.1). It is suggested that electrostatic charges have affected the coefficient of restitution. This is supported by the results from impact experiments with more conductive materials. In these experiments, the measured coefficient of restitution for the impact of copper particles on a stainless steel surfaces were correctly predicted by the model for the coefficient of restitution. With respect to the friction coefficient the measured value of 0.17 complies with the range of values expected as discussed in section 5.4.

Proportionality factor

In the experiments a proportionality factor of 3.5 is found for the impact of glass spheres on a powdery layer composed of glass spheres with the same size as that of the impacting particles (standard layer). This factor is different from the value of 2 found by Werner on the basis of his 2-D computer simulations in which also the incident and the bed particles were equally sized. The fact that the simulations were 2-D and not 3-D as in the experiments could explain the difference in proportionality factor. In a 2-D configuration of bed particles the target particle is in contact with two other particles. For a 3-D configuration this number is likely to be larger than two (see figure 7.13). Thus, the number of particles accelerated in the 3-D configuration is larger than the number accelerated in the 2-D case. It can, therefore, be expected that also the proportionality factor (defined as the effective number of particles accelerated) is larger for a 3-D case.

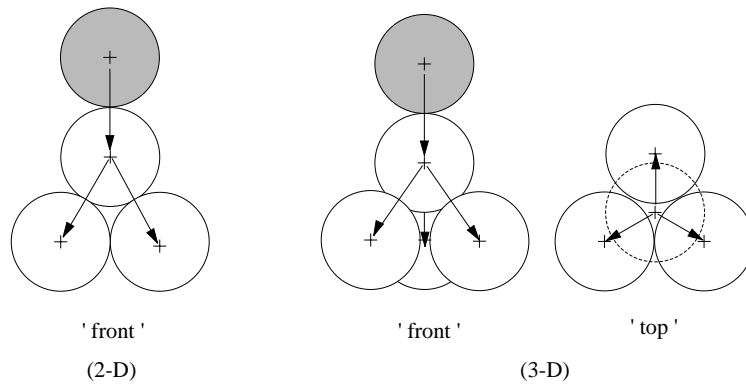


Figure 7.13 Contact force transmission in a 2-D and a 3-D configuration of bed particles

Based on the results of the impact experiments on a standard layer with various incident velocities and impact angles, it is concluded that the assumption in the two-body model that the proportionality factor is independent of the incident velocity and of the angle of impact is appropriate. The proportionality factor is only found to be dependent on the ratio between the size of the incident particles and those in the layer (d_p/d_b). For the experiments where the powdery layer was made of particles with an average size 6.6 times smaller than that of the incident particles, a proportionality factor of 2.6 is found which is well below the reference value of 3.5. To describe this relation an empirical function is proposed which is given by:

$$C_m = 2.4 + 1.1 \left(\frac{d_p}{d_b} \right)^{-1} \quad (7.4)$$

The functionality of this empirical relation is chosen such that for particles impacting a flat solid surface ($d_p/d_b \rightarrow 0$) the proportionality factor goes to infinity. The constants in the equation are determined from a least squares fit of the experimentally found proportionality factors. Because the equation above is only based on two measured values, it should be handled with care. Both the measured values as the fitted function are given in figure 7.14.

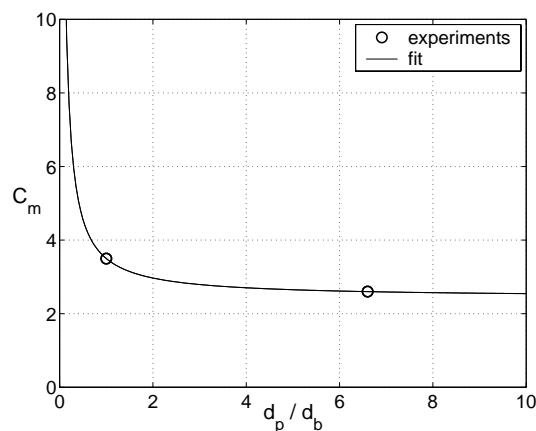


Figure 7.14 Influence of the ratio in the diameter between the incident and the bed particles on the measured proportionality factor.

Splash factor

In the experiments where the incident velocity was varied a significant change was found in the amount of additional particles ejected from the bed. For an incident velocity of 1 m/s the splash factor found is 2.9. In preliminary experiments Werner [71] found a similar splash factor of 2.8 for millimetre sized sand particles impacting a sand surface with an incident velocity of 6.5 m/s at an impact angle of 75° . Although the absolute velocity in the experiment of Werner is almost an order of magnitude larger than for the present experiment, the normal incident velocities are comparable because of the large impact angle for the experiment by Werner. The correspondence in splash factor and normal incident velocity indicates that the number of particles ejected from a powdery layer is probably related to the normal component of the incident velocity. The ejection of bed particles by the incident particle contributes to the removal of deposited material from the heat exchange surface and it provides a useful mechanism to minimize the growth rate of powdery layers on heat exchange surfaces.

Predicted distributions

The two-body model is capable to reproduce the measured distributions in the relative rebound velocity for the impact of particles on a standard layer at $\alpha=0^\circ$ (figure 7.7). With respect to the distribution of rebound angles the two-body model on average predicts too large rebound angles. This effect can also be seen in the average rebound angle for experiments with a non-zero impact angle (figure 7.9). This difference between predicted and measured rebound angles could be the result of the assumption made in the model that bed particles during the impact are fixed to their initial position while in reality they start moving. Movement of bed particles during the impact can affect the rebound angle of particles impacting the target particle with a large local impact angle as is schematically shown in figure 7.15.

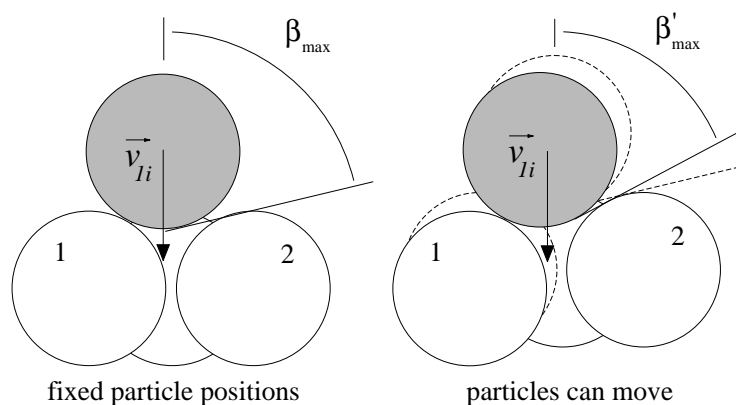


Figure 7.15 Influence of a change in the position of the target particle on the rebound angle. Dashed lines indicate position particles before the impact.

A particle can only rebound with a large rebound angle if it impacts the target particle with a large local impact angle, as is the case for the situation sketched in

figure 7.15. For such an impact, movement of the target particle into the layer during the impact reduces the span of rebound angles over which the incident particle can leave the surface.

For the impact on a powdery layer composed of particles with a much smaller diameter than that of the incident particles, the distribution predicted by the model does not agree with the measured distribution (figure 7.12). Possibly the variation in the coefficient of restitution, as measured for the impact on a solid layer (figure 7.1) but not included in the model, results in the broader distributions of the measurements. The reason why this effect was not noticed for the powdery layers with larger particles is given by the contact angles possible in the impact. For the impact of a particle on a similar particle a wide variation in local impact angle θ exists. In contrast, for the impact on a powdery layer of finer particles, the impact is limited to positions near the top of the target particle (see figure 7.16). Therefore, the variation in relative rebound velocity and rebound angle as measured and predicted for a layer with the same size of particles as the incident particle is the direct result of the possible contact angles.

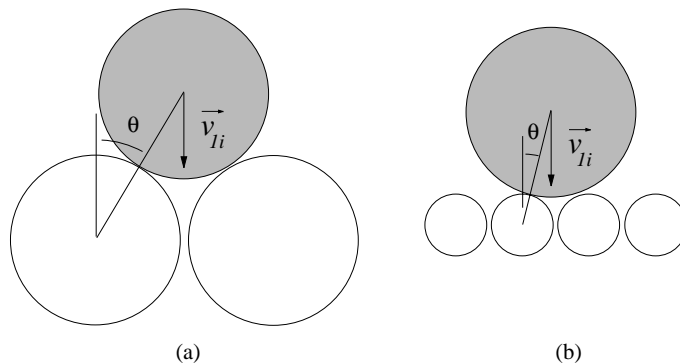


Figure 7.16 Difference in possible contact angles for the impact of a particle with a layer of equal sized and much smaller particles.

If the variation as measured for the coefficient of restitution would be included in the model, the model predictions become in closer agreement with the experiments as shown in figure 7.17. To include the variation, in the model the coefficient is sampled from a Gaussian probability function with a mean calculated from equation 7.3 and a standard deviation of 0.15. The used distribution is a very crude approximation of the measured distributions and is only applied to illustrate the effect of a variation in the coefficient of restitution on the model predictions.

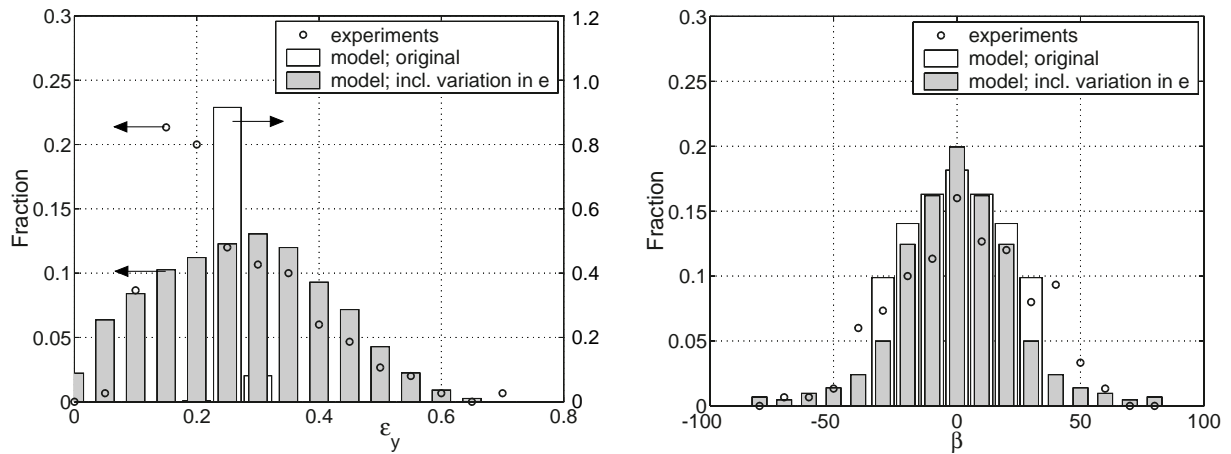


Figure 7.17 Measured (circles) and modelled (bars) distribution of the relative rebound velocity and the rebound angle for the impact of particles on a powdery layer composed of finer particles ($d_p/d_b = 6.6$, $C_m = 2.6$).

When including a variation in the coefficient of restitution, the predicted distributions are in closer agreement with the measurements. However, there are still some differences in the shape of the distribution for the relative rebound velocity. Besides the effect of the actual distribution in the coefficient of restitution, the difference could also be the result of the relatively large variation in the particle sizes in the layer. For this layer the relative variation in particle size was 100%, while for the experiments on a standard layer this variation was only 25%. The variation of particle sizes in the layer is not taken into account by the present model. A third explanation for the observed difference could be that because of the difference in particle sizes a small displacement of the target particle can make the incident particle to come in contact with more than 1 bed particle. Because this situation is not accounted for in the theoretical model, the applicability of the two-body approach is probably limited to a certain range in ratios between the size of the bed particles and the incident particle. In the asymptotic case with infinite small bed particles the layer would behave as a viscous fluid. In that case some kind of effective viscosity replaces the net effect of the proportionality factor, the coefficient of restitution and the friction coefficient.

Applicability of the two-body approach

To conclude, the two-body approach as applied in the theoretical sticking model is shown to be a useful and valid approach to model the impact of a fly-ash particle on a powdery layer as can develop on the tubes in a heat-recovery boiler. For a layer consisting of the same size particles as the incident ones, it is experimentally determined that the proportionality factor is equal to 3.5. It should be noted that from one experiment to another small variations in the mean relative rebound velocity i.e. the proportionality factor are observed that are associated with differences in the quality of the layer. Using a proportionality factor of 3.5, the model is capable to reproduce the measured distributions in the rebound angle β

and the relative rebound velocity ε_y (figure 7.6). This implies that when applying the two-body model in the final deposition calculations, not only the average effect of the layer but also the effect of the surface roughness is taken into account. With respect to the mean rebound angle and the mean relative rebound velocity, the model predicts the correct trend between these quantities and the impact angle. Although the trend between mean rebound and impact angle is correctly reproduced, the model in general predicts too large rebound angles. This is believed to be a feature of the chosen model in which is assumed that the particles in the layer have fixed positions, while in reality they can move.

The applicability of the model for layers with finer particles is less evident. Using a determined proportionality factor of 2.6 for this layer, the predicted distribution in relative rebound velocity by the model does not match the measured one. The difference can be explained by a variation in the coefficient of restitution as was measured in the same set-up for glass particles impacting a solid glass layer. Nevertheless, the model appeared capable to reproduce the correct trends between the mean relative rebound velocity, the mean rebound angle and the impact angle. Qualitatively, the predictions matched the measured values for the rebound angle but small differences were observed for the relative rebound velocities. The two-body model will be used in the next chapter to calculate the deposition rates in a tube bundle.

Chapter 8

Fouling and design

With the numerical deposition model and the derived sticking model, it is now possible to perform deposition calculations for various tube bundle geometries. The tube bundle geometry is optimized with respect to the formation of a powdery deposit using minimization of the overall deposition rate for a downstream tube row as a design criterion. The method and conditions applied in the calculations are treated in section 8.1. For comparison, in section 8.2 deposition rates are calculated for the formation of a powdery deposit on a single cylinder in cross-flow. In section 8.3 the deposition in an in-line tube bundle arrangement is treated as a reference situation. Compared to this reference, in section 8.4 the influence of the tube pitch, tube arrangement, tube shape and the application of a spoiler in front of the bundle is discussed. Concluding, some design recommendations are given in section 8.5.

8.1 Method and conditions

Deposition calculations are performed for a single cylinder and for different tube bundle arrangements. In the calculations the sticking efficiency is either assumed perfect ($s = 1$) or the sticking efficiency is determined by the two-body model. The values applied in the calculations for the Reynolds number, Stokes number and particle Reynolds number correspond with the values already given in table 4.6. In the simulations for a single cylinder and a tube bundle, respectively 30,000 and 50,000 particles, initially equally divided over the inlet, are tracked through the domain. With respect to the transport of particles (perfect sticking) these numbers gave statistically satisfying results. Because the sticking model contains a random component in the relative position of the incident particle to the particles in the layer, the number of particles in the calculations using the two-body model needs to be increased to obtain statistically satisfactory results. Due to computer limitations, the maximum number of particles that could be tracked was limited to 50,000. To increase the number of particles, without tracking more particles, it is assumed that each particle tracked in the first run from inlet to either impact or outlet represents n particles. In other words, for each tracked particle that impacts one of the tubes the sticking model is repeated n times. After this first impact each rebounding particle is followed until it sticks somewhere or leaves the flow domain at the outlet. This

procedure makes that the total number of particles becomes equal to 30,000 n and 50,000 n , respectively. In most cases a value of 10 for n was enough to yield statistically satisfying results.

For the two-body model applied in the calculations, three variants are applied of which the parameters are given in table 8.1.

Model variant	s_1	s_2	s_3
d_p/d_b	1	6.6	1
C_m	3.5	2.6	3.5
Δ	0.1	0.1	0.1
f	0.2	0.2	0.17
e	original	original	eq. 7.3
material properties	table 5.3	table 5.3	table 5.3
y	3.2 Y	3.2 Y	-
Γ	0.30 J/m ²	0.30 J/m ²	0.30 J/m ²

Table 8.1 Parameters applied in the sticking model

In the first variant (referred to as s_1), it is assumed that the K_2SO_4 particles in the bed have the same diameter as the incident particles and the corresponding proportionality factor is taken equal to 3.5 as is measured in the impact experiments. The value for the friction coefficient of the K_2SO_4 particles is taken equal to the rounded off value as measured for glass spheres on a glass surface. With respect to the coefficient of restitution e , the original model as treated in section 5.3 is preserved. In variant s_2 the only change is that the layer is composed of smaller particles and, accordingly, the proportionality factor is taken equal to 2.6 as measured in the impact experiments on a powdery layer. In variant s_3 the parameters as used for the experiments of glass particles impacting on a powdery layer made of the same particles are applied (section 7.1). The coefficient of restitution is calculated using equation 7.3.

The calculated deposition rates are expressed using the Stanton number and the collection efficiency. The Stanton number defined in equation 3.8 gives the local deposition rates as a function of the cylinder angle θ . The Stanton number is used to calculate the overall deposition rate as expressed with the collection efficiency η_{coll} (defined in equation 4.26). For the upstream side (us) the collection efficiency is given by:

$$\eta_{coll,us} = \frac{\pi}{2} \overline{St}_{0-\frac{\pi}{2}} \quad (8.1)$$

with $\overline{St}_{0-\frac{\pi}{2}}$ the average Stanton number over the upstream heat exchange surface. A comparable relation holds for the downstream collection efficiency but with the average Stanton number between $\frac{\pi}{2}$ and π . The overall collection efficiency is given by the sum of the upstream and downstream collection efficiency.

8.2 Deposition on a cylinder in cross-flow

Deposition rates are calculated for the formation of a powdery deposit on a single cylinder in cross-flow. The same problem was studied at the end of chapter 4 for the perfect sticking case. In the calculations the parameters of variant s_1 are used. The results for a single tube are later compared with the results for a tube bundle. In table 8.2 the deposition rates expressed by the collection efficiency are given for three different particle sizes with a Stokes number of 0.05, 0.15 and 0.5. In this table also the deposition rates assuming perfect sticking are included between brackets.

Collection efficiency $\eta_{coll} \cdot 10^2$	Stk = 0.05	Stk = 0.15	Stk = 0.50
upstream (us)	0.04 (0.34)	0.16 (0.95)	0.16 (14.6)
downstream (ds)	0.32 (0.58)	0.17 (0.36)	0.07 (0.03)
overall (us+ds)	0.36 (0.93)	0.33 (1.31)	0.23 (14.6)

Table 8.2 Collection efficiencies for the formation of a powdery deposit on a cylinder in cross-flow using variant s_1 . Values between brackets are for perfect sticking conditions.

Compared to perfect sticking conditions, deposition rates for the formation of a powdery layer are substantially lower. Although transport rates towards the cylinder (perfect sticking case) rapidly increase with particle size, overall deposition rates show an opposite trend and decrease with particle size. For the particles with a Stokes number of 0.15, the distribution of deposition over the cylinder expressed by the Stanton number is given in figure 8.1 for both analysed situations.

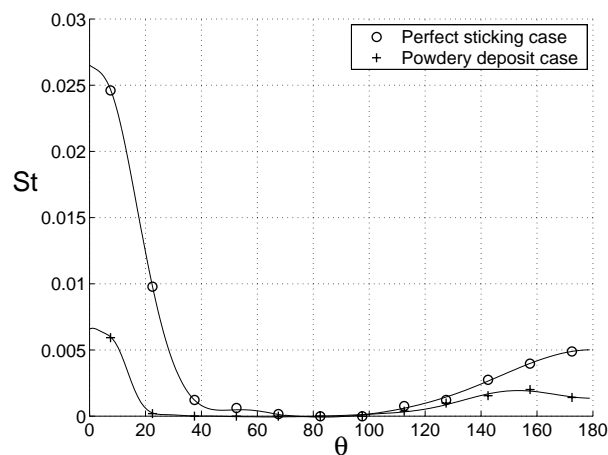


Figure 8.1 Deposition rates on a cylinder in cross-flow ($Re = 5000$ and $Stk = 0.15$).

The shape of the deposition-curve for a powdery deposit is not really different from the perfect sticking case. The decrease in downstream deposition rates is not as pronounced as for the upstream side. For the upstream side a decrease in collection efficiency of 83% is found while for the downstream side it is only 53%.

8.3 Deposition in a tube bundle geometry

Deposition rates are calculated for the formation of a powdery deposit in the in-line tube bundle geometry given in figure 8.2.

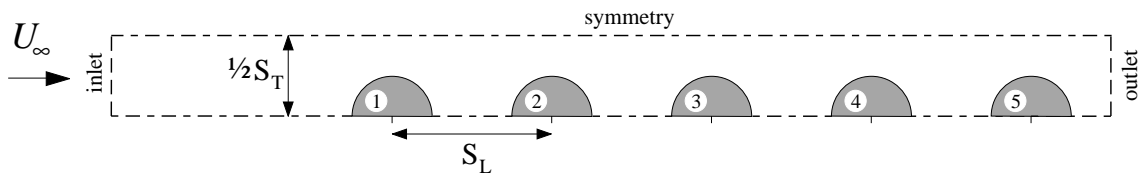


Figure 8.2 Reference geometry: in-line tube arrangement
($S_T/D_{\text{tube}} = S_L/D_{\text{tube}} = 2$).

The geometry comprises the first five tube rows in the bundle and is confined using a symmetry axis on the top and the bottom-side. For both the perfect sticking case as for the sticking model with the parameters of variant s_L , the deposition rates for the five tubes in the bundle are given in table 8.3 (page 119) and in figure 8.3.

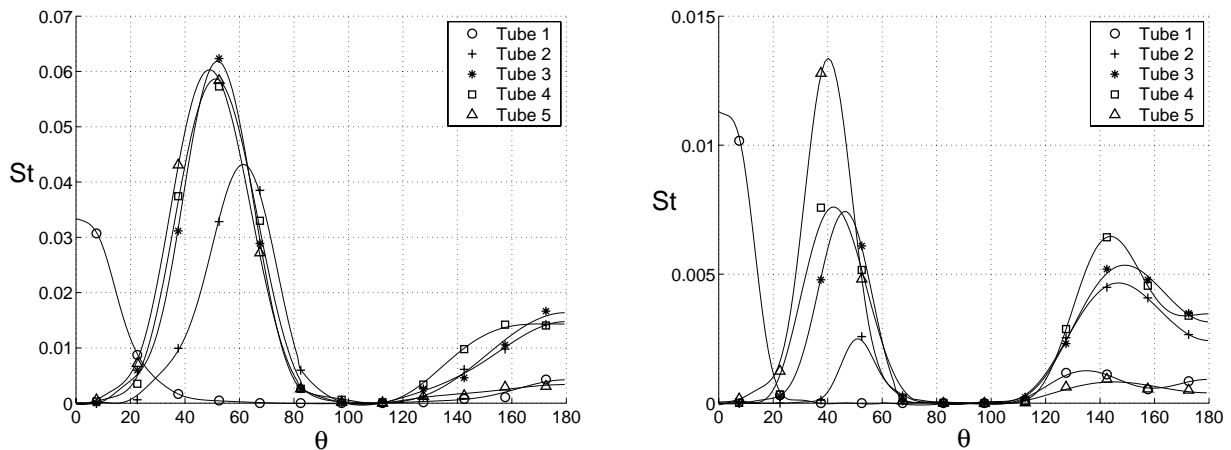


Figure 8.3 Stanton number for the deposition on an in-line tube bundle for the perfect sticking case (left) and for the powdery deposit case (right), ($S_T/D_{\text{tube}} = S_L/D_{\text{tube}} = 2$, $Re = 5000$ and $Stk = 0.15$).

Perfect sticking

In the perfect sticking case, the distribution of the Stanton number with the cylinder angle for the first tube is comparable with the distribution as calculated for a single cylinder (figure 8.1). Also quantitatively the deposition rates are comparable. For a single cylinder the upstream collection efficiency is $0.95 \cdot 10^{-2}$ where it is $1.09 \cdot 10^{-2}$ for the first tube in the bundle. For the tubes in row 3 up to 5 the upstream deposition rates have increased with a factor 3 to $3.5 \cdot 10^{-2}$ (table 8.3). Besides this overall increase also the distribution over the cylinder has changed. Maximum deposition no longer occurs at a cylinder angle of zero but at an angle of about 50° for rows 3 up to 5. This shift coincides with a shift in the stagnation point on these tubes as can be seen from the streamlines in figure 8.4. The angle where deposition is maximal is affected by the application of the stationary flow field calculation as performed here.

This calculation does not capture the oscillatory motion of the shed vortices in the wake. In that case the peak at 50° would be more distributed.

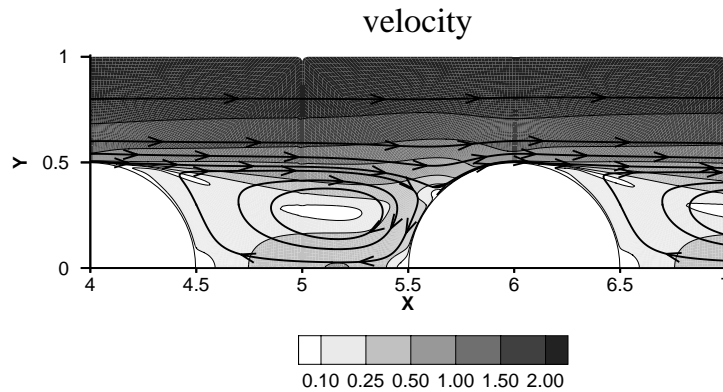


Figure 8.4 Velocity plot with streamlines for the 4th row tube in an in-line bundle at $Re=5000$

For the in-line bundle with a relative transverse pitch of 2, the increase in deposition for downstream rows is strongly reduced at the 4th row but is not yet fully developed. The slow increase from the 3rd to the 4th row is probably caused by the not yet fully developed flow field at the 4th row as can be seen from figure 8.5. From literature, it is known that the flow becomes periodic in space somewhere between the 4th and the 6th row depending on the Reynolds number and the tube bank configuration [40].

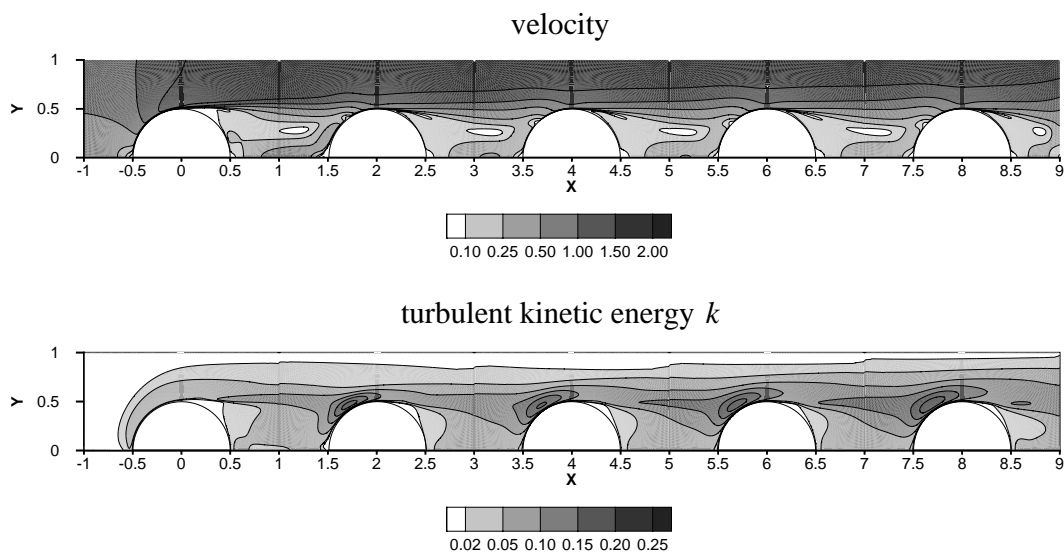


Figure 8.5 Plot of the velocity and the turbulent kinetic energy in an in-line tube bundle at $Re=5000$

For the 5th row a strong decrease in downstream collection efficiency is found. This is due to the fact that the outlet is located in the recirculation zone. Particles once entered this recirculation zone pass through the outlet and are removed from the tracking calculations where they normally would be transported towards the cylinder again. Therefore, with respect to the downstream and the overall deposition rates, the results for the 5th tube are disregarded in the analysis.

Powdery deposit

In the case of a non-perfect sticking efficiency of a powdery deposit, deposition has by far not reached a stationary situation at the 4th row of the in-line bundle (figure 8.3-b). The still increasing deposition rates are caused by particles that have rebounded from more upstream tubes as is illustrated in figure 8.6. In this figure the particle paths are shown from the inlet until they reach a tube or leave at the outlet (first transport run) and from the position of the first impact until they impact a tube again or leave at the outlet (second transport run).

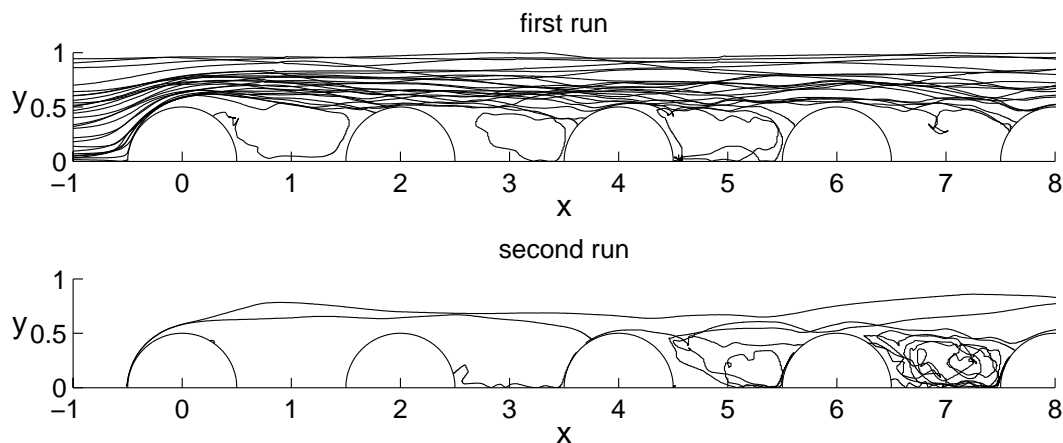


Figure 8.6 Particle tracks as calculated for 100 particles in the first two transport runs. Upper figure; tracks from the inlet to the first impact position on a tube or to the outlet. Lower figure; tracks from the first impact position to the second impact position or the outlet.

A rebounding particle can either impact the preceding tube, the same tube, one of the downstream tubes or it can leave the flow domain. The effect of rebounding particles from upstream tubes on the deposition rates of more downstream tube rows is shown in figure 8.7 with the deposition rate as a function of the number of impacts. For a single cylinder a particle deposits on the upstream side of the cylinder after maximal 2 impacts where for downstream deposition it can take up to 8 impacts. The large number of impacts that account for deposition at the downstream side is caused by a limited likelihood for a particle leaving the recirculation area behind a cylinder, once it has entered this zone. Therefore, most particles remain there until they eventually stick. This explains why the decrease in deposition rates for a powdery deposit compared to the perfect sticking case is less pronounced for the downstream side. For a 4th row tube in an in-line bundle the number of impacts that determine deposition are different. For the 4th row tube the number of impacts that account for 99% of the deposition is 6 for the upstream and 10 for the downstream side.

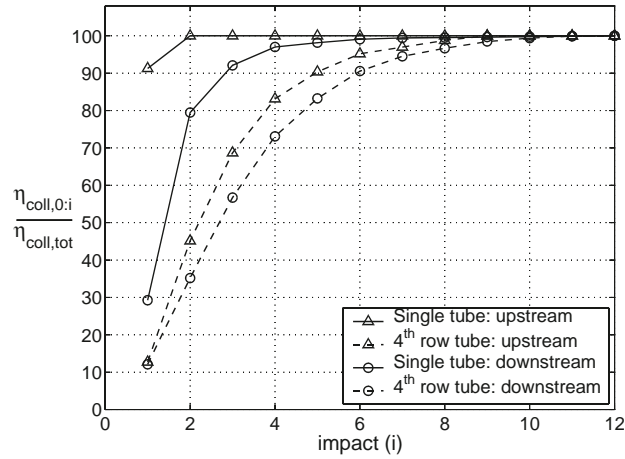


Figure 8.7 Relative deposition rate as a function of the number of impacts.

The overall deposition rates expressed with the collection efficiency are given in table 8.3 for the three applied variants of the sticking model and the perfect sticking situation. In the same table also the results for a single cylinder have been included.

Tube side	Sticking model	Collection efficiency $\eta_{coll} \cdot 10^2$					
		Single cylinder	Tube in bundle				
			1	2	3	4	5
Upstream	$s = 1$	0.95	1.09	2.30	3.43	3.51	3.64
	s_1	0.16	0.27	0.08	0.29	0.35	0.50
	s_2	-	0.25	0.06	0.23	0.29	0.44
	s_3	-	0.49	0.25	0.75	0.84	1.12
Downstream	$s = 1$	0.36	0.16	0.84	0.91	1.10	0.23
	s_1	0.17	0.10	0.37	0.42	0.45	0.07
	s_2	-	0.06	0.25	0.30	0.36	0.05
	s_3	-	0.18	0.66	0.77	0.86	0.14

Table 8.3 Collection efficiencies for an in-line tube bundle using different sticking variants ($S_T/D_{tube} = S_L/D_{tube} = 2$, $Re = 5000$ and $Stk = 0.15$).

Compared with the deposition on a single cylinder, upstream deposition is a factor 2 higher for a 4th row tube in an in-line bundle using variant s_1 . This increase is smaller than for the perfect sticking case indicating a reduced sticking efficiency for a tube in the bundle compared to a single tube. The same argument holds for the downstream side. The effect of the size of the particles in the layer on the deposition rates is simulated for an in-line tube bundle geometry using the parameters of variant s_2 (table 8.1). The main effect is that the deposition rates are somewhat smaller than with variant s_1 . For the upstream side of the 4th row tube in the bundle, deposition has decreased with 17% and for the downstream side the decrease is

20%. The effect of a reduced coefficient of restitution as measured in the impact experiments is simulated using the parameters of variant s_3 . The reduced coefficient of restitution results in an increase of deposition as can be seen from the values given in table 8.3. Compared with variant s_1 , deposition has increased with 140% for the upstream side and 90% for the downstream side of the 4th row tube in the bundle.

Comparison of predicted values with experimental values

The calculated dimensionless deposition rates are converted to actual deposition rates using equation 3.8. They are given in table 8.4 together with the deposition rate as estimated from the decrease in heat transfer coefficient of the economiser bundle in the boiler of a refuse-waste incinerator (section 3.2). The estimated value is representative for the average deposition rate on a tube in the bundle. Because of the large number of tube rows in the economiser bundle, the average value is about equal to the deposition rate for one of the more downstream rows where deposition is fully developed. For the calculated deposition rates use is made of the results for the 4th row tube. It should be realized that deposition is not yet fully developed for this tube and based on the calculated trend, deposition is expected to be somewhat higher for more downstream rows.

	$\eta_{\text{coll, us}}$ $\cdot 10^3$	$\eta_{\text{coll, ds}}$ $\cdot 10^3$	\overline{St} $\cdot 10^3$	$\phi_d \cdot 10^7$ kg/m ² s
Estimated	-	-	-	10 ± 5
Predicted				
$s = 1$	35.1	11.0	14.7	67
s_1	3.5	4.5	2.5	12
s_2	2.9	3.6	2.1	9
s_3	8.4	8.6	5.4	25

Table 8.4 Deposition rates for an in-line bundle ($C_{p,d} = 0.10 \text{ g/m}^3$, $Re = 5000$)

When applying either variant s_1 or variant s_2 in the developed two-body sticking model, calculated deposition rates are in the same range as estimated from the decrease in heat transfer coefficient. Assuming perfect sticking or applying the parameters of variant s_3 in the sticking model leads to deposition rates which are a factor of 6.7 and 2.5 larger than the estimated value, respectively. The values found show that a reliable sticking model is required to predict the deposition rates for the formation of a powdery deposit. The application of the two-body approach proves to yield deposition rates comparable to the one estimated from the decrease in heat transfer for the economisers. This gives confidence in the chosen approach. The comparison shows that the parameters of the layer actually influence deposition and need to be known for a reliable comparison between experimental values and the

model. In the remaining of this chapter in the sticking model the parameters of variant s_I will be used.

8.4 Design optimization

To improve the design of a tube bundle such that the formation rate of a powdery deposit is minimized, changes are made to the reference geometry and the resulting deposition rates are calculated. With respect to the geometries studied, it is not tried to keep the overall heat transfer coefficient constant. The results of the simulations are compared with respect to the distribution of deposition over the different tube rows and with respect to the overall deposition rate of the 4th row tube. The differences at this row are regarded as representative for the deposition rates at more downstream rows where deposition is constant for each row. Later in section 8.5 the results of the simulations will be discussed taking also changed heat transfer and pressure drop characteristics into consideration. The geometries used in the simulations are given in figure 8.8.

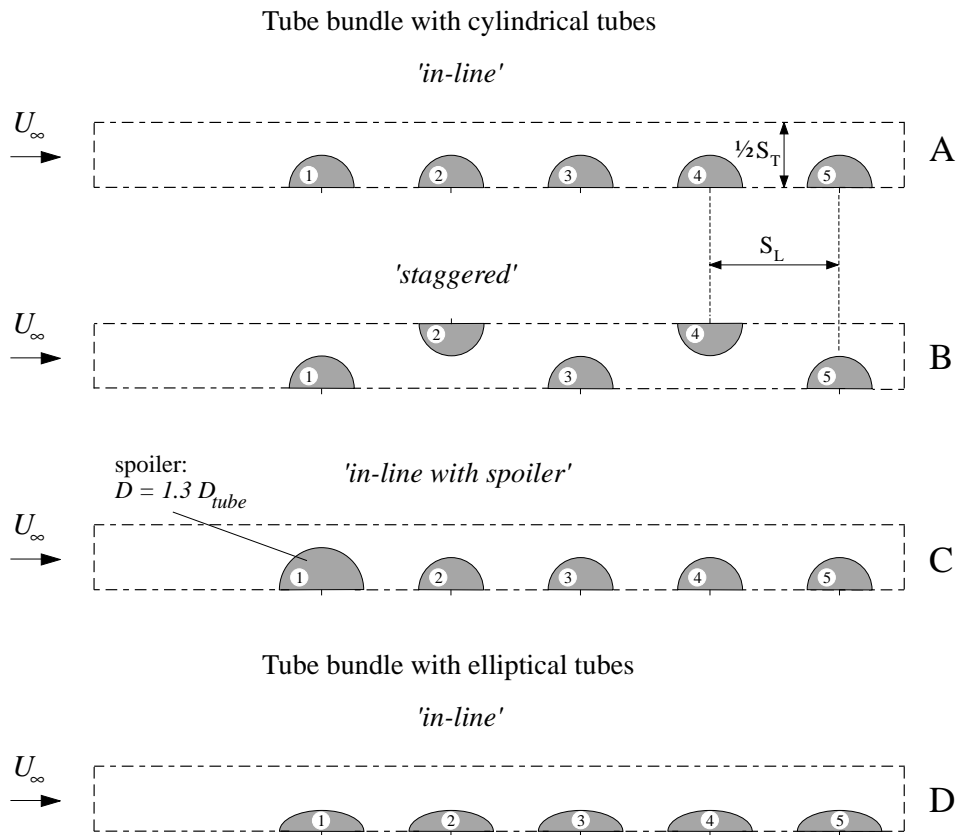


Figure 8.8 Geometries used in the simulations

In the simulations the transverse pitch of the in-line bundle is both increased and decreased with half a tube diameter yielding a relative pitch in transverse direction of 2.5 and 1.5 compared to the reference pitch of 2. In the second variation of the geometry the in-line arrangement is exchanged with a staggered arrangement while maintaining both a transverse and a longitudinal relative pitch of 2. Returning to the in-line arrangement, the first tube in the reference geometry is

replaced with a tube having a 1.3 times larger diameter that serves as a spoiler for the downstream tube rows. The spoiler is positioned at the original position of the first tube in the reference geometry. In the last variation of the geometry the original tubes with a circular cross-section are replaced with tubes that are elliptical, figure 8.9. The dimensions of the ellipse are chosen such that the circumference is identical to that of the original tube. When referring to the relative pitch of a bundle with elliptical tubes, the equivalent diameter of the ellipse equal to D_{tube} is used.

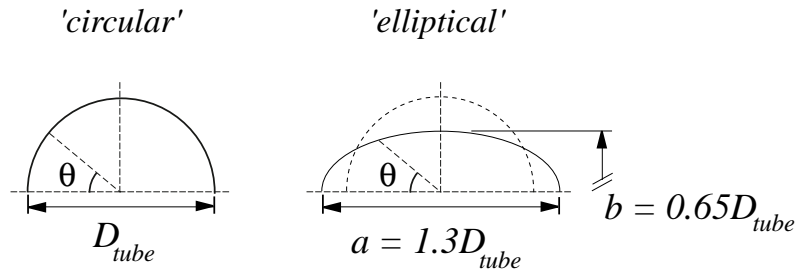


Figure 8.9 Elliptically shaped tubes

In the simulations the Reynolds number and the Stokes number are again set to 5000 and 0.15, respectively. For the sticking efficiency both the perfect sticking assumption is applied as the sticking efficiency determined by the two-body model when using the parameters of variant s_1 . In table 8.5 the results of the simulations are given in terms of the collection efficiency.

Geometry	Pitch S_T/D_{tube}	Sticking model	Collection efficiency $\eta_{coll} \cdot 10^2$									
			Tube in bundle									
			1		2		3		4		5	
us	ds	us	ds	us	ds	us	ds	us	ds	us	ds	
A	1.5	perfect sticking	2.22	0.18	5.54	0.67	8.59	0.98	9.89	1.13	10.9	0.14
A	2.0		1.09	0.16	2.30	0.84	3.43	0.91	3.51	1.10	3.64	0.23
A	2.5		1.06	0.18	1.18	0.85	1.93	0.92	1.87	0.96	2.00	0.29
B	2.0		1.26	0.04	21.7	0.02	26.4	0.07	22.2	0.26	18.2	0.12
C	2.0		2.40	0.28	1.31	1.96	2.18	1.57	3.11	2.07	4.45	0.68
D	2.0		3.85	0.10	0.88	0.35	0.82	0.49	1.04	0.59	0.97	0.08
A	1.5	two-body model var. s_1	0.58	0.14	0.02	0.16	0.09	0.16	0.16	0.20	0.19	0.01
A	2.0		0.27	0.10	0.08	0.37	0.29	0.42	0.35	0.45	0.50	0.07
A	2.5		0.28	0.04	0.09	0.35	0.33	0.40	0.36	0.45	0.45	0.10
B	2.0		0.34	0.01	0.61	0.01	0.33	0.02	0.24	0.02	0.22	0.01
C	2.0		0.46	0.08	0.07	0.50	0.29	0.65	0.51	0.76	0.71	0.17
D	2.0		0.10	0.05	0.16	0.15	0.30	0.20	0.38	0.22	0.38	0.03

Table 8.5 Collection efficiencies for various tube bundle arrangements using sticking variants s_1 , us = upstream and ds = downstream ($S_L/D_{tube} = 2$, $Re = 5000$ and $Stk = 0.15$).

Influence of pitch

As can be seen in table 8.5 and figure 8.11, the pitch has a significant effect on the deposition rate. When assuming perfect sticking, deposition strongly increases when decreasing the pitch from 2.5 to 1.5. A smaller pitch results in higher velocities in the bundle and the particle's inertia becomes relatively more important or in other words a particle gets a higher local Stokes number. Because of the higher flow velocities also the impact velocities increase as shown in figure 8.10.

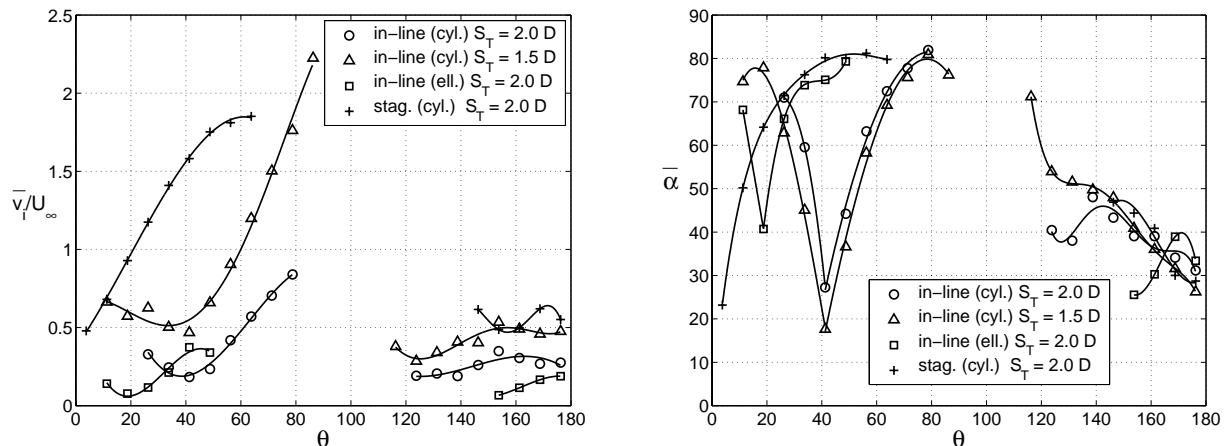


Figure 8.10 Impact velocity and angle of impact for the 4th row bundle in various bundle geometries

For a pitch of 1.5, impact velocities are almost a factor 2 higher than for a relative pitch of 2. The higher impact velocities strongly reduce the sticking efficiency for the formation of a powdery deposit, resulting in a 55% decrease of deposition on the 4th tube in the bundle with a relative pitch of 1.5. Oppositely, increasing the pitch from 2 to 2.5 reduces transport rates (perfect sticking case) for the 4th row tube with 40% but deposition increases with 1% for the powdery deposit case with a non-perfect sticking efficiency.

In-line versus staggered

A comparable reasoning as for the influence of pitch can be held for the deposition rates as calculated for the staggered tube bundle in comparison with the in-line reference geometry. Again deposition rates are higher in case of a perfect sticking efficiency but with a non-perfect sticking efficiency simulated with the two-body sticking model, deposition rates are lower in the staggered arrangement from the 3rd row onwards. For the 4th row the decrease is 67%. Surprisingly, for the staggered arrangement deposition rates first increase from row 1 to 2 and then start to drop again to reach a constant value. This behaviour is opposite to the reference geometry where deposition is the lowest for the first row and increases for downstream rows. The decrease in deposition for downstream rows in the staggered arrangement is induced by the increased flow velocities in the bundle, as shown in 8.12, that result in higher impact velocities (see figure 8.10).

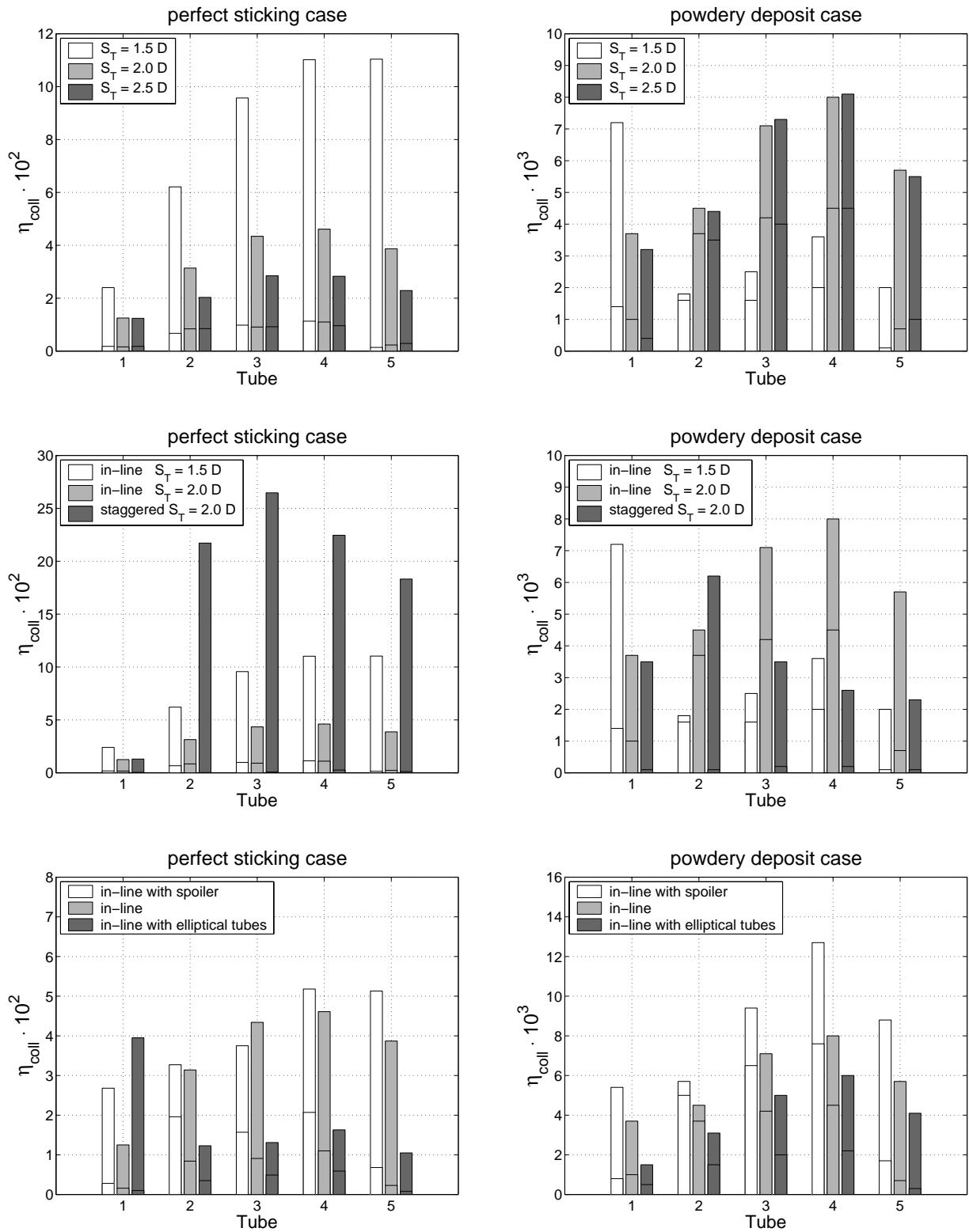


Figure 8.11 Comparison of overall collection efficiencies for different tube bundle geometries. The lower and upper part of the bars indicate downstream and upstream deposition rates, respectively.

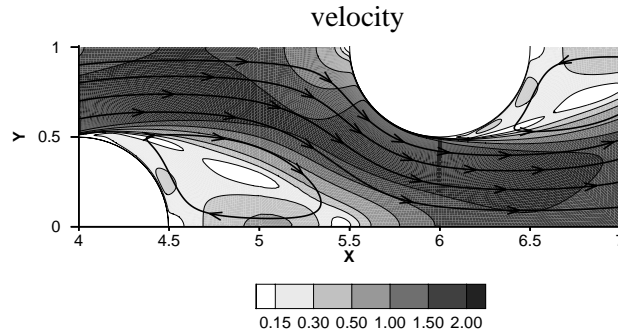


Figure 8.12 Velocity plot with streamlines for 4th row tube in a staggered in-line bundle at Re=5000

Because the velocities in the staggered bundle are about twice the main stream velocity for the flow approaching the downstream tubes in the bundle, the Stokes number based on this velocity is also twice as high and becomes about 0.3. In that case, as was also found for a single cylinder in cross-flow, deposition almost disappears for the downstream side of the tubes. For the upstream side the shape of the deposition-curve is comparable to that at the upstream side of a single cylinder in cross-flow or at the first tube in an in-line bundle (figures 8.1 and 8.13).

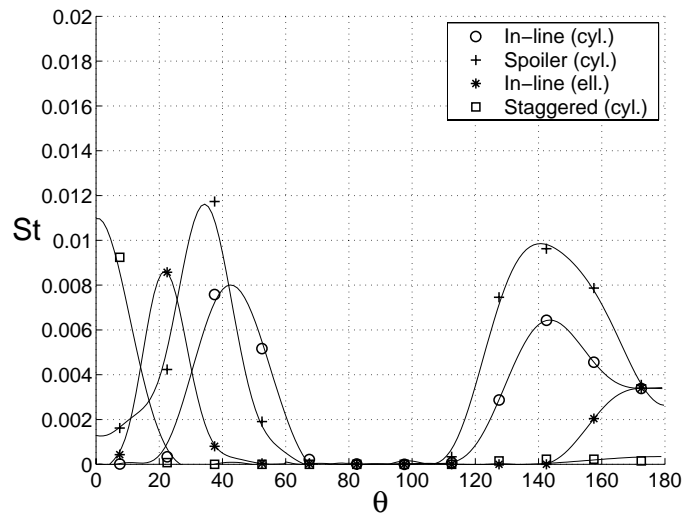


Figure 8.13 Deposition rates for the 4th row tube in various bundle geometries ($S_T/D_{\text{tube}} = S_L/D_{\text{tube}} = 2$).

Application of a spoiler

The application of a larger tube in front of the other tubes that acts like a spoiler is expected to reduce deposition rates for the tubes in the shade of the spoiler. It is found that transport rates (perfect sticking case) are indeed lower for the upstream side of the 2nd, 3rd and 4th row tube (table 8.5). However, for the downstream side of these tube rows transport rates increased resulting in overall transport rates comparable to those in the reference geometry (table 8.5).

With the non-perfect sticking efficiency of a powdery deposit, the application of a spoiler does not reduce but augments deposition compared to the reference geometry as shown in figure 8.5. Lower impact velocities (see figure 8.10) increase the sticking efficiency and, therefore, the overall deposition rate which is 59% higher for the 4th row tube compared to the same tube in the reference geometry.

Circular versus elliptical tubes

By applying elliptical tubes the frontal area of the tubes is reduced and the flow pattern around the tubes is changed compared to the reference geometry with circular tubes. In figure 8.14 the collection efficiencies for a single elliptical tube and a circular tube in cross-flow are compared as a function of the Stokes number

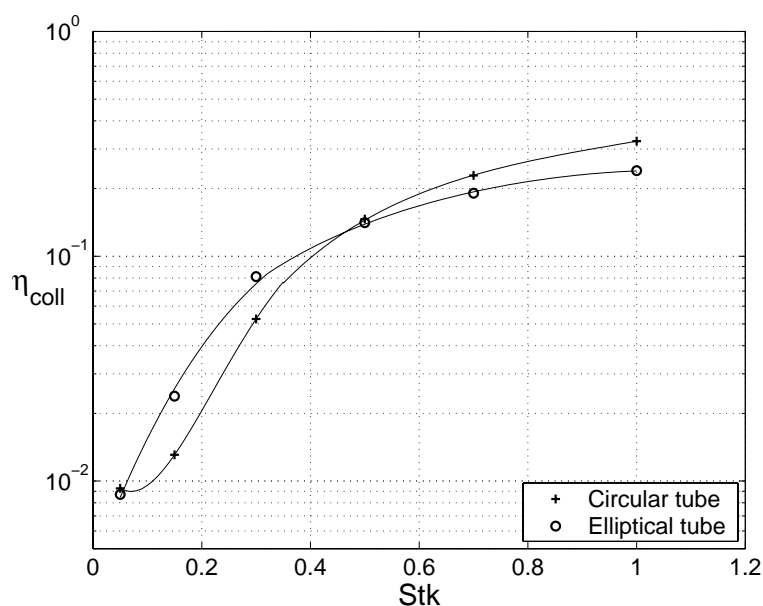


Figure 8.14 Collection efficiencies for an elliptical tube and a circular tube.

The collection efficiency is different for an elliptical tube but not always lower than for a circular one. In the Stokes region between 0.05 and 0.4 deposition is higher for the elliptical tube and above a Stokes number of 0.4 deposition becomes smaller. This explains the enhanced deposition of the first row in the bundle with elliptical tubes compared to the reference geometry. For more downstream rows transport is smaller and the relative decrease is 70 and 54% for the upstream and the downstream sides of the 4th tube, respectively. When including the non-perfect sticking of a powdery deposit, the overall decrease for again the 4th row tube is only 25%. Because of the reduced frontal area of the tubes in the bundle, flow velocities and also impact velocities are lower here than in the reference geometry (figure 8.10). The relatively low impact velocities with relatively large impact angles together result in a more efficient sticking efficiency compared to the reference situation. The enhanced sticking efficiency partly cancels the effect of the strongly reduced transport rates.

The shape of the deposition curve is also different for the elliptical tubes compared to the circular tubes (figure 8.13). Deposition is more concentrated towards a tube angle of 0° and 180° while the region between 40° and 140° remains almost clean.

8.5 Design recommendations

To come to design recommendations, the results of the simulations are discussed taking into account also the heat transfer and pressure drop characteristics of the different geometries. The design of a tube bundle includes selection of the main stream velocity and the tube diameter (together setting the Reynolds number), the tube shape, the tube bundle arrangement (in-line, staggered or with spoiler) and the pitches of the bundle. When designing a tube bundle, maximum heat transfer is desired. Higher heat transfer rates reduce the heat exchange surface required and, therefore, reduce the investment costs. Besides heat transfer also the required boiler volume, the pressure drop over the bundle and the fouling tendency of the bundle are important design criteria. A more compact bundle because of smaller pitches reduces the boiler volume required and, therefore, also investment costs. Selection of a bundle with a larger pressure drop requires a ventilator with different characteristics consuming more energy. With respect to fouling, a design is preferred where deposition is minimal such that the effect of fouling on the initial heat transfer coefficient is minimized. The recommendations made assume a fixed Reynolds number and apply for the case that no liquid phase is present at either the particle or the heat exchange surface. This situation corresponds to layers developing in the economiser bundle of a refuse waste incinerator as discussed in chapter 3.

From the simulations, it is found that deposition rates are significantly lower for the downstream tube rows in a staggered bundle compared to those in an in-line geometry with equal pitches (67% lower with respect to the deposition on the 4th row tube). The main reason for the decreased deposition rates is the higher velocities in the bundle. For the range of Reynolds number considered the overall heat transfer coefficient of an in-line bundle is approximately equal to that of a staggered bundle [73]. Thus, for both tube bundle arrangements the same number of tubes is required to transfer a given amount of heat. Because the pitches of the bundles are equal also the required boiler volume is equal for both type of bundles. So, in case only a powdery layer will form, a staggered bundle is to be preferred above an in-line arrangement.

The transverse pitch (S_T) should be chosen minimal. From the simulations, it is found that deposition strongly decreases for the in-line bundle if the transverse pitch is reduced from 2.5 to 1.5. Because this decrease is again associated with a reduction in the sticking efficiency due to higher impact velocities, it is expected that deposition rates also will fall when decreasing the pitch for a staggered bundle. For both the in-line as the staggered bundle a decreasing pitch increases the overall heat transfer coefficient of a bundle. Because also the fouling rates drop, a minimum

transverse pitch is preferred. Decreasing the pitch, however, also increases the pressure drop over the bundle. The choice for the pitch is, therefore, constrained by a maximum allowable pressure drop over the bundle.

The addition of a spoiler in front of the bundle to reduce fouling is not recommended. Zhang reported a reduction in deposition for a staggered bundle with finned tubes when a spoiler was installed upstream of the first row of tubes [74]. The reduction was influenced by the shape of the spoiler, its size and the relative position from the spoiler to the bundle indicating that for each bundle geometry and Reynolds number the spoiler configuration needs to be optimized. This is supported by the simulation results where for an in-line arrangement with spoiler an increase rather than a decrease in deposition rates is found. So, to reduce fouling with the application of a spoiler more effort has to be put on finding the right configuration. Because changing the tube arrangement and transverse pitch already results in a significant improvement, application of a spoiler seems not worth the effort.

Changing the shape of the tubes from circular to elliptical proves to be a promising option to reduce fouling in tube bundles. Compared to the in-line arrangement deposition for a powdery deposit is reduced with 25%. The average heat transfer coefficient of a tube bundle with circular or elliptical tubes can be expected to be approximately the same when the relative pitches are equal [28,48,49]. However, because of a reduced frontal area the pressure drop will be smaller and allows for a smaller pitch to be applied compared to an in-line bundle with circular tubes. A smaller pitch reduces fouling even further but also would increase heat transfer, thereby reducing the number of tubes and boiler volume required. The most optimal choice with respect to minimal fouling is probably to apply the elliptical tubes in a staggered tube bundle arrangement with a slightly reduced transverse pitch (figure 8.15).

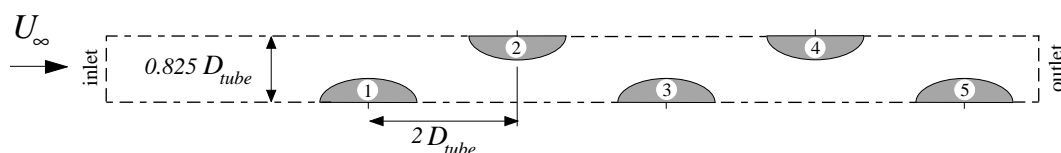


Figure 8.15 New improved tube bundle geometry

For the suggested improved geometry deposition is calculated and the results are given in table 8.6. In the table the values between brackets indicate the deposition rates in case of perfect sticking. The pitch in this new improved geometry is taken equal to 0.825 such that the transverse passage between two tube rows is equal to the reference geometry (figure 8.2). Because the frontal area per unit length in transverse direction is equal, it is expected that the pressure drop of both the new and the reference geometry are comparable.

Tube side	Geometry	Collection efficiency $\eta_{coll} \cdot 10^2$				
		Tube in bundle				
		1	2	3	4	5
us	Reference	0.27 (1.09)	0.08 (2.30)	0.29 (3.43)	0.35 (3.51)	0.50 (3.64)
	New	0.11 (3.97)	0.25 (11.63)	0.12 (5.90)	0.16 (5.75)	0.10 (6.22)
ds	Reference	0.10 (0.16)	0.37 (0.84)	0.42 (0.91)	0.45 (1.10)	0.07 (0.23)
	New	0.01 (0.03)	0.01 (0.03)	0.01 (0.04)	0.02 (0.04)	0.00 (0.00)
tot	Reference	0.37 (1.25)	0.45 (3.14)	0.71 (4.34)	0.80 (4.61)	0.57 (3.87)
	New	0.12 (4.00)	0.26 (11.66)	0.13 (5.94)	0.18 (5.79)	0.10 (6.22)

Table 8.6 Collection efficiency of the reference and the new tube bundle geometry ($S_T/D_{tube} = 0.825$, $S_L/D_{tube} = 2$, $Re = 5000$ and $Stk = 0.15$).

When focussing on the fourth row tube, it is found that the deposition rate is reduced with 78%. In that case deposition rates would fall from $12 \cdot 10^{-7}$ kg/m²s as numerically calculated for the reference geometry to $3 \cdot 10^{-7}$ kg/m²s for the new design. In that case also the asymptotic fouling resistance which is proportional to the deposition rate (equation 3.4) would decrease from 0.009 to 0.002 m²K/W. Because the decrease in heat transfer of the bundle is related to the inverse of the fouling resistance (equation 2.2), the decrease in heat transfer is reduced from 27% in the original design to 8% in the new design.

Chapter 9

Conclusions and recommendations

Conclusions

For the boiler in a refuse waste incinerator, it is found that the character of the fouling that occurs on the tube bundles placed in the convective part of the boiler is strongly affected by the local gas and tube temperatures. On the superheaters in the boiler a thick, hard and sintered layer is formed where on the economisers the layer is thin and powdery. From an analysis of process data, it appeared that both types of layers resulted in a 27% reduction of the overall heat transfer coefficient. This reduction results in a decrease in efficiency of about 2% on average. For the application in all Dutch refuse waste incinerators this means that without fouling at least 20,000 households more could be supplied with electricity.

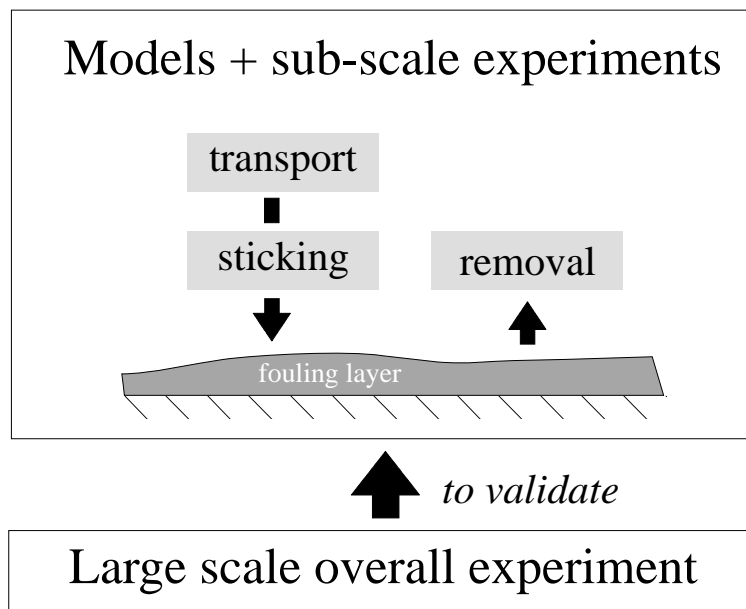


Figure 9.1 Positioning of the present work in a larger framework

In the present study a model is developed to predict the growth of a powdery fouling layer. With the model the growth of the layer can be calculated as a function of the process conditions and the geometry of the boiler. In a combustion environment the growth of a layer is the net result of different contributing

mechanisms of which the deposition of particles, denoted as particulation, is known to be the most important. To predict deposition rates by particulation both the transport of particles through the tube bundle geometry and the sticking of these particles to the wall or layer are covered in the model (figure 9.1).

To reveal the controlling transport mechanism, deposition rates as estimated from the measured decrease in overall heat transfer coefficient are compared with theoretical values for the deposition of sub-micron particles by diffusion and thermophoresis. This comparison revealed that for the conditions as apply at the economiser bundle in the boiler, deposition rates by diffusion and thermophoresis would be at least two orders of magnitude smaller than the estimated deposition rate. Therefore, it is concluded that deposition is mainly controlled by particles for which transport is inertia controlled and transport rates are higher. Comparison of the particle relaxation times with the time scales of the turbulent flow in the bundle revealed that for the particles found in the deposits with sizes up to 30 μm especially the eddy-impaction regime is important. In this regime, the influence of turbulent eddies controls deposition.

The model used to calculate inertia controlled transport uses a flow field computed with the low Reynolds $k-\varepsilon$ model and a Lagrangian particle tracking method. The particle tracking method includes an eddy-interaction model to account for the influence of turbulent eddies. The model compensates for the anisotropy in the boundary layer by the use of a corrected turbulent kinetic energy in this region. Besides, in the model a constraint has been imposed on the eddy lifetime upstream of the cylinder to correct for unrealistically high deposition rates for particles with Stokes numbers below 0.3. With the modified model it was possible to obtain deposition results in agreement with measurements reported in literature.

To model the sticking efficiency for a particle transported to and impacting with the heat exchange surface a theoretical sticking model has been developed. This model assumes that the impact of a particle with a layer consisting of particles can be represented by a two-body collision. In this approach the second body represents the layer and is given a mass proportional to the mass of the incident particle. The ratio between the mass of the second body and that of the incident particle is referred to as the proportionality factor. Based on well-defined impact experiments carried out with a new developed set-up, the approach is found to be a valid one. From the experiments the proportionality factor of two kinds of powdery layers is retrieved. For a layer with particles of the same size as that of the incident ones the proportionality factor is equal to 3.5 while for smaller particles the factor is 2.6.

The developed sticking model has been used in combination with the transport model to simulate deposition rates for an in-line bundle arrangement as is applied in the boiler of a refuse waste incinerator. With the overall model, calculated deposition rates matched the rates as estimated from the measured decrease in heat transfer for the economiser. The agreement between estimated and predicted deposition rates gives confidence to the developed sticking model. With the overall model deposition rates have also been calculated for different tube bundle geometries. Deposition proved to be reduced by decreasing the pitch, using a

staggered tube arrangement in the bundle instead of an in-line arrangement and by applying elliptical tubes in the bundle. Placing a spoiler in front of the bundle augmented deposition showing that the application of a spoiler does not always result in a decrease of deposition. Based on the results of the simulations a new design is proposed with a staggered arrangement of elliptical tubes placed with a slightly reduced transverse pitch. It is shown that for this design, deposition is reduced with 78% for the fourth tube row in the bundle. This reduction makes that the decrease in heat transfer would be limited to about 8% compared to the 27% for the original in-line design with circular tubes.

In conclusion, it is stated that with the developed sticking model in combination with the particle transport model reliable deposition rates can be predicted. The model, therefore, is a suitable tool to optimize the design of a tube-bundle in a heat-recovery boiler. First calculations showed that optimization can indeed yield a significant reduction in deposition rates.

Recommendations

Because in the present transport model some modifications were made to include anisotropy in the boundary layer and to correct for unrealistic deposition rates for small particles, in succeeding studies the application of a different transport model needs to be considered. The use of a large eddy simulation in combination with a particle tracking algorithm seems an attractive option. The large eddy simulation is capable of resolving the flow field in both space and time for the larger and possibly an-isotropic structures. The influence of the smaller structures is accounted for by a sub-grid model. The critical time scale that can implicitly be resolved is a function of the grid size applied. With respect to the transport of particles, it is important that in the simulation all structures that influence the movement of a particle are resolved completely, thus making the use of an eddy-interaction model obsolete.

A point of concern that needs attention in future impact experiments is the influence of electrostatic charges. These charges are believed to have affected the coefficient of restitution in the experiments. It should be looked into how these charges can be neutralized for the glass-glass experiment or the experiment needs to be repeated using more conductive materials. A second item is that, so far, the particles in both the model and the experiments were spherical. It needs to be studied how the shape of the particles influences the impact process and its outcome. Possibly, the influence is limited to a change in the coefficient of restitution and a slightly different proportionality factor. A varying local contact radius over the surface of the particle can change the coefficient of restitution. A smaller local radius could result in the occurrence of plastic deformation at velocities below the limiting elastic velocity as based on the average particle diameter. The proportionality factor could be different because of fewer contact points between particles in the layer as a result of less efficient packing. Test experiments can reveal whether the present model with some changed parameters is adequate to predict the sticking efficiency and rebound velocities for the impact of differently shaped particles.

For a complete prediction of the growth of a fouling layer also the removal mechanism needs to be included (figure 9.1). Deposited particles can be removed from the layer by the shear stress of the fluid flow but also because of the impact of particles. Especially the latter mechanism can have a significant influence, as is shown in one of the impact experiments where one incident particle on average resulted in the removal of approximately 2 bed particles. This ejection of particles is probably related to the amount of kinetic energy of the particle lost over the impact and transferred into the layer. To model the removal rate, this loss of energy needs to be related to the amount of energy required to give a bed particle enough momentum to leave the surface. Because the loss of kinetic energy can be directly retrieved from the two-body model, this model could be expanded to also predict removal rates. The real difficulty is to determine the critical amount of energy to give an ejection. The experimental set-up as developed to validate the two-body approach provides a useful tool to detect this critical amount of energy.

The removal model and its experimental validation would complete the model to predict the growth of a fouling layer by the particulation mechanism. Still, to demonstrate the validity of the overall model an experiment is required in which indeed the growth of a layer due to particulation is measured (bottom item figure 9.1). In figure 9.2 a schematic representation of a possible experimental set-up is given.

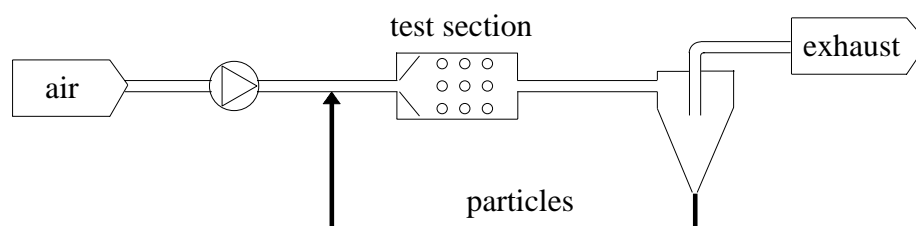


Figure 9.2 Experimental set-up to measure deposition rates

In this set-up an air-stream, loaded with particles, flows around a tube bundle geometry. With a tube diameter of 25 mm, a main stream velocity of 3 m/s and assuming the air to be at room temperature, the Reynolds number based on the tube diameter would become 5000. To cover the eddy-impaction regime of particle transport, under these conditions the particles have to be between approximately 1 and 10 μm yielding Stokes numbers between 0.005 and 0.35, respectively. More experimental considerations, including thermophoresis, are given in [36]. For a reliable experiment, a bundle would require 4 to 5 rows in transverse and 8 rows in longitudinal direction. In that case typical dimensions of a rectangular cross-section would become 30 x 30 cm. With such a cross-section, the required volume flow through the set-up would be 1000 m^3/hr . For the particles in the set-up glass spheres could be used, entered into the set-up by means of screw-feeder. By placing a cyclone behind the test-section, the particles can be separated from the gas-stream and used again after weighing to check mass balances over the system. Initially, the set-up can be used without the test-section to split up a batch of glass beads in

several size fractions. Another option to generate particles of the required sizes could be to use a vibrating orifice particle generator or an ultrasonic atomizer [5].

In the set-up local impact characteristics as impact velocity, rebound velocity and sticking efficiency can be investigated using the camera system as described in section 6.2 and applied in the experiments of this study. It might even be possible to use the system with some modifications to measure the growth rate of the layer locally. Besides a local measurement, also global growth rates need to be measured. An interesting option to accomplish this could be to equip the support of the tubes with electrical strain gauges such that the change in mass of the tube can be monitored during an experiment without having to stop the experiment, remove the tube and weighing it. This global measurement of the growth rate could be combined with a measurement of the shape of the deposited layer using a probe that can be displaced in three dimensions. With the measured global and local growth rates the validity of the overall developed model can be demonstrated.

Bibliography

- [1] Al-Rabghi, O.L., Beirutty, M., Akyurt, M., Najjar, Y., Alp, T., Recovery and utilisation of waste heat, *Heat Recovery Systems & CHP*, vol.13 (5), pp. 463-470, 1993.
- [2] Achenbach, E., Distribution of local pressure and skin friction around a circular cylinder in cross-flow up to $Re = 5 \times 10^6$, *Journal of Fluid Mechanics*, vol. 34 (4), pp. 625-639, 1968.
- [3] Balabani, S., Yianneskis, M., An experimental study of the mean flow and turbulence structure of cross-flow over tube bundles, *Proc. Instn. Mech. Engrs. Part C: Journal of Mechanical Engineering Science*, vol. 210, pp. 317-331, 1996.
- [4] Ballangee, D.W. and Chen, C.F., Experimental determination of the separation point of flow around a cylinder, *Flow; its Measurement*, pp. 419-427, 1971.
- [5] Bailer, F., Etude des differents mecanismes de depot conduisant a l'encrassement particulaire en phase gazeuse des tubes d'exchangeurs de chaleur, *PhD Thesis*, l'Institut National Polytechnique de Grenoble, 1998.
- [6] Beek, M.C., Rindt, C.C.M., Wijers, J.G. and van Steenhoven, A.A., Analysis of fouling in refuse waste incinerators, *Journal of Heat Transfer Engineering*, In press, 2001.
- [7] Beek, M.C., Rindt, C.C.M., Wijers, J.G. and van Steenhoven, A.A., Experiments on the sticking behaviour of particles impacting a fouled surface, *Proc. 1998 AIChE Annual Meeting: Symposium on Advanced Technologies for Particle Processing*, vol. 1, pp. 343-348, Miami Beach USA, 1998.
- [8] Berlemont, A., Desjonqueres P. and Gouesbet G., Particle lagrangian simulation in turbulent flows, *Int. Journal of Multiphase Flow*, vol. 16 (1), pp. 19-34, 1990.
- [9] Bitter, J.G.A., A study of erosion phenomena part I, *Wear*, vol.6, pp. 5-21, 1963.
- [10] Bouris, D. and Bergeles, G., Numerical calculation of the effect of deposit formation on heat exchanger efficiency, *Int. Journal of Heat and Mass Transfer*, vol. 40 (17), pp. 4037-4084, 1997.
- [11] Brookes, G., Reay, D.A., Comparative merits of heat recovery equipment, *Heat Recovery Systems*, vol.2 (5), pp. 419-436, 1982.

- [12] Broom, G.P., Adhesion of particles in fibrous air filters, *Filtration and Separation*, pp. 661-669, 1979.
- [13] Bryers, R.W., Fireside slagging, fouling, and high-temperature corrosion of heat-transfer surfaces due to impurities in steam-raising fuels, *Progress Energy Combustion Science*, vol.22, pp. 29-120, 1996.
- [14] Buckley, D.H., Surface effects in adhesion, friction, wear, and lubrication, *Tribology Series 5*, Elsevier, 1981.
- [15] Coutanceau, M. and Bouard, R., Experimental determination of the main features of the viscous flow in the wake of a circular cylinder in uniform translation. Part 1. Steady flow, *Journal of Fluid Mechanics*, vol.79 (2), pp. 231-256, 1977.
- [16] Davies, R.M., The determination of static and dynamic yield stresses using a steel ball, *Proceedings Royal Society A*, vol. 197, pp. 417-432, 1949.
- [17] Figliola, R.S., Beasley, D.E., *Theory and Design for Mechanical Measurement*, John Wiley and Sons, New York, 1991.
- [18] Fowkes, F.M., Calculation of work of adhesion by pair potential summation, *Journal of Colloid and Interface Science*, vol.28 (3/4), pp. 493-505, 1968.
- [19] Gilman, J.J., Direct measurements of the surface energies of crystals, *Journal of Applied Physics*, vol.31 (12), pp. 2208-2218, 1960.
- [20] Glen, N.F., Howarth J.H., Modelling refuse waste incineration fouling, *2nd National UK Heat Transfer Conference*, vol. 1, pp. 401-420, 1988.
- [21] Gököglu, S.A. and Rosner, D.E., Correlation of thermophoretically-modified small particle diffusional deposition rates in forced convection systems with variable properties, transpiration cooling and/or viscous dissipation, *Int. Journal of Heat and Mass Transfer*, vol.27 (45), pp. 639-646, 1984.
- [22] Goldsmith, W., *Impact*, Edward Arnold Ltd. London, 1960.
- [23] Graham, D.I. and James, P.W., Turbulent dispersion of particles using eddy interaction models, *Int. Journal of Multiphase Flow*, vol.22 (1), pp. 157-175, 1996.
- [24] Hirsch, Ch., *Numerical Computation of Internal and External flows – vol.2 Computational Methods for In-viscid and Viscous Flows*, John Wiley and Sons, New York, 1988.
- [25] Howarth J.H., Seguin, P., Tabaries, F. and Osborn, G., Characterisation of incineration fouling, *ICHEME Symposium Series*, vol. 2, pp. 1029-1036, 1992.
- [26] HVC Alkmaar, *Personal Communication*, 1997.
- [27] Israel, R., Rosner, D.E., Use of a generalized Stokes number to determine the aerodynamic capture efficiency of non-Stokesian particles from a compressible gas flow, *Aerosol Science and Technology*, vol. 2, pp. 45-51, 1983.
- [28] Janna, W.S., *Engineering Heat Transfer*, PWS Publishers, 1986.
- [29] Jiménez, J., The physics of wall turbulence, *Physica A*, vol. 263, pp. 252-262, 1997.
- [30] Johnson, K.L., Kendall, K., Roberts, A.D., Surface energy and the contact of elastic solids, *Proceedings Royal Society A*, vol.324, pp. 301-313, 1971.

- [31] Johnson, K.L., Adhesion at the contact of solids, *Theoretical and Applied Mechanics*, ed.: Koiter, W.T., North-Holland Publishing Company, pp. 133-143, 1976.
- [32] Jones, W.P. and Launder, B.E., The prediction of laminarization with a two-equation model of turbulence, *Int. Journal of Heat and Mass Transfer*, vol. 15, pp. 301-314, 1972.
- [33] Kallio, G.A. and Reeks, M.W., A numerical simulation of particle deposition in turbulent boundary layers, *Int. Journal of Multiphase Flow*, vol. 15 (3), pp. 433-446, 1989.
- [34] Kerekes, Z.E., Bryers, R.W., Sauer, A.R., The influence of heavy metals Pb and Zn on corrosion and deposits in refuse-fired steam generators, *Ash Deposits and Corrosion due to Impurities in Combustion Gases*, ed. R.W. Bryers, Hemisphere Pub. Co., pp. 455-472, 1978.
- [35] Kern, D.Q., Seaton, R.E., A theoretical analysis of thermal surface fouling, *British Chemical Engineering*, vol. 4 (5), pp. 258-262, 1959.
- [36] Kikkert, B.L.J.P., Gas side fouling in waste heat recovery systems, *MSc. Thesis*, WOC-WET 97.002, Eindhoven University of Technology, 1997.
- [37] Konstandopoulos, A.G., Effects of particle inertia on aerosol transport and deposit growth dynamics, *PhD Thesis*, Yale University, 1991.
- [38] Launder, B.E. and Spalding, D.B., The numerical computation of turbulent flows, *Computer Methods in Applied Mechanics and Engineering*, vol. 3, pp. 269-289, 1974.
- [39] Launder, B.E. and Sharma, B.I., Application of the energy-dissipation model of turbulence to the calculation of flow near a spinning disc, *Letters in Heat and Mass Transfer*, vol. 1, pp. 131-138, 1974.
- [40] Leschziner M.A., Launder, B.E., Turbulent flow through tube bank sub-channel, *2nd Ercoftac-IAHR Workshop on Refined Flow Modelling*, Manchester, 1993.
- [41] Lesieur, M., *Turbulence in Fluids*, Kluwer Publishers, Dordrecht, 1990.
- [42] Mavko, G., Mukerji, T., Dvorkin, J., *The Rock Physics Handbook*, Cambridge University Press, 1998.
- [43] Maw, N., Barber J.R., Fawcett, J.N., The role of elastic tangential compliance in oblique impact, *Journal of Lubrication Technology*, vol. 103, pp. 74-80, 1981.
- [44] Mei, R., Adrian R.J. and Hanratty, T.J., Particle dispersion in isotropic turbulence under Stokes drag and Basset force with gravitational settling, *Journal of Fluid Mechanics*, vol. 225, pp. 481-495, 1991.
- [45] Meng, H., On dispersed two phase flow past obstacles, *PhD Thesis*, Eindhoven University of Technology, The Netherlands, 1993.
- [46] Mulhearn, T.O., Tabor, D., Creep and hardness of metals: A physical study, *Journal of the Institute of Metals*, vol. 89, pp. 7-12, 1960.
- [47] Mutsaers, P.L.M., Beerkens, R.G.C., de Waal, H., Fouling of heat exchanger surfaces by dust particles from flue gases of glass furnaces, *Glastechnische Berichte*, vol. 62 (8), pp. 266-272, 1989.

- [48] Ota, T., Aiba, S., Tsurata T., Kaga M., Forced convection heat transfer from an elliptical cylinder of axis ratio 1:2, *Bulletin of the JSME*, vol. 26 (212), pp. 262-267, 1983.
- [49] Ota, T., Nishiyama H., Kominami J., Sato, K., Heat transfer from two elliptic cylinders in tandem arrangement, *Journal of Heat Transfer*, vol. 108, pp. 525-531, 1986.
- [50] Potters and Ballotini, Product information spherical glass beads, 1998.
- [51] Prein, H.J.P.M., Experiments on the sticking behaviour of particles impacting a surface, *M.Sc. Thesis*, WOC-WET 98.035, Eindhoven University of Technology, 1998.
- [52] Raask E., *Mineral Impurities in Coal Combustion*, Hemisphere Publishing Corporation, 1985.
- [53] Rindt, C.C.M., *Personal Communication*, 1999.
- [54] Reed, J., Impact adhesion of particles, *Tribology in Particulate Technology*, ed.: De Barr, A.E., pp. 123-134, IOP Publishing Ltd., 1987.
- [55] Roach, P.E. and Brierly, D.H., The influence of a turbulent free-stream on zero pressure gradient transitional boundary layer development, Part I: test cases T3A and T3B, *Numerical Simulation of Unsteady Flows and Transition to Turbulence*, Proceedings of the Ercoftac workshop held at EPFL, Lausanne, pp. 319-343, 1990.
- [56] Rogers, D.E. and Reed, J., The Adhesion of Particles undergoing an Elastic-Plastic Impact with a Surface, *Journal of Physics D: Applied Physics*, vol. 17, pp. 677-689, 1984.
- [57] Rosner, D.E., Thermal (Soret) diffusion effects on interfacial mass transport rates, *PhysicoChemical Hydrodynamics*, vol.1, pp. 159-185, 1980.
- [58] Schlichting, H., *Boundary Layer Theory*, McGraw-Hill, New York, 1979
- [59] Schelde, *Personal Communication*, 1997.
- [60] SEP, *Annual Report*, 1995.
- [61] Shuen, J-S., Chen, L-D. and Faeth, G.M., Evaluation of a stochastic model of particle dispersion in a turbulent round jet, *AIChE Journal*, vol.29 (1), pp. 167-190, 1983.
- [62] Simons, S.J.R., Seville, J.P.K. and Adams, M.J., An analysis of the rupture energy of pendular liquid bridges, *Chemical Engineering Science*, vol.49 (14), pp. 2331-2339, 1994.
- [63] Smouse, S.M. and Wagoner, C.L., Deposit initiation via thermophoresis: Part 2 - Experimental verification of hypothesis using a simulated superheater tube, *Inorganic Transformations and Ash Deposition during Combustion*, ed. S.A. Benson, pp. 625-638, ASME New York, 1991.
- [64] Son, J.S. and Hanratty, T.J., Velocity gradient at the wall for flow around a cylinder at Reynolds numbers from 5×10^3 to 10^5 , *Journal of Fluid Mechanics*, vol. 35 (2), pp. 353-368, 1969.

- [65] Steadman, E.N, Erickson, T.A., Folkedahl, B.C., Coal and ash characterization: Digital image analysis applications, *Inorganic Transformations and Ash Deposition during Combustion* ed. S.A. Benson, pp. 147-164, 1991.
- [66] Tabor, D., Hardness of Solids, *Endeavour*, vol. 13, pp. 27-32, 1954.
- [67] *VDI-Wärmeatlas*, 7. Auflage, VDI-Verlag, Düsseldorf, 1994.
- [68] VVAV, *Personal Communication*, 1998.
- [69] Wagoner, C.L., Yan, X-X, Deposit initiation via thermophoresis: Part 1 - Insight on deceleration and retention of inertially transported particles, *Inorganic Transformations and Ash Deposition during Combustion*, ed. S.A. Benson, pp. 607-624, ASME New York, 1991.
- [70] Wain, S.E., Livingston, W.R., Sanyal, A. and Williamson, J., Thermal and mechanical properties of boiler slags of relevance to sootblowing, *Inorganic Transformations and Ash Deposition during Combustion*, ed. S.A. Benson, pp. 459-470, ASME New York, 1991.
- [71] Werner, B.T., A physical model of wind-blown sand transport, *PhD Thesis*, California Institute of technology, 1987.
- [72] Wessel, R.A., Wagoner, C.L., Ash deposits- initiating the change from empiricism to generic engineering Part2: Initial results, *Paper 86-JPGC-FACT-7*, ASME, New York, 1986.
- [73] Wung T.S., Niethammer J.E., Chen C.J., Measurements of heat-mass transfer and pressure drop for some non-standard arrays of tubes in cross flow, *Proc. of the Eighth Int. Heat Transfer Conference*, pp. 1041-1066, San Francisco, California, 1986.
- [74] Zhang, G., Bott, T.R., Bemrose, C.R., Reducing particle deposition in air-cooled heat exchangers, *Heat Transfer Engineering*, vol.13 (2), pp. 81-87, 1992.

Appendix A

Deposition rates by diffusion and thermophoresis

For the deposition of particles the deposition rate per unit area ϕ_d can be written as:

$$\phi_d = St C_{p,d} U_\infty \quad (\text{A.1})$$

with St the Stanton number, $C_{p,d}$ the particle concentration in the bulk and U_∞ the main stream velocity. For sub-micron particles, the Stanton number is given by [21]:

$$St = St_o \left(\frac{-B_T}{1 - \exp B_T} \right) \exp(-Da) \quad (\text{A.2})$$

In equation A.2 St_o is the Stanton number that accounts for the mass transfer by convection and Brownian diffusion and is defined by:

$$St_o = \frac{Sh}{Re Sc} \quad (\text{A.3})$$

with $Re = \frac{U_\infty D_{cyl}}{v_g}$ and $Sc = \frac{v_g}{D_b}$ in which D_b represents the Brownian diffusion

coefficient. The Sherwood number in this relation is a function of the Reynolds and Schmidt number and depends on the type of flow and the geometry. For a cylinder in cross-flow the Sherwood number is dependent on the cylinder angle θ [47]:

$$Sh_\theta = C_1 Re^{C_2} Sc^{C_3} \quad (\text{A.4})$$

with the parameters C_1 , C_2 and C_3 related to the angle θ as given in table A.1. The function $(-B_T / (1 - \exp B_T))$ in equation A.2 is a correction term to account for the influence of thermophoresis on the mass transfer inside the Brownian diffusion boundary layer. B_T is dimensionless number that, according to [21], reads:

$$B_T = -\alpha_{T,i,w} (Le_w)^{1/3} \left(\frac{T_{g,b} - T_{g,w}}{T_{g,w}} \right) \quad (\text{A.5})$$

In this relation $\alpha_{T,i,w}$ is the thermal diffusion factor (given in table A.2 for Na_2SO_4 particles) for the particles with size i and Le_w is the Lewis number, both evaluated at the wall temperature. The last term gives the relative gas temperature difference between the bulk (subscript b) and the wall (subscript w).

θ	C_1	C_2	C_3
0°	0.958	0.54	0.36
90°	0.969	0.37	0.33
180°	0.216	0.58	0.05

Table A.1 Dependency of the parameters C_1 , C_2 and C_3 on the cylinder angle θ ($\theta = 0$ corresponds to the upstream stagnation point)

The Lewis number is defined by:

$$Le = \frac{D_{b,i} \rho_g c_{p,g}}{k_g} \quad (\text{A.6})$$

where $c_{p,g}$ and k_g are the heat capacity and conductivity of the gas, respectively and $D_{b,i}$ is the Brownian diffusion coefficient of the particles with size i (given in table A.3 for Na_2SO_4 particles).

$\log(\alpha_{T,i}) -$	$T = 450 \text{ K}$	$T = 473 \text{ K}$	$T = 573 \text{ K}$	$T = 673 \text{ K}$
$d_p = 0.12 \text{ }\mu\text{m}$	2.3	2.9	3.8	4.1
$d_p = 0.24 \text{ }\mu\text{m}$	3.4	4.0	4.8	5.1

Table A.2 Thermal diffusion factor $\alpha_{T,i}$ for Na_2SO_4 particles as a function of temperature and particle diameter [47]

The function $\exp(-Da)$ in equation A.2 is the second correction term to account for the influence of thermophoresis on the mass transfer within the thermal boundary layer outside the thinner Brownian diffusion boundary layer. This correction term is related to the dimensionless Damköhler number that is given by:

$$Da = \alpha_{T,i,b} Le_b \left(\frac{T_{g,b} - T_{g,w}}{T_{g,w}} \right) \quad (\text{A.7})$$

In this relation the subscript refers to the conditions as apply in the bulk.

$D_{b,i} \text{ } 10^{-9} \text{ m}^2/\text{s}$	$T = 450 \text{ K}$	$T = 473 \text{ K}$	$T = 573 \text{ K}$	$T = 673 \text{ K}$
$d_p = 0.12 \text{ }\mu\text{m}$	0.85	0.95	1.19	1.44
$d_p = 0.24 \text{ }\mu\text{m}$	0.28	0.30	0.37	0.44

Table A.3 Brownian diffusion coefficient D_i for Na_2SO_4 particles as a function of temperature and particle diameter [47]

Appendix B

Equation of motion

The transport of a particle from a carrier gas stream to a cylinder placed in cross flow is calculated by solving the equation of motion for a particle. In this appendix the equation of motion is described in its most complete form when excluding the effect of thermophoresis. Besides, for the motion of particles in the flow around a cylinder the simplified equation of motion is discussed. Based on this equation, the particle relaxation time and the Stokes number that are used to characterize the transport regime are derived.

B.1 Equation of motion for a particle

The relations used in this section are, unless stated otherwise, taken from Meng [45]. The equation of motion for a particle is given by:

$$m_p \frac{d\vec{u}_p}{dt} = \sum \vec{F}_i \quad (\text{B.1})$$

where \vec{F}_i represents all the possible forces that can act on a particle. For a spherical particle the following forces can be distinguished.

Drag Force

The first force is the steady state or Stokes drag force that can be written as:

$$\vec{F}_D = \frac{1}{8} \pi d_p^2 \rho_g C_D |\vec{u}_g - \vec{u}_p| (\vec{u}_g - \vec{u}_p) \quad (\text{B.2})$$

with C_D the drag coefficient. This coefficient is given with an empirical relation that is a function of the local particle Reynolds number. This Reynolds number is based on the slip-velocity between particle and fluid as given by:

$$Re_p' = \frac{\rho_g |\vec{u}_g - \vec{u}_p| d_p}{\mu_g} \quad (\text{B.3}).$$

For Reynolds numbers lower than 200 the drag coefficient is given by [8]:

$$C_D = 24 \frac{(1 + 0.15 Re_p^{0.687})}{Re_p} \quad (B.4)$$

For Reynolds numbers smaller than 0.01 the drag factor is usually taken as $24/Re_p$.

Added Mass Force

The added mass force accounts for the force a particle experiences when it accelerates. For an accelerating particle also the surrounding fluid needs to be accelerated which results in a force on the particle in the direction opposite to the acceleration. The added mass force is given by:

$$\vec{F}_{AM} = -C_{AM} \rho_g \frac{\pi}{6} d_p^3 \left(\frac{d\vec{u}_p}{dt} - \frac{d\vec{u}_g}{dt} \right) \quad (B.5)$$

with C_{AM} equal to 0.5.

Basset History Force

The Basset history force accounts for the unsteady effects on the drag of a sphere. This force is related to the history of the fluctuations in the relative velocity and reads:

$$\vec{F}_{BH} = -\frac{3}{2} d_p^2 C_{BH} \sqrt{\pi \rho_g \mu_g} \int_{t_0}^t \left(\frac{d\vec{u}_p}{dt} - \frac{d\vec{u}_g}{dt} \right) \frac{d\tau}{\sqrt{t-\tau}} \quad (B.6)$$

with C_{BH} equal to 1.

Pressure Gradient

The Pressure Gradient force accounts for the force a fluid or particle volume experiences as a result of the pressure gradient present in the fluid flow. This force is given by:

$$\vec{F}_{PG} = \rho_g \frac{\pi}{6} d_p^3 \left(\frac{d\vec{u}_g}{dt} - \frac{\mu_g}{\rho_g} \nabla \vec{u}_g \right) \quad (B.7)$$

Lift Force

For non-rotating particles the only contribution to the lift force results from the presence of a velocity gradient in the ambient flow. The shear lift force for a particle moving in a 2-D plane defined by the x and y-direction is given by:

$$\vec{F}_L = C_L \frac{\rho_g d_p^2}{4} \sqrt{\kappa \frac{\mu_g}{\rho_g}} \left(\vec{z} \times (\vec{u}_p - \vec{u}_g) \right) \quad (B.8)$$

with κ the rate of strain defined by $|du_i/dx_j|$ and C_L equal to 81.2.

Buoyancy Force

The buoyancy force is given by:

$$\vec{F}_g = (\rho_p - \rho_g) \frac{\pi}{6} d_p^3 \vec{g} \quad (\text{B.9})$$

with \vec{g} the acceleration vector by gravitation.

B.2 Simplified equation of motion

With respect to the general form of the equation of motion as described in the previous section some simplifications can be made for the motion of solid particles with a diameter smaller than 100 μm in a gaseous medium. The buoyancy force is not taken into account because the numerical computations will be carried out in a 2-D plane with the direction of gravitation perpendicular to it. The influence of the Basset history and the Added Mass forces on the transport of particles in turbulent flows is investigated in Mei *et al* [44]. After making the equation of motion, including the Basset and the Added Mass terms, dimensionless the Basset term is found to be a factor of ε_B smaller than the Stokes drag term, where ε_B is given by:

$$\varepsilon_B^2 = \frac{9}{4} \frac{\rho_g}{\rho_p} \text{Stk} \quad (\text{B.10})$$

For solid particles in a gas the ratio of densities is very large and ε_B becomes much smaller than 1 and the influence of the Basset term can be neglected. The same holds for the Added Mass term which was shown to be a factor of ε_B^2 smaller than the Stokes drag term. Also, the pressure gradient force and the lift force are not taken into account. According to Bailer [5], the pressure gradient force can be ignored when the density of the particle is much larger than the density of the fluid. Also, for the particle sizes considered in this study, the lift force due to shear is small compared to the drag force and can also be assumed negligible. With these simplifications, the equation of motion applied in the numerical calculations is given by:

$$m_p \frac{d\vec{u}_p}{dt} = \vec{F}_D \quad (\text{B.11})$$

B.3 Particle relaxation time and Stokes number

The particle relaxation time and the Stokes number can be used to characterize the transport regime of particles from the carrier gas stream to the cylinder. Both parameters are found when assuming that the local particle Reynolds number Re_p is

much smaller than 1. In that case, when substituting $24/Re_p'$ for the drag coefficient in equation B.2 and substituting the derived equation for the drag force in equation B.11, after some rewriting the equation of motion becomes:

$$\frac{d\vec{u}_p}{dt} = \frac{1}{\tau_p} (\vec{u}_g - \vec{u}_p) \quad (\text{B.12})$$

Here τ_p is the particle relaxation time being the characteristic time scale for a particle to respond to a change in fluid flow which is given by:

$$\tau_p = \frac{\rho_p d_p^2}{18 \mu_g} \quad (\text{B.13})$$

Equation B.12 is made dimensionless using the main stream velocity U_∞ and the tube radius $\frac{1}{2} D_{tube}$. The dimensionless equation of motion then becomes:

$$\frac{d\vec{u}_p}{dt} = \frac{1}{Stk} (\vec{u}_g - \vec{u}_p) \quad (\text{B.14})$$

with Stk the Stokes number that reads:

$$Stk = \frac{U_\infty \tau_p}{\frac{1}{2} D_{tube}} = \frac{\rho_p d_p^2 U_\infty}{9 \mu_g D_{tube}} \quad (\text{B.15})$$

The Stokes number represents the ratio between the particle relaxation time and the time scale imposed by the flow around the cylinder. It is noted that the velocities in equation B.14 are dimensionless quantities.

As treated in Israel [27], the equation of motion given by equation B.14 was solved using a potential flow field approximation to yield the collection efficiency for a cylinder in cross flow. For particles with a Stokes number below 0.125 the collection efficiency was found to be zero, meaning that none of the particles in the main stream is able to reach the cylinder. This Stokes number of 0.125 is referred to as the critical Stokes number for inertia-controlled transport.

Appendix C

Calibration of length scale parameter C_l

In section 4.4 the length scale parameter C_l is introduced to correct for a discrepancy between deposition rates as measured and calculated by Bailer [5] and the deposition rates calculated in this study using the eddy-interaction model of Shuen [61]. The length scale parameter limits the maximum length scale used in the eddy-interaction model to determine the eddy lifetime. The maximum length scale is assumed to be equal to the length scale parameter C_l times the distance with the tube wall.

Using different values for the length scale parameter C_l , the distribution of deposition rates over the cylinder surface as expressed with the Stanton number is calculated and given in figure C.1.

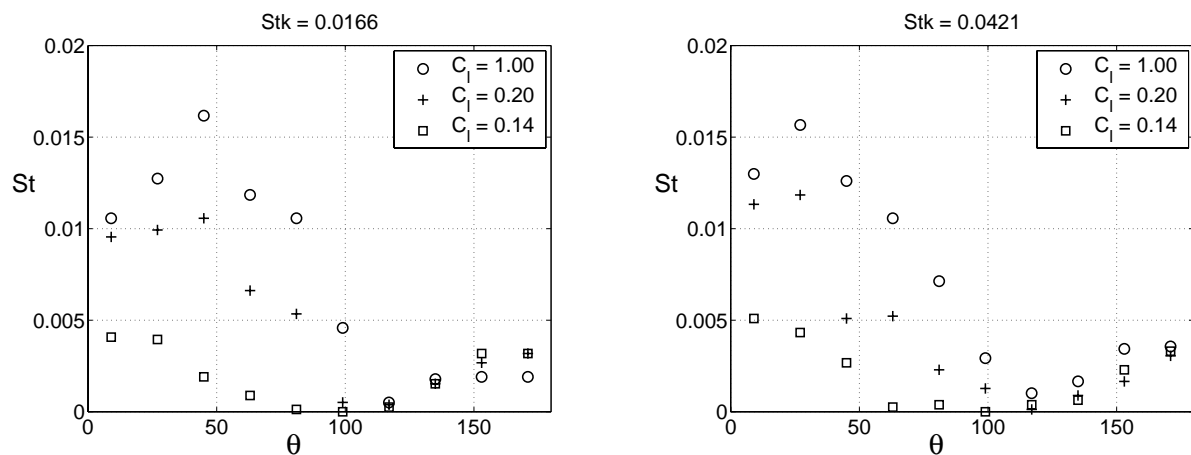


Figure C.1 Influence of length scale parameter C_l on local deposition rates as expressed with Stanton number as a function of the cylinder angle θ . ($Re=1900$, $Stk = 0.0166$ (left) and 0.0421 (right)).

Reducing the length scale parameter results in a decrease of the mean deposition rate at the front of the cylinder but also the distribution at the front is altered. With a length scale parameter of unity, depending on the Stokes number

maximum deposition occurs at about 20 to 40° from the upstream stagnation point. For a smaller length scale parameter this angle shifts to the upstream stagnation point as is also expected on basis of the results reported in Bailer [5] and other studies. The distribution at the rear of the cylinder is hardly affected by application of the length scale correction.

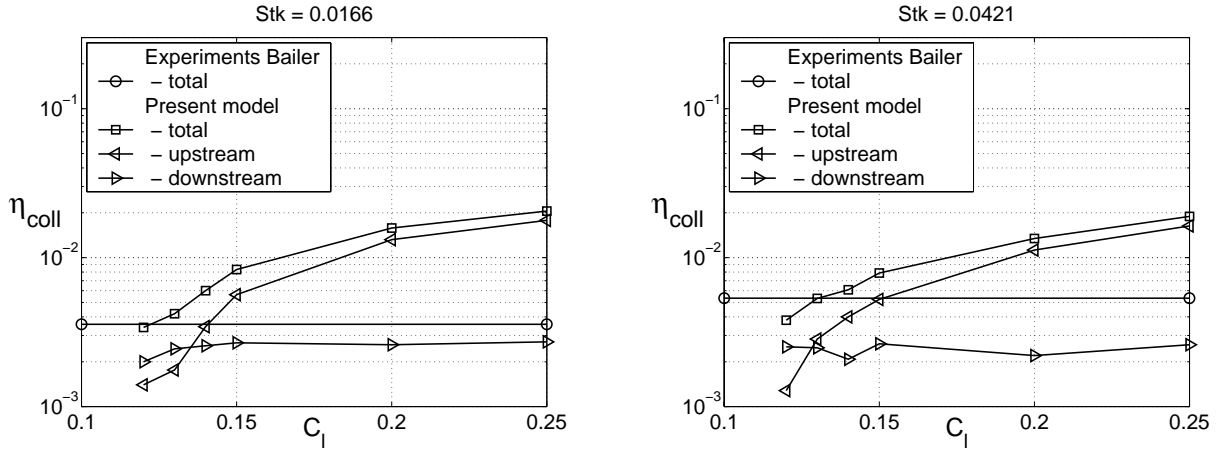


Figure C.2 Collection efficiency as a function of length scale parameter C_l for particles depositing on a cylinder in cross-flow at $Re=1900$.

To calibrate the value to be used for the length scale parameter C_l , deposition rates are calculated for different values of C_l . The deposition rates that are expressed using the collection efficiency are compared with the experimental results of Bailer. The measured values give the total collection efficiency, upstream and downstream, for particles depositing on a cylinder in cross-flow with a Stokes number of 0.0166 and 0.0421, respectively. In the experiments, it was found that for both Stokes numbers the deposition rate was higher for the upstream than for the downstream-side. The calculated collection efficiencies: total, upstream and downstream are given in figure C.2 as a function of the length scale parameter C_l and the Stokes number. The value to be used in the particle transport model is chosen equal to 0.14. This value is chosen such that the difference between the calculated total collection efficiency and the experiments of Bailer are minimal and that for both Stokes numbers the collection efficiency is higher for the upstream than for the downstream side.

Appendix D

Impact of two bodies

In this appendix the relations describing the impact of two bodies will be described. In the first section the equations are given for an impact of two bodies in plane motion. This derivation is based on the theory of colliding solids as found in Goldsmith [22]. In the second section, the relations are extended to cover the impact of two bodies in a three-dimensional motion.

D.1 Impact of two-bodies in plane motion

Figure 5.4 shows the collision between two bodies with masses m_1 and m_2 and radii R_1 and R_2 .

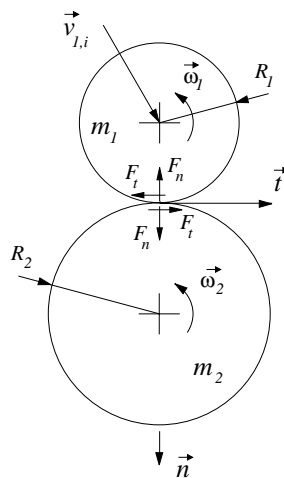


Figure D.1 Definitions two-body collision

In the collision the first body impacts the second body which is assumed to have no initial linear velocity or rotation. The impact of these two bodies can be described using the linear and angular impulse momentum laws for a body k , as given by:

$$\Delta(m_k \vec{v}_k) = m_k \vec{v}_k - m_k \vec{v}_{k,i} = \int_0^t \vec{F} dt \equiv \vec{P} \quad (\text{D.1})$$

$$\Delta(I_k \vec{\omega}_k) = I_k \vec{\omega}_k - I_k \vec{\omega}_{k,i} = \int_0^t \vec{F} \times \vec{r} dt \quad (\text{D.2})$$

with I_k the moment of inertia of a body around the axis of rotation. For a sphere the moment of inertia is given by:

$$I_k = \frac{2}{5} m_k R_k^2 \quad (\text{D.3})$$

For the collision the momentum equations are formulated for the directions normal and tangential to the local contact surface. For the two bodies in plane motion the linear impulse momentum equations yield:

$$\begin{aligned} m_1 (v_{1,t} - v_{1i,t}) &= -P_t, & m_2 (v_{2,t} - v_{2i,t}) &= P_t \\ m_1 (v_{1,n} - v_{1i,n}) &= -P_n, & m_2 (v_{2,n} - v_{2i,n}) &= P_n \end{aligned} \quad (\text{D.4})$$

and the linear momentum equations read:

$$I_1 (\omega_1 - \omega_{1i}) = -P_t R_1, \quad I_2 (\omega_2 - \omega_{2i}) = -P_t R_2 \quad (\text{D.5})$$

During the impact the centres of the two bodies approach one another with the relative compression velocity v_n :

$$v_n = v_{1,n} - v_{2,n} \quad (\text{D.6})$$

and slide on one another with the relative slip-velocity v_s :

$$v_s = v_{1,t} + R_1 \omega_1 - (v_{2,t} - R_2 \omega_2) \quad (\text{D.7})$$

Substituting the momentum equations D.4 and D.5 in equations D.6 and D.7, the compression and slip-velocities become:

$$v_n = v_{i,n} - P_n \left\{ \frac{m_1 + m_2}{m_1 m_2} \right\} \quad (\text{D.8})$$

and

$$v_s = v_{i,s} - P_t \left\{ \frac{2}{7} \frac{m_1 + m_2}{m_1 m_2} \right\} \quad (\text{D.9})$$

respectively, where $v_{i,n}$ represents the initial compression velocity and $v_{i,s}$ the initial slip-velocity as defined by:

$$v_{i,n} = v_{1i,n} \quad (\text{D.10})$$

and

$$v_{i,s} = v_{1i,t} + R_1 \omega_{1i} \quad (\text{D.11})$$

respectively. This is under the assumption of the second body to have no initial velocity or rotation.

Because in most collisions some part of the kinetic energy of the impacting bodies is lost, the coefficient of restitution e is introduced to describe the degree of plasticity. The coefficient is a function of the materials involved in the impact and is defined as the ratio of the final to initial relative velocity in normal direction. This ratio is equal to the ratio in impulses applied during the approach and the restitution phase. The approach phase starts upon first contact of the bodies and ends when the relative velocity in normal direction becomes zero. The approach phase (subscript a) is followed by the restitution phase (subscript r) that ends when the bodies no longer touch. The impulse applied in the approach phase is found from equation D.8 for a zero relative velocity in normal direction and is given by:

$$P_{a,n} = \frac{m_1 m_2}{m_1 + m_2} v_{i,n} \quad (\text{D.12})$$

The total impulse applied in normal direction is then found by applying the definition for the coefficient of restitution given by:

$$e = \frac{(v_{2r,n} - v_{1r,n})}{(v_{1i,n} - v_{2i,n})} = \frac{P_{r,n}}{P_{a,n}} \quad (\text{D.13})$$

to yield:

$$P_{tot,n} = P_{a,n} + P_{r,n} = (1+e) \frac{m_1 m_2}{m_1 + m_2} v_{i,n} \quad (\text{D.14})$$

With the total impulse applied over the impact in normal direction, the rebound velocity in normal direction can be found from equation D.4 and is given by:

$$v_{1r,n} = v_{1i,n} - (1+e) \frac{m_2}{m_1 + m_2} v_{i,n} \quad (\text{D.15})$$

By using the same approach, also the post-impact velocity in normal direction of the second body can be found and this velocity is given by:

$$v_{2r,n} = v_{2i,n} - (1+e) \frac{m_1}{m_1 + m_2} v_{i,n} \quad (\text{D.16})$$

Substituting equation D.15 and equation D.16 in the definition for the change in kinetic energy over the impact (given in the equation below), the change in kinetic energy becomes:

$$\Delta Q_k \equiv \frac{1}{2} \sum_k m_k v_{kr,n}^2 - \frac{1}{2} \sum_k m_k v_{ki,n}^2 = \frac{1}{2} \left(\frac{m_1 m_2}{m_1 + m_2} \right) (1 - e^2) v_{i,n}^2 \quad (\text{D.17})$$

So if e equals 1 (no plasticity) ΔQ_k equals zero, as expected.

The tangential rebound velocity depends on the magnitude of the impulse applied in tangential direction. This impulse results from the friction force that exists

at the contact point and which is present as long as the slip-velocity is non-zero. Hence, the relation between the tangential and normal impulses become:

$$P_t = f P_n \quad (\text{D.18})$$

with f the friction coefficient, the second parameter in the model that is a function of the materials involved in the impact. The tangential impulse required to bring the slip-velocity to zero over the impact and to change the contact mode from sliding to rolling is found from equation D.9 and reads:

$$P_{t,v_s=0} = \frac{2}{7} \frac{m_1 m_2}{m_1 + m_2} v_{i,s} \quad (\text{D.19})$$

From the required tangential impulse to bring the slip-velocity to zero, the minimum friction coefficient required is given by:

$$f_{v_s=0} = \frac{P_{t,v_s=0}}{P_{tot,n}} = \frac{\frac{2}{7} v_{i,s}}{(1+e) v_{i,n}} \quad (\text{D.20})$$

In case the real friction coefficient in the impact is larger than the minimum required friction coefficient the slip-velocity is brought to zero and the particles no longer slide over one another, but start rolling. The rebound velocity in tangential direction and the angular velocity of the rebounding particle are then found by substituting equation D.19 in the linear and angular impulse momentum equations given in equations D.4 and D.5 and read:

$$v_{1r,t} = v_{1i,t} - \frac{2}{7} \frac{m_2}{m_1 + m_2} v_{i,s} \quad (\text{D.21})$$

$$\omega_{1r} = \omega_{1i} - \frac{5}{7} \frac{m_2}{m_1 + m_2} \frac{v_{i,s}}{R_1} \quad (\text{D.22})$$

However, if the friction coefficient is smaller than the minimum required friction coefficient the particles in the impact will remain sliding and the rebound velocities become:

$$v_{1r,t} = v_{1i,t} - f (1+e) \frac{m_2}{m_1 + m_2} v_{i,n} \quad (\text{D.23})$$

$$\omega_{1r} = \omega_{1i} - \frac{5}{2} f (1+e) \frac{m_2}{m_1 + m_2} \frac{v_{i,n}}{R_1} \quad (\text{D.24})$$

D.2 Impact of two-bodies in a three-dimensional motion

In the previous section the impact of the two-bodies was defined in a 2-D plane. The relations derived slightly change in case the motion contains a third component.

For the 3-D case the impact is again defined by the normal and tangential directions to the local impact surface as defined in figure D.2.

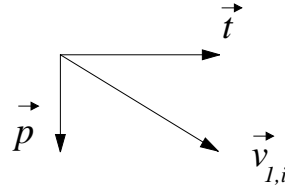


Figure D.2 Slip-velocity defined in the local contact plane

For the impact of two spheres, the normal direction is defined by the line connecting their centres. The tangential direction is located in the local contact plane perpendicularly to the normal. This tangential direction is chosen such that:

$$\vec{v}_{li,t} = \vec{v}_{li} - \vec{v}_{li,n} \quad (\text{D.25})$$

with

$$\vec{v}_{li,n} = (\vec{v}_{li} \cdot \vec{n}) \vec{n} \quad (\text{D.26})$$

However, because the slip-velocity in the local contact plane also includes a possible contribution of the angular velocities of the spheres a third direction \vec{p} is required to define the 3-D coordinate-system. In the local contact plane as defined in figure D.2, the slip-velocity becomes:

$$\vec{v}_{i,s} = \vec{v}_{i,t} + R_1 (\vec{\omega}_{li} \times \vec{n}) \quad (\text{D.27})$$

when again assuming that the second body has no initial velocity or rotation.

The total impulse applied over the impact in normal direction is equal to the one defined in equation D.14 and results in the following relation for the rebound velocity:

$$\vec{v}_{1r,n} = \vec{v}_{1i,n} - (1+e) \frac{m_2}{m_1+m_2} \vec{v}_{1i,n} \quad (\text{D.28})$$

The tangential rebound velocity depends on the initial slip-velocity and the magnitude of the applied impulse in tangential direction. Because the tangential impulse applied is directed opposite to the slip-velocity, the impact velocity in tangential direction is modified in both magnitude and direction. The direction of the rebound velocity in the local contact plane is denoted by \vec{t}' . Comparable to the analysis for the two bodies in plane motion, the impact can end with the bodies sliding, or rolling on one another. The criterion for the change from sliding to rolling is formulated in terms of the minimum required friction coefficient as defined in equation D.20.

In case the real friction coefficient in the impact is larger than the minimum required friction coefficient the slip-velocity is brought to zero and the particles no longer slide over one another, but start rolling. The rebound velocity in tangential direction and the angular velocity of the rebounding particle are then given by:

$$\vec{v}_{1r,t'} = \vec{v}_{1i,t} - \frac{2}{7} \frac{m_2}{m_1 + m_2} \vec{v}_{i,s} \quad (\text{D.29})$$

$$\vec{\omega}_{1r} = \vec{\omega}_{1i} + \frac{5}{7} \frac{m_2}{m_1 + m_2} \frac{(\vec{v}_{i,s} \times \vec{n})}{R_1} \quad (\text{D.30})$$

However, if the friction coefficient is smaller than the minimum required friction coefficient the particles in the impact will remain sliding and the rebound velocities become:

$$\vec{v}_{1r,t'} = \vec{v}_{1i,t} - f(1+e) \frac{m_2}{m_1 + m_2} \frac{|\vec{v}_{1i,n}|}{|\vec{v}_{i,s}|} \vec{v}_{i,s} \quad (\text{D.31})$$

$$\vec{\omega}_{1r} = \vec{\omega}_{1i} + \frac{5}{2} f(1+e) \frac{m_2}{m_1 + m_2} \frac{|\vec{v}_{1i,n}|}{|\vec{v}_{i,s}|} \frac{(\vec{v}_{i,s} \times \vec{n})}{R_1} \quad (\text{D.32})$$

Appendix E

Model of Rogers and Reed

In this appendix the contact energies required for the model of Rogers and Reed are derived. Rogers and Reed developed a model that describes the elastic-plastic impact of a particle with mass m^* and radius R^* on a surface with infinite radius and mass.

E.1 Elastic impact

In the elastically deformed contact area between the particle and the surface an Hertzian distribution of stresses is assumed. The pressure distribution, as shown in figure E.1, exhibits a maximum pressure p_{max} on the centre-line going to zero at the outside of the contact area.

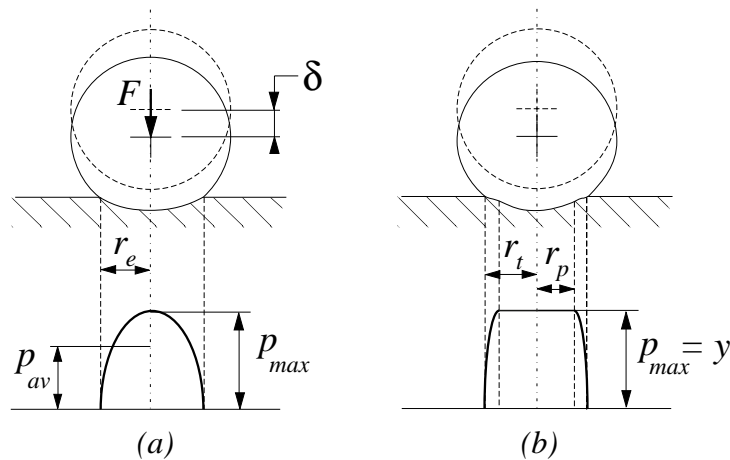


Figure E.1 Pressure distribution in the contact area for respectively a pure elastic impact, figure (a), and an elastic-plastic impact, figure (b).

For an Hertzian pressure distribution in the elastic contact between two bodies, the average stress in the contact area is two thirds of the maximum stress, which results in the following contact load:

$$F = \frac{2}{3} \pi r_e^2 p_{max} \quad (\text{E.1})$$

If the contact force is such that the maximum pressure does not exceed the elastic load limit y , the contact is only elastically deformed and the Hertz equations apply. In the Hertz equations the contact radius is given with:

$$r_e^3 = \frac{R^* F}{\frac{4}{3} E^*} \quad (\text{E.2})$$

with E^* the material parameter defined by:

$$\frac{1}{E^*} = \frac{1 - \nu_1^2}{E_1} + \frac{1 - \nu_2^2}{E_2} \quad (\text{E.3})$$

where ν_i is the Poisson ratio and E_i the Young's modulus of material i . The distance δ over which the centres of the two bodies approach each other is in the Hertz equations given by:

$$\delta = \frac{r_e^2}{R^*} = \frac{F^{2/3}}{\left(\frac{4}{3} E^*\right)^{2/3} \left(R^*\right)^{1/3}} \quad (\text{E.4})$$

The elastic energy stored in the contact area is given by the integral of the contact force F over the distance between the limits 0 and the distance δ and can be written as:

$$Q_e = \int_0^{\delta} F d\delta = \frac{2}{5} \frac{F^{5/3}}{\left(\frac{4}{3} E^*\right)^{2/3} \left(R^*\right)^{1/3}} \quad (\text{E.5})$$

The elastic energy stored in the contact can also be written in terms of the maximum pressure by substituting equation E.2 in equation E.1 to give a relation for the contact load F as a function of the maximum pressure, the radius R^* and the material parameter E^* . Substituting this relation in equation E.5 yields:

$$Q_e = \frac{2}{5} \left(\frac{2}{3}\right)^5 \frac{\pi^5 R^{*3} P_{\max}^5}{\left(\frac{4}{3} E^*\right)^4} \quad (\text{E.6})$$

Because in the impact a mutual surface is formed with a lower energy level than two separate surfaces, a surface energy term is required in the model of Rogers and Reed. The surface energy $Q_{A,a}$ is defined with:

$$Q_{A,a} = \Gamma \pi r_e^2 \quad (\text{E.7})$$

with Γ the work of adhesion (section E.3). For an elastic impact also the surface energy can be written in terms of the maximum contact pressure. Substituting equation E.1 in equation E.2 and subsequently substituting the obtained relation for the contact radius in equation E.7 results in the following relation for the surface energy:

$$Q_{A,a} = \Gamma \frac{\pi^3 R^{*2} \left(\frac{2}{3} p_{\max}\right)^2}{\left(\frac{4}{3} E^*\right)^2} \quad (\text{E.8})$$

E.2 Elastic – plastic impact

If the maximum contact pressure exceeds the elastic load limit, plastic deformation starts to occur in the contact. In the limiting case, where the maximum pressure is equal to the elastic load limit, the contact load is defined as F_{el} and is found by substituting y for the maximum pressure in equation E.1 and substituting this relation in equation E.2. The contact load F_{el} is then found to be:

$$F_{el} = \left(\frac{2}{3}\pi\right)^3 \frac{R^{*2}}{\left(\frac{4}{3}E^*\right)^2} y^3 \quad (\text{E.9})$$

The distance of approach h_{el} , the contact radius r_{el} and the elastic energy Q_{el} in the limiting case are found by substituting the above relation in equations E.4 , E.2 and E.5, respectively, yielding:

$$h_{el} \equiv \delta (F = F_{el}) = \left(\frac{2}{3}\pi\right)^2 \frac{R^*}{\left(\frac{4}{3}E^*\right)^2} y^2 \quad (\text{E.10})$$

$$r_{el} = \frac{\pi R^*}{2 E^*} y \quad (\text{E.11})$$

$$Q_{el} = \frac{2}{5} \left(\frac{2}{3}\right)^5 \frac{\pi^5 R^{*3}}{\left(\frac{4}{3}E^*\right)^4} y^5 \quad (\text{E.12})$$

If the pressure in the contact exceeds the elastic load limit, the contact area around the centre-line is plastically deformed over an area with radius r_p . This area is surrounded by an annular area of only elastic deformations and the total deformed area is given by:

$$r_t^2 = r_{el}^2 + r_p^2 \quad (\text{E.13})$$

The derivation of energy dissipated in plastic flow is based on the work of Bitter [9] in which it is presumed that only in one of the two contacting bodies plastic deformations take place and that in both the bodies elastic deformations occur. Also, it is assumed that no work-hardening effects occur, so that the elastic load limit remains constant. If the total area of deformation is small compared to the cross-section of the sphere with radius R^* the total area of deformation can be approximated with

$$\pi r_t^2 \approx 2\pi R^* (H + h_{el}) \quad (\text{E.14})$$

with H the remnant deformation that can also be written as $\delta-h_{el}$. Given this relation, it can be shown that the area of only elastic deformation stays constant during plastic flow. When assuming that also the pressure distribution remains the same, the elastic energy stored in the annulus is constant and equal to Q_{el} .

In addition, the total contact load can also be written as the sum of a constant elastic and a plastic component as given by:

$$F = F_{el} + F_p \quad (\text{E.15})$$

where F_p reads:

$$F_p = \pi r_p^2 y \approx 2\pi R^* H y \quad (\text{E.16})$$

Using this approximation, the in the contact dissipated energy required to give the contact a remnant indentation H , can be calculated from:

$$Q_p = \int_0^H F_p dH \approx \frac{(F - F_{el})^2}{4\pi R^* y} \quad (\text{E.17})$$

The area in which plastic flow occurs is also subject to elastic deformations. This gives rise to an extra term Q_{pe} for the total elastic energy stored in contact that is recovered when the contact load is released, given by:

$$Q_{pe} = \frac{1}{2} h_{el} (F - F_{el}) \quad (\text{E.18})$$

Using the definition for the surface energy given in equation E.7 the surface energy in the approach phase of an elastic-plastic impact can be written as:

$$Q_{A,a} = \Gamma \pi \left(r_{el}^2 + \frac{F - F_{el}}{\pi y} \right) \quad (\text{E.19})$$

in which use is made of the relation for the radius of the total deformed area as given by:

$$r_t = \sqrt{r_{el}^2 + \frac{F - F_{el}}{\pi y}} \quad (\text{E.20})$$

E.3 Adhesion energy

As the particle approaches the impact surface it is attracted towards it because of the interaction of the molecules located near the surface of both bodies. The net effect of this interaction can be described using the work of adhesion, Fowkes [18]. The work of adhesion is given by:

$$W_A = \sum_k W_A^k \quad (\text{E.21})$$

with the index k referring to the different intermolecular interactions as the London dispersion forces, dipole-dipole interactions and electrostatic interactions. For most materials, the work of adhesion is solely determined by the dispersion forces. However, for ionic solids like the crystalline materials encountered in the deposits on the boiler tubes the electrostatic interactions predominate. In case one of the interactions predominates over the rest of the interactions, the work of adhesion can be determined from the surface free energy, γ , of the bodies i and j as given by:

$$W_A = 2\sqrt{\gamma_i \gamma_j} \equiv \Gamma \quad (\text{E.22})$$

To predict the adhesion energy required to separate the surfaces $Q_{A,r}$ use is made of the Johnson, Kendall and Roberts (JKR) adhesion model as given in Johnson [30,31].

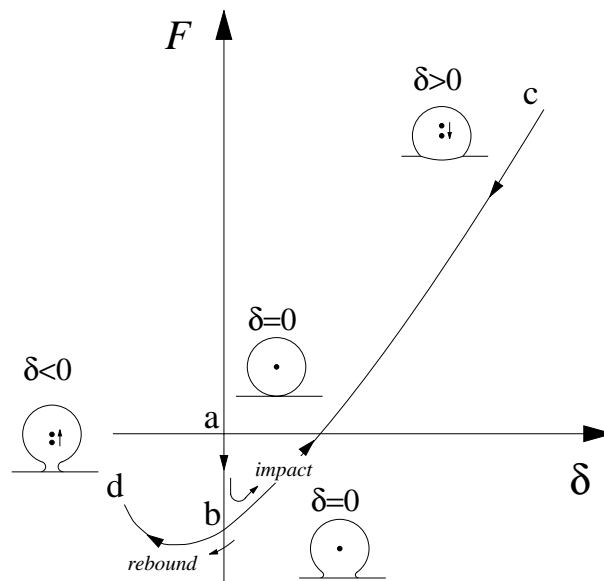


Figure E.2 Schematic representation of the contact force developing in the elastic impact of a particle on a surface (Johnson [31])

The underlying process for the JKR theory, schematically given in figure E.2, starts when upon contact the particle is attracted towards the surface by a negative force (a-b). By virtue of the adhesion force the surface area grows with δ remaining zero. Because of deformations in the contact the force in the contact changes to repulsive to reach a maximum at the end of the approach phase (c). During the rebound the force follows the same curve as in the approach phase until (b). However, the separation of the particles has to be continued up to a negative distance δ_c (d) before the particles are definitely separated. Because of this hysteresis there is net amount of energy which is lost and which (by integrating the force displacement relation as given in Johnson [31] between 0 and $-\delta_c$) is found to be:

$$Q_{A,r} - Q_{A,a} = 7.09 \left(\frac{R_c^4 \Gamma^5}{E^{*2}} \right)^{1/3} \quad (\text{E.23})$$

with R_c the appropriate contact radius. For an elastic impact R_c is equal to R^* , where for an elastic-plastic impact it is different due to plastic flow in the approach phase.

To determine the new R_c after plastic flow has resulted in a remnant deformation, it is assumed that the deformations in the contact remain elastic during the restitution phase. The assumption is valid because Rogers and Reed showed that, based on measurements, the energy dissipated in plastic flow during the restitution phase is negligible. Because only elastic deformations are assumed to occur during the restitution phase, the relevant contact radius can be found using the Hertz equations:

$$R_c = \frac{4/3 E^* r_t^3}{F} \quad (\text{E.24})$$

with F and r_t the contact force and radius at the end of the approach phase.

Appendix F

Experimental set-up

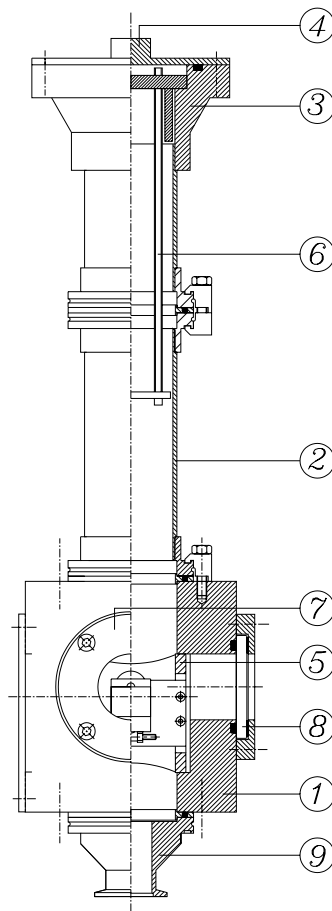


Figure F.1 Composition of the experimental set-up

In figure F.1 a composition drawing is given of the experimental set-up. The vacuum chamber (1) is the centre of the set-up. On the vacuum chamber the vacuum column (2) is mounted which consists of modular pipe segments that can be connected to one another by flanges glued to the segments. The column is closed by the head end of the column (3) and the head end's cover (4). The vacuum chamber is vacuumed from below through the pump's connection flange (9).

In the head end of the column the fall mechanism (6) is installed. The fall mechanism consists of a plate holder which can be varied in height by means of spindle and two guiding rods. An aluminium plate with particles at the bottom is

inserted in the plate holder after which an electromagnet is installed above the plate. Two metal wires, cast in holes made in the head end's cover (4), realize the electrical connections to the electromagnet. By means of the electromagnet a steel ball is dropped on the aluminium plate thereby releasing the particles. The height from which the particles fall can be varied by the earlier described spindle and by installing additional column segments (2).

In a cylindrical cavity in the vacuum chamber an object table (5) carrying the surface on which the particles impact is installed. Because the impact of these particles is recorded using a camera system, the set-up is made optical accessible by two windows (8) and (7). The window at the front is used for the camera where the window at the right is used for the light-sheet.

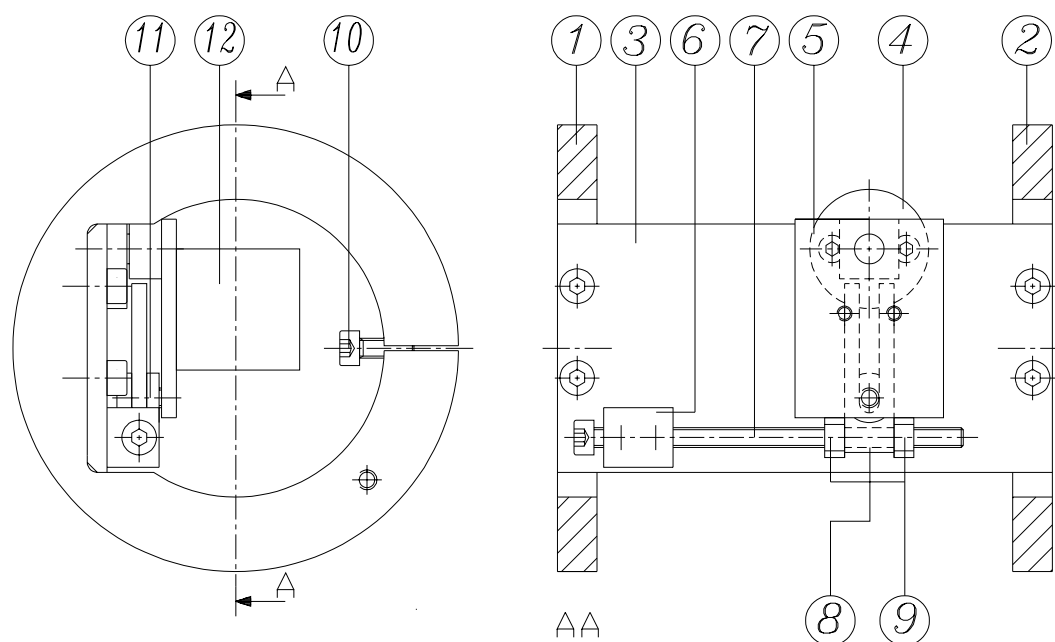


Figure F.2 Composition of the object table

In figure F.2 a more detailed drawing of the object table is given. The object table consists of two circular disks (1, 2) which fit the cylindrical cavity such that they are able to slide in. A screw (10) can be tightened to clamp the first disk such that the position of the object table in the cavity is fixed. Between the two cylindrical disks a flat base plate (3) is positioned. The flat base plate serves to mount the system which carries the object surface and makes the rotation for the surface possible. On the base plate a turning-point (4) is mounted. On the shaft of this turning-point a part (5) is mounted on which different object surfaces (12) can be installed, the object plate. The angle of impact is fixed by use of a spindle (7). A block with inside thread (6) supports the spindle. By means of the spindle a fork (8) (fixed in position by two nuts (9)) is translated parallel to the top-side of the base plate. Because of this movement, a rod (fixed on one end to the object plate) translates in vertical direction thereby creating a rotation around the turning point. The maximum achievable impact angle is around 70° .

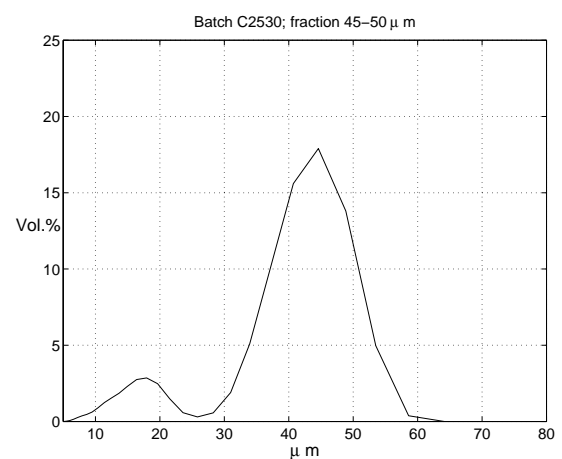
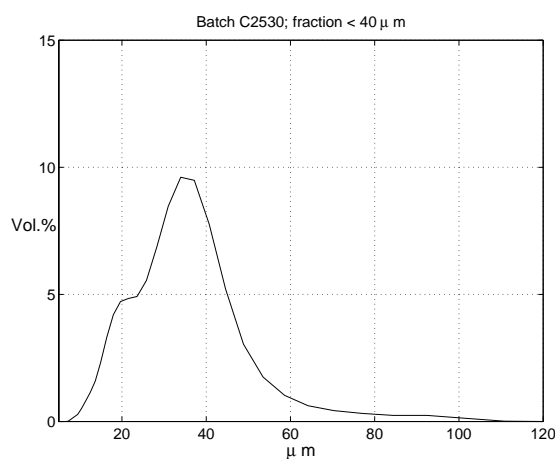
Appendix G

Particle size distributions

In the experiments spherical glass spheres are used. The particles were obtained from Potters Ballotini in two different batches e.g. C2530 and C5000. Batch C5000 contained smaller particles than batch C2530 and was not sieved. Batch 2530 was split up in different size fractions using standard sieves. The fractions are defined by the sieve sizes used to obtain the fraction. For the three fractions of batch C2530 and for batch C5000 the particle size distribution, measured using a Coulter LS particle sizer, are given in table G.1 and figure G.1.

Batch	fraction	$d_{p,10}$	$d_{p,50}$	$d_{p,90}$
C5000	-	2.4	7.6	27
C2530	< 40	0.7	30	47
C2530	45-50	8.3	41	52
C2530	50-56	38	50	62

Table G.1 Particle size distributions (in μm) for the particles used in the experiments.



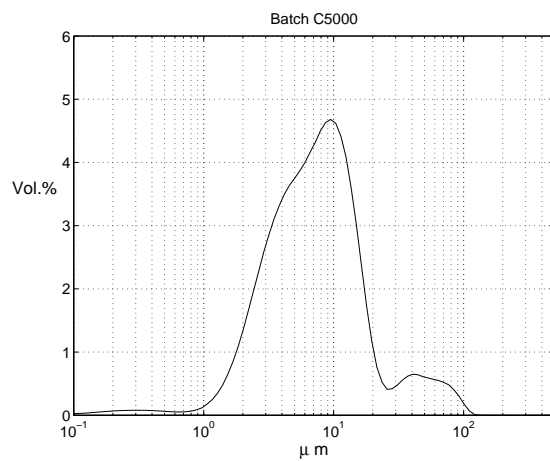
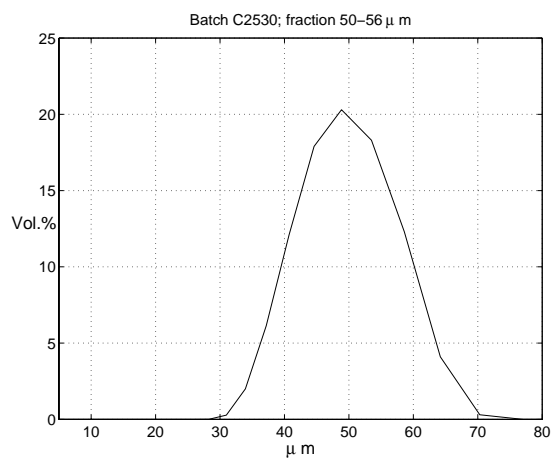


Figure G.1 Particle size distributions

Nomenclature

A	surface	m^2
B_r	width rebound curve	m
B_T	dimensionless correction number	-
b_{im}	width camera image	m
C_p	particle concentration	$kg\ m^{-3}$
C_D	drag coefficient	-
C_μ	model constant k - ε model	-
$C_{\varepsilon 1}$	model constant k - ε model	-
$C_{\varepsilon 2}$	model constant k - ε model	-
C_f	skin friction coefficient	-
C_l	length scale parameter	-
C_m	proportionality factor	-
c_p	constant pressure specific heat	$J\ kg^{-1}\ K^{-1}$
Da	Damköhler number	-
D_b	Brownian diffusion coefficient	$m^2\ s^{-1}$
D_{tube}	tube diameter	m
D_{cyl}	cylinder diameter	m
d	diameter	m
E	Youngs modulus	$N\ m^{-2}$
e	coefficient of restitution	-
e_{syst}	relative systematic error	-
F	correction factor	-
F	cumulative mass distribution function	-
\vec{F}	force vector	N
\vec{F}_{AM}	added mass force	N
\vec{F}_{BH}	Basset history force	N
\vec{F}_D	drag force	N
\vec{F}_g	gravitation force	N
\vec{F}_L	lift force	N

\vec{F}_{PG}	pressure gradient force	N
f_{μ}, f_1, f_2	damping functions low-Reynolds $k - \varepsilon$ model	-
f	friction coefficient	-
f_{ch}	chopper frequency	-
g, \vec{g}	gravitation acceleration, gravitation vector	$m s^{-2}$
H	fall height	m
H_{inj}	injection height	m
H_r	height rebound curve	m
H_v	Vickers hardness	$N m^{-2}$
h	distance of approach	m
h_i	height used for correction incident velocity	m
h_{im}	height camera image	m
h_o	heat transfer coefficient from the tube to the gas	$W m^{-2} K^{-1}$
h_r	height used for correction incident velocity	m
I	turbulence intensity	-
I_k	moment of inertia of body k	$kg m^2$
k	thermal conductivity	$W m^{-1} K^{-1}$
k	turbulent kinetic energy	$m^2 s^{-2}$
l_E	dimensionless dissipation length scale	-
L	length scale	m
Le	Lewis number	-
$LMTD$	log mean temperature difference	K
M	Moh's hardness	-
N	relative error	-
m	mass	kg
\dot{m}	mass flow rate	$kg s^{-1}$
n	number of particles tracked	-
\vec{n}	unit vector in normal direction	-
\vec{P}	impulse vector	Ns
p	pressure or dimensionless pressure	$N m^{-2}, -$
Q	energy	J
\dot{Q}	heat transfer rate	$J s^{-1}$
R	radius	m
R_c	contact radius in restitution phase	m
Re	Reynolds number	-
Re_p	particle Reynolds number	-
Re_p'	local particle Reynolds number	-
R_f	fouling resistance	$m^2 K W^{-1}$
$R_{f,\infty}$	asymptotic fouling resistance	$m^2 K W^{-1}$
R_T	turbulent Reynolds number	-
r	dimensionless distance to tube, radius	-, m

S_L	pitch in longitudinal direction	m
S_T	pitch in transverse direction	m
St	Stanton number	-
St_o	Stanton number for convection and Brownian diffusion	-
Sc	Schmidt number	-
Sh	Sherwood number	-
Stk	Stokes number	-
s	sticking coefficient	-
T	temperature	K
t	time	s
t_E	dimensionless eddy life time	-
\vec{t}	unit vector in tangential direction	-
U	velocity scale	m s^{-1}
U_o	overall heat transfer coefficient	$\text{W m}^{-2} \text{K}^{-1}$
U_∞	main stream velocity	m s^{-1}
u^*	friction velocity	m s^{-1}
$\vec{u} = [u \ v \ w]$	velocity vector, dimensionless velocity vector	$\text{m s}^{-1}, -$
V_d	deposition velocity	m s^{-1}
v	velocity or dimensionless velocity	$\text{m s}^{-1}, -$
W_A^k	work of adhesion for interaction k	J m^{-2}
$\vec{x} = [x \ y \ z]$	position vector or dimensionless position vector	m, -
Y	yield stress	N m^{-2}
y	elastic load limit	N m^{-2}
y^+	dimensionless wall coordinate	-

Greek symbols

α	impact angle	-
α_T	thermal diffusion factor	-
β	rebound angle	-
Δ	dimensionless roughness parameter	-
$\Delta x, \Delta y$	displacement in x and y-direction	m
δ	thickness; displacement	m
δ	boundary layer thickness	m
ε	rate of turbulent energy dissipation per unit mass	$\text{m}^2 \text{s}^{-3}$
ε_B	ratio between Basset history force and Stokes drag	-
ε_y	relative rebound velocity in y-direction	-
η	efficiency	-
κ	rate of strain	s^{-1}
θ	angle on tube, local contact angle	-
θ_s	separation angle	-

μ	dynamic viscosity	$\text{kg m}^{-1} \text{s}^{-1}$
μ_T	turbulent viscosity	$\text{kg m}^{-1} \text{s}^{-1}$
ν	kinematic viscosity	$\text{m}^2 \text{s}^{-1}$
ν	Poisson constant	-
ϕ	mass flux rate	$\text{kg m}^{-2} \text{s}^{-1}$
ϕ_l	porosity layer	-
ρ	density	kg m^{-3}
σ	standard deviation	-
σ_k	model constant $k - \varepsilon$ model	-
σ_ε	model constant $k - \varepsilon$ model	-
τ	time constant, shear stress	s, N m^{-2}
τ_p	particle relaxation time	s
τ_w	wall shear stress	N m^{-2}
$\vec{\omega}$	angular velocity vector	s^{-1}
γ	surface free energy	J m^{-2}
Γ	work of adhesion	J m^{-2}

Notations

ϕ'	fluctuation relative to mean
$\bar{\phi}$	normal mean or Reynolds-averaged quantity

Subscripts

1	incident body or particle
2	second body i.e. fouling layer
A	adhesion
a	approach
av	average
b	bulk, bed
c	clean, camera
$coll$	collection
$crit$	critical
d	deposition
ds	downstream
el	limiting elastic case
exp	experimental
f	fouled, fouling
g	flue gas, gas
i, j, k	index
i	impact, incident
inj	injection

<i>K</i>	Kolmogorov
<i>k</i>	kinetic
<i>L</i>	large scale fluid motions
<i>l</i>	limiting
<i>loss</i>	loss
<i>max</i>	maximal
<i>n</i>	normal direction
<i>num</i>	numerical
<i>o</i>	outer surface tube bundle
<i>p</i>	particle, plastic
<i>pe</i>	plastic-elastic
<i>pix</i>	pixels
<i>r</i>	rebound; removal
<i>ref</i>	reference
<i>s</i>	slip, surface
<i>st</i>	steam
<i>t</i>	total; tangential direction
<i>t'</i>	tangential direction rebound
<i>us</i>	upstream
<i>w</i>	wall
<i>x</i>	x-direction
<i>y</i>	y-direction

Superscripts

*	effective
<i>m</i>	measured value
<i>r</i>	real value

Summary

The formation of an insulating layer on heat transfer surfaces, known as fouling, is a common problem in heat-recovery applications. The boiler in a refuse waste incinerator is an example of such an application. On the gas-side of the tubes in this boiler a layer develops because of the deposition of fly-ash particles. As observed, the character of the layer formed is related to the local gas and tube temperatures. On the superheater tube bundle the layer is thick and sintered while on the economiser bundle the layer is thin and powdery. The difference in both types of layers is attributed to the presence of local melts in the superheater layer. From process data it appeared that both types of layers resulted in a 27% reduction of the overall heat transfer coefficient. In this investigation a model is developed with which the rate of deposition can be calculated as a function of the process conditions and the geometry of the bundle. The model is confined to the formation of a powdery layer.

In the developed model the transport of particles from the gas to the tube walls is simulated by individual particle tracks in a computed flow field. The turbulent flow field is calculated using a low-Reynolds $k-\varepsilon$ model and for the particle tracking use is made of an eddy-interaction model. This model has been modified to take anisotropy in the boundary layer into account and to compensate for steep gradients in the flow characteristics upstream of the tube. Using the modified model calculated transport rates agreed well with values reported in literature.

After a particle has reached the tube wall a sticking model determines whether the particle sticks and deposits or rebounds. The sticking model is based on the assumption that the impact of the particle on the layer can be modelled as a two-body collision with the second body representing the layer. The mass of this second body is assumed to be proportional to the mass of the incident particle. Besides the proportionality factor between the two masses, also the coefficient of restitution and the friction coefficient are important model parameters. For the coefficient of restitution, a measure for the amount of energy losses over an impact, a separate model is presented.

To validate the two-body approach and to determine the model parameters an experimental set-up has been built. In this set-up impact experiments are performed on different surfaces. From an experiment on a solid glass surface the

coefficient of restitution and the friction coefficient are measured. Experiments on a powdery layer show that the proportionality factor is 3.5 for a layer composed of particles with the same size as that of the incident particles and 2.6 for a layer consisting of 6.6 times smaller particles. With these proportionality factors, it is found that the agreement between the two-body model and the experiments performed at different impact angles and incident velocities is satisfactory.

Using the developed deposition model calculations have been performed for various tube bundle geometries. In the original economiser geometry, it is found that predicted deposition rates closely resemble the deposition rates as estimated from the observed decrease in heat transfer for the economisers. Furthermore, it is found that deposition is reduced when the distance between two tube rows in the direction normal to the main stream velocity is decreased, a staggered instead of an in-line arrangement is applied and when elliptical instead of circular tubes are used. On the basis of these recommendations, the deposition rates for the economiser can be reduced with more than 75%, limiting the decrease in heat transfer coefficient due to fouling to 8% compared to the original 27%.

Samenvatting

De vorming van een slecht warmtegeleidende laag op een warmtewisselend oppervlak is een bekend probleem bij warmteterugwinningsinstallaties. De vervuiling zoals deze optreedt in een afgassenketel is hiervan een voorbeeld. Door het neerslaan van vliegasaandeeltjes vormt zich een laag aan de gaszijde van de pijpen in de ketel. De aard van de laag is afhankelijk van lokale gas- en pijptemperaturen. De laag op de pijpenbundels in de oververhitter is dik en gesinterd terwijl de laag op de economisers dun en poederachtig is. Het verschil wordt veroorzaakt door het lokaal smelten van materie in de laag van de oververhitter. Uit procesgegevens is gebleken dat beide laagsoorten de warmteoverdracht van de pijpenbundel met 27% verminderen. In dit onderzoek is een model ontwikkeld waarmee de depositiesnelheid berekend kan worden als functie van de procescondities en de geometrie van de bundel. Het model beperkt zich tot de vorming van een poederachtige laag.

In het ontwikkelde model is het transport van deeltjes van het gas naar de pijp wand bepaald door het berekenen van individuele deeltjesbanen in een vooraf berekend stromingsveld. Voor de berekening van het turbulente stromingsveld is gebruik gemaakt van het 'low-Reynolds $k-\varepsilon$ model' en voor het berekenen van de deeltjesbanen is een 'eddy-interaction' model toegepast. Dit laatste model is aangepast om ook de invloed van anisotropie in de grenslaag te kunnen verdisconteren en om te compenseren voor de steile gradiënten in het stromingsveld aan de aanstroomzijde van de pijpen. De met het gemodificeerde model berekende waarden voor het transport van deeltjes zijn in goede overeenkomst met de waarden bekend uit de literatuur.

Nadat een deeltje de wand heeft bereikt, bepaalt een 'sticking' model of een deeltje blijft plakken of terugbotst. Het sticking model veronderstelt dat de botsing van een deeltje met een laag van deeltjes beschreven kan worden als een botsing tussen twee deeltjes. In deze botsing representeert het tweede deeltje de laag en wordt verondersteld dat dit tweede deeltje een massa heeft die evenredig is met de massa van het inkomend deeltje. Naast de factor die de massa van de deeltjes aan elkaar relateert, de evenredigheidsconstante, bevat het sticking model nog twee parameters; de restitutiecoëfficiënt en de wrijvingscoëfficiënt. De restitutie-

coëfficiënt is een maat voor de hoeveelheid energie die bij de botsing verloren gaat en wordt berekend met een apart model.

Om het twee-deeltjes model te valideren en de belangrijkste parameters te bepalen is een experimentele opstelling gebouwd. In deze opstelling zijn botsingsexperimenten uitgevoerd op verschillende oppervlakken. Uit een experiment op een vlakke glazen plaat zijn de restitutie- en de wrijvingscoëfficiënt bepaald. Vervolgens is uit een experiment op een poederachtige laag de evenredigheidsconstante bepaald. Deze constante is 3.5 voor een laag met deeltjes van dezelfde grootte als die van de inkomende deeltjes en 2.6 voor een laag waar de deeltjes gemiddeld 6.6 keer kleiner zijn. Met de gemeten evenredigheidsconstante blijkt het twee-deeltjes model geschikt om de resultaten van de experimenten op een poederachtige laag met verschillende invalshoeken en snelheden te beschrijven.

Het ontwikkelde depositiemodel is gebruikt om de depositiesnelheid te berekenen voor verschillende pijpenbundels. De door het model voorspelde depositiesnelheid in het oorspronkelijke ontwerp van de economiser is in overeenstemming met de depositiesnelheid zoals bepaalt uit de afname van de warmteoverdracht. De berekeningen laten bovendien zien dat de depositiesnelheid afneemt als de afstand tussen de pijpenrijen in de richting loodrecht op de hoofdstroomsnelheid verkleind wordt, een ‘staggered’ in plaats van een ‘in-line’ pijpenpatroon toegepast wordt en wanneer elliptische in plaats van ronde pijpen gebruikt worden. Op basis van deze aanbevelingen kan de depositiesnelheid voor de economiser met meer dan 75% gereduceerd worden waardoor de vermindering van warmteoverdracht van 27% in het oorspronkelijke ontwerp tot 8% teruggebracht kan worden.

Nawoord

Een bijzonder moment, na bijna 5 jaar is het proefschrift klaar. De tegenstelling met mijn uitspraak; “Ik ga nooit promoveren” is evident. Geïnteresseerd en geprikkeld door het projectvoorstel ben ik destijds gelukkig van mening veranderd en aan het onderzoek begonnen. Het is een hele boeiende en bovenal leerzame periode geweest. De ontspannen en prettige sfeer binnen de groep Energietechnologie aan de TU in Eindhoven was daarbij erg fijn.

Om tot het resultaat, zoals gepresenteerd in dit proefschrift, te komen ben ik dank verschuldigd aan de volgende personen; in de eerste plaats mijn promotor Anton van Steenhoven en mijn begeleiders Camilo Rindt en Johan Wijers voor het kritisch volgen van de vorderingen in het onderzoek en het nauwgezet corrigeren van de door mij aangeleverde stukken. Daarnaast Jos Keurentjes bedankt voor zijn bijdrage als tweede promotor en Rob, Bas, Hans en Arjan voor hun gewaardeerde bijdrage aan het onderzoek als afstudeerder of stagiair. Ook Frits en Frank bedankt voor hun ondersteuning in het laboratorium, Peter en Lambert voor het bouwen van de opstelling, Gert voor de assistentie bij de meetmethode, Ad, Jan en Roy voor alles wat met PC's te maken heeft en Rian en Marjan die de groep, vanuit het secretariaat, completeren.

Naast alle collega's in de groep Energietechnologie wil ik vooral mijn kamergenoten René en Misheck bedanken voor de leuke (en soms zelfs serieuze) gesprekken en Maurice, Bart, Marco, Camilo en Rob voor de welkome onderbrekingen tijdens de borrel, de koffie of op de gang.

Mijn huidige werkgever EPON gaf mij de nodige ruimte en flexibiliteit tijdens het afronden van het proefschrift en daarvoor bedankt.

Tot slot wil ik Lianne bedanken voor haar steun in de afgelopen jaren maar met name in de afgelopen zes maanden. Ook bedank ik in dit verband mijn ouders en schoonouders voor hun op velerlei wijze geboden ondersteuning.

Curriculum Vitae

- 1972, March 31st Born in Waalwijk, The Netherlands
- 1984 - 1990 Pre-university education (Atheneum)
Willem van Oranje College, Waalwijk
- 1990 - 1995 Mechanical Engineering
Technische Universiteit Eindhoven
M.Sc. Degree on the design of a steam injection system for an experimental gasturbine set-up
- 1997 - 1999 Evening-course: Management, economics and law
HEAO, Breda
- 1996 - 2000 Ph.D. project: “Gas-side fouling in heat-recovery boilers”
Faculty of Mechanical Engineering, section Energytechnology
Faculty of Chemistry, section Process Development
- 2000 - Advisor Gasturbines at EPON a Dutch electricity producing company

Stellingen

behorende bij het proefschrift

Gas-side fouling of heat-recovery boilers

Marco van Beek

- 1) Het gebruik van elliptische in plaats van cilindrische pijpen als warmteoverdragend oppervlak in een afgassenketel kan de vervuiling van deze pijpen sterk reduceren (dit proefschrift).
- 2) Ook een vervuilingsslaag die er zo onschuldig uitziet als de dunne poederachtige laag op de economisers kan een sterk negatief effect hebben op de warmteoverdrachtscoëfficiënt (dit proefschrift).
- 3) De experimentele validatie van het model voor de ‘coefficient of restitution’ is, anders dan gesuggereerd in het artikel van Rogers and Reed, verre van triviaal (dit proefschrift; Rogers, D.E. and Reed, J., *Journal of Physics D: Applied Physics*, vol. 17, pp. 677-689, 1984).
- 4) Een ontwerp dat slecht scoort op het punt van vervuiling biedt perspectief als filter.
- 5) Netzomin als het stenen tijdperk geëindigd is door een gebrek aan stenen zal ook het ‘olie tijdperk’ niet eindigen door een gebrek aan olie (Jeroen van der Veer, Shell).
- 6) De discussie over het bereiken van een duurzame samenleving kan pas goed beginnen als de definitie van duurzaamheid, zoals geformuleerd door Angela Merker, gehanteerd wordt. Duurzaamheid: “Het niet sneller gebruiken van natuurlijke bronnen dan dat zij zichzelf kunnen regenereren en het niet sneller emitteren van schadelijke stoffen dan dat de natuur kan assimileren.” Aldus geformuleerd kan alleen een ecologische ramp binnen afzienbare tijd tot duurzaamheid leiden.
- 7) Het delen van een kamer met iemand uit Zambia heeft meer dan eens bewezen dat voor het functioneren van een multi-culturele samenleving het kunnen inleven in de cultuur van de ander onderschat wordt. Hieruit blijkt dat het aantrekken van buitenlandse promovendi door universiteiten meer dan één doel dient.
- 8) “We komen gauw eens langs” is een op feestjes veel gebruikte maar niet vaak nagekomen afspraak, maar omdat net als een auto ook vrienden onderhoud verdienen, zou afspraak is afspraak ook dan moeten gelden.
- 9) Niet elke vraag mag gesteld worden.
- 10) Een sterke koersdaling is voor een actieve belegger het meest interessant.